Technische Universität München
Fakultät für Physik
Physics of Energy Conversion and Storage

Prussian Blue Analogs For Aqueous Na-Ion Batteries: Identification, Understanding and Optimization

Jeongsik Yun

Vollständiger Abdruck der von der Fakultät für Physik der Technischen Universität München zur Erlangung des akademischen Grades eines Doktors der Naturwissenschaften (Dr. rer. nat.) genehmigten Dissertation.

Vorsitzende: Prof. Dr. Nora Brambilla

Prüfer der Dissertation:

1. Prof. Dr. Aliaksandr S. Bandarenka
2. Prof. Dr. Alessio Gagliardi

Die Dissertation wurde am 12.03.2020 bei der Technischen Universität München eingereicht und durch die Fakultät für Physik am 10.06.2020 angenommen.

Table of Contents

Acknowledgment

This dissertation would have not been accomplished without the help and support of many people. I would like to express my acknowledgment to…

… Prof. Dr. Aliaksandr Bandarenka for giving me the opportunity to work on these interesting topics and supervising me throughout my master thesis and PhD studies. During my five years in at the group of Physics of Energy Conversion and Storage, I have learned and understood electrochemistry from fundamentals to applications under great supervision. He was a strict teacher, raising me as an individual scientist with the professional mind. Last but not least, I also appreciate his non-scientific advice during my time in his group.

… Prof. Dr. Alessio Gagliardi for being the second reviewer of my dissertation.

… Prof. Se Yeong Jeong and Prof. Chae Ryong Cho for giving me excellent Physics lectures and much advice which made me decide to go to the Technical University of Munich to do my PhD in Physics. Also, I would like to acknowledge them for giving me opportunities to collaborate on interesting research.

… Prof. Naoaki Yabuuchi for accepting me as a special research student in his group for three months. During my stay in his group, I have learned different research methods to investigate batteries, which greatly extends my research ability.

… Dr. Batyr Garlyyev, Dr. Daniel Scieszka, Johaness Fichtner, Dr. Yunchang Liang, Dr. Sebastian Watzele, Theophilus Kobina Sarpey, Regina Kluge, Richard Haid, and Philipp Marzak for their constructive feedbacks to correct not only my dissertation but also in scientific work and daily German translations.

… Dr. Jonas Pfisterer, Florian Schiegg, Franz Dinkelacker, Albrecht Dorsel, Radu Bors, Christian Sohr, Paul Scheibenbogen, Marc Kosiahn, Oliver Schneider, Philipp Moser for collaborations and discussions for successful publications.
… Siegfried Schreier and Markus Haß for their professional technical assistance during my stay at the ECS group. I would also like to thank Siegfried for having a conversation with me in German.

… ECS members: Dr. Viktor Čolić, Dr. Marcus Pohl, Enggar Wibowo, Christoph Csoklich, David Reinisch, Bianca Paulitsch, Jongho Kim, Dr. Wei-Jin Lin, Swaroopa Ganti, Namitha Rajendran, Xing Ding, Florian Schieg, Alexander Wieczorek, Pascal Hauenstein, Angus Laurenson, Mike Dao, Johannes Figueiredo, Muhammad Umair Ul Hassan, Nasim Tavakoli, and Borja Pano for having an enjoyable atmosphere during my studies.

... our secretaries Manuela Ritter and Susanne Tillich for handling all the bureaucratic works during my stay at the TUM.

... my local church community for being my second family in Munich. I would like to express a special acknowledgment to Pastor Nam and his family for their care.

I would like to thank Nagelschneider Stiftung for financial support during my studies.

Lastly, I would like to express my sincere love to my family. All I have achieved would have not been possible without their support and love.

Abstract

The transition of energy generation and consumption from fossil fuels towards clean and sustainable energy provision schemes has been accelerated with worldwide public and governmental recognition of environmental pollutions and depletion of fossil fuels. Renewable energy such as solar- and wind power provides a significant amount of energy in many countries. However, the intermittency of this energy generation requires the development of safe and reliable storage systems being an essential element for drawing a road map towards a green and sustainable society. The energy demands are expected to substantially increase in a few decades, mainly due to population growth and the modernization of developing countries. Hence, the identification of energy storage materials based on low-cost and earth-abundant elements is essential to mediate the energy crisis of upscaling the renewable powers, namely the “Terawatt-Challenge”, in time.

Rechargeable batteries are considered to be an appropriate energy storage system for different countries having different geographic conditions. The most advanced batteries, Li-ion batteries, seem to meet most of the functional requirements, such as high energy and power density, high round-trip efficiency and acceptable cycle life. Nevertheless, the sustainability and availability of raw materials for the current Li-ion batteries are not sufficiently high to cope with the anticipated growth of the deployment of renewable energy. Further, safety issues associated with environmentally unfriendly and flammable organic electrolytes of Li-ion batteries are another problem to be addressed for large-scale applications.

Na-ion batteries operating in aqueous electrolytes redeem the drawbacks of Li-ion batteries in large-scale applications. The second element of the alkali metal group, Na, is highly abundant in the earth’s crust and evenly distributed worldwide. The global production of Na is known to be at least one order of magnitude higher compared to that of Li, and it is highly feasible to scale up the Na production. Similar electrochemical properties of Na enable to accommodate Li-ion battery technologies into developing Na-ion batteries. The use of aqueous electrolytes, which are generally less toxic and inexpensive, fundamentally resolves the safety concerns and reduces maintenance costs. Besides, the ionic conductivity

of aqueous electrolytes is much higher than that of organic electrolytes.

Despite many advantages of aqueous Na-ion batteries, there are a few challenges to be addressed. Due to the bigger size of Na-ions compared to that of Li-ions, Na-ions may pose more mechanical stress at intercalation compounds in operation, which leads to a decline of the life cycle and round-trip efficiency. The aqueous electrolytes have a much narrower electrochemical stability window (typically less than 2 V) compared to that of organic electrolytes (typically over 4 V). Thus, the choice of electrode materials is restricted, especially for anode materials. The main focus of my work is to develop electrode materials for aqueous Na-ion batteries and to understand their intercalation physics and chemistry. State-of-the-art electrode materials, namely Prussian blue analogs (PBAs), were investigated because of their desired properties as battery materials. For instance, they exhibit the facile tunability of chemical composition, moderate energy density, high power density, and excellent material durability against the reversible intercalation and deintercalation of alkali metal cations.

In this dissertation, four different PBAs, namely $Na_2Ni[Fe(CN)_6]$, $Na_2VO_x[Fe(CN)_6]$, $Na_2Cr[Fe(CN)_6]$, and $Na_XMn[Mn(CN)_6]$, are in focus of investigations due to their remarkable performance and interesting physicochemical properties. These four PBAs were prepared by electrochemical deposition and investigated with various characterization techniques. The essential interfacial processes in aqueous Na-ion batteries, namely Na-intercalation mechanisms, were studied in-depth using electrochemical impedance spectroscopy. A hypothetical model for the Na-intercalation mechanism in aqueous and non-aqueous media was proposed and verified for different intercalation systems. With the gained understanding of the intercalation process, model battery systems based on PBA electrodes were optimized, and their battery performances were tested. Beyond their battery performances, crucial factors in determining their electrochemical properties are presented.

Zusammenfassung

Der beschleunigte Wandel der Energieerzeugung von fossilen Brennstoffen hin zu einer sauberen und nachhaltigen Lösung ist dem weltweiten öffentlichen und staatlichen Bewusstseins der Umweltverschmutzung und der Erschöpfung der fossilen Brennstoffe zu verdanken. Erneuerbare Energien wie Sonnen- und Windenergie liefern in vielen Ländern einen erheblichen Anteil der Energie. Die Unterbrechung dieser Energieerzeugung erfordert jedoch die Entwicklung sicherer und zuverlässiger Energiespeichersysteme, welche ein wesentliches Element für die Erstellung eines Fahrplans für eine grüne und nachhaltige Gesellschaft darstellen. Es wird erwartet, dass der Energiebedarf in einigen Jahrzehnten erheblich ansteigen wird, hauptsächlich aufgrund des Bevölkerungswachstums und der Modernisierung in den Entwicklungsländern. Daher ist die Identifizierung von Energiespeichermaterialien, die auf kostengünstigen und reichlich vorkommenden Elementen basieren, von wesentlicher Bedeutung, um Probleme bei dem Ausbaus der erneuerbaren Energien, wie beispielsweise der "Terawatt-Herausforderung", rechtzeitig zu vermitteln.

Wiederaufladbare Batterien werden als ein geeignetes Energiespeichersystem für verschiedene Länder mit unterschiedlichen geographischen Bedingungen angesehen. Die fortschrittlichste Batterietechnologie, die Li-Ionen-Batterien, scheint die meisten funktionalen Anforderungen, wie hohe Energie- und Leistungsdichte, hohe Lade-Entladewirkungsgrad und eine akzeptable Zykluslebensdauer, zu erfüllen. Jedoch sind die Nachhaltigkeit und die Verfügbarkeit von Rohstoffen für die derzeitigen Li-Ionen-Batterien nicht ausreichend hoch, um das erwartete Wachstum der Entwicklung erneuerbarer Energiequellen zu bewältigen. Darüber hinaus stellen Sicherheitsfragen im Hinblick auf den umweltfreundlichen und brennbaren organischen Elektrolyten von Li-Ionen-Batterienweitere Probleme dar, die für großtechnische Anwendungen berücksichtigt werden müssen.

Na-Ionen-Batterien, die in wässrigen Elektrolyten betrieben werden, gleichen die Nachteile von Lithium-Ionen-Batterien in großtechnischen Anwendungen aus. Das zweite Element aus der Gruppe der Alkalimetalle, Na, ist in der Erdkruste sehr reichlich

vorhanden und global gleichmäßig verteilt. Die weltweite Produktion von Na ist bekanntermaßen mindestens eine Größenordnung höher als die von Li, und es ist sehr einfach, die Na-Produktion signifikant zu steigern. Die ähnlichen elektrochemischen Eigenschaften von Na ermöglichen es, Erkenntnisse aus der Li-Ionen-Batterietechnologien auf die Entwicklung von Na-Ionen-Batterien zu übertragen. Die Verwendung von wässrigen Elektrolyten, welche im Allgemeinen weniger giftig und kostengünstiger sind, löst grundsätzlich die Sicherheitsbedenken und reduziert die Wartungskosten. Außerdem ist die Ionenleitfähigkeit von wässrigen Elektrolyten viel höher als die von organischen Elektrolyten.

Trotz vieler Vorteile wässriger Na-Ionen-Batterien gibt es einige Herausforderungen, die es noch zu bewältigen gilt. Aufgrund der größeren Durchmesser der Na-Ionen im Vergleich zu den Li-Ionen stellen Na-Ionen im Betrieb eine größere mechanische Belastung an die Elektrodenmaterialien dar, was zu einer Verringerung der Lebensdauer und des Wirkungsgrades führt. Die wässrigen Elektrolyte haben ein viel engeres elektrochemisches Fenster (typischerweise weniger als 2 V) im Vergleich zu den organischen Elektrolyten (typischerweise über 4 V). Daher ist die Auswahl der Elektrodenmaterialien, insbesondere bei Anodenmaterialien, eingeschränkt.

Der Hauptfokus dieser Arbeit liegt auf der Entwicklung und Identifizierung von Elektrodenmaterialien für wässrige Na-Ionen-Batterien und auf der Untersuchung ihreres Interkalationsmechanismuses. Modernste Elektrodenmaterialien, nämlich Preußisch-Blaue-Analoge (PBAs), wurden wegen ihrer vorzüglichen Eigenschaften als Batterie-Materialien untersucht. Sie weisen beispielsweise eine einfache Abstimmbarkeit der chemischen Zusammensetzung, eine moderate Energiedichte, eine hohe Leistungsdichte und eine ausgezeichnete Materialbeständigkeit gegen reversible Interkalation und Deinterkalation von Alkalimetallkationen auf.

Vier verschiedene PBAs, nämlich $Na_2Ni[Fe(CN)_6]$, $Na_2VO_x[Fe(CN)_6]$, $Na_2Cr[Fe(CN)_6]$, and $Na_XMn[Mn(CN)_6]$, werden in dieser Dissertation vorgestellt und ihre bemerkenswerte Leistung und interessante Elektrochemie werden gezeigt. Die vier PBAs wurden durch elektrochemische Abscheidung hergestellt und mit verschiedenen Charakterisierungstechniken untersucht. Der wesentliche Grenzflächenprozess wässriger

Na-Ionen-Batterien, nämlich der Na-Interkalationsmechanismus, wurde mittels elektrochemischer Impedanzspektroskopie eingehend untersucht. Ein hypothetisches Modell für den Na-Interkalationsmechanismus in wässrigen Medien wurde vorgeschlagen und für verschiedene Interkalationssysteme verifiziert. Mit dem gewonnenen Verständnis des Interkalationsprozesses wurden Modellbatteriesysteme auf der Basis von PBA-Elektroden optimiert und ihre Batterieleistung getestet. Über ihre Batterieleistungen hinaus wird eine wichtige Erkenntniss die Aufschluss auf die entscheidenden Faktoren zur Bestimmung ihrer elektrochemischen Eigenschaften gewonnen.

Publications

1. J. Yun, J. Pfisterer, A. S. Bandarenka. How Simple Are the Models of Na Intercalation in Aqueous Media? *Energy Environ. Sci.* **2016**, 9, 955−961.

2. E. Ventosa, B. Paulitsch, P. Marzak, J. Yun, F. Schiegg, T. Quast, A. S. Bandarenka. The Mechanism of the Interfacial Charge and Mass Transfer during Intercalation of Alkali Metal Cations. *Adv. Sci.* **2016**, 3, 1600211.

3. D. Pham-Cong, J. H. Choi, J. Yun, A. S. Bandarenka, J. Kim, P. V. Braun, S. Y. Jeong, C. R. Cho. Synergistically Enhanced Electrochemical Performance of Hierarchical $MoS_2/TiNb_2O_7$ Hetero Nanostructures as Anode Materials for Li-Ion Batteries. *ACS Nano* **2017**, 11, 1026−1033.

4. B. Paulitsch, J. Yun, A.S. Bandarenka. Electrodeposited $Na_2VO_x[Fe(CN)_6]$ Films as a Cathode Material for Aqueous Na-Ion Batteries *Appl. Mater. Interfaces* **2017**, 9 8107-8112

5. D. Scieszka(1), J. Yun(1), A. S. Bandarenka. What Do Laser-Induced Transient Techniques Reveal for Batteries? Na- and K-Intercalation from Aqueous Electrolytes as an Example. *ACS Appl. Mater. Interfaces* **2017**, 9, 20213−20222.

6. J. Yun(1), F. A. Schiegg(1), Y. Liang, D. Scieszka, B. Garlyyev, A. Kwiatkowski, T. Wagner, A. S. Bandarenka. Electrochemically Formed $Na_xMn[Mn(CN)_6]$ Thin Film Anodes Demonstrate Sodium Intercalation and De-Intercalation at Extremely Negative Electrode Potentials in Aqueous Media. *ACS Appl. Energy Mater.* **2018**, 1, 123−128.

7. F. Dinkelacker(1), P. Marzak(1), J. Yun, Y. Liang, A. S. Bandarenka. A Multistage Mechanism of Lithium Intercalation into Graphite Anodes in Presence of the Solid Electrolyte Interface. *ACS Appl. Mater. Interfaces* **2018**, 10, 14063–14069.
8. R. Bors, J. Yun, P. Marzak, J. Fichtner, D. Scieszka, A. S. Bandarenka. Chromium(II) Hexacyanoferrate-Based Thin Films as a Material for Aqueous Alkali Metal Cation Batteries. *ACS Omega* **2018**, 3, 5111-5115.

9. P. Marzak, J. Yun, A. Dorsel, A. Kriele, R. Gilles, O. Schneider, A. S. Bandarenka. Electrodeposited $Na_2Ni[Fe(CN)_6]$ Thin Film Cathodes Exposed to Simulated Aqueous Na-Ion Battery Conditions *J. Phys. Chem. C* **2018**, 122, 8760–8768.

10. D. Scieszka, C. Sohr, P. Scheibenbogen, P. Marzak, J. Yun, Y. Liang, A. S. Bandarenka. Multiple Potentials of Maximum Entropy of a $Na_2Co[Fe(CN)_6]$ Battery Electrode Material: Does the Electrolyte Composition Control the Interface? *ACS Appl. Mater. Interfaces* **2018**, 10, 21688–21695.

11. P. Marzak, M. Kosian, J. Yun, A.S. Bandarenka. Intercalation of Mg^{2+} into Electrodeposited Prussian Blue Analogue Thin Films from Aqueous Electrolytes. *Electrochim. Acta* **2019**, 307, 157-163

12. P. Marzak,(1) P. Moser,(1) S. Schreier, D. Scieszka, J. Yun, O. Schneider, A.S. Bandarenka. A Cell for Controllable Formation and in-operando Electrochemical Characterization of Intercalation Materials for Aqueous Metal-Ion Batteries. *Small Methods* **2019**, 3, 1900445

13. J. Yun, R. Sagehashi, Y. Sato, S. Hoshino, H. B. Rajendra, A. S. Bandarenka, N. Yabuuchi, Nanosize and Metastable Molybdenum Oxides as Negative Electrode Materials for Durable High-energy Aqueous Li-ion Batteries. (in preparation)

14. M. Krbal, J. Yun, H. Sopha, L. Hromadko, A. S. Bandarenka, J. M. Macak. Reduced TiO_2 Nanotube Layers Electrochemically Coated by $Na_xMn[Mn(CN)_6]$: a Promising Na^+ Ion Battery Anode. (in preparation)

Conference Attendance

Oral Presentation

1. Collaborative Conference on 3D & Materials Research 2016, Incheon/Seoul, South Korea, 20th – 24th of June 2016, *Na-Intercalation: Multiparametric in-situ characterization* - *How Simple Are the Models of Na-Intercalation in Aqueous Media*?
2. Nanosystems Initiative Munich Summer Retreat, Herrsching, Germany, 27th – 29th of July 2016, *How Simple Are the Models of Na-Intercalation in Aqueous Media*.

Post Presentation

1. 8th Energy Colloquium of the Munich School of Engineering, Garching, Germany, 19th of July 2018*, Prussian Blue Analogues: Electrode Materials for High Voltage Aqueous Na-Ion Batteries.*
2. 11th Europe-Korea Conference on Science and Technology (EKC) 2018, Glasgow, UK, 20th – 24th of August 2018, *Electrodeposited Prussian Blue Analogues for High Voltage Aqueous Na-Ion Batteries*. - Best Poster Award

3. 69th Annual Meeting of the International Society of Electrochemistry, Bologna, Italy, 2nd – 7th of September 2018, *Electrodeposited Prussian Blue Analogues for High Voltage Aqueous Na-Ion Batteries.*

Attendance

1. The 59th Battery Symposium in Japan, Osaka, Japan, 27th – 29th of November 2018.

Abbreviations

AFM	Atomic Force Microscopy
AM	Alkali Metal
CAES	Compressed Air Energy Storage
CrHCF	Chromium Hexacyanoferrate
CV	Cyclic Voltammogram
DoD	Depth of Discharge
EC	Ethylene Carbonate
EEC	Equivalent Electric Circuit
EIS	Electrochemical Impedance Spectroscopy
EQCM	Electrochemical Quartz Crystal Microbalance
ESCA	Electron Spectroscopy for Chemical Analysis
ESI	Earth Similarity Index
ESS	Energy Storage System
EV	Electric Vehicle
FCC	Face-Centered Cubic
FES	Flywheel Energy Storage
GHG	Greenhouse Gas
HER	Hydrogen Evolution Reaction
IHP	Inner Helmholtz Plane
IPCC	Intergovernmental Panel on Climate Change
LiB	Li-ion Battery
MnHCMn	Manganese Hexacyanomanganate
NaOAc	Sodium Acetate
NASICON	Na Super Ionic Conductor

NiHCF	Nickel Hexacyanoferrate
Ni-MH	Nickel-Metal Hydride
NTCDA	1,4,5,8-Naphthalenetetracarboxylic Dianhydride
OAc^-	Acetate Anion
OHP	Outer Helmholtz Plane
PB	Prussian Blue
PBA	Prussian Blue Analog
PC	Propylene Carbonate
PHS	Pumped Hydroelectric Storage
QCM	Quartz Crystal Microbalance
SHE	Standard Hydrogen Electrode
SPM	Scanning Probe Microscopy
SSC	Silver/Silver Chloride
TES	Thermal Energy Storage
TM	Transition Metal
TMHCF	Transition Metal Hexacyanoferrate
UHV	Ultra-High Vacuum
VO_xHCF	Vanadium Hexacyanoferrate
XPS	X-ray Photoelectron Spectroscopy
ZEBRA	Zero Emission Battery Research Activity

1. Introduction

Despite the discovery of thousands of exoplanets,[1] to the best of current humankind's knowledge, there are only less than a dozen of potentially habitable planets in a conservative sense (ESI[1] > 0.8), and the earth is the sole planet in our galaxy where life exists.[2] Even if a habitable planet is explored in the future, its terraforming will require the astronomical advancement of science and technology with colossal capital and labor investments. This will not be realized in the near future. The best is to preserve the earth habitable. One of the basic requirements for "planetary habitability" is the existence of an atmosphere that is hospitable for life.[3] The climate of a planet, which substantially influences life, is highly dependent on the nature of its atmosphere. For instance, less than one Celsius degree change in atmospheric temperature significantly changes the frequency and magnitude of occurrence of natural disasters such as floods, droughts, typhoons, hurricanes, and tornados.[4-8]

Owing to the accumulation of greenhouse gases (GHGs) in the atmosphere, the average temperature increase of the earth's surface, *i.e.,* global warming, with respect to the pre-industrial level reached over 1 °C already in 2017 as shown in **Figure 1.1**.[7] According to the special report on Global Warming of 1.5 ºC of IPCC (Intergovernmental Panel on Climate Change), the Paris Agreement, which is an international pledge to regulate CO_2 emission against global warming well below 2 ºC regards to the pre-industrial level and to pursue 1.5 ºC above the level, is not enough to avoid hazardous climate changes.[7] However, the decline of CO_2 emission in line with the pledges at the Paris Agreement is reviewed to be tardy, even though the emission rate has been falling in a large part of advanced developed countries.[9] If the global temperature increases at the current rate (approximately + 0.2 °C per decade), 1.5 °C of global warming will be reached by 2040 (see **Figure 1.1**), which will then endanger the most vulnerable in the first place and potentially threatens all living things on the earth.[10]

---

1. ESI (Earth Similarity Index): A measure of similarity in planetary properties to the Earth (Earth is set to 1.0).

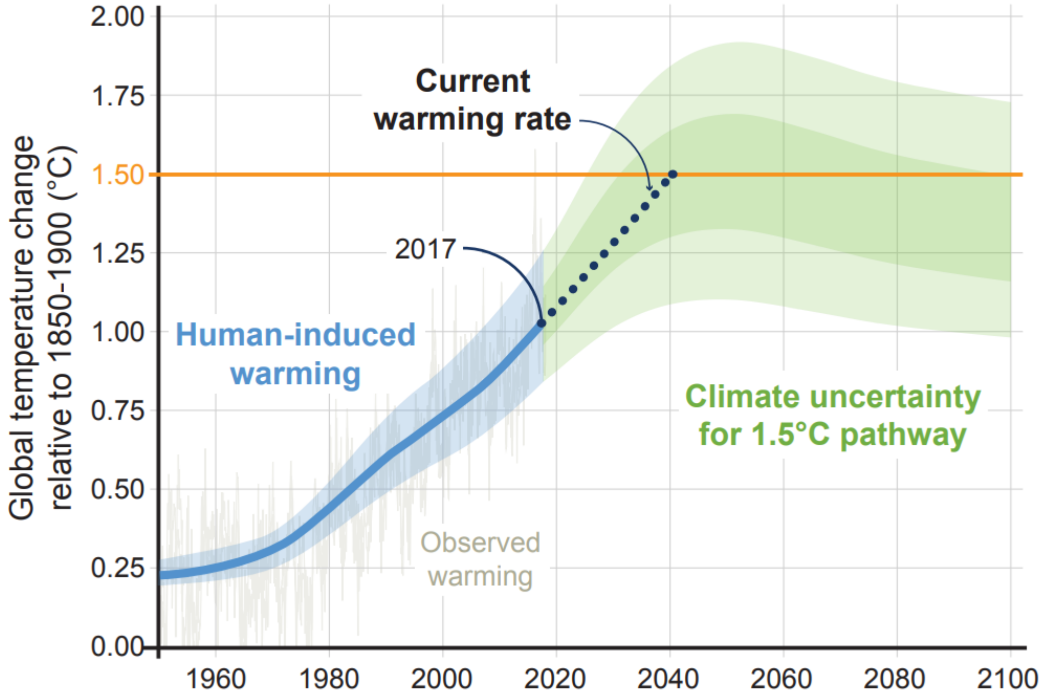

Figure 1.1. Global temperature change with respect to the pre-industrial level. The blue line shows human-induced warming, while the fluctuating grey line exhibits the observed warming. The dotted line is the projection of the temperature increase with the current warming rate. The green area displays a possible global temperature range. Adapted from reference.[7]

Moreover, modernization and electrification of developing countries in line with the expansion of the human population will accelerate the increase of CO_2 concentration in the atmosphere unless more strict disciplines for decarbonization of the atmosphere are conducted.[11-13] It should be noted that the projections of global population growth have often been underestimated.[14] Very recent reports warned us that many countries failed to achieve the level of the pledges of the Paris Agreement.[9, 15, 16]

With considerable subsidies for cleaner energy technologies since the Paris Agreement, there have been significant technological advancements of low-carbon energy productions, namely renewable energies. In 2017, the global renewable power capacity exceeded 2 TW with an enormous growth of the installation of non-hydropower renewables (over 1 TW) over 10 years, whereas hydropower showed a marginal contribution to the growth.[17]

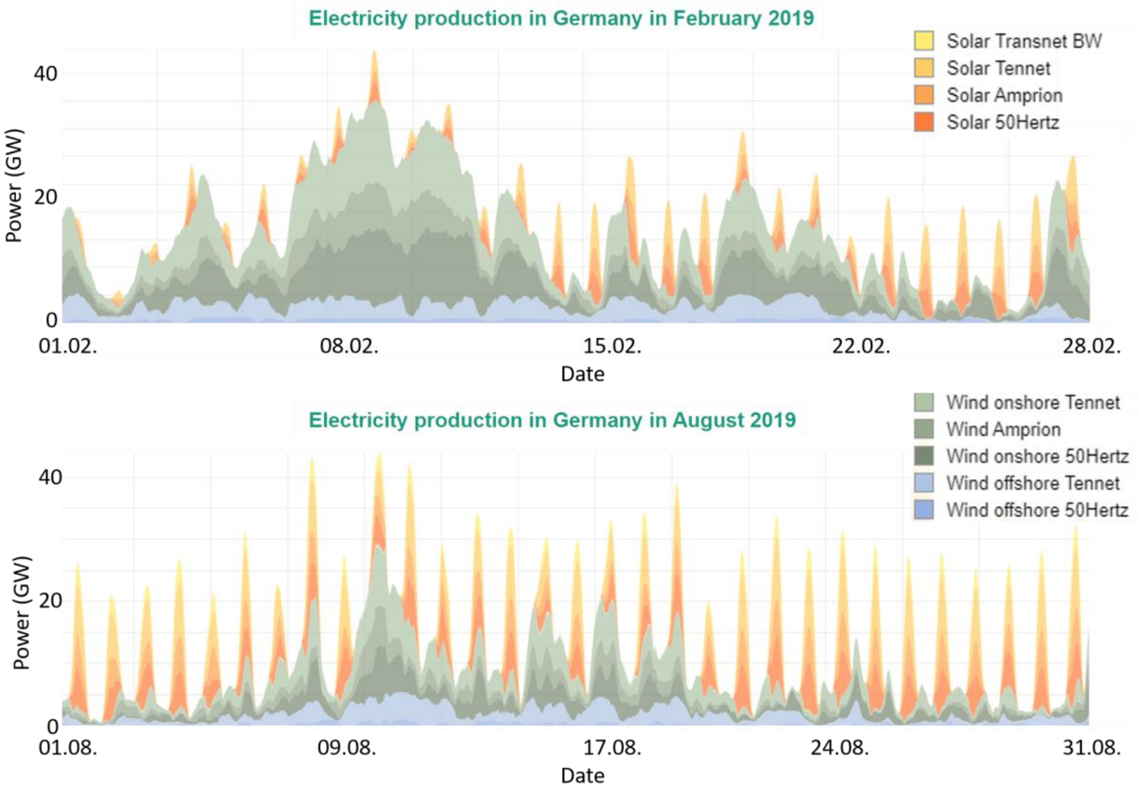

Figure 1.2. Electricity production based on solar and wind powers in Germany in February and in August 2019. Electricity generation is highly fluctuating daily and seasonally. Source: Fraunhofer ISE[18]

Solar- and wind power takes a significant share of the non-hydro renewable energy generation in the world.[17] However, the estimated share of renewable energies is only *ca* 26.2 % in total energy production in 2018.[19] In keeping with the human population growth, the increase in the energy demand will lead to increased energy production not solely from the renewables but also fossil fuels; the latter one will substantially contribute to the increase in GHG emissions. The total power generating capacity in the world was over 7 TW in 2018, and the global average energy consumption rate increased from *ca* 13.5 TW in 2001 to *ca* 18.6 TW in 2018.[19-21] It will continue to increase and reach *ca* 30 TW by 2050.[20] If we do not actively seek to upscale the low-carbon energy productions, global warming with climate and environmental changes will not be far from us.

In 2016, roughly 14 % of the world population (*ca* 1.06 billion people) lived without electricity. The majority of them are in sub-Saharan Africa, developing Asia, and rural regions, where the centralized electricity generation is inefficient to address the lack of electricity.[17] Distributed renewable power for energy access systems seems to be especially attractive for macro- and micro-grid applications not only in developed countries but also particularly in low population villages.

However, renewable energy provision schemes suffer from the stochastic and intermittent nature of atmospheric processes. For instance, **Figure 1.2** displays the highly fluctuating electricity generation from solar- and wind powers in Germany in winter (February) and summer (August) in 2019. There is a high likelihood of the mismatch of energy demand and provision, namely "generation vs consumption" problem.[22] For filling the time gap between the demand and supply of electricity, renewable energy systems should be equipped with energy storage systems (ESSs). ESSs for renewable energy applications should meet several requirements such as i) reasonable costs for installation and maintenance, ii) high energy and power densities, iii) high efficiency, iv) quick response rate, v) little losses of stored energy due to self-discharge and vi) long lifetime.[23] Various types of energy storage systems have been developed and can be classified by way of energy storage: mechanical, chemical, electrochemical, electric (and electromagnetic) or thermal.[23-35]

Mechanical energy storage systems include pumped hydroelectric storage (PHS), compressed air energy storage (CAES) and flywheel energy storage (FES). The technology of PHSs is the most advanced, and they are in operation in many countries. PHSs typically have a large capacity (MW- to GW-level), long life cycle, and high efficiency. The capacity of PHSs is highly dependent on the geographical nature of the location, such as the reservoirs' sizes and the height differences. Currently, the PHSs offer over 125 GW of total installed capacity in the world, which is equivalent to *ca* 3.6 % of the total energy consumption and 99% of the electricity storage capacity.[19, 21, 36, 37] However, PHSs have fundamental limitations, such as geographic conditions (great height difference, sufficient rainfalls, large lands), a very low energy density (3 Wh m^{-3} with 1 m of height difference), intensive capital investments, long construction time and substantial environmental issues.[36, 38-40]

Compressed air energy storage systems (CAESs) is another type of currently-available mechanical ESSs. There are two plants of CAES in operation, one in Germany and the other in the USA. CAESs provide a large capacity (MW-level), high power capacity and small self-discharge losses.[23, 41] Nonetheless, CAESs are not appropriate for ESSs of renewable energies due to their limitations that they can apply to particular topography and also consume fossil fuels.[36] Flywheel energy storages (FESs) have advantages of high energy efficiency (over 85 %), long life cycles (> 15 years), low environmental impacts, little maintenance cost and high power and energy density compared to other mechanical ESSs.[42] However, short operation life-time and high self-discharge losses are the main challenges to overcome.[25]

Electrochemical energy storage systems are based on the reversible conversion of chemical and electrical energy in a substance. Capacitors and batteries are the most known types that are commercially available. Capacitors store energy through the polarization of charge carriers at two electrodes. Conventional capacitors consist of two metal plates with (electrically) insulating media between them. They exhibit a swift response, tens of thousands of life cycles and high efficiency; but their energy density is very low to be deployed as ESSs. In order to increase the energy density, different types of capacitors are being developed, such as pseudocapacitors, double-layer capacitors and supercapacitors.[36] The advanced types of capacitors yet possess short storage time caused by high self-discharge loss; and the high cost (1100 – 1500 euro/kW)[43] is a significant demerit.

Batteries deliver electricity through internal electrochemical reactions. The rechargeability categorizes batteries into primary- and secondary (rechargeable) batteries. As ESSs for renewable powers, rechargeable batteries are applicable. The featured characteristics of secondary batteries are quick response time, high energy and power density, little self-discharge, high round-trip efficiency and relatively long cycle life.[44, 45] There is a great variety of commercialized rechargeable batteries. Lead-acid batteries have been widely used over 100 years in automotive and industrial applications. The cost of lead-acid batteries is relatively low, and their technology is mature. However, somewhat low energy density, short cycle life, low depth of discharge (DoD), slow rate capability and requirement of frequent maintenance are significant drawbacks for grid-scale ESS applications.[44] Ni-Cd batteries have higher energy density and longer cycle life than lead-acid batteries.[46] The comparatively low price, less complicated maintenance and robustness of Ni-Cd batteries are advantageous, but the so-called memory effect, the toxicity of Cd, relatively low efficiency and a high initial cost are the main barriers for the grid-applications.[36, 47, 48] Ni-MH (nickel-metal hydride) batteries are commercialized in the automotive sector, portable devices, and medical applications, but their high self-discharge, low cycle life, and failure due to the high pressure are major challenges to overcome.[47] Li-ion batteries (LiBs) are the most advanced battery systems that exhibits the highest energy density, long lifetime and high efficiency. The technology of LiBs has been significantly improved due to the growth of electric vehicle (EV) markets, but at the same time, the price of the raw materials of electrode compounds, namely Li, and Co, has also been increased. The scarcity, low abundance of Li and high demands for Li might become problematic for large-scale ESS applications.[49, 50] In contrast to the abovementioned battery systems, Na-S and Na-$NiCl_2$ batteries (also known as ZEBRA – Zero Emission Battery Research Activity) use electrodes in the liquid phase. Due to the high operation temperature of 270 - 350 ºC and the aggressive reaction of molten Na with water, they will most likely not be practical for residential applications.[51-53]

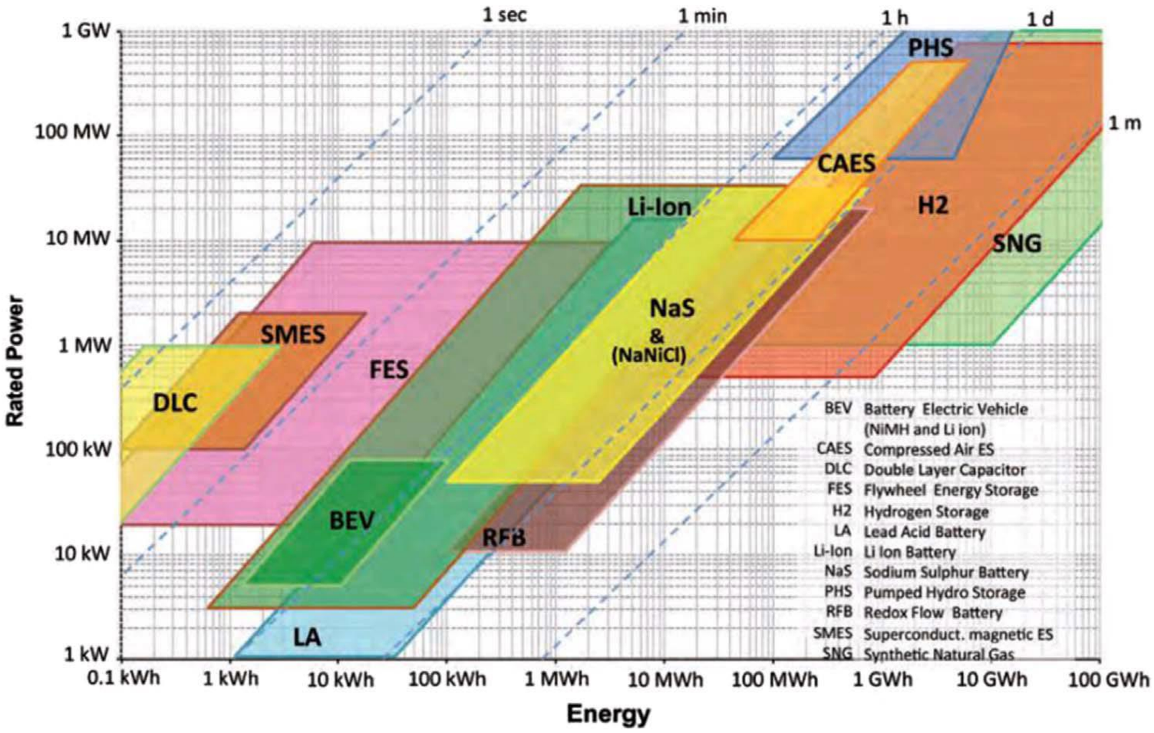

Figure 1.3. Various energy storage systems diagramed by power and energy. Reproduced from the reference [54] with permission from Elsevier.

The other types of energy storage systems are chemical energy storage, thermal energy storage (TES) and electromagnetic energy storage systems. Chemical energy storage can be categorized by the sort of substances that undergo reversible chemical reactions. Typical examples of the energy carriers are hydrogen, synthetic natural gas, and biofuels.[54-56] TES systems utilize heat storage media to store energy as sensible heat, latent heat, or by absorption and adsorption processes.[54, 56, 57] Superconducting magnetic energy storage is an electromagnetic ESS, which utilizes superconducting materials to store electricity in the magnetic fields under the critical temperature of a superconductor.[36, 55, 58] **Figure 1.3** summarizes the ranges of power and energy of various kinds of ESSs.

Compared to the other above-described ESS techniques, secondary battery ESSs have numerous desirable characteristics for renewable energy applications, namely high scalability in storage capacity, quick rate response, design flexibility, high round-trip efficiency (~99 %), zero-emission operation, less geographical restrictions, less environmental and ecological impacts and relatively simple maintenance.[26, 59-61] Among various battery technologies commercially available at this stage, Li-ion batteries are the most advanced type for mobile applications due to the highest gravimetric energy density.[62] However, for grid-scale stationary ESSs, other requirements take more significance over gravimetric energy density. Safety and costs for installation and operation will be of crucial concern.[63, 64] For instance, safety issues regarding Li-ion batteries have been raised after explosion accidents occurred from several commercialized products based on Li-ion batteries. There have been at least 14 explosions of Tesla cars since 2013 including an explosion at parking lots,[65] at least 35 cases for Samsung Galaxy Note 7 in 2016 worldwide[66] and at least 27 cases for ESSs in Korea, where 17 out of 27 were reported to be equipped with batteries of LG Chem., which is one of the largest and most advanced battery companies.[67]

The costs of battery raw materials have been substantially increased due to the vast demands for portable electric devices and electric vehicles.[68] For instance, the price of lithium carbonates, typical raw materials of Li, increased over 4 times within a few years.[19, 69, 70] The demand for Li is expected to substantially increase in the future, mainly by the electrification of automobiles with governmental policies in many countries.[69, 71-76] In addition to the growth of demands, political issues can further raise the price of essential elements. Natural lithium compounds occur in a few places in the world, and most of Li-reserves are located in politically sensitive locations.[64, 71, 77, 78] The price of cobalt, another main cathode element of Li-ion batteries, has also sharply increased over the past few years because of the expectation of an increase in the EV production in conjunction with political issues in Democratic Republic of Congo, which is the largest cobalt producing country.[79, 80] Sustainability factors are of another importance to facilitate green energy provision. The global energy consumption is expected to be doubled in a few decades, but for example, the accumulation time for Li is assessed to be over 100 years with the global current production rate if simply Li-ion batteries are deployed for EESs of renewable energies.[21, 22, 50, 81] The growth of the production of EVs equipped with Li-ion batteries will further limit Li-availability for grid-scale ESSs. Thus, it is necessary to develop and identify alternatives for Li-ion batteries to keep up with the increasing energy demands.

Aqueous Na-ion batteries appear to be a feasible system for the deployment in grid-scale ESSs due to their desirable properties in large-scale applications.[64, 82-93] The utilization of Na-ions instead of Li-ions as a charge carrier has many benefits. Sodium is the sixth most abundant element (the fourth most among metal) in the earth's crust and occurs in the form of numerous minerals or compounds in the oceans.[94] Because of the high abundance and even distribution of sodium resources, the accumulation of sodium does not seem to be an issue to address the so-called "terawatt challenge".[50] Moreover, the advanced Li-ion battery technology can be transferred into developing Na-ion batteries thanks to similar physical and electrochemical properties of Na to those of Li.[85, 95] The use of aqueous electrolytes additionally offers numerous benefits: i) it fundamentally removes the safety concern arising from toxic and flammable non-aqueous electrolytes. ii) Aqueous Na-electrolytes are generally cheaper, safer, and environmentally less noxious. iii) Aqueous electrolytes typically have higher ionic conductivity, which in turn provides higher power, compared to that of commonly-used non-aqueous electrolytes, *e.g.,* ethylene carbonate (EC) and propylene carbonate (PC).[96-99] iv) Heat capacity of aqueous electrolytes is roughly three times higher than that of EC or PC, which could minimize the battery failure due to the change of internal battery temperature.[100]

Nevertheless, aqueous Na-ion batteries also possess some drawbacks in comparison to Li-ion batteries. For instance, the bigger size and heavier weight of Na-ions compared to those of Li-ions not only reduce the energy density but also pose more stress on the electrode materials in the course of intercalation and deintercalation, which might cause shortening of the battery life cycle. The electrochemical stability window of aqueous electrolytes is generally much narrower compared to that of organic electrolytes. Beyond the stable potential window, water electrolysis takes place; thus, the choice of electrode compounds is more restricted.

Therefore, the focus of the development of aqueous Na-ion batteries lies in identifying electrode materials that not only show high energy, long life cycle and low costs but also operate within the electrochemical stability window. Recently, Prussian blue (PB) and its analogs (PBAs) were reviewed as promising electrode materials for aqueous alkali metal batteries for stationary applications due to their low-cost synthesis, long life cycles and high rate capability with moderate capacity.[92, 99, 101-103] However, there is still a room to enhance the working potentials and specific capacities reported in the available literature. A practical approach to improve the battery material performance can be formulated by understanding the fundamentals of battery charging and discharging processes, namely the intercalation mechanism.

The objective of this dissertation is, therefore, placed on developing high-performance electrode materials for aqueous Na-ion batteries and understanding the Na-intercalation mechanisms by utilizing model battery systems based on PBAs. Four different electrodes based on PBAs, which show remarkable performances, are presented in this dissertation. In Section 5.1, the synthesis and characterization of $Na_2Ni[Fe(CN)_6]$ thin films are described, and the Na-intercalation mechanism in aqueous media is studied utilizing mainly electrochemical impedance spectroscopy together with cyclic voltammetry and electrochemical quartz crystal microbalance. A hypothetical model for the Na-intercalation mechanism (the so-called “three-stage mechanism”) is proposed with the interpretation of obtained impedance spectra for $Na_2Ni[Fe(CN)_6]$ thin films. The significance of the electrolytes’ nature in determining the electrode properties and the relationship between the hydration energy of intercalating alkali metal cations and the potentials of their intercalation are demonstrated.

In Section 5.2, $Na_2VO_x[Fe(CN)_6]$ thin films are discussed as a high voltage cathode material. The validity of the three-stage mechanism was assessed in this system as well to check the applicability of the proposed hypothesis. A strategy to mediate the stability issues of $Na_2VO_x[Fe(CN)_6]$ thin films in less acidic media is suggested, and the stability enhancement was observed. Surprisingly, the hydration effect did not appear to be outstanding in the case of $Na_2VO_x[Fe(CN)_6]$ in contrast to the studied $Na_2Ni[Fe(CN)_6]$. An interesting correlation was found between the potentials of Na-intercalation in different PBAs with the radii of the transition metals that are coordinated to nitrogen.

Section 5.3 introduces $Na_2Cr[Fe(CN)_6]$ thin films as a high-performance and low-cost cathode material. A model cell consisting of two identical $Na_2Cr[Fe(CN)_6]$ thin films showed a moderate energy density with considerably high power density. Similarly to the case of $Na_2VO_x[Fe(CN)_6]$, the hydration effect was not pronounced in the $Na_2Cr[Fe(CN)_6]$ system. The size of the N-linked transition metals of the investigated systems appeared to be associated with the intercalation potentials of Na-ions in various electrodes based on PBAs.

Investigation of $Na_XMn[Mn(CN)_6]$ thin films as a promising anode material for aqueous Na-ion batteries is presented in Section 5.4. $Na_XMn[Mn(CN)_6]$ thin films exhibited a very low potential for Na-intercalation that is close to the limit of electrochemical stability potential windows of aqueous electrolytes without noticeable side reactions. The significantly high Coulombic efficiency and long cycle life of $Na_XMn[Mn(CN)_6]$ thin films were obtained. The study of the Na-intercalation mechanism in $Na_XMn[Mn(CN)_6]$ thin films is presented to verify the validity of the three-stage mechanism in different systems. The properties of the electrolyte components appear to be substantially related not only to the battery performance but also to the manipulation of hydrogen evolution reactions at $Na_XMn[Mn(CN)_6]$ thin films.

2. Electrochemistry

2.1 Short History of Electrochemistry

Electrochemistry is a branch of physical chemistry and chemical physics to study chemical reactions involving electricity generated or consumed by the reactions. The birth of electrochemistry is often attributed to the end of the 18th century in Italy when the famous Italian scientist Luigi Galvani published the study on the movement of the frog's legs by electrostimulation, which he concluded that it is from "*animal electricity*".[104] His consideration to link living muscles to electricity attracted considerable interest in the scientific community. Later, Alessandro Volta, who developed the first battery – "*voltaic piles*", disproved the theory of the animal electricity and found out that the origin is the potential difference between two different metals that were connected to the animal tissue.[105] Another important discovery, "*water electrolysis*", was made by Nicholson and Carlisle in the same year in England. They revealed that water is decomposed by electricity passing through it into H_2 and O_2, producing bubbles at the respective electrodes.

Meanwhile, in Germany, Johann Wilhelm Ritter was inspired by the voltaic pile and developed his first electrochemical cell. He discovered the "*electroplating process*", which is a critical process of, for instance, mass production of batteries.[106] Later, a brilliant scientist, Faraday, formulated the "Faraday's law" that describes the proportionality between the mass-produced by the electrolysis and the charge passed.[106] In 1836, John Frederic Daniell developed the famous "*Daniell cell*", which is often used for the education of the electrochemical battery.[106] A few years later, the first "*fuel cell*", which produces electrical energy using the chemical reaction between hydrogen and oxygen, was invented by William Robert Grove. In 1859, the French scientist Gaston Plante invented the "*lead-acid battery*", which is still used in many vehicles to date. In 1889, the most fundamental and essential equations, "*Arrhenius equation*" and "*Nernst equation*", were developed by Arrhenius and Nernst, who studied the dependence of the reaction rates on temperature and the electrochemical processes with the thermodynamic interpretation.[107]

Just before the beginning of the 20th century, the first "*electric vehicle*" was invented by Jamais Content, and it reached a speed of 100 km h^{-1}. In 1902, Cottrell formulated the equations describing the electrode kinetics with mass transport by diffusion. Three years later, Swiss chemist Julius Tafel empirically formulated the "*Tafel equation*", which describes the relationship between the electrode overpotential and the current. In 1914, Thomas Edison made the "*Ni/Fe alkaline battery*". The theory of charge transfer at the electrode, "*Butler-Volmer equation*", was founded by John Alfred Valentine Butler and Max Volmer in 1924-1930.[106]

Nowadays, electrochemistry has various scientific and industrial applications such as electrolysis, energy storage, and conversion, electrosynthesis, coating, corrosion and bio-electrochemistry. This chapter briefly describes the fundamentals of electrochemistry that are necessary for comprehending this dissertation.

2.2 Electrochemical Systems

Chemical reactions involving the electricity flow, "*electrochemical reactions*", are studied in an electrochemical cell consisting of electronic conductors, *i.e.,* "*electrodes*", and at least one ionic conductor, *i.e.,* "*electrolyte*". The electrodes and electrolytes can be either liquid or solid, but many electrochemistry studies utilize solid electrodes and liquid electrolytes. The electrolytes are ionically conductive and nearly electronically insulating, and the electron transfer caused by electrochemical reactions takes place at the interface between the electrolyte and the electrode.

At the interface between the electrode and the electrolyte, some species can gain or lose electrons depending on their nature, and the resulting current will flow through an external electric circuit. The chemical reaction in which the species gain electrons is called "*reduction*", and the electrode at which the reduction reaction takes place is termed "*cathode*". On the other hand, when the species lose electrons, the reaction is called "*oxidation*", and the electrode at which the oxidation occurs is termed "*anode*".

In brief, in electrochemistry, the reduction is the reaction when chemical species are reduced by gaining electrons at the cathode, and the oxidation is the reaction when chemical species are oxidized by losing electrons at the anode. This terminology is often confusing, but there is a convenient way to remember these terms. **Figure 2.1** shows the graphical illustration of redox reactions at a cathode and an anode. In the **Red**uction, **Cat**ions go to the **Cat**hode to be **Red**uced (gain negative charge), and in **Ox**idation, **An**ions go to the **An**ode to be **Ox**idized (being more positive). As highlighted with the bold texts, this can be illustrated with a "*red cat*" and "*an ox*" as shown in **Figure 2.1**. However, it should be noted that the sign of the redox species (either positive or negative) does not necessarily indicate the type of reactions. The matter is gaining or losing charges (electrons). For instance, Li, $Fe^{2+,}$ and $Fe(CN)_6^{4-}$ can be oxidized at the anode, and their conjugates species (Li^+, Fe^{3+}, and $Fe(CN)_6^{3-}$) can be reduced at the cathode, even though not all of them are "anions" or "cations." Therefore, this sentence should be used only for the sake of better memorization of the terms.[106]

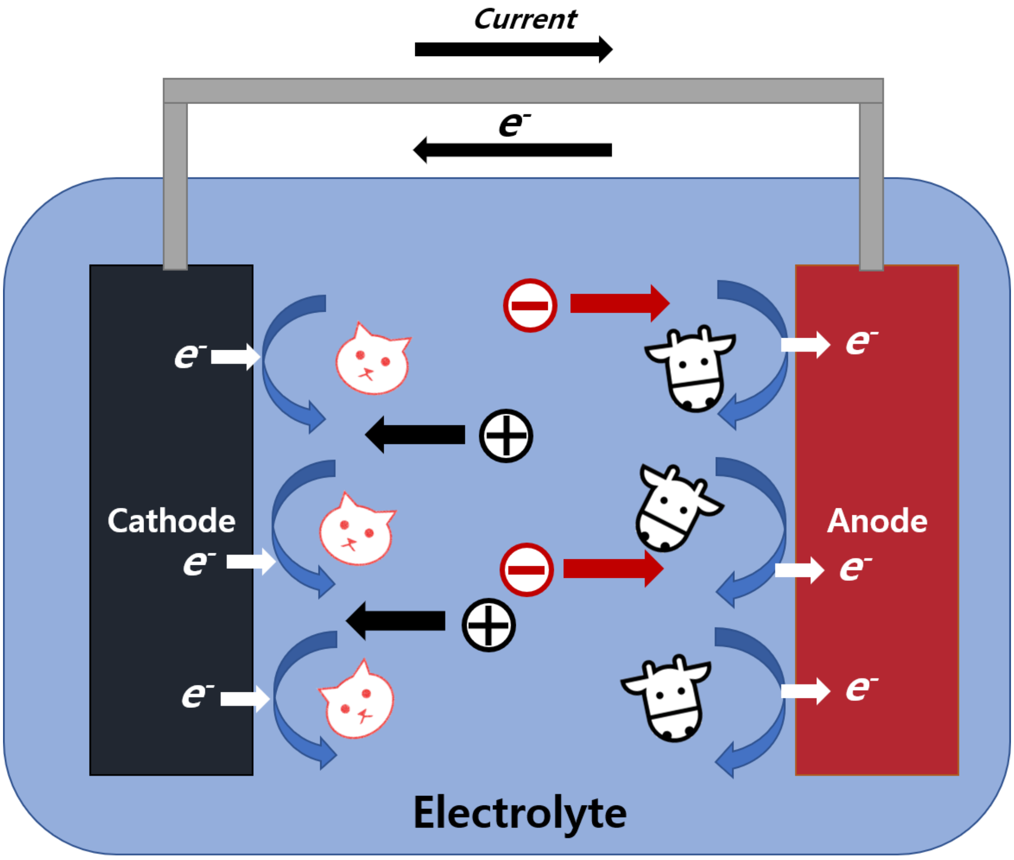

Figure 2.1. Schematics of an electrochemical cell. A red cat and an ox symbolize the reduction at the cathode and oxidation at the anode, respectively. Cations move towards the cathode, and anions go to the anode. Cations and anions are symbolized with ⊕ and ⊖, respectively.

The oxidation and reduction reactions are collectively termed as the "*redox reaction*". The species that experience the oxidation and reduction reactions are called "*redox couples*". An electrochemical system where chemical energy converts into electrical energy is called a "*galvanic cell*". On the other hand, a system that needs external electrical energy to cause redox reactions is called an "*electrolytic cell*". In this case, the applied electrical energy is converted to chemical energy. Therefore, the primary battery is an electrochemical cell, which can only serve as the galvanic cell. The secondary battery (rechargeable battery) is the electrochemical cell that serves as both the galvanic cell and the electrolytic cell in discharge and charge modes, respectively.

A redox reaction can occur at the same place, or it can be spatially separated. If the redox species exchange electrons, the redox reaction takes place at the interface of those species. In order to focus on an electrochemical reaction of interest, the oxidation and reduction reactions are spatially separated and studied by manipulating the electrical inputs. One of either oxidation or reduction reactions is called "*half-reaction*" or "*electrode reaction*", and one set of electrode and electrolyte is called "*half-cell*". The half-reaction can be described as:

$$S_{Red} \underset{reduction}{\overset{oxidation}{\rightleftarrows}} S_{Ox} + ne^- \qquad \textbf{Equation 2.1}$$

where S_{Red} and S_{Ox} denote the reduced and oxidized species, respectively, and n is the total number of electrons involved in the redox reaction.

As a redox reaction results in the charge transfer, the overall chemical reaction equation can be quantitatively formulated with the number of reactants, products, and charges. During an oxidation reaction, for instance, the difference between the sum of the number of oxidized species and the number of reduced species must be equal to the number of electrons gained at the electrode (the overall reaction must be stoichiometrically balanced, *i.e.*, charge conservation):

$$\textstyle\sum_{Red} v_{red} S_{Red} - \sum_{Ox} v_{ox} S_{Ox} = ne^- \qquad \textbf{Equation 2.2}$$

where v_{Red} and v_{Ox} are stoichiometric mole numbers of reduced and oxidized species, and n is the number of electrons involved in the overall reaction.

2.3 Electrical Double Layer

In practice, electrochemical studies often focus on a reaction at one electrode, *i.e.*, half-cell, by controlling the potential on an electrode. When a charged electrode is in contact with an electrolyte (often liquid) in the electrochemical cell, an electrified interface can be formed between the electrode and the electrolyte. Suppose an electrode is in contact with a liquid electrolyte containing mobile species (cations, anions and solvents). The charged surface of the electrode repels ions having the same polarity and attracts oppositely charged ions from the electrolyte. This interaction of the charged surface with the oppositely charged ions will form a new interface consisting of two “parallels” of opposite charges. This model of the interface was termed as the “compact double layer” by Hermann von Helmholtz in 1853 as illustrated in **Figure 2.2 (a)**.

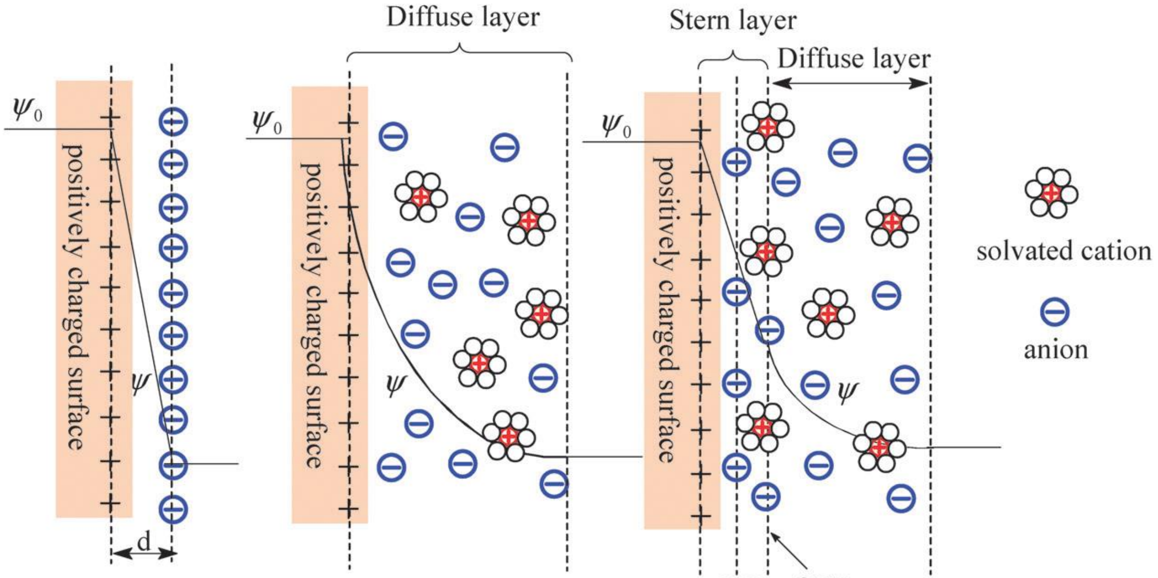

(a) (b) (c)

Figure 2.2. Schematic representation of the development of the electrical double layer: (a) the Helmholtz model, (b) the Gouy-Chapman model, and (c) the Stern model. Reproduced from reference [108] with permission from the Royal Society of Chemistry.

The layer thickness is determined from the surface of the electrode to the center of the adsorbed ions at the electrolyte side. A plane passing through the adsorbed ion centers is called the “*Helmholtz plane*” (**Figure 2.2 (a)**). The electrode surface and the virtual layer of the adsorbed ions can be assumed as a parallel capacitor, and the electric potential at the interface sharply drops from the electrode surface. However, the Helmholtz model is not complete because it does not consider the thermal motion of the ions in the double layer. Louis Georges Gouy and David Leonard Chapman observed that the capacitance of the layer varies depending on the applied potential and the ion concentration of the electrolyte. They considered the thermal motion of the ions near the electrode surface and introduced a diffuse model at the interface of the electrode and electrolyte. The modeled layer is called the “*diffuse layer*”, which describes the distribution of the cations and anions due to the thermal motion in the electrolyte. The length of the diffuse layer varies depending on the concentration and conductivity of the electrolyte.[109] The charge distribution of the ions in the diffuse layer can be expressed as a function of the distance from the electrode surface, following the Maxwell-Boltzmann statistics. Thus, the electric potential in this region is expressed with an exponential function as schematically depicted in **Figure 2.2 (b)**.

Otto Stern suggested a more complex model. He combined the Helmholtz model and the Gouy-Chapman model as shown in **Figure 2.2 (c)**. Stern’s model describes that the Helmholtz plane can be located at a different distance from the electrode surface depending on the sort of adsorbed ions. David Caldwell Grahame further modified this Stern's model. According to his model, some ions or non-ionic species (for instance, water) can penetrate the Stern layer. In the case of ions, some of them partially lose the solvation shell as they approach the surface. These ions that are directly in contact with the electrode surface are termed as “*specifically adsorbed ions*”. In this model, the Helmholtz plane can be divided into two planes, the “inner Helmholtz plane (IHP)” and the “outer Helmholtz plane (OHP)”. IHP is placed at the plane of the centers of the specifically adsorbed ions, whereas OHP is located at the plane of the centers of the solvated ions that are located at their closest approach.

In principle, any ions, either solvent molecules or any species, can be adsorbed at the electrode surface by different forces: ions are strongly attracted or repelled by the Coulomb forces across the electrolyte, some molecules are adsorbed at the substrate surface due to van der Waals force (physisorption), or a chemical reaction between the surface and adsorbates can take place (chemisorption). **Figure 2.3** illustrates the abovementioned adsorption types.

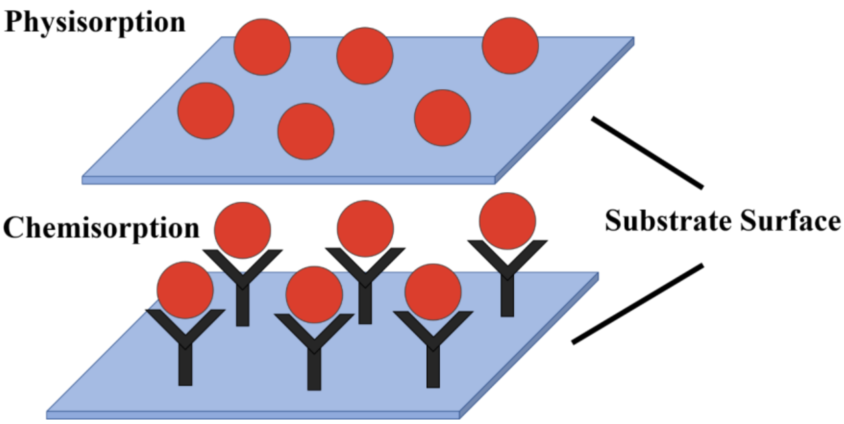

Figure 2.3. Types of adsorptions. (Top) physisorption describes direct adsorption of adsorbates at the substrate surface by the van der Waals forces. (Bottom) chemisorption is the adsorption caused by the chemical bonding of adsorbates and the substrate surface.

2.4 Faraday's Law

Faraday's law of electrolysis states that the quantity of a substance involved in the electrochemical reaction is proportional to the quantity of charge passed during the reaction. Accordingly, the mass of the produced or consumed substances due to the redox reaction can be calculated:

$$\Delta m = ZQ \qquad \textbf{Equation 2.3}$$

where m is the mass of the produced substances in grams, Q is the measured charge in coulomb, and Z is the coefficient of proportionality in grams coulomb^{-1}. Z is also called electrochemical equivalent, which is the mass of the produced substances by one coulomb.

Equation 2.3 is the basic argument of Faraday's law. Faraday also discovered the relationship between the electrochemical equivalent (Z), the molar mass (M) of the substances, and the valency number of ions in the substance (z). This relationship is expressed with the well-known "Faraday constant" F (96485.33289 C mol^{-1}).

$$Z = \frac{M}{zF} \qquad \textbf{Equation 2.4}$$

The mass resulted from the electrochemical reaction can be calculated as below

$$\Delta m = \frac{MQ}{zF}$$ **Equation 2.5**

This equation is used for the calculation of the deposited mass of battery materials used in this dissertation.

2.5 Nernst Equation

In electrochemistry, electric parameters and quantities are used as input and output signals to study electrochemical processes. Charge, current, and potential are frequently used among fundamental electric quantities. To analyze electrochemical processes using those quantities, one should primarily formulate a fundamental equation under the standard conditions to find relationships between them. It is desirable to start with determining the potential of a redox process under the standard conditions, as the potential of a redox process is an intensive property, unlike charge and current, which vary depending on the amount of reacting species.

Electrochemical reactions do not always take place under the standard conditions. If an electrochemical reaction occurs under non-standard conditions, a specific equation is necessary to determine the potential under given conditions. This equation can be theoretically formulated with several assumptions. As electrochemical properties of reacting species change during the reaction, the number of the electrochemically identical species between before and after the reaction will be different. The theory of thermodynamics provides the necessary information to formulate the potential of redox reactions out of the standard conditions. In thermodynamics, the chemical potential μ (J/mol) deals with the composition change in a system. The chemical potential of the component *k* (in J/mol) is defined as below:

$$\mu_k \equiv \frac{dG}{dn_k}$$ **Equation 2.6**

The value of the chemical potential of the component k, μ_k, varies depending on the concentration of the component k in the substance having a specific phase and composition. In the ideal solution, the chemical potential μ_k can be reformulated by

$$\mu_k = \mu_k^0 + RT \ln c_k \qquad \textbf{Equation 2.7}$$

where R is the universal gas constant, T is temperature in Kelvin, c_k is the concentration of component k, and μ_k^0 is the standard chemical potential of component k (when c_k is unity).

If a system is not in the ideal solution, **Equation 2.7** should be slightly modified. In order to facilitate the same form of the equation, the thermodynamic activity a was suggested to be used in the equation instead of concentration c_k according to Gilbert N. Lewis (1907). The thermodynamic activity a_k is defined as the multiplication of the activity coefficient γ_k with the concentration c_k (**Equation 2.8**). If $\gamma_k = 1$, the system shows the ideal behavior.

$$a_k \equiv \gamma_k c_k \qquad \textbf{Equation 2.8}$$

With the thermodynamic activity a, the equation of the chemical potential of the component k in a system can be rewritten as

$$\mu_k = \mu_k^0 + RT \ln a_k \qquad \textbf{Equation 2.9}$$

It should be noted that this equation cannot be directly employed in electrochemical systems because the electric contribution to the reaction processes is not considered. Butler and Guggenheim suggested the introduction of electrical contribution to the equation of the chemical potential.[110-112] With consideration of the electrical contribution to the chemical potential, **Equation 2.9** is modified to

$$\bar{\mu}_k = \mu_k^0 + RT \ln a_k + z_k F \varphi \qquad \textbf{Equation 2.10}$$

where z_k is the charge of the component k, F is the Faraday constant, and φ is the electrostatic potential. This new term $\bar{\mu}_k$ (J/mol) is called "electrochemical potential", and it becomes identical to the chemical potential μ_k when the component k has zero-charge (neutral species).

The inner potential difference between the two dissimilar phases is called the "Galvani potential difference" ($\Delta\varphi$), and it can be calculated under the equilibrium condition (no net current flow). Electrochemical systems often consist of solid electrodes and a liquid electrolyte. Suppose a solid metal (Me) is immersed in an aqueous solution containing the metal ions (Me^{z+}), then the chemical reaction of the metal at the equilibrium can be expressed as

$$Me_{(s.)} \rightleftharpoons Me^{z+}{}_{(aq.)} + ze^{-}{}_{(s.)}$$ **Equation 2.11**

Thus, the corresponding chemical equation in the form of the electrochemical potential can be written as

$$\bar{\mu}_{Me\,(s.)} = \bar{\mu}_{Me^{z+}(aq.)} + z\bar{\mu}_{e^{-}(s.)}$$ **Equation 2.12**

$\bar{\mu}_{Me\,(s.)}$, $\bar{\mu}_{Me^{z+}(aq.)}$ and $\bar{\mu}_{e^{-}(s.)}$ are the electrochemical potentials of the metal atoms in the solid metal, metal ions in an aqueous electrolyte and electrons in the solid metal, respectively.

Assuming the metal atoms in the solid metal are electrically neutral ($\bar{\mu}_{Me\,(s.)} = \mu^{0}_{Me\,(s.)}$), the equation can be expanded as

$$\mu^{0}_{Me\,(s.)} + RT\ln a_{Me\,(s.)} = \mu^{0}_{Me^{z+}(aq.)} + RT\ln a_{Me^{z+}(aq.)} + zF\varphi_{(aq.)} + z\mu^{0}_{e^{-}(s.)} + zRT\ln a_{e^{-}(s.)} - zF\varphi_{(s.)}$$ **Equation 2.13**

The concentration terms of metal atoms and electrons in the solid phase can be neglected as their concentrations are effectively constant in the solid metal: $a_{Me^{z+}(aq.)}$ and $a_{e^{-}(s.)}$ in the solid are conventionally assumed as unity. Then, the Galvani potential difference between the solid phase and the liquid phase, in this case, can be calculated as below

$$\Delta\varphi \equiv \varphi_{(s.)} - \varphi_{(aq.)} = \frac{\mu^{0}_{Me^{z+}(aq.)} + z\mu^{0}_{e^{-}(s.)} - \mu^{0}_{Me\,(s.)}}{zF} + \frac{RT}{zF}\ln a_{Me^{z+}(aq.)}$$

$$\equiv \Delta\varphi^{0} + \frac{RT}{zF}\ln a_{Me^{z+}(aq.)}$$ **Equation 2.14**

Where $\Delta\varphi^{0}$ is called the "standard Galvani potential difference" at the unit activity of the metal ions in the aqueous electrolyte.

Unfortunately, the Galvani potential difference is not experimentally measurable. Any attempt to measure the Galvani potential difference will perturb the original potential difference due to the formation of at least one more interface between a measuring probe and the system. Provided a second electrode, which has a constant Galvani potential difference ($\Delta\varphi' = const.$), is introduced into the system, then the potential of the electrode of interest (working electrode) is practically measurable by referring it to the second electrode ($E = \Delta\varphi - \Delta\varphi'$). This second electrode is called "reference electrode", and the potential difference between the working and reference electrodes, E, is termed as "electrode potential". Under the standard conditions, where the activity is unity, the "standard electrode potential" can be defined as $E^0 = \Delta\varphi^0 - \Delta\varphi'$. Thus, one can practically determine the potential of interest by referring it to the reference electrode: $E - E^0 = \Delta\varphi - \Delta\varphi^0$. By substituting this into **Equation 2.14**, the electrode potential of interest can be calculated as

$$E = E^0 + \frac{RT}{zF}\ln a_{Me^{z+}(aq.)} \qquad \textbf{Equation 2.15}$$

which is called the "Nernst equation." With the Nernst equation, one can predict how a system behaves when the concentration of species in the solution or electrode potential changes. It should be noted that the Nernst equation can be used only at equilibrium conditions since the standard electrode potential is defined at equilibrium.

If an electrochemical process involves several redox reactions, the Nernst equation can be generalized. Considering a stoichiometric reaction of the following

$$v_1S_1 + \cdots + v_iS_i + ne^- \rightleftharpoons v_jS_j + \cdots + v_kS_k \qquad \textbf{Equation 2.16}$$

which can be mathematically simplified as

$$\sum_{Ox} v_{ox}S_{Ox} + ne^- \rightleftharpoons \sum_{Red} v_{red}S_{Red} \qquad \textbf{Equation 2.17}$$

then the "generalized Nernst equation" can be obtained after some laborious mathematical work as

$$E = E^0 + \frac{RT}{nF} ln \frac{\prod_{ox} a_{ox}^{v_{ox}}}{\prod_{red} a_{red}^{v_{red}}} \qquad \textbf{Equation 2.18}$$

where $\prod_i a_i^{v_i} \equiv a_{S_1}^{v_1} a_{S_2}^{v_2} \ldots a_i^{v_i}$.

The potential of the reference electrode should be determined to measure the potential of the electrode of interest. As the potential itself describes a difference between two measurement points, the absolute potential, which will be the reference point, is necessary to calculate the potential of redox reactions (redox potentials). However, it is impossible to establish absolute potential experimentally. Moreover, even if the absolute potential can be determined, the use of the absolute value will not be practical, because the rigorous thermodynamic conditions should be regulated during the experiments. Alternatively, other reference points were established using electrodes that show stable potentials ensuring the accurate measure of the potential values. Redox reactions of reference electrodes should stay at thermodynamic equilibrium so that their potentials can practically remain constant. There are various reference electrodes for aqueous systems and non-aqueous systems. One of the important reference electrodes is "Standard Hydrogen Electrode" (SHE). Its potential is set to ground at the standard state (p = 1 bar, T = 298.15K, c_{ion} = 1 M), and it serves as a basis for comparison to other electrode reactions.

2.6 Formal Potential and Standard Electrode Potential

It is not efficient to always calculate the potential from the activity values, as activity coefficients are usually unknown. A practical way to determine the electrode potential is to calculate the electrode potential by comparing the values from the table of the standard electrode potentials for various redox reactions. The reduction potentials for different electrochemical reactions under the specified conditions are already well-tabulated. These reduction potentials are called "formal potentials". Electrode reactions are fundamentally dependent on different parameters such as temperature, pressure, and concentration of reactants or products. Thus, it is useful to determine the electrode potentials of redox reactions under the standard conditions as a benchmark for the electrode potentials. It is not surprising why the SHE is chosen to be used here when recalling the beginning of the electrochemistry: Electrolysis is of great interest in electrochemistry since it begins. By setting the SHE to zero, formal potentials at equilibrium and standard conditions are referred to the SHE. These potentials with respect to the SHE is termed as the "standard electrode potential (E^o)". Conventionally, the standard electrode potentials are defined as reduction potentials. A few examples are presented in **Table 2.1**. However, not all reactions are observable at the exact reduction potential that was thermodynamically predicted. The reaction often takes place at a distant potential. The potential difference between the standard electrode potential and the applied potential, where the measurable reaction occurs, is called "overpotential," and it can be written as

$$\eta = E - E_{eq} \qquad \textbf{Equation 2.19}$$

where E is the electrode potential at which a particular reaction occurs, and E_{eq} is the thermodynamically determined equilibrium potential.

Reaction	E^o (V) vs. SHE	Reaction	E^o (V) vs. SHE
$Li^+ + e^- \rightleftharpoons Li$	-3.045	$Sn^{4+} + 2e^- \rightleftharpoons Sn^{2+}$	0.098
$K^+ + e^- \rightleftharpoons K$	-2.935	$Cu^{2+} + 2e^- \rightleftharpoons Cu^+$	0.153
$Ca^{2+} + 2e^- \rightleftharpoons Ca$	-2.866	$AgCl + e^- \rightleftharpoons Ag^+ + Cl^-$	0.2224
$Na^+ + e^- \rightleftharpoons Na$	-2.714	$Cu^{2+} + 2e^- \rightleftharpoons Cu$	0.337
$Mg^{2+} + 2e^- \rightleftharpoons Mg$	-2.363	$Fe(CN)_6^{3-} + e^- \rightleftharpoons Fe(CN)_6^{4-}$	0.36
$Zn(OH)_2 + 2e^- \rightleftharpoons Zn + 2OH^-$	-1.245	$O_2 + 2H^+ + 2e^- \rightleftharpoons H_2O_2$	0.682
$Mn^{2+} + 2e^- \rightleftharpoons Mn$	-1.180	$Fe^{3+} + e^- \rightleftharpoons Fe^{2+}$	0.771
$Zn^{2+} + 2e^- \rightleftharpoons Zn$	-0.764	$O_2 + 4H^+ + 4e^- \rightleftharpoons 2H_2O$	1.229
$Fe^{2+} + 2e^- \rightleftharpoons Fe$	-0.441	$Cl_2 + 2e^- \rightleftharpoons 2Cl^-$	1.3581
$Ni^{2+} + 2e^- \rightleftharpoons Ni$	-0.250	$PbO_2 + 4H^+ + e^- \rightleftharpoons Pb^{2+} + 2H_2O$	1.455
$2H^+ + 2e^- \rightleftharpoons H_2$	0		

Table 2.1 Standard Electrode Potentials for different redox reactions at 25°C.[113]

The overpotential can be either "negative" or "positive" depending on the type of electrochemical system. In an electrolytic cell, more energy is required than the thermodynamically determined value, and in a galvanic cell, less energy is converted than the theoretical value.

There are different sources of the overpotential, namely electron-transfer, diffusion, reaction, and concentration, and their magnitudes vary depending on the experimental condition. At low current, the rate of electron-transfer is a major limiting factor (electron-transfer overpotential), but at a high current diffusion rate (diffusion overpotential) or sluggish reaction kinetics (reaction overpotential) become more dominant. The reaction kinetics may depend on the rate of adsorption or desorption of reactants or products.

2.7 Butler-Volmer Equation

As the electrode potential can be formulated by relating the electrochemical process with measurable quantities, the equation for the current flow can be also derived in a similar way. Suppose that an electrochemical system consists of a metallic working electrode immersed into a highly concentrated electrolyte. When the potential applied on the working electrode is large enough to trigger an electrochemical reaction, a net electric current can be observed. Since the electric potential is a driving force for the chemical reaction, the magnitude of the obtained current shall be dependent on the potential applied. Hence, the net electric current can be described with the potential. The Faradaic current is closely related to the rate (v) of chemical reactions taking place at the electrode. Therefore, the derivation of the equation for the current starts from the general redox process:

$$S_{Ox} + ne^{-} \underset{\boldsymbol{backward\ (anodic)}}{\overset{\boldsymbol{forward\ (cathodic)}}{\rightleftarrows}} S_{Red} \qquad \textbf{Equation 2.20}$$

Regardless of the type of reaction taking place, forward (cathodic) and backward (anodic) reactions simultaneously occur. Even if the measured net current is zero, the rate of each reaction is not necessarily zero: The sum of each current contribution from the forward- and backward reactions is zero. If the applied potential is larger than the equilibrium potential, the net current and its magnitude will deviate from zero depending on the applied potential and the rate of the electrochemical reactions. Thus, the magnitude of the net current can be expressed with the rate of the reactions.

According to the activated-complex theory (also called transition state theory[114]), in the course of the reaction, reactants pass through a transient intermediate state ("activated complex"), which will finally convert into the product(s). Among diverse intermediate states, the activated complex with the highest potential energy configuration is called "transition state". In order for reactants to be converted into the products, the energy difference (energy barrier) between the reactant and the transition state needs to be overcome. This energy difference is called "activation energy" (E_a). Later, the concept of the standard Gibbs free energy of activation ($\Delta G_f,\ \Delta G_b$)[2] was introduced by René Marcelin. Using the standard Gibbs free energy, the rate constants for the forward- and backward reactions can be written as

$$k_f = k_f^0 exp\left(-\frac{\Delta G_f}{RT}\right)$$ **Equation 2.21**

$$k_b = k_b^0 exp\left(-\frac{\Delta G_b}{RT}\right)$$ **Equation 2.22**

where k_f^0 and k_b^0 are the rate constants of the forward- and backward reactions at the equilibrium.

As the reaction is proportional to the concentration of the reactants ($C_{S_{Ox}}$, $C_{S_{Red}}$ in mol m^{-3}), the rate of the forward- and backward reactions can be written as:

$$v_f = k_f^0 C_{S_{Ox}} exp\left(-\frac{\Delta G_f}{RT}\right)$$ **Equation 2.23**

$$v_b = k_b^0 C_{S_{Red}} exp\left(-\frac{\Delta G_b}{RT}\right)$$ **Equation 2.24**

By convention, the terms of "cathodic," *c*, and "anodic," a, will be used, in the following, instead of forward and backward, respectively.

Figure 2.4 illustrates how the Gibbs free energy of an electron alters during the conversion of reactants into products as a function of reaction coordinates. The Gibbs free energy of $S_{Ox} + ne^-$ is on the left-hand side of the diagram, and the right-hand side shows the Gibbs free energy of S_{Red}. In the course of the redox reaction, reacting species transform into the activated complex that has more negative Gibbs free energy. The electron transfer occurs where the potential deviation from its mean measured value is a maximum.[115] Out of this potential region, the influence of the electrode potential changes is not significant in the redox processes. Thus, the total Gibbs free energy changes in the process are attributed mainly to the Gibbs free energy changes of the electrons in the electrode. Then, the Gibbs free energy of activated complexes owing to the potential perturbation is expected to be

---

2. Here, f and b denote the forward and backward reaction

changed by $|nF\Delta E|$ for n moles of electrons. However, not all the energy is contributed to the Gibbs free energy of the activated complexes. Only a fraction of the free energy will appear at the intermediate states.

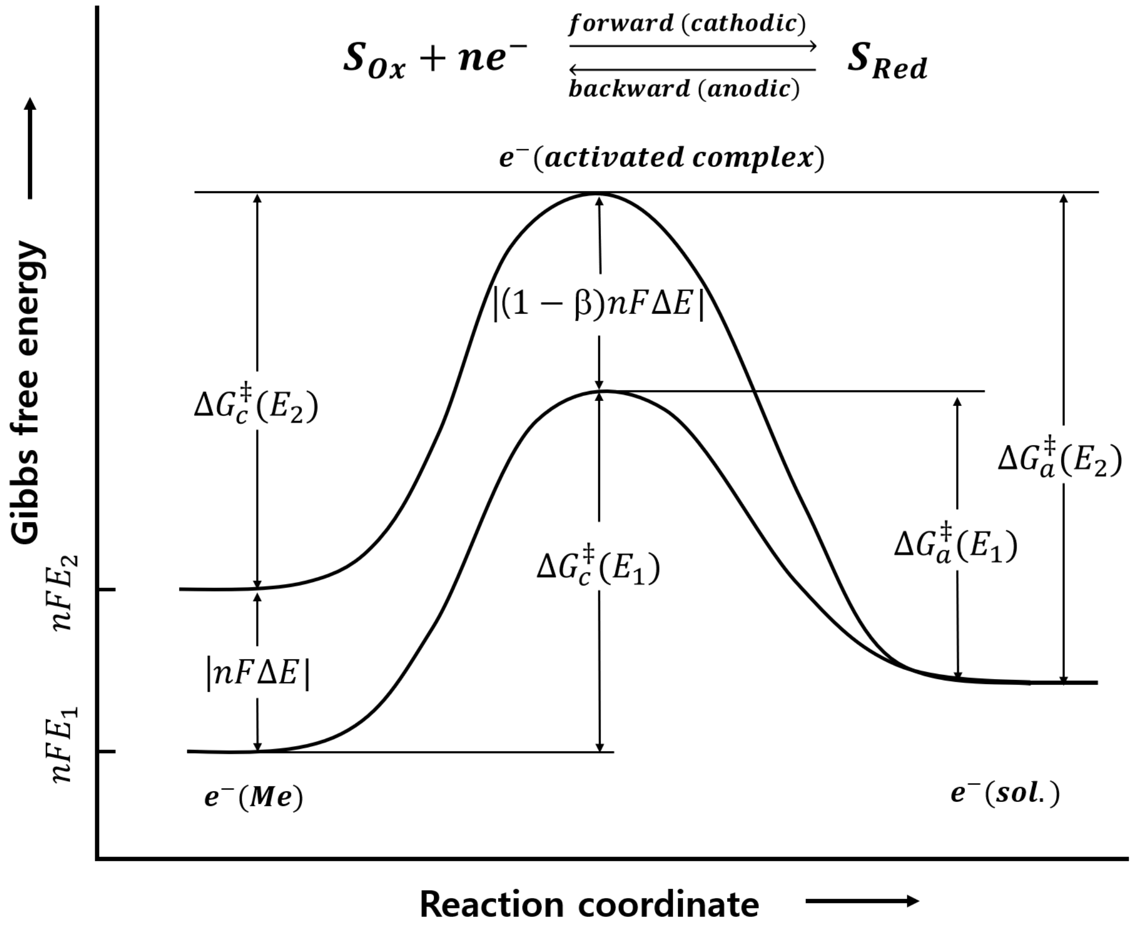

Figure 2.4. The internal energy of an electron in the electrode in the course of its transition from the electrode to a redox component in the solution. The arrow for Gibbs free energy indicates to a more negative value (so, $\Delta E = E_2 - E_1 < 0$). The notation $\ddagger$ indicates the active complex. $e^-(elec.)$, $e^-(activated\ complex)$ and $e^-(sol.)$ are the electrons in the electrode, activated complex and solution, respectively.

With this consideration, the equations for the cathodic, $\Delta G_c^\ddagger(E)$, and anodic, $\Delta G_a^\ddagger(E)$, activation energies can be written as

$$\Delta G_c^\ddagger(E_2) = \Delta G_c^\ddagger(E_1) + \beta nF\Delta E$$ **Equation 2.25**

$$\Delta G_a^{\ddagger}(E_2) = \Delta G_a^{\ddagger}(E_1) - (1-\beta)nF\Delta E$$ **Equation 2.26**

where $\Delta G_c^{\ddagger}(E)$, and $\Delta G_a^{\ddagger}(E)$ are the activation energies of the cathodic and anodic reactions at a given potential, and β is the "asymmetry parameter"[3] (also called "transfer coefficient" with the symbol, $\alpha = 1-\beta$).

The overall rate of the reactions can also be expressed with the flux density, which can be formulated with the rate of the reaction:

$$J_c(E_1) = -k_c' C_{S_{Ox}} exp\left(-\frac{\Delta G_c^{\ddagger}(E_1)}{RT}\right)$$ **Equation 2.27**

$$J_a(E_1) = k_a' C_{S_{Red}} exp\left(-\frac{\Delta G_a^{\ddagger}(E_1)}{RT}\right)$$ **Equation 2.28**

$$J_c(E_2) = -k_c' C_{S_{Ox}}\, exp\left(-\frac{\Delta G_c^{\ddagger}(E_2)}{RT}\right) = -k_c' C_{S_{Ox}} exp\left(-\frac{\Delta G_c^{\ddagger}(E_1)+\beta nF\Delta E}{RT}\right)$$ **Equation 2.29**

$$J_a(E_2) = k_a' C_{S_{Red}} \exp\left(-\frac{\Delta G_a^{\ddagger}(E_2)}{RT}\right) = k_a' C_{S_{Red}} \exp\left(-\frac{\Delta G_a^{\ddagger}(E_1)-(1-\beta)nF\Delta E}{RT}\right)$$ **Equation 2.30**

where $J_c(E)$ and $J_a(E)$ are the flux densities of the reduced and oxidized species at the given potential E. k_c' and k_a' are the rate constants for the cathodic and anodic reactions, respectively. The units of k_c' and k_a' are m s^{-1} because they are related to the zero-order reactions, *i.e.*, they do not depend on the concentration. The concentration of electrons in a metal electrode is high enough to be considered as constant.

Suppose that the potential E_1 is zero with respect to the reference potential. Then the term $exp\left(-\Delta G_a^{\ddagger}(E_1)/RT\right)$ can be considered as a constant and incorporated into the rate constants without changing the nature of the rate constants: $k_c = k_c' exp\left(-\Delta G_c^{\ddagger}(E_1)/RT\right)$ and $k_a = k_a' exp\left(-\Delta G_a^{\ddagger}(E_1)/RT\right)$.

By replacing E_2 and ΔE with an arbitrary potential E, the fluxes can be reformulated as:

---

[3] Asymmetry parameter, β, describes the kinetics of an electrochemical reaction. It indicates the closeness (similarity) of activated complexes to the reactant or the product in terms of electrochemical behavior. Its magnitude ranges from zero to one, and it is close to 0.5 in the case of a quite symmetric energy-potential curve.

$$J_c(E) = -k_c C_{S_{Ox}} \exp\left(-\frac{\beta nFE}{RT}\right)$$ **Equation 2.31**

$$J_a(E) = k_a C_{S_{Red}} \exp\left(\frac{(1-\beta)nFE}{RT}\right)$$ **Equation 2.32**

The net current density j is proportional to the total flux $(J = J_c + J_a)$ caused by the electrochemical process. The proportionality factor will be nF according to the Faraday's law (so, $j = nFJ$ in the unit of A m^{-2}). By multiplying nF with **Equations 2.31** and **2.32**, the partial current densities can be obtained as:

$$j_c(E) = -nFk_c C_{S_{Ox}} exp\left(-\frac{\beta nFE}{RT}\right)$$ **Equation 2.33**

$$j_a(E) = nFk_a C_{S_{Red}} exp\left(\frac{(1-\beta)nFE}{RT}\right)$$ **Equation 2.34**

where $j_c(E)$ and $j_a(E)$ are the partial current densities caused by the cathodic and the anodic reactions.

At a Nernst equilibrium potential E_r, where the net current is zero, both $j_c(E)$ and $j_a(E)$ have the same magnitude (but the sign is opposite), which is called the "exchange current density", j_0:

$$j_c(E_r) = -j_0 = -nFk_c C_{S_{Ox}} exp\left(-\frac{\beta nFE_r}{RT}\right)$$ **Equation 2.35**

$$j_a(E_r) = j_0 = nFk_a C_{S_{Red}} exp\left(\frac{(1-\beta)nFE_r}{RT}\right)$$ **Equation 2.36**

It is worth emphasizing again that zero net current does not necessarily mean zero activity at the Nernst equilibrium potential, but rather the cathodic and the anodic currents cancel each other, establishing a "dynamic" equilibrium. By reformulating **Equations 2.35** and **2.36** with respect to E_r, the Nernstian equation can be expressed as:

$$E_r = \frac{RT}{nF}\ln\left(\frac{k_c}{k_a}\right) + \frac{RT}{nF}\ln\left(\frac{C_{S_{Ox}}}{C_{S_{Red}}}\right) = E^0 + \frac{RT}{nF}\ln\left(\frac{C_{S_{Ox}}}{C_{S_{Red}}}\right)$$ **Equation 2.37**

Now, if the potential E is an actual potential deviated from the rest potential by an overpotential, $E_r + \eta$, then **Equation 2.35** and **2.36** can be expressed as:

$$j_c(E) = -nFk_c C_{S_{Ox}} exp\left(-\frac{\beta nFE_r}{RT} - \frac{\beta nF\eta}{RT}\right) = -j_0 exp\left(-\frac{\beta nF\eta}{RT}\right)$$ **Equation 2.38**

$$j_a(E) = nFk_a C_{S_{Red}} exp\left(\frac{(1-\beta)nFE_r}{RT} + \frac{(1-\beta)nF\eta}{RT}\right) = j_0 exp\left(\frac{(1-\beta)nF\eta}{RT}\right) \quad \textbf{Equation 2.39}$$

The net current density will be the sum of the cathodic and the anodic current ($j = j_c(E) + j_a(E)$):

$$j = j_0\left\{exp\left(\frac{(1-\beta)nF\eta}{RT}\right) - exp\left(-\frac{\beta nF\eta}{RT}\right)\right\} \qquad \textbf{Equation 2.40}$$

This is the famous Butler-Volmer equation, which is one of the most fundamental and essential equations describing the electrochemical kinetics with the consideration of both the cathodic and the anodic contribution at the same electrode.

3. Prussian Blue Analogs as Battery Materials

3.1 Fundamentals of Batteries

A battery is an energy storage device, which can supply electricity through the conversion of chemical energy into electrical energy. When the terminals of a battery are connected to an external electrical load, it releases electrical energy generated by the chemical reaction taking place in the battery. The reusability primarily categorizes batteries. A battery that cannot be or not designed to be recharged after consuming all stored electricity is called the primary (or "disposable") battery. In contrast, the secondary (or "rechargeable") battery can be used multiple times. In principle, the primary battery can be built using any conductive materials having different internal potentials. For instance, two different metals, or some oxides can work as electrode materials, while living organisms like frog's legs, foods (lemon or potato) can be used as electrolytes.[116]

The type of electrolytes or electrodes can further categorize secondary batteries. Li-ion or Na-ion batteries, Li-ion polymer batteries, aqueous Li-ion batteries, all-solid-state batteries or aqueous alkali metal ion batteries are some typical examples. Currently, many secondary batteries utilize liquid electrolytes. Lead-acid batteries, Li-ion batteries, nickel-cadmium batteries, nickel-zinc and nickel-metal hydride batteries belong to those types of batteries that are commercially available nowadays. Both primary and secondary batteries are used in our daily life such as a coin cell in a watch, a lead-acid battery in a car, a Li-ion battery in a mobile phone or in electric vehicles.

Technically, the battery is composed of two electrodes (positive and negative), an electrolyte (usually liquid), a separator and two current collectors. **Figure 3.1** shows a typical structure of a Li-ion battery. The cathode and anode materials of the current Li-ion batteries (LiBs) are typically transition metal oxides and graphite, respectively. Organic electrolytes are often utilized in LiBs to achieve high voltages. A separator is a thin porous membrane that prevents physical contact between two electrodes while allowing ion-transport. Some state-of-the-art separators have an extinguishable feature through filling the pores at thermal runaway, which physically blocks the contacts of two electrodes and the ion-transport shutting down the battery operation.[117] Al and Cu are frequently used as current collectors at the cathode and anode sides, respectively.[118] The electrodes are attached to current collectors (terminals), which collect electrons from the electrodes and transmit them to externally connected devices.

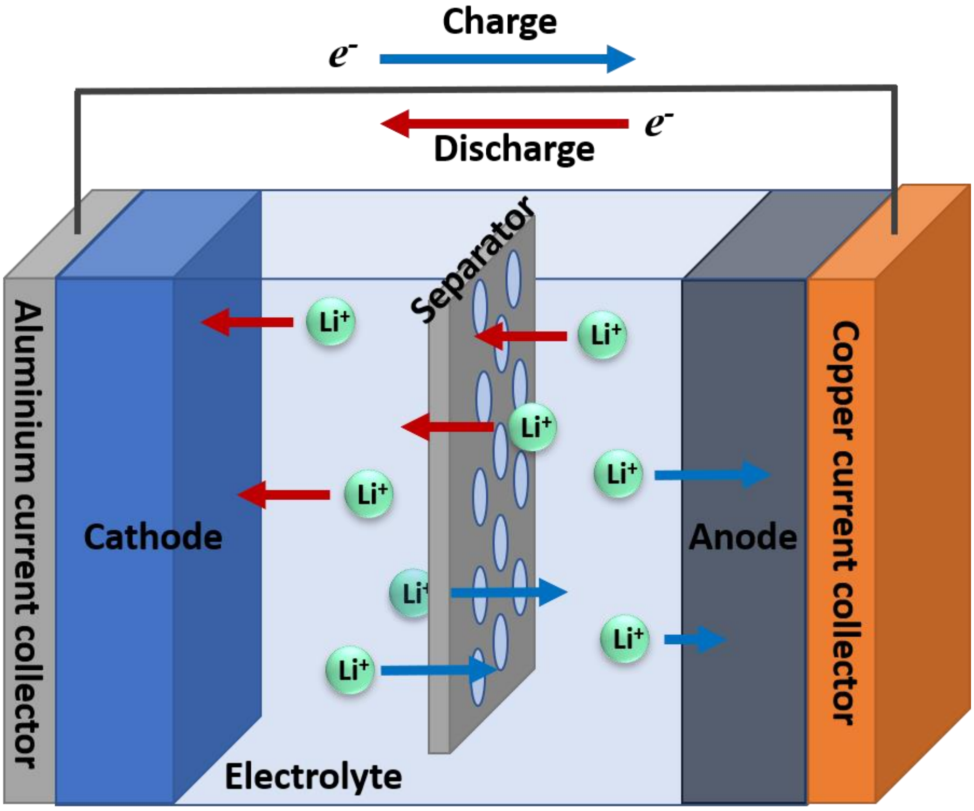

Figure 3.1. Typical structure of a Li-ion battery. The battery consists of two electrodes (cathode and anode), an electrolyte, a separator and two current collectors. In the charging process, Li-ions and electrons go towards the anode (blue arrows), and in the discharge process Li-ions and electrons move towards the cathode (red arrows).

Since the secondary batteries store and supply electricity, they have two operation modes as seen in **Figure 3.2**. When a battery provides electricity (power source mode), the reduction reaction takes place at the positive electrode, and the oxidation reaction occurs at the negative electrode. In other words, in the power source mode, the positive and negative electrodes become the cathode and the anode, respectively. In contrast, when a secondary battery is charged (electrolytic mode), the oxidation reaction occurs at the positive electrode, and the reduction reaction takes place at the negative electrode. In this case, the positive and negative electrodes become the anode and the cathode, respectively in the charging mode. Thus, both electrodes can be formally called either cathode or anode depending on the operation mode.

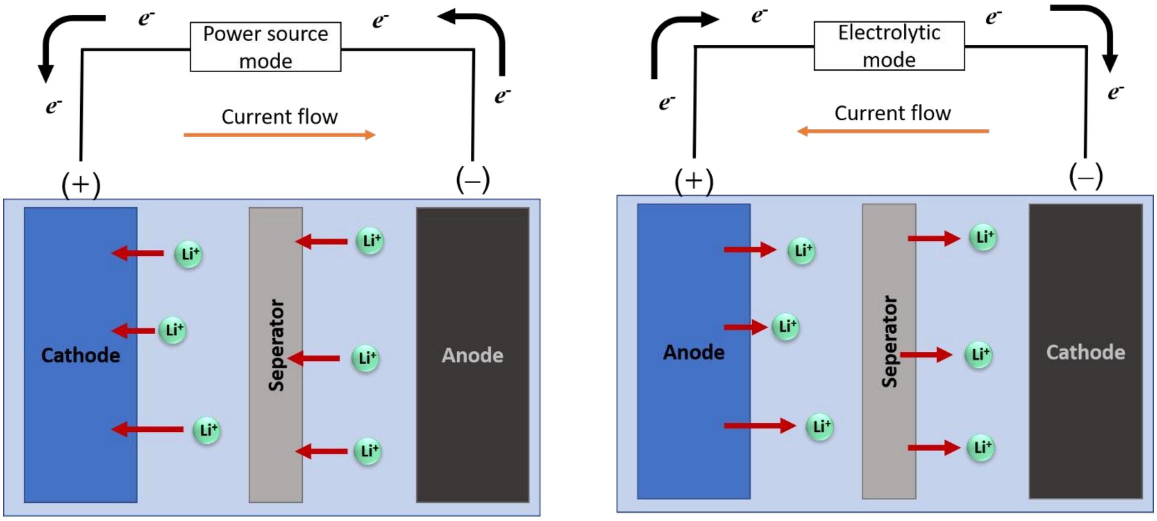

Figure 3.2. Battery operation modes: Power source mode (left) and electrolytic mode (right).

However, in the battery community, “cathode” and “anode” are often used instead of the positive and negative electrode, respectively. Strictly speaking, it is not scientifically correct as any electrode of a rechargeable battery can exhibit oxidation or reduction reactions, but these terms seem to be conventionally accepted. The origin of this might be attributed to that when only primary batteries were available, the terminology of the cathode for positive electrode and anode for negative electrode might have been fixed. This terminology can be confusing, so one should be informed that the cathode and the anode of a battery are defined for the discharge mode. In this dissertation, the cathode will be referred to as the positive electrode, and the anode will be the negative electrode following the convention of the battery community.

The redox reaction at electrodes generates the electrical current flow in the battery. During the redox reaction, electrodes can be chemically bound with charge carriers or host charge carriers into their structure, nearly not destroying the base structure. The latter phenomenon is called intercalation, which is an essential process in Li-ion batteries. For instance, the graphite electrodes of Li-ion batteries (typical anode material) accommodates Li-ions between its layers (see **Figure 3.3**). In the course of charge or discharge, the battery electrodes gain excess positive or negative charges due to the redox reactions.

Subsequently or simultaneously, the intercalation and deintercalation of Li-ions in the electrodes take place to compensate (neutralize) these excess charges.

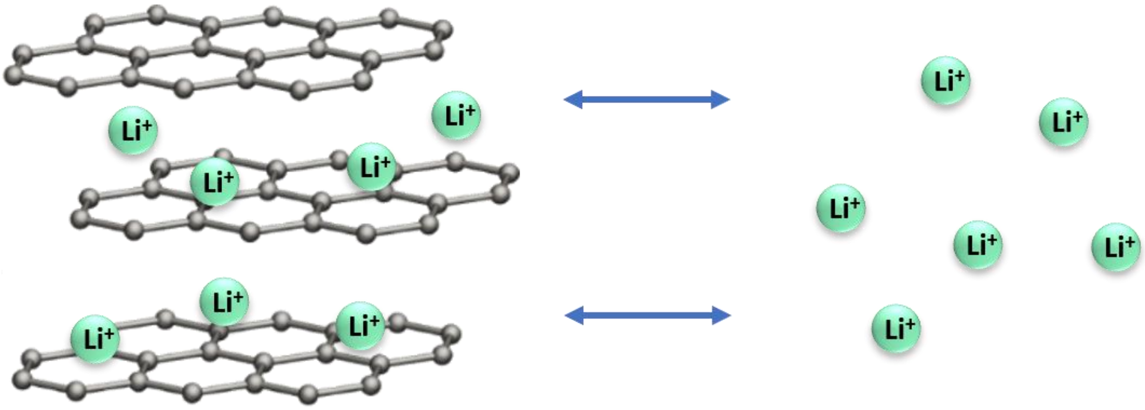

Figure 3.3. Intercalation of Li-ions into the graphite electrodes. Li-ions are intercalated between the graphite layers or deintercalated from the graphite depending on the battery operation modes.

The main features of battery performances (figures of merit) are energy density, power density, calendar life, and cycle life.[119] Energy density is the total amount of energy per unit of mass or volume (Wh kg^{-1} or Wh L^{-1}). The energy density of batteries is determined by multiplying the operating voltage with the averaged specific capacity of both electrodes. In the literature, the specific capacity of an electrode is typically calculated with the active material of the electrode. Thus, the energy density in a real device can be lower since real devices include many other components. Power density is the rate of energy (power) per unit volume or mass (W kg^{-1} or W L^{-1}). It should be noted that density refers to the amount of a certain quantity per unit volume. Theoretically, the total energy per unit mass should be called specific energy. However, conventionally, energy and power density are often referred to as the total energy and power per unit mass (Wh kg^{-1} or W kg^{-1}) in the battery community. The calendar life is the expected lifetime of a battery regardless of its use. The performance of batteries deteriorates over time, even if they are not used at all. The cycle life defines how many cycles a battery can operate.[120-123] Safety and costs are also of importance in the applications. Batteries should contain non-toxic (or less toxic) materials and equip some protective system to prevent the explosion. Last, the materials of batteries should be affordable at a reasonable price.

3.2 Prussian Blue Analogs (PBAs)

As described in the introduction, aqueous Na-ion batteries are particularly attractive for large-scale stationary applications. The similarity of Na^+ and Li^+ in terms of their electrochemical nature facilitates the development of Na-ion batteries by mimicking the Li-ion battery technology. Many electrode materials of Li-ion batteries are applicable in aqueous Na-ion batteries. For instance, traditional Li-intercalation compounds, such as transition metal oxides and polyanionic compounds, can work as electrode materials for aqueous Na-ion batteries.[124-126] However, many of them suffer from a short life cycle and severe degradation due to the larger ionic radius of Na-ions than that of Li-ions.[85] Another outstanding type of electrode materials for aqueous Na-ion batteries is Prussian blue ($Fe^{III}_4[Fe^{II}(CN)_6]_3$) and its derivatives, which exhibit a superior life cycle and moderate performance.[85]

The discovery of Prussian blue traces back to the early 18th century.[127] It is the first purely synthetic blue pigment, which is still used in painting and also listed as essential medication in the World Health Organization. Before its discovery, blue color was a costly one since blue colors were made from expensive pieces of jewelry such as Lapis Lazuli. Prussian blue is also one of the oldest chemicals. Although it has been known for the last four centuries, the research on Prussian blue and its analogs is still very active in various fields.[128-134]

The generic formula of PB and PBAs can be expressed as $AM_xTM_y[Fe(CN)_6]\cdot zH_2O$ (x, y, z = stoichiometric numbers, AM = (alkali) metal cations, TM = transition metal ions). **Figure 3.4** shows representative schemes of the crystallographic structure of PB and PBAs. They typically have a face-centered cubic (FCC) structure with a unit cell length of about 10 Å, which slightly varies depending on their chemical compositions. The transition metal (TM) and Fe are octahedrally-coordinated to cyan ligands (TM-C≡N-Fe), and alkali metal cations locate themselves in the tetrahedral sites of PB and PBAs.[135] Zeolitic water molecules or some anions can also occupy these positions. The physicochemical properties of PBAs can change by combining different kinds of transition metal ions. Due to the versatile and tunable properties, PB and PBAs are applicable in different fields such as photo- and optical magnetism, electrochromism, thermochromism, ionic sensors, electrocatalysis and batteries.[136-153]

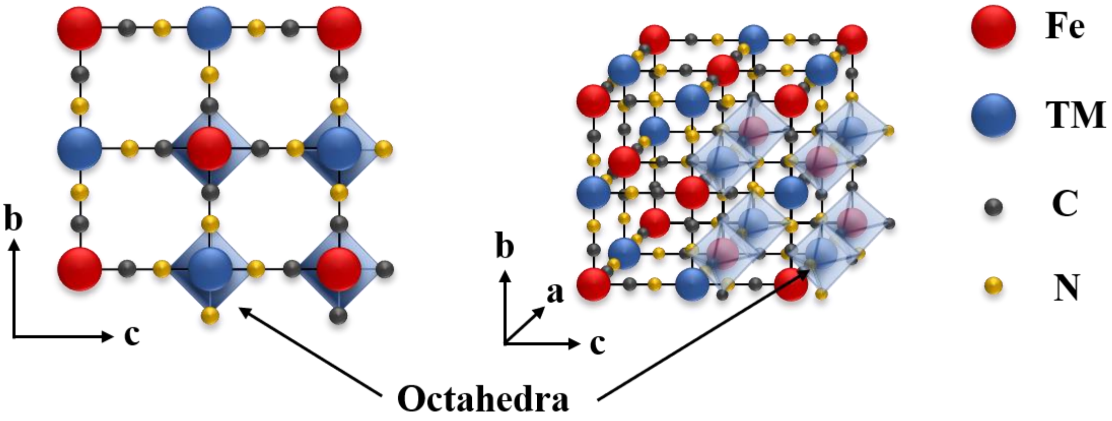

Figure 3.4. The left figure shows the (100) plane of the PBA unit cell, and the right represents the crystallographic structure of PBAs. The crystallographic axes are presented with a, b, and c (the axes are perpendicular to each other). Fe and TM are octahedrally coordinated with carbon and nitrogen, respectively (see the blue octahedra).

It is known that Neff firstly reported the application of PB and PBAs for battery electrodes in 1985.[154] But, their performance did not seem promising enough to replace the Li-ion batteries. With the development of new energy technologies and increasing concern about the environment and affordability of materials, PB and PBAs have been recently reviewed as battery electrode materials. Cui *et al*. reported low-cost synthesis methods for various PBAs materials based on co-precipitation methods.[92, 101-103] The capacities of the reported PBAs were measured to be between 50 and 60 mAh g^{-1}. These values are very low compared to the state-of-art cathode materials for LiBs (>250 mAh g^{-1}).[155, 156] However, PBAs electrodes do not benefit from the capacity, but from the low-cost synthesis and extremely long cycle life (thousand cycles). Furthermore, they exhibit very high power and excellent energy efficiency in inexpensive aqueous electrolytes. Therefore, the cost-efficiency of PBA-based batteries is the most outstanding feature for large-scale stationary

ESS applications.[128, 129, 157, 158] Among various applications of PB and PBAs, this dissertation focuses on their applications in aqueous Na-ion batteries and the intercalation mechanism using different techniques.

4. Characterization Methods

4.1 Cyclic Voltammetry

Cyclic voltammetry is one of the most powerful and widely-used techniques to investigate various electrochemical processes such as electron-transfer kinetics, reversibility of the redox process, intercalation, adsorption and desorption.[159, 160] A potentiostat applies a periodic triangular potential on the working electrode and records the resulting current. **Figure 4.1(a)** shows an exemplary periodic potential function, where E_i and E_f are the initial and final potentials, respectively.

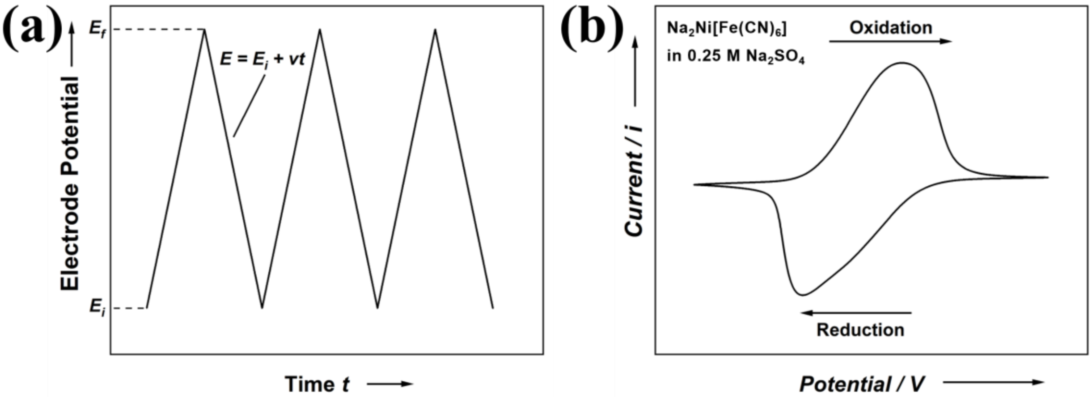

Figure 4.1. (a) Typical triangular waveform of the electrode potential for CV measurements and (b) an exemplary cyclic voltammogram (CV) of a quasi-reversible electrode process (v is a scan rate). The CV was obtained for a $Na_2Ni[Fe(CN)_6]$ thin films immersed into an aqueous 0.25 M Na_2SO_4 electrolyte. Since the detailed interpretation and explanation of the CV will be discussed later in **Chapter 6.1**, the potential and current values are not given here.

The rate of potential change is defined by a scan rate v (typically few mV s^{-1} to hundreds mV s^{-1} depending on the system). To determine an appropriate scan rate, one should consider the capability of the investigated system's response rate to the input signal. For instance, one can apply higher scan rates in aqueous systems compared to non-aqueous systems because aqueous electrolytes usually have higher ionic conductivities. Most commonly, such a cyclic voltammogram (CV) is depicted by plotting the resulting current versus the applied potential. The applied electrode potential is measured against a reference electrode, and the obtained current is often expressed as the current density (*e.g.*, surface-specific, volumetric or gravimetric). The CV plots possess information regarding different electrochemical processes such as capacitive processes and Faradaic processes.

There are two conventions to represent cyclic voltammograms: The US and IUPAC conventions.[106, 161] The former shows decreasing electrode potential on the x-axis versus increasing current on the y-axis. The latter plots increasing electrode potential on the x-axis versus increasing current on the y-axis. This dissertation follows the IUPAC convention. Thus, oxidation and reduction currents are shown in the upper half and the lower half of the plot, respectively. For instance, **Figure 4.1 (b)** shows a CV of $Na_2Ni[Fe(CN)_6]$ in 0.25 M Na_2SO_4 aqueous electrolyte in the IUPAC convention. Cyclic voltammetry was used for the deposition and characterization of the electrode materials in this dissertation.

4.2 Electrochemical Impedance Spectroscopy

Electrochemical impedance spectroscopy (EIS) is a non-destructive technique for investigating electrochemical systems and processes and physicochemical properties of electrodes. Due to the capability to distinguish the contributions of different constituents, the applications of EIS are numerous: Mechanisms of electrochemical processes (corrosion, adsorption and desorption, catalytic reactions and intercalation), dielectric and transport properties, properties of porous electrodes, and passive surfaces.[162-164] EIS can also be used to estimate physical parameters, namely the surface roughness or the porosity of an electrode.[165] The analysis of impedance data is essentially an inverse problem, which is to elucidate a physical model and find its parameters from the data. In many cases, however, the analysis can result in multiple solutions that cannot explain the electrochemical processes. Therefore, other complementary techniques should often be used to avoid misinterpretation.

The basic working principle of EIS is to measure the impedance response of the investigated system perturbed by a sinusoidal signal of potential or current over a range of frequencies. In many applications, the potential perturbation with a small amplitude (typically 5 to 10 mV) is often utilized in practice.

The sinusoidal input signal can be described as

$$E(\omega, t) = E_0 \sin(\omega t) \quad \textbf{Equation 4.1}$$

where E_0 is the amplitude, ω is the angular frequency, and t is time.

The output of a system, *i.e.*, the resulting current, is then obtained with a different amplitude and phase as

$$i(\omega, t) = i_0 \sin(\omega t + \theta) \quad \textbf{Equation 4.2}$$

where i_0 is the amplitude of the recorded current and θ is the phase shift.

According to Ohm's law, the measured impedance, $Z(\omega, t)$, of the system can be formulated as

$$Z(\omega, t) = \frac{E(\omega,t)}{i(\omega,t)} = \frac{E_0}{i_0} e^{j\theta} = |Z(\omega)| e^{j\theta} \quad \textbf{Equation 4.3}$$

where $|Z(\omega)|$ is the modulus of the impedance.

Using Euler's equation, **Equation 4.3** can be expressed as complex numbers as

$$Z(\omega, t) = |Z(\omega)| e^{j\theta} = |Z(\omega)|(\cos\theta + j\sin\theta) = Z_{Re}(\omega) + Z_{Im}(\omega) \quad \textbf{Equation 4.4}$$

where $Z_{Re}(\omega)$ and $Z_{Im}(\omega)$ are the real and imaginary parts of the impedance at the frequency ω.

The modulus and phase angle of the impedance can also be expressed by the real and imaginary parts of the impedance as

$$|Z(\omega)| = \sqrt{Z_{Re}^2(\omega) + Z_{Im}^2(\omega)} \quad \textbf{Equation 4.5}$$

$$\theta(\omega) = \tan^{-1}\left[\frac{Z_{Im}(\omega)}{Z_{Re}(\omega)}\right] \quad \textbf{Equation 4.6}$$

The EIS data can be represented in various ways. A popular example is a Nyquist plot, which presents real *vs* imaginary impedance (**Figure 4.2 (a)**). In Nyquist plots, one can see the shape of impedance spectra, which can be used as a "fingerprint" of electrochemical processes. By reading intercepts of EIS spectra, it is possible to roughly estimate some important parameters such as solution resistance, charge-transfer resistances, double-layer capacitances and Warburg impedance. The Bode plot is another way that displays EIS spectra in either the magnitude or the phase shift of the impedance as a function of the frequency, respectively (**Figure 4.2 (b,c)**). Bode plots show the impedance frequency dependency, which is useful to investigate the capacitive or inductive effects in investigated systems.[166]

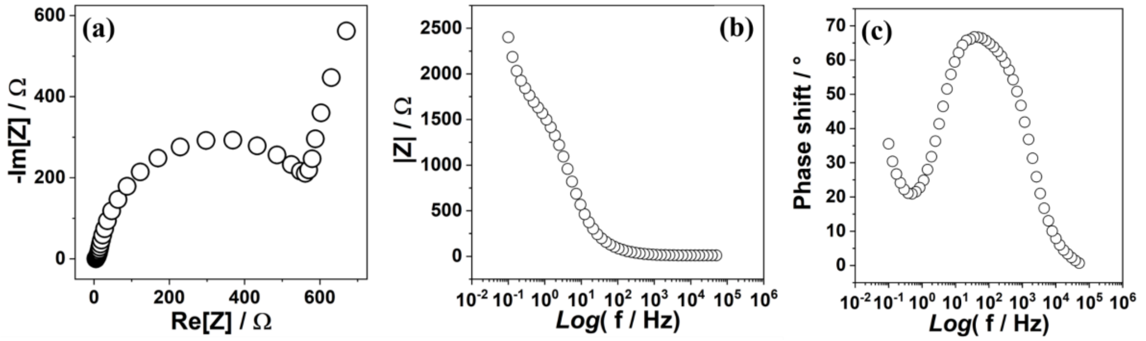

Figure 4.2. Exemplary impedance plots: (a) Nyquist plot and (b, c) Bode plots.

In order to acquire valid EIS data, four criteria must be fulfilled before the measurements: Linearity, causality, stability, and fitness.[166] The first approximation for the analysis of EIS data is linearity that the output of the system is linear with respect to the input. EIS analysis is based on the linear time-invariant system theory.[166] As electrochemical reactions are typically highly non-linear, the linear approximation is conducted by applying a perturbation with a small amplitude (typically 1-10 mV). If the applied AC signal is small enough, the system's response shows pseudo-linear responses. However, it must be large enough to be measured. Causality states that the applied perturbation solely causes the system's response. In other words, the system should not generate any signals or responses before and after the experiment. Stability declares that the investigated system must be stable in the sense that the system does not degrade during the data acquisition and return to the original state after the measurement. Lastly, the real and imaginary components of the impedance must be finite values over the whole frequency range.

The validity and quality of the obtained EIS data can be confirmed by testing the so-called Kramers-Kronig relations. Those are the bidirectional integral transformations of the real parts from the imaginary parts of the impedance values over a range of frequency from zero to infinity. In a real system, however, the deviation between the calculated values from the real part and the imaginary part may appear due to the imperfection of practical experiments (for instance, it is not possible to measure the impedance in the complete frequency range). In practice, less than 3 % of the deviation is conventionally deemed as acceptable.[166]

The analysis of EIS data includes the complicated calculation of complex impedance values, which makes it difficult to distinguish different parameters. Instead of the direct calculation, the interpretation of EIS data is often conducted by comparing the recorded impedance with the corresponding fit obtained by constructed physical models analogous to the electrochemical system. The physical model is composed of electrical elements such as resistors, capacitors, or inductors, and is, thus, called an equivalent electric circuit (EEC). The advantages of using EECs for the impedance analysis are the visualization of the individual electrochemical contributions with electric circuit elements and the computational calculation to find the solutions.

Dolin, Ershler, and Randles proposed the classical interpretation of an electrode process at the interface of an electrode and an electrolyte using physical models composed of electric elements.[167, 168] According to their theory, the EIS model representing the electrochemical process at the interface of the electrode and electrolyte can be generalized with (at least) three major components as displayed in **Figure 4.3**:

1. The impedance response of the electrolyte (Z_{el}). In liquid electrolytes, it behaves analogously to that of a resistor. Thus, an (uncompensated) resistor (R_u) can approximately represent the impedance of liquid electrolytes.
2. The interface itself (Z_i) responds like a capacitor; however, its response often deviates from that of the ideal capacitor. Thus, it can be approximated with a constant phase element (CPE): $Z_{CPE} = Q_{DL}^{-1} (j\omega)^{-n}$, where Q_{DL} is a CPE coefficient (proportional to the double layer capacitance), and n is a fractional exponent between 0 and 1. If n is 1, the impedance response of the interface shows the

behavior of the ideal double-layer capacitor.

3. The impedance of Faradaic processes (Z_F) depends on various factors, namely the kinetics of electrochemical reactions, the mode of mass transport, or the reaction mechanism.[169] The Faradaic processes within this approximation are considered as a "leakage" of the double-layer capacitance.

4.

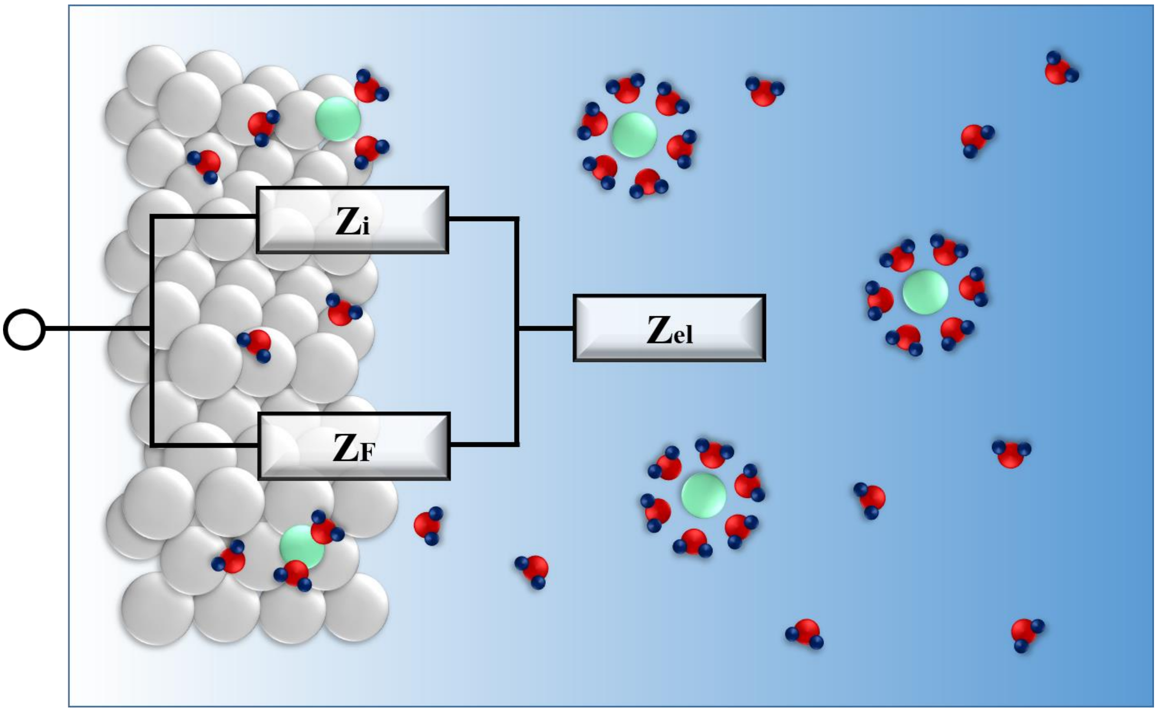

Figure 4.3. Illustration of the interface between the electrode and electrolyte generalized with a physical model consisting of electric circuit elements according to the Dolin–Ershler–Randles approximation. The impedance response of the electrode process contains the contribution of the interface (Z_i), the Faradaic processes (Z_F) and the electrolyte (Z_{el}).

Using the physical model based on the approach of Dolin, Ershler, and Randles, the total impedance can be formulated as $Z_{tot} = Z_{el} + (Z_i^{-1} + Z_F^{-1})^{-1}$. It should be noted that each impedance component can be mathematically expressed using equations describing physicochemical processes at the interface.[166] Since the impedance of, *e.g.*, the Faradaic processes can contain many factors, the total impedance equations can be lengthy and complicated to formulate. A detailed example is presented in **Appendix A**.

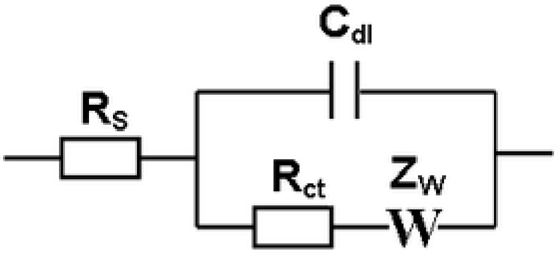

Figure 4.4. Randles circuit model. R_s, C_{dl}, R_{ct}, and Z_w represent uncompensated resistance (or solution resistance), double layer capacitance, charge transfer resistance and Warburg diffusion impedance, respectively. $Z_w = A_W/(j\omega)^{0.5}$, where A_W is the Warburg coefficient.

Figure 4.4 shows the famous Randles equivalent circuit[161], which is frequently used in the EIS analysis of the redox processes with a semi-infinite linear diffusion. Since Randles developed this model from the study of mercury and amalgam electrodes, which are different from currently used solid metal electrodes such as gold, platinum, or palladium, the impedance response of the noble metal electrodes or other electrodes may differ. Thus, the Randles' model cannot account for impedance spectra in many cases. If the analysis of a system with the Randles circuit does not result in an appropriate interpretation, one should design an EEC model with other electric circuit elements. However, it should be noted here that it is recommended to keep the number of elements in the EEC as little as possible. Otherwise, there is the danger of "overfitting", since a model with many unknowns fits well to any impedance spectra. The number of circuit components is not often determined (underdetermined system); thus, the analysis of impedance data is generally an inverse problem that can formally have multiple solutions.[170] In other words, the obtained fitting results might not be a valid physical explanation of the real system, but just a "mathematical solution" of the impedance equations.

Furthermore, the design of a proper EEC model corresponding to the studied system is not always straightforward, as the electric circuit elements (a resistor, a capacitor, and an inductor) do not practically exist in the electrochemical system. For instance, the interface of an electrode and electrolyte does not behave like an ideal resistor or capacitor. Reacting species also "differ" from real resistors. Moreover, electrochemical processes often have a temporal structure that cannot be easily drawn with real electric circuit elements. A. Laisa mathematically well explained some good examples of electrochemical processes (Faradaic and non-Faradaic processes).[171] Therefore, it is vital to rationally design physical EEC models with a reasonable number of circuit elements, which describe the EIS spectra well at the same time.

4.3 Electrochemical Quartz Crystal Microbalance

Electrochemical quartz crystal microbalance (EQCM) is an advanced application of a quartz crystal microbalance (QCM) to measure the mass changes due to the electrochemical processes. Firstly, a QCM was used in the gas phase, but later it was reported by Nomura and Okuhara that a QCM could also be used in a liquid.[172, 173] Kanazawa et al. experimentally proved the validity of the application of the QCM in liquid environments, which facilitates the applications of the QCM in electrochemistry.[174] A QCM measures the resonance frequency changes of a quartz crystal resonator, which is related to the mass changes on the surface with micro- to nanogram sensitivity in mass per unit area. Due to its excellent mass sensitivity and real-time monitoring, it finds various applications such as thin-film thickness monitoring, electrochemistry of interfacial process, biotechnology, surfactant and drug research.[175, 176]

The working principles of the QCM are based on the piezoelectric effect. The application of an electric field onto piezoelectric material generates its mechanical deformation (and *vice versa*). If a periodic potential function is applied to the quartz crystals, the oscillatory movement is generated. Quartz crystals exhibit various vibration modes depending on their frequency and the orientation of cut.[177] For instance, an AT-cut quartz crystal has a thickness-shear vibration mode. If the acoustical wavelength of the generated oscillation is twice the total thickness of the quartz crystal electrode (t_q), a standing wave with a particular frequency can be established. At this condition, the frequency is called the resonant frequency (f_o). The resonant frequency is firstly determined by the physical properties of quartz crystals such as size, shape, and orientation of the cut with respect to the crystallographic axis. The relationship between the resonant frequency and the crystal's thickness can be described as:[178]

$$f_o = \sqrt{\frac{\mu_q}{\rho_q}}/2t_q \qquad \textbf{Equation 4.7}$$

where μ_q is the shear modulus of AT-cut quartz crystal (2.947×10^{11} g cm^{-1} s^{-1}), ρ_q is the density of the piezoelectric crystal (quartz: 2.648 g cm^{-3}), and t_q is the crystal's thickness.[140]

The resonant frequency can be shifted by external factors such as mass deposition onto the quartz crystal, density or viscosity change of neighboring media and surface roughness. Günter Sauerbrey firstly explored the quantitative relationship of frequency shifts with the mass changes on a quartz crystal resonator in 1959.[179] He discovered a linear relationship between the resonant frequency and the mass loading. In his equation, Sauerbrey assumed that the added mass on the quartz could be treated as the extension of the quartz in thickness;[179] the deposited or adsorbed materials oscillate together with the quartz crystal at the same frequency. Hence, the Sauerbrey equation is applicable under certain conditions: i) rigid attachment of deposited films or adsorbed mass, ii) their homogeneous distribution, iii) no slip or deformation of the deposited films, and iv) small mass loading (less than 5% of the total mass of the quartz). When these conditions are fulfilled, one can use the Sauerbrey equation to calculate the mass change on the quartz crystal as described below:

$$\Delta f = -\frac{2f_0^2}{A\sqrt{\mu_q \rho_q}}\Delta M = -C_f \Delta m \qquad \textbf{Equation 4.8}$$

where Δf is the frequency change (Hz), ΔM is the total mass change (g), A is the piezoelectrically active area (the effective area between electrodes, cm^2), Δm is the mass change in the unit area (g cm^{-2}), and C_f is the sensitivity factor (Hz cm^2 g^{-1}).

In the Sauerbrey equation, the mass change is linearly proportional to the sensitivity factor, which is the fundamental property of the quartz crystal. Thus, the properties of foreign films on the quartz crystal are not needed to be considered in the equation when the requirements mentioned above are fulfilled.

Since the Sauerbrey equation was firstly developed for the use of QCM in a gas phase, if a QCM is used in a liquid phase, an additional contribution of the liquid to the oscillation should be considered such as viscosity and density of the solution, hydrostatic pressure, surface roughness, slippage effect, and temperature.[180, 181] The frequency change includes these parameters in addition to the mass loading, and the resonant frequency shift can be described as below:

$$\Delta f = \Delta f_m + \Delta f_\eta + \Delta f_p + \Delta f_R + \Delta f_{sl.} + \Delta f_T \qquad \textbf{Equation 4.9}$$

where Δf_m is mass loading, Δf_η is the viscosity and density of the liquid, Δf_p is hydrostatic pressure, Δf_R is surface roughness, $\Delta f_{sl.}$ is slippage effect, and Δf_T is temperature.

In this dissertation, AT-cut quartz crystals were used as the QCM sensors. The advantage of the AT-cut quartz crystals is that they have nearly zero frequency drift around room temperature. For instance, if an AT-cut quartz crystal has a thickness of ca 330 μm, a resonant frequency of 5 MHz is generated at room temperature, and its sensitivity factor, C_f, is approximately equal to 17.7 ng cm^{-2} Hz^{-1}.[182]

4.4 Atomic Force Microscopy

Atomic force microscopy (AFM) belongs to the scanning probe microscopies (SPMs) that maps a three-dimensional surface image, often with the atomic resolution. Unlike other optical or electron microscopes, AFM directly “touches” or “feels” the surface with the tip, which makes AFM have several advantages over the other microscopies based on the light or electrons. For instance, AFM can operate under atmospheric conditions. As AFM utilizes the interatomic force for recording the surface image of a specimen, it does not require any vacuum system which is necessary for many other microscopies based on the detection of the outcoming electrons from the specimen. Moreover, AFM measurements do not require complicated specimen preparation steps. Because of its very high resolution and simple measurement, AFM is applied in various fields of physics, chemistry, biology and medicine, where atomic-scale topography investigations are needed.[183-187]

AFM records the 3D-topographical image of a sample by analyzing the cantilever deflection caused by interatomic forces between the tip and the surface atoms. **Figure 4.5** shows a typical configuration of an AFM. The main components of the AFM are a cantilever, a laser source, a photodetector and a sample platform with the XYZ scanner. A cantilever is typically made of silicon or silicon nitride, and it has a very sharp tip at the free end. A piezoelectric element is attached at the other end to precisely control the oscillation of the cantilever. A laser beam is irradiated on the backside of the cantilever, and its reflection is detected at the photodetector to record the displacement of the cantilever. A sample platform is used to carefully place the position of the sample in x-, y-, and z-directions. In general, the cantilever is fixed, but the sample platform is moved with respect to the tip apex.

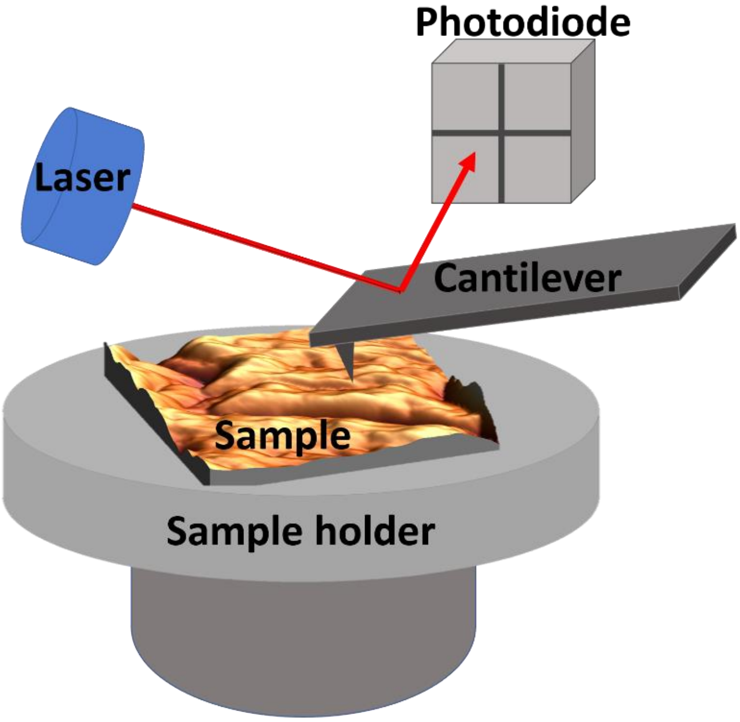

Figure 4.5. AFM configuration. AFMs are composed mainly of a laser, photodiode, a cantilever with a sharp tip and a sample holder.

AFMs operate in three different modes: contact mode, non-contact mode and tapping mode. **Figure 4.6** shows the sketch of the interaction regimes as a function of distance. The contact mode utilizes the repulsive force between the tip and surface atoms. In this mode, the tip is brought in the proximity of the sample surface with a particular height or a constant force where the repulsive force between them is dominant (see the blue area in **Figure 4.6**) The contour of the sample surface is drawn by directly measuring the deflection of the cantilever or by utilizing feedback loops, which maintain the position of the cantilever. The contact mode is typically used for imaging hard samples. The choice of a scan rate and a cantilever with a particular spring constant is important depending on the sample.

For soft samples, the non-contact mode is preferable. In the non-contact mode, the tip is placed relatively away from the surface (1 nm to 10 nm above), where the attractive force is dominant (see the green area in **Figure 4.6**). In this mode, the cantilever oscillates near its resonant frequency during the scan. As the tip approaches the surface or retracts from it, the oscillation is perturbed by the attractive force between the tip and the surface, resulting in the change of the resonant frequency and the amplitude. By measuring and adjusting the distance between the tip and the surface at each (x,y) point with the combined feedback-loop system, the topographic surface image of the sample is constructed.

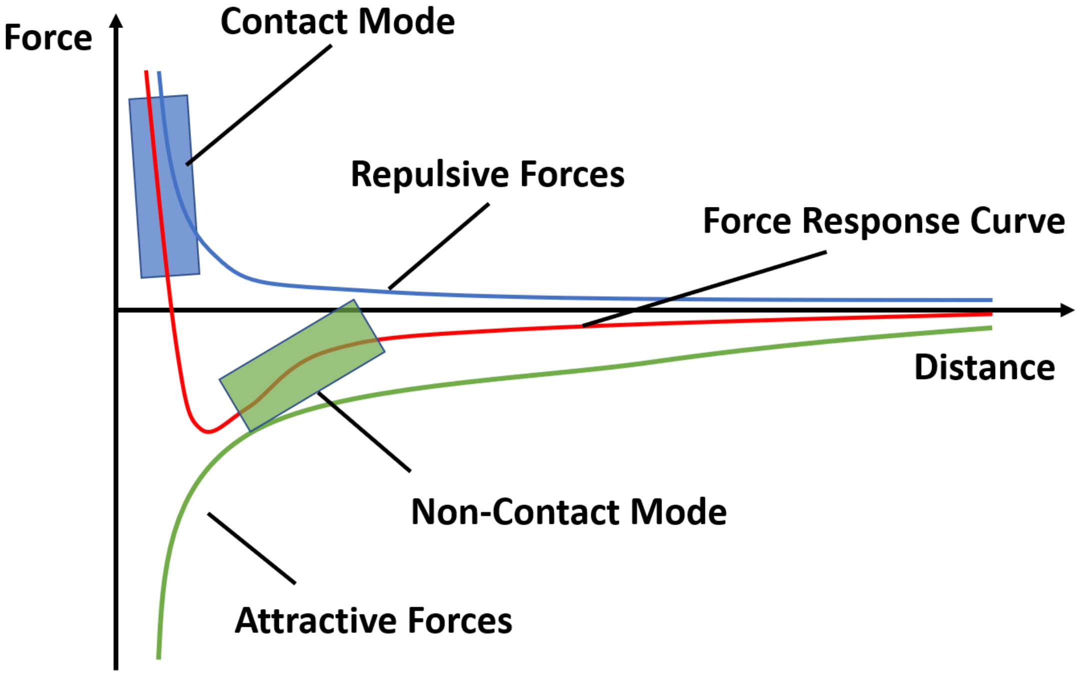

Figure 4.6. Sketch of the interaction forces of the AFM as a function of the distance. The range of the contact and non-contact modes are expressed with the blue and green square, respectively.

The tapping mode is an intermittent mode of the contact and non-contact mode. In the tapping mode, the tip periodically strikes/retracts at/from the sample surface with the oscillating cantilever. The problem of the contact mode (damage to the specimen) and non-contact mode (imaging of adsorbed layers) can be bypassed using the tapping mode.[188]

Nowadays, tapping mode is the most frequently used AFM mode when operating in ambient conditions or liquids. In this dissertation, the tapping mode was applied to investigate the topography of the samples.

4.5 X-Ray Photoelectron Spectroscopy

X-ray photoelectron spectroscopy (XPS), also called electron spectroscopy for chemical analysis (ESCA), is one of the most widely used surface analysis techniques due to its extensive information contents. XPS data possess various information about samples such as the elemental composition, the “empirical formula” of the sample surface and the chemical and electronic state of the elements at it. Thanks to its excellent ability to reveal fundamental properties of the sample, XPS is applied in numerous fields of physics, chemistry, biology and material science.

The working principle of XPS is based on the photoelectric effect. **Figure 4.7** illustrates the mechanism of the photoelectron emission by X-ray irradiation. If a solid sample is irradiated with X-ray photons, the photons with energy (hv) can be absorbed by core-level electrons of the sample, and then the electrons are emitted with the kinetic energy (E_{kin}) that is the reduced photon energy by the work function (Φ) and the binding energy (E_B) with respect to the Fermi level. These emitted electrons are called photoelectrons. The kinetic energy of photoelectrons is formulated as

$$E_{kin} = hv - E_B - \Phi \qquad \textbf{Equation 4.10}$$

where E_{kin} is the kinetic energy of the photoelectron, hv is the photon energy of the X-ray, E_B is the binding energy of the core electron, and Φ is the work function which is determined by both the spectrometer and the sample.

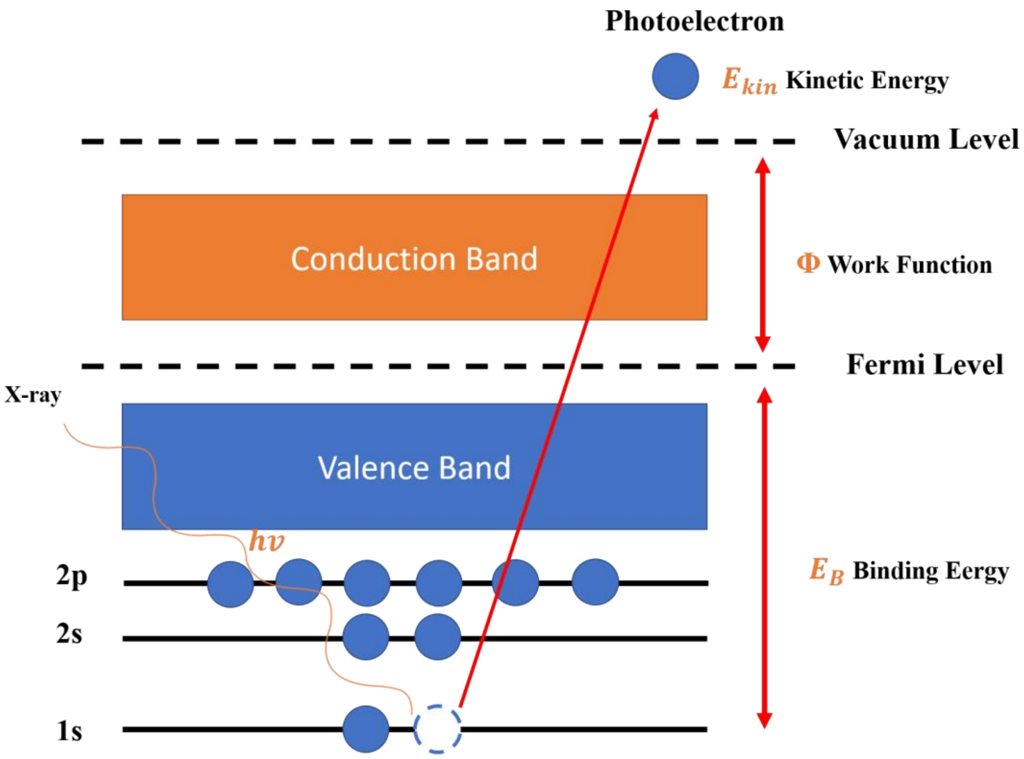

Figure 4.7. Schematics of the mechanism of photoelectron emission. A core-level electron is expelled as a photoelectron to the vacuum level as a consequence of the irradiation of the sample by X-rays.

The kinetic energy of photoelectrons alters depending on their source: the sort of atoms, the orbitals from which photoelectrons escape, the surroundings of atoms from which photoelectrons are emitted, etc. By analyzing the kinetic energy of emitted photoelectrons, it is possible to extract the information regarding the elemental composition and the electronic configuration of the samples.

The binding energy of the core electrons (E_B) can be calculated by simple algebra with experimentally known values (E_{kin}, hv, and Φ). Because the binding energies of the core electrons are not the same for different elements, observed XPS peaks are the characteristic of different elements. Therefore, XPS spectra can be used as “fingerprints” for the respective elements. Practically, XPS can detect all elements with an atomic number larger than 3 (^{3}Li).[189] There are several reasons why hydrogen is not detected in practice. First, hydrogen does not have core electrons (the 1s electron of hydrogen is a valence electron). Second, the photoelectric cross-section of hydrogen is extremely small. For instance, the cross-section of the hydrogen 1s orbital is 5000 times smaller than that of the 1s orbital of carbon.[189] For helium, it does not form solid-phase in the practical XPS measurement conditions. Even if He is solidified, the 1s orbital of He has a very small cross-section (only one electron) for X-ray, which makes the detection of He very difficult. It should be noted that XPS requires an ultra-high vacuum (UHV) to minimize the scattering of the photoelectrons with particles in the air because only the photoelectrons, which finally reach the detector, can be recorded.

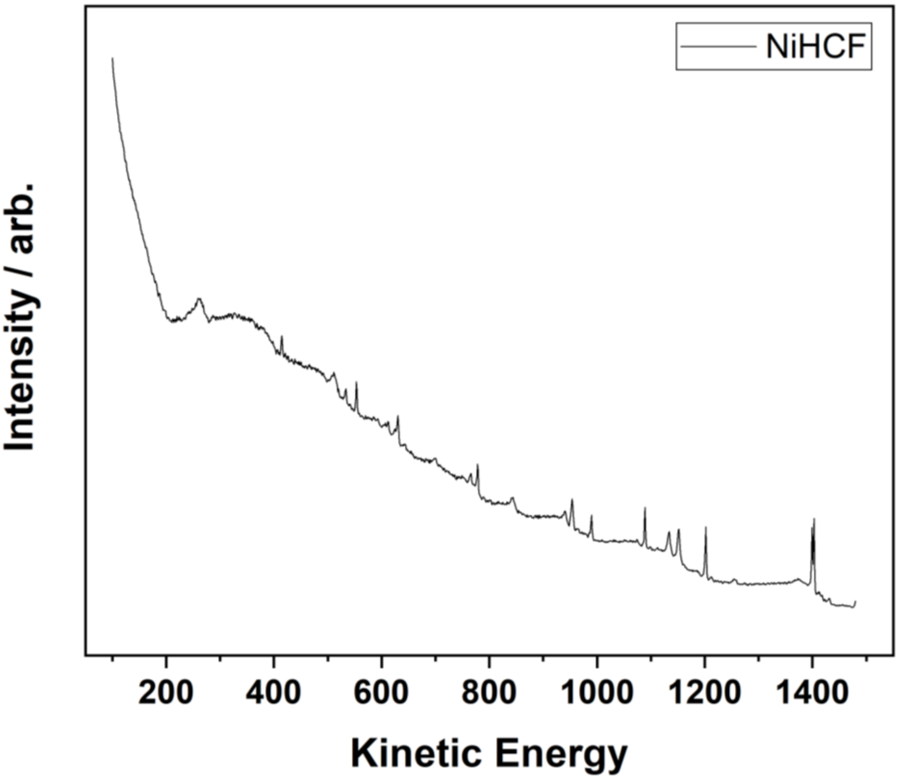

Figure 4.8. Exemplary XPS survey spectrum obtained from a NiHCF sample. One can see characteristic XPS peaks and a large background at the low kinetic energy region (high binding energy).

The recorded XPS spectra include not only the characteristic peaks but also large backgrounds in the low kinetic energy region (see **Figure 4.8**). The characteristic peaks indicate what elements are present in the material and their specific electronic configuration (oxidation states). The characteristic peaks of elements can be slightly shifted depending on the nearest-neighbor atoms. This is especially useful for the analysis of carbon-based materials. The noise in the XPS spectra is mainly accused of the inelastic scattering of the photoelectrons in the materials, thus the background noise is pronounced at lower kinetic energy (larger binding energy). The generated photoelectrons can also undergo inelastic scattering, recombination, excitation of other atoms, re-capture or trapping in various excited states within the material. These effects hinder the escapement of photoelectrons from the material. Thus, the detected signals are mostly attributed from a few nm depths from the top surface.[190]

Apart from photoelectrons, the excitation of atoms by the irradiation of X-ray can also produce other signals such as Auger electrons, and X-ray fluorescence by the decay of the empty core hole. Since the vacancy at the core-level is not energetically stable, this hole is filled with another electron from an outer orbital. When an electron of an outer orbital fills the vacancy at the core level, the energy difference between the core level and the outer orbital can produce other signals. If this energy is released in the form of X-rays, it is called X-ray fluorescence, or if this energy leads the emission of another electron from other orbitals, the emitted electron is called Auger electron.

5. Experimental

5.1 Experimental Setup

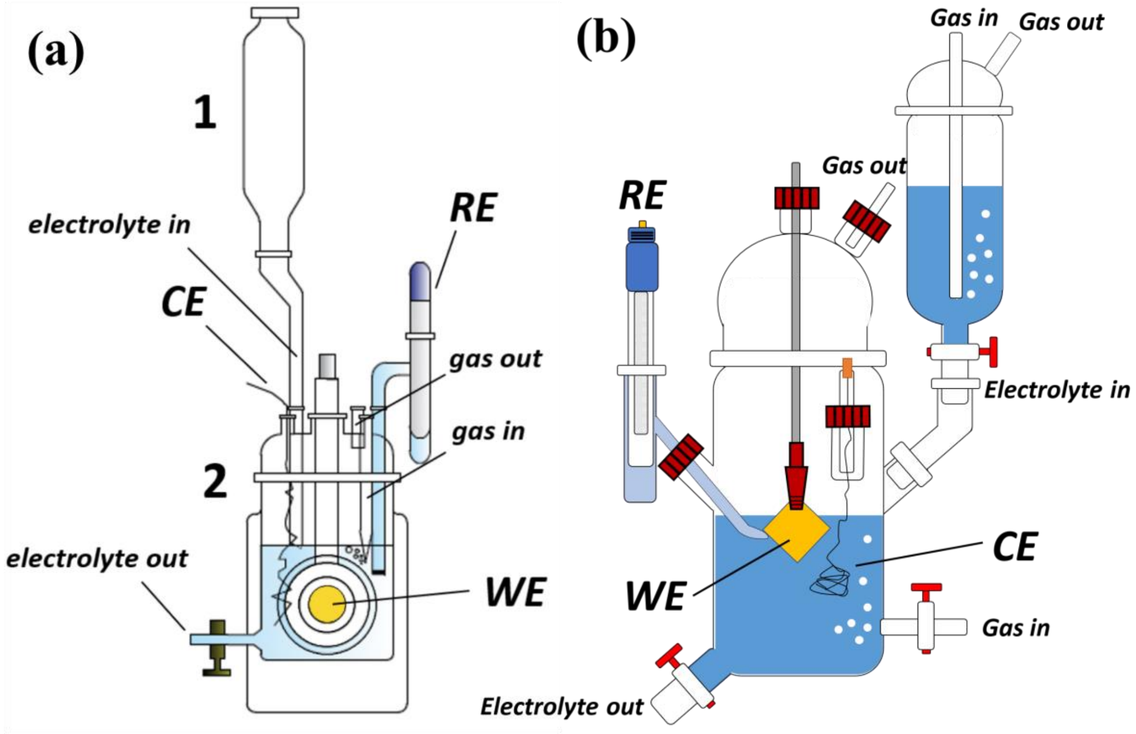

Figure 5.1. Schemes of the electrochemical cells used for electrochemical measurements. (a) Electrochemical cell with a quartz crystal working electrode and (b) a typical electrochemical cell with an arrandee^{TM} gold or graphene foam working electrodes. (a) is adapted from reference.[191]

All electrochemical experiments were performed in the customized glass cells under an Ar atmosphere (Ar 5.0, Westfalen AG). **Figures 5.1(a)** and **(b)** are the schematic representations of the used glass cells. The electrochemical cells are mainly composed of two compartments. The main compartment, where experiments are performed, accommodates a working electrode, a Luggin-capillary with a reference electrode, and a counter electrode. The other compartment is the preconditioning cell, where experiment solutions are prepared. The two compartments are connected through a glass pipe. The second cell (**Figure 5.1 (b)**) was utilized mainly for the deposition and characterization of $Na_2Cr[Fe(CN)_6]$ thin films, as they do not grow well on Au quartz crystal electrodes but on 3D graphene foams. Also, the second cell can accommodate various electrodes and more electrolytes, which provide more reacting species, effectively keeping their concentration during the deposition constant.

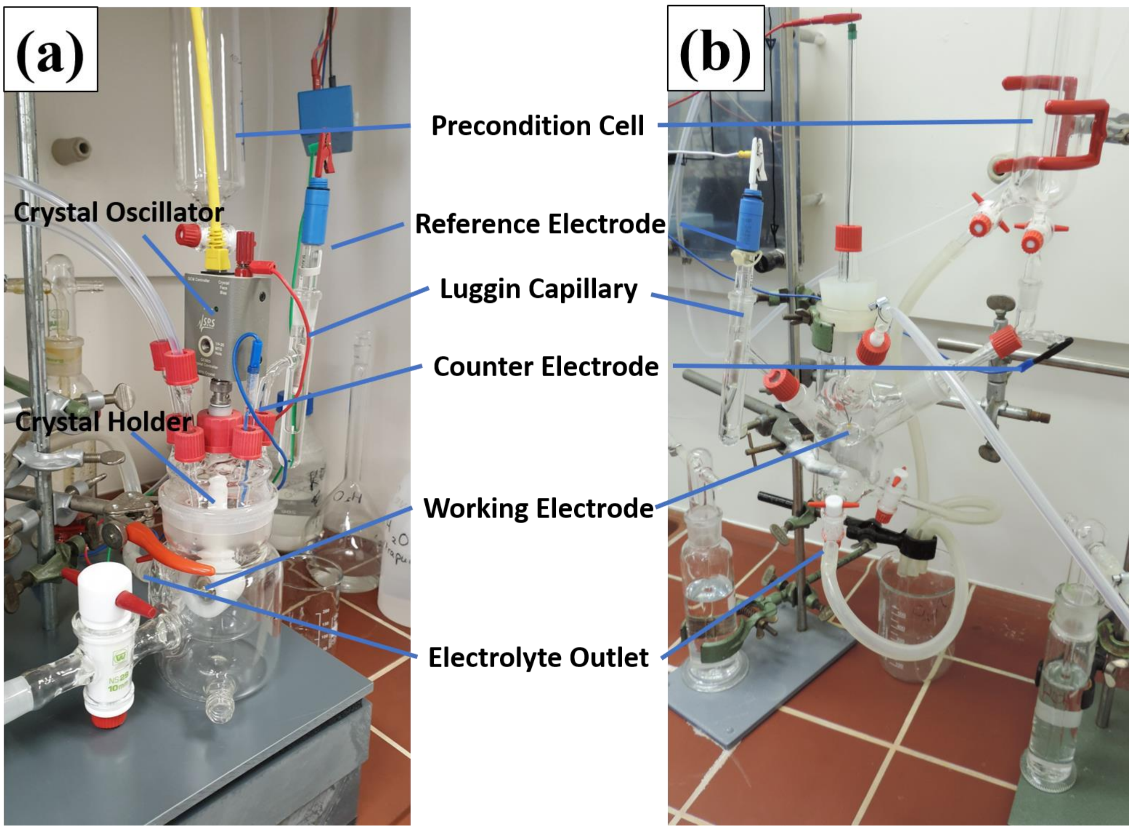

Figure 5.2. Images of the electrochemical cells used for electrochemical measurements. (a) Electrochemical cell with a quartz crystal working electrode and (b) a typical electrochemical cell with a working electrode.

Before conducting experiments, the glass cells were entirely cleaned with a piranha solution (a mixture of H_2SO_4 and H_2O_2, 30 wt%: 70 wt%) to remove unwanted (organic) residues. Subsequently, the cells were thoroughly rinsed with ultrapure water (18.2 MΩ, Evoqua, Germany) and boiled in ultrapure water for one and a half days. After boiling it, the glassware was covered with Al-foil and dried under atmospheric conditions. **Figures 5.2 (a)** and **5.2 (b)** show representative images of the used glass cells. The gas outlets of the electrochemical cells are connected to gas washing bottles that contain aqueous $FeSO_4$

solution in order to remove cyanides that might occasionally be produced during the experiments.[192] For safety reasons, a cyanide sensor (Honeywell Analytics™) was placed close to the experimental setups during the experiments.

In this dissertation, AT-Au quartz crystal electrodes (S_{geo} = 1.37 cm^2), Au (111) single crystals (S_{geo} = 19.635 mm^2), arrandee^{TM} gold on glass substrates or 3D graphene foams were used as the substrate materials. Note that S_{geo} of arrandee^{TM} gold substrate and 3D Graphene foams are not determined, since they were only partially immersed in the electrolyte, making the precise assessment of the surface area difficult. A silver/silver chloride (SSC) electrode filled with 3 M KCl and a Pt wire were used as reference and counter electrodes, respectively. In this work, the potentials are referred to SSC unless noted differently. The reference electrode was placed in a Luggin capillary whose tip was located in the closet vicinity of the working electrode in order to minimize the ohmic potential drop between the working electrode and the tip.[193]

There are important prerequisites for the experiments. (1) The conductivity between the working electrode and the terminal of the cable must be checked. Especially great care is necessary for the second electrochemical cell (**Figure 5.1 (b)**), as the metal part of crocodile clips can be corroded during the introduction of aqueous solutions. (2) The Luggin capillary should be entirely filled with the reference electrolyte without any gas bubbles. The bubbles can interrupt the electrolyte path, which causes a very high impedance.[194, 195] (3) The counter electrode (*e.g.*, Pt wire) should have a larger surface area than the working electrode to ensure that half-reaction at the counter electrode takes place fast enough, not limiting the process at the working electrode.

5.2 Electrode Preparation

All solutions were purged with Ar for at least 10 minutes to minimize possible unwanted side reactions. It was reported that dissolved oxygen in the aqueous electrolyte has adverse effects on the electrode growth and battery performance.[196] Before electrode film deposition, gold substrates were electrochemically cleaned, firstly using 0.1 M NaOH and subsequently utilizing 0.1 M H_2SO_4. This procedure has significance not only for the cleaning of the substrate, but also it makes the surface of a new substrate more active; after the cleaning procedure, more accelerated and pronounced deposition of the electrode material takes place. **Figure 5.3** shows representative CVs for the cleaning procedure of $Na_2Ni[Fe(CN)_6]$ thin films deposited on Au substrates in (a) 0.1 M NaOH and (b) 0.1 M H_2SO_4.

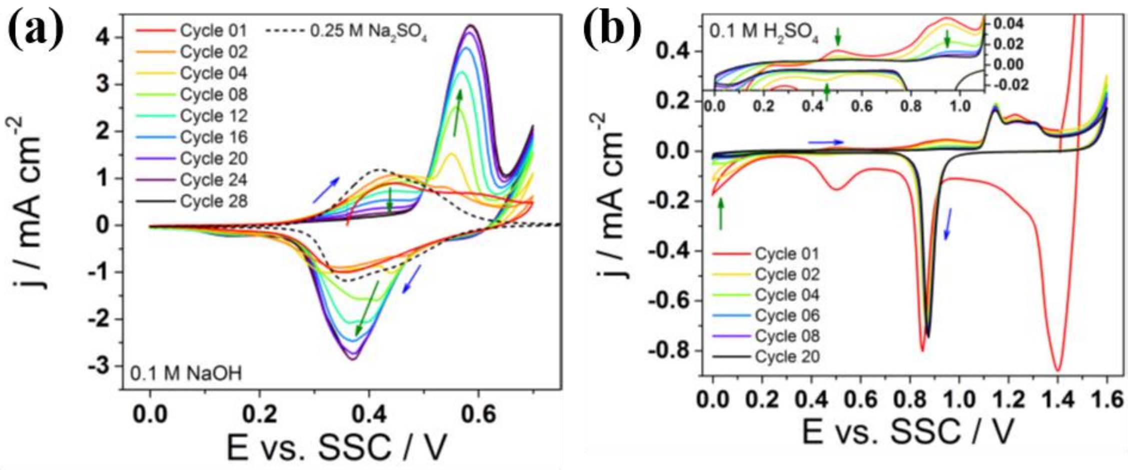

Figure 5.3. CVs of $Na_2Ni[Fe(CN)_6]$ thin films deposited on Au substrates in (a) 0.1 M NaOH and (b) 0.1 M H_2SO_4. The arrows indicate the evolution of CVs along with the increase of the cycle numbers. Adapted from references [197] and [198].

Cleaning of the gold substrates was performed by applying the potential between 0 V and 0.7 V for 0.1 M NaOH and 0 V and 1.5 V for 0.1 M H_2SO_4. The cycle numbers were typically from 10 to ~30 cycles, depending on the conditions of the substrates. In **Figure 5.3 (a)** and **(b),** typical CVs of the cleaning procedure are shown. The characteristic CVs were obtained for the $Na_2Ni[Fe(CN)_6]$ thin films deposited on Au substrates immersed in 0.1 M NaOH and 0.1 M H_2SO_4 aqueous solutions, respectively. **Figure 5.3 (a)** displays the

CVs of $Na_2Ni[Fe(CN)_6]$ thin films deposited on a gold substrate in 0.1 M NaOH (solid lines) and 0.25 M Na_2SO_4 (dashed line). The cathodic peak around 0.4 V vanishes along with the increasing the cycle number; however, a new cathodic peak appears around 0.6 V, and the anodic peaks around 0.4 V become more pronounced. After this procedure, the deposited $Na_2Ni[Fe(CN)_6]$ thin films were found to be transformed into nickel oxides, being easily removable in acidic media.[197, 198] **Figure 5.3 (b)** shows typical CVs demonstrating the subsequent cleaning in 0.1 M H_2SO_4 solution. After several cycles, some pronounced peaks around 0.5 V and 1.4 V disappear. Moreover, relatively small cathodic peaks around 0.5 V and 0.95 V also disappear. Notably, catalytic reactions at 0 V is significantly suppressed after 20 cycles of the cleaning. At the final cycle (20th), the CV of pure Au substrate in 0.1 M H_2SO_4 electrolyte can be obtained.

It should be noted that the cleaning procedure for the case of the deposited $Na_2Ni[Fe(CN)_6]$ thin films is just shown as an example; how CVs evolve in the course of the cleaning may differ depending on the residuals on the Au substrate. Consequently, one has to focus on the shape of the final CV cycle of **Figure 5.3 (b)** (black line), which confirms the completeness of the cleaning procedure as a benchmark. **Figure 5.4** shows a typical CV of a clean gold substrate in 0.1 M H_2SO_4 for comparison.

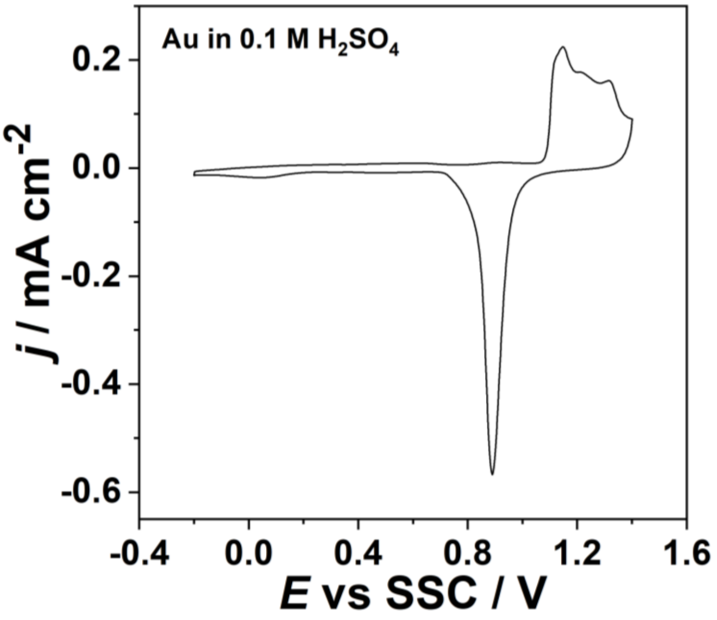

Figure 5.4. CV of a bare (cleaned) gold substrate recorded in Ar-saturated 0.1 M H_2SO_4 at a scan rate of 50mV s^{-1}.

The deposition of PBAs was carried out using an aqueous deposition solution by the cyclic voltammetry technique. The deposition solutions were diluted to few millimoles in different supporting electrolytes, depending on targeted electrode materials. The compositions of the aqueous deposition solutions are listed in **Table 5.1**. The solutions were purged with Ar in the preconditioning cell for at least 10 min and then introduced into the main cell. The deposition of PBA thin films on gold substrates was performed in the deposition solution by cycling the electrode potential in a desirable potential range for the different number of cycles. In all cases, the scan rate was set to 50 mV s^{-1}. The corresponding potential ranges and the cycle numbers for the different electrode materials are listed in **Table 5.2**. During the deposition, the frequency changes of the quartz crystal were measured simultaneously in order to calculate the mass gain directly. The detailed procedures for the deposition of PBAs are described later in **Chapter 6, Results and Discussion**.

Target Material	Composition of the Deposition Solution
$Na_2Ni[Fe(CN)_6]$	0.5 mM $NiCl_2$ + 0.5mM $K_3[Fe(CN)_6]$ + 0.25 M Na_2SO_4
$Na_2VO_x[Fe(CN)_6]$	5 mM $NaVO_3$ + 5 mM $K_3[Fe(CN)_6]$ + 3.6 M H_2SO_4
$K_2Cr[Fe(CN)_6]$	10 mM $CrCl_3$ + 5 mM $K_3Fe[(CN)_6]$ + 0.25 M KNO_3
$Na_2Mn[Mn(CN)_6]$	7 mM $MnSO_4$ + 11 mM $K_3[Mn(CN)_6]$ + 0.25 M Na_2SO_4

Table 5.1 The composition of the deposition solutions for $Na_2Ni[Fe(CN)_6]$, $Na_2VO_x[Fe(CN)_6]$, $K_2Cr[Fe(CN)_6]$ and $Na_2Mn[Mn(CN)_6]$, respectively.

Target Material	Potential Range	Cycles
$Na_2Ni[Fe(CN)_6]$	0.05 V – 0.85 V	~60 cycles
$Na_2VO_x[Fe(CN)_6]$	0.45 V – 1.2 V	~110 cycles
$K_2Cr[Fe(CN)_6]$	-1.1 V – 1.25 V	~100 cycles
$Na_2Mn[Mn(CN)_6]$	-1.18 V – -0.6V	~50 cycles

Table 5.2 The applied potential ranges and the cycle numbers for $Na_2Ni[Fe(CN)_6]$, $Na_2VO_x[Fe(CN)_6]$, $K_2Cr[Fe(CN)_6]$ and $Na_2Mn[Mn(CN)_6]$ deposition, respectively.

5.3 List of Equipment, Materials, Chemicals, and Software

Equipment:

AFM: MultiMode EC-STM/EC-AFM with a Nanoscope IIID controller, Veeco Instruments Inc., USA.

EQCM: QCM 200, Stanford Research Systems, USA.

Potentiostat: VSP-300, Bio-Logic, France.

Reference electrodes: SSC, SI Analytics, Germany.

Water purification system: Evoqua Ultra Clear 10 TWF 30 UV, Evoqua, Germany.

Materials:

Ar 5.0, Air Liquid, Germany.

AT-cut Au quartz crystal wafer, d_{qcw}: 2.54 cm, d_{Au}: 1.37 cm, Stanford Research Systems, USA.

Pt wire, 99.99 %, d: 0.3 mm, GoodFellow, Germany.

Chemicals:

H_2SO_4, 96 %, Suprapur, Merck, Germany	NaOH, ≥98%, Sigma Aldrich, Germany
Na_2SO_4, 99.0%, Sigma Aldrich, Germany	K_2SO_4, 99.0%, Sigma Aldrich, Germany
NaCl, 99.0%, Sigma Aldrich, Germany	KCl, 99%, Sigma Aldrich, Germany
$NaClO_4 \cdot H_2O$, 98%, Alfa Aesar, Germany	$MnSO_4$, 99%, Merck, Germany
$NaCH_3COO$, 99%, Sigma Aldrich, Germany	KNO_3. 99.0%, Sigma Aldrich, Germany
KCH_3COO, 99%, Sigma Aldrich, Germany	$RbNO_3$, 99.7%, Sigma Aldrich, Germany
$K_3[Fe(CN)_6]$, 99.0%, Sigma Aldrich, Germany	$CsNO_3$, 99%, Sigma Aldrich, Germany
$NaNO_3$, 99.0%, Sigma Aldrich, Germany	
$LiNO_3$, ReagentPlus®, Sigma Aldrich, Germany	
$NaHCO_3$, 99.7-100.3% Ph. Eur, VWR Chemicals, Germany	
KCN, Reagent Ph. Eur. zur Analyse, Merck, Germany	

Software:

EC-LAB 10.40- Potential control and Data collection.

EIS Data Analysis 1.1 and 1.2- Fitting of EIS spectra.

Nanoscope 5.31r1- AFM data collection.

OriginPro 2019- Data analysis, Treatment, and Display.

SRS QCM200- EQCM data collection.

WSxM 4.0 Beta 8.3- AFM data analysis.

6. Results and Discussion

This chapter describes the preparation and characterization of four different battery electrode materials based on PBAs and the study of the Na-intercalation mechanism in the studied materials. This section is divided into four subchapters according to the electrode materials. The first three subchapters discuss the three cathode materials, namely $Na_2Ni[Fe(CN)_6]$ (nickel hexacyanoferrate), $Na_2VO_x[Fe(CN)_6]$ (vanadium hexacyanoferrate), and $Na_2Cr[Fe(CN)_6]$ (chromium hexacyanoferrate), respectively. The last subchapter demonstrates the synthesis of $Na_xMn[Mn(CN)_6]$ (manganese hexacyanomanganate) and its promising characteristics as an anode material for aqueous Na-ion batteries. Strictly speaking, the precise chemical names of the four PBAs should include sodium (*e.g.*, $Na_2Ni[Fe(CN)_6]$ is disodium nickel hexacyanoferrate), but those materials will be called (also in their abbreviation) without Na in this dissertation. This should help readers quickly recognize the compounds' names with ease as frequently named in the literature.[199-213]

The four materials mentioned above were synthesized by electrochemical deposition and characterized by various *in-situ* and *ex-situ* techniques. A tentative reaction model of the Na-intercalation mechanism was established by primarily analyzing the EIS data collected from the PBA materials immersed in aqueous Na-electrolytes with the elaborate interpretations. The correctness of the suggested model was assessed with various approaches, whose results have shown a good agreement with the proposed model. The validity and applicability of the hypothesis of the intercalation mechanism have been further confirmed in various systems ranging from other PBA materials to other Li-ion battery systems in organic media. However, they are not discussed in this dissertation and are instead referred to the references.[200-202]

6.1 Nickel Hexacyanoferrate

The studies of nickel hexacyanoferrate (NiHCF) have been widely reported in the literature since approximately 50 years earlier.[214-216] In the beginning, they had focused on the fundamentals and applications for electrochromism, ion exchangers, catalysts, chemical and biosensors as well as Cs-ion removers. Recently, NiHCF has been re-spotlighted as a potential energy storage material for aqueous alkali metal ion batteries or supercapacitors.[83, 102, 103, 217-224] In the literature, NiHCF electrodes demonstrated specific capacities ranging from 40 mAh g^{-1} to 60 mAh g^{-1} with excellent cycling stabilities over thousands of cycles in aqueous Na-electrolytes.[83, 102, 224] A significant portion of the studies utilized slurry of NiHCF powder that is prepared by a precipitation method with post-processes to improve the electrode quality such as vacuum drying at an elevated temperature and mixing with conductive additives. However, for the fundamental investigation of the Na-intercalation and -deintercalation mechanism, this preparation method may not be proper, as the slurry contains not only NiHCF powder but also other chemicals, such as conductive additives or mixing agents. The additional components are necessary or at least beneficial to improve battery performances; however, their influence might appear in electrochemical measurements. In this dissertation, therefore, NiHCF electrodes were prepared solely by electrochemical deposition for studying their electrochemical behaviors and Na-intercalation and -deintercalation with the minimal degree of perturbation caused by other chemicals.

6.1.1 Preparation of $Na_2Ni[Fe(CN)_6]$ Electrodes

The electrochemical deposition and characterization of $Na_2Ni[Fe(CN)_6]$ electrodes were performed in the glass cell using a three-electrode configuration as shown in **Figures 5.1 (a)** and **5.2 (a)**. AT-cut Au QCM crystals were used as substrates for the deposition of $Na_2Ni[Fe(CN)_6]$ thin films. An aqueous solution containing 0.25 M Na_2SO_4, 0.5 mM $K_3Ni[Fe(CN)_6]$, and 0.5 mM $NiCl_2$ was used as the deposition solution. Before the deposition, the prepared solutions were purged with Ar gas longer than at least 5 minutes to remove dissolved oxygen thoroughly.[196] Subsequently, the electrode potential was cycled between 0.05 V and 0.85 V vs Ag/AgCl (SSC) at a scan rate of 50 mV s^{-1} for ~60 cycles resulting in a deposited material.

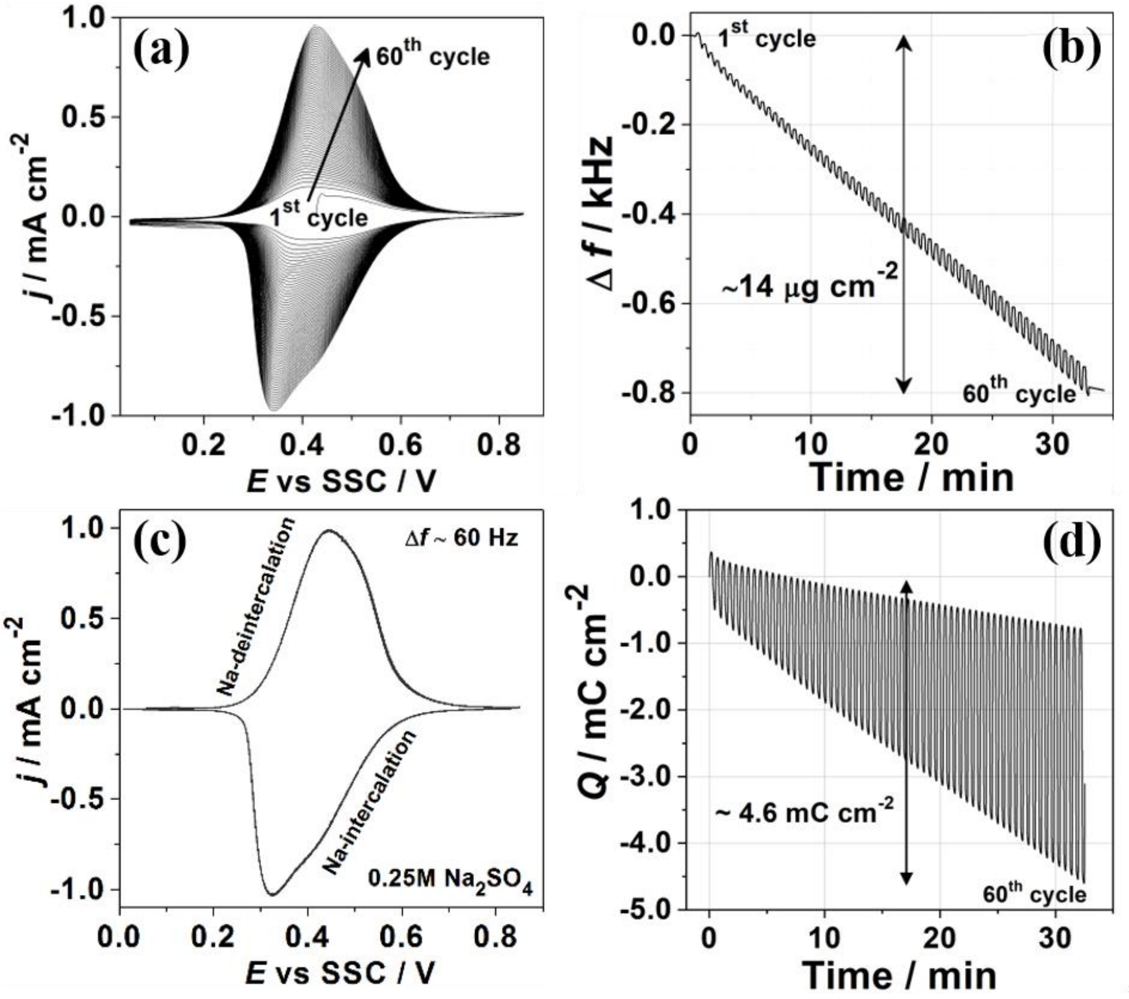

Figure 6.1. (a) Cyclic voltammograms obtained during the electrochemical deposition of $Na_2Ni[Fe(CN)_6]$ thin films on the Au QCM crystal and (b) the EQCM curves recorded in the course of the deposition. (c) A representative CV of the $Na_2Ni[Fe(CN)_6]$ films in a 0.25 M Na_2SO_4 aqueous electrolyte. The scan rate was set to 50 mV s^{-1}. (d) Charge vs time curves registered during the deposition.[22]

Figure 6.1 (a) shows representative CVs of the NiHCF thin film deposition. In the CVs, one can see the increment in the magnitude of the anodic and cathodic peak currents along with the cycling, which reveals the growth of the NiHCF films. The origin of the anodic and cathodic current is attributed mainly to the change in the oxidation state of Fe present in the $Na_2Ni[Fe(CN)_6]$ films, which is the driving force for Na-intercalation and -deintercalation. Thus, it can be observed that the deposition process also is accompanied by the intercalation and deintercalation of Na-ions. The mass change of the QCM crystal during the deposition was measured with the EQCM as demonstrated in **Figure 6.1 (b)**. The resulting mass of the NiHCF film was calculated using the Sauerbrey equation. The final frequency change of the QCM crystal was measured as *ca* 8 kHz, which is equivalent to the mass change of *ca* 14 µg cm^{-2}.[225] In comparison to the mass calculated with the final charge consumed (*ca* 4.6 mC cm^{-2}, see **Figure 6.1 (d)**), the mass deviation between the value from the EQCM and that of the calculated from the charge is within ~5 %. This shows high reliability of the mass balancing of the EQCM for this system. Here, the molar mass of $Na_2Ni[Fe(CN)_6]$ (Na-intercalated film) was used to calculate the weight of the film. The experiments related to the Na-intercalation and -deintercalation in the NiHCF thin film were performed in a 0.25 M Na_2SO_4 aqueous electrolyte. **Figure 6.1 (c)** exhibits a typical CV characterizing Na-intercalation and -deintercalation. The frequency change due to the Na-intercalation and -deintercalation was measured as *ca* 60 Hz, which is equal to *ca* 1 µg cm^{-2} as displayed in **Figure A3** (see **Appendix B**). It should be remarked here that the electrochemical deposition and Na-intercalation into the NiHCF thin films were highly reproducible. This deposition procedure was equivalently conducted for the preparation of NiHCF electrodes for the subsequent measurements. The morphology of the NiHCF thin films was investigated with SEM, electron microprobe, and AFM.

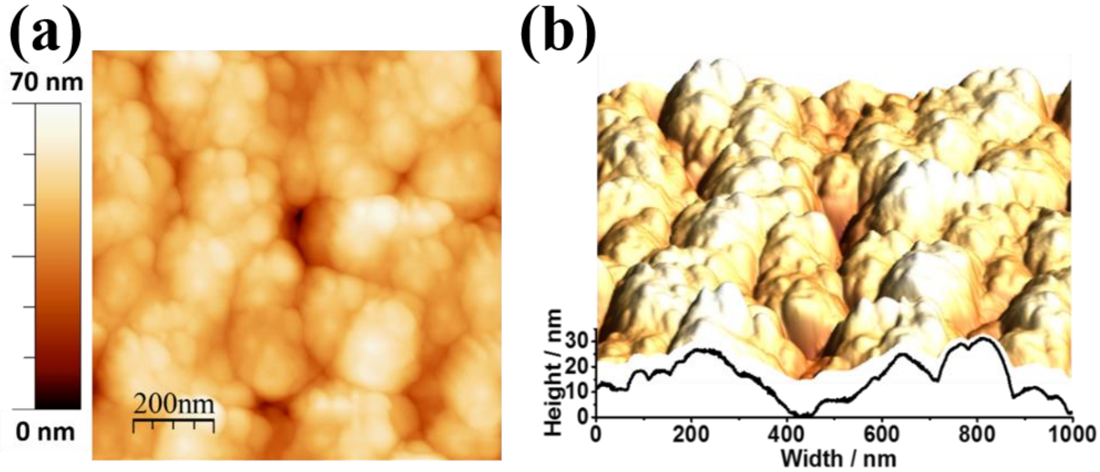

Figure 6.2. (a) 2D and (b) 3D AFM images of the deposited $Na_2Ni[Fe(CN)_6]$ thin films.

Figure 6.2 (a) and **6.2 (b)** shows the 2D and 3D AFM images of the deposited $Na_2Ni[Fe(CN)_6]$ thin films, respectively. The smoothness of the electrodeposited NiHCF thin films was verified by 3D AFM profiling. The resulting surface roughness was estimated as ~10 nm**.**

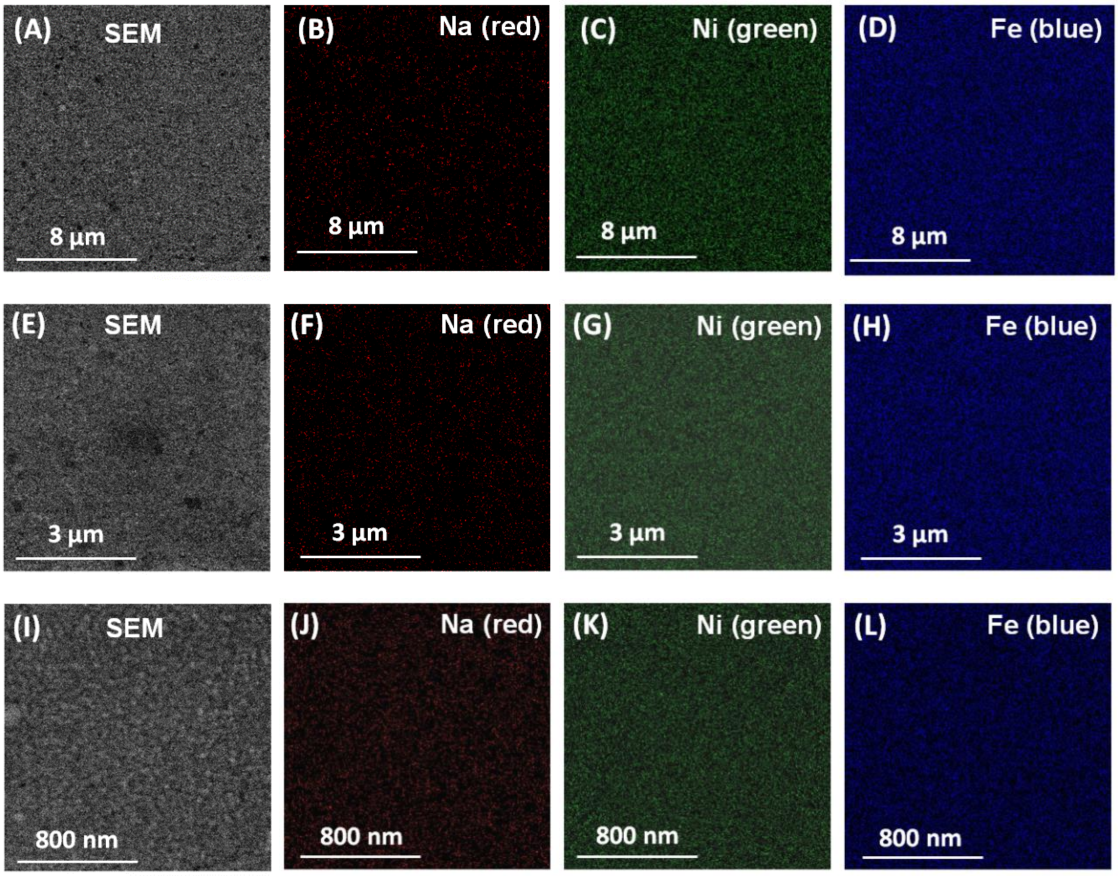

Figure 6.3. SEM images and elemental distribution images of the $Na_2Ni[Fe(CN)_6]$ films at scale bars : (a-d) 8µm, (e-h) 3µm and (i-l) 800 nm. (a), (e), and (i) are the SEM images of the film, and the red, green, and blue colors represent Na, Ni, and Fe atoms, respectively.

The SEM and elemental analysis of the deposited NiHCF films were conducted using "Mira" (Tescan, Czech Republic) and "INCA Energy 350" (Oxford Instruments Analytical, UK), respectively. The used electron beam has an energy of 20 kV. **Figure 6.3** shows SEM images and the distribution of the main elements (Na, Ni, and Fe) of the NiHCF thin films at different scales. As can be seen in **Figure 6.3 (a-l)**, the NiHCF thin films were uniformly deposited.

6.1.2 Mechanism of Na-Intercalation into NiHCF

Considering the total mass of the $Na_2Ni[Fe(CN)_6]$ films (~14 µg cm^{-2}) and the mass alteration of ~1 µg cm^{-2} owing to the Na-intercalation and -deintercalation, it is reasonable to conclude that one Na-ion per unit structure ($Na_2Ni[Fe(CN)_6]$) participates in the intercalation and deintercalation processes within the given potential range (0.05 V ~0.85 V). This can be expressed as the following reaction formula:

$$NaNi[Fe^{III}(CN)_6] + Na^+ + e^- \leftrightarrow Na_2Ni[Fe^{II}(CN)_6] \qquad \textbf{Equation 6.1}$$

Equation 6.1 is a generally accepted model for Na-intercalation in $Na_2Ni[Fe(CN)_6]$ in aqueous electrolytes.[85] Here, the mechanism of Na-intercalation and -deintercalation is simply described with a one-step process that does not involve any other components in the system, such as a solvent or any other electrolyte components. In order to challenge the validity of the generally accepted model described above, the electrochemical impedance spectroscopy (EIS) measurement was performed.

For the EIS measurements, 10 mV of sinusoidal probing signals with a varying frequency between 10 kHz and 0.5 Hz were applied to the deposited NiHCF thin films that were immersed into a 0.25 M Na_2SO_4 aqueous electrolyte. The impedance data were collected at the electrode potentials between 0.1 V and 0.8 V vs SSC. A shunt capacitor of 2.2 µF was connected in parallel between the reference and counter electrodes to minimize possible instrumental artifacts at the high-frequency range in resulting impedance spectra.[195] The fitting results were evaluated by analyzing root-mean-square deviations and the error of the individual parameters using the “EIS Data Analysis 1.2” software as described in the literature.[226, 227] The recorded impedance data were evaluated with Kramers-Kronig analysis revealing no issues with the quality of the recorded impedance spectra.

The resulting impedance spectra are presented in **Figure 6.4**. They have different shapes depending on the electrode potentials at which the impedances were measured. As seen in **Figure 6.4 (a)**, the impedance spectra measured at 0.25 V and 0.27 V, at which no Na-intercalation nor -deintercalation occurred, exhibit the shape of a semi-circle together with a (quasi-) straight line at the low-frequency region. This shape is well-known for diffusion-limited systems. Interestingly, the “loop-shaped” impedance spectra were observed at the electrode potentials (*ca* 0.30 V – 0.65 V) where Na-intercalation and -deintercalation take place (see **Figure 6.4 ((b-d)**).

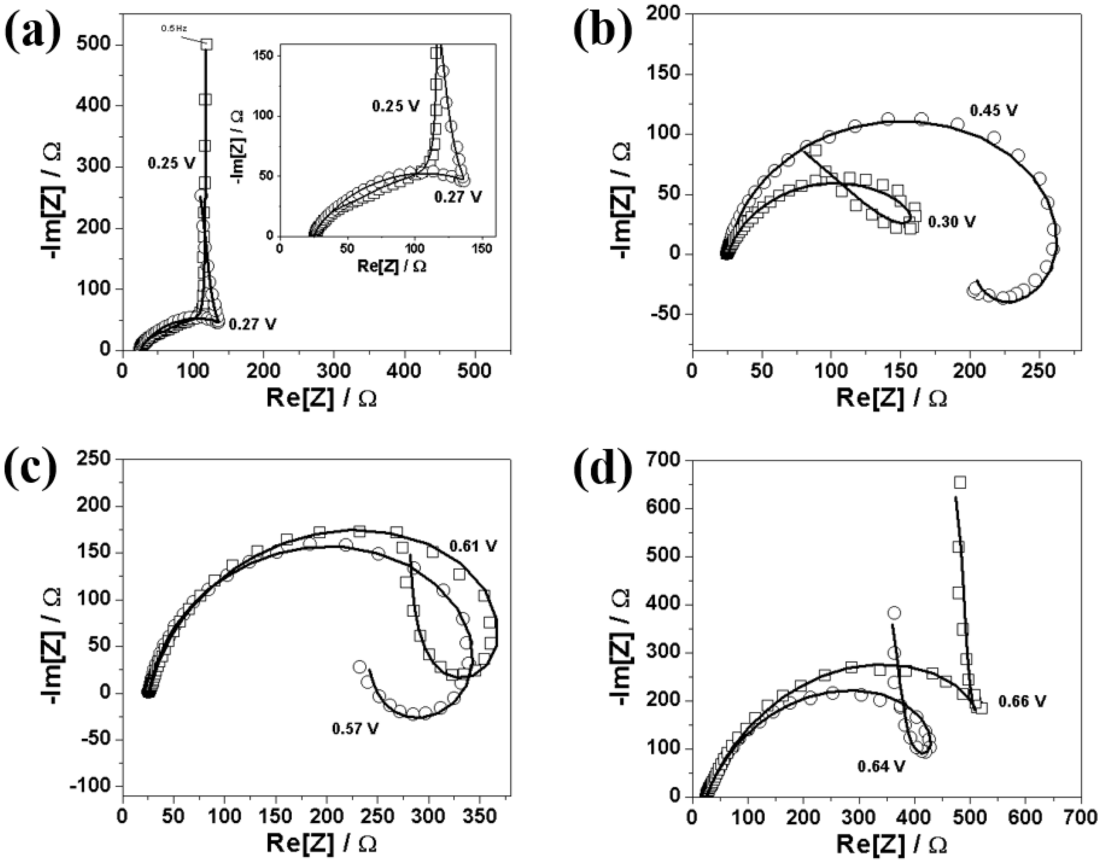

Figure 6.4. (a-d) Impedance spectra (open symbols) of $Na_2Ni[Fe(CN)_6]$ thin films in a 0.25 M Na_2SO_4 aqueous electrolyte and their fitting (solid lines) at different potentials. The used equivalent electric circuit model will be thoroughly discussed below.

In order to describe the particular shape of the impedance spectra, a rather complex model is required. According to the literature, the loop-shaped impedance spectra can be seen in the electrode process involving two reversible intermediate steps and one additional stage, which do not contribute to the net interfacial charge transfer.[22, 171] The “loop” is *e.g.* frequently observed in corrosion processes, which often involve multi-step mechanisms.[166, 228-234] However, it is not likely the case in this particular material because of its extremely high stability. Nonetheless, the loop shape of the impedance spectra suggests that the Na-intercalation mechanism in the case of the NiHCF electrodes in aqueous media involves at least three stages. For instance, the Na-intercalation mechanism may encompass the relaxation process by anion adsorption and desorption. If there are several stages during Na-intercalation and -deintercalation, it can be assumed that the reaction rates of each stage may differ. Under this assumption, the first step (the fastest) can be the alteration of the oxidation state of Fe, which is the driving force of the intercalation and deintercalation of Na-ions. For the sake of a concise description of the equations, only the deintercalation is formally described, while all steps are (quasi-) reversible. The first step is the redox reaction of Fe in the NiHCF films.

(1) Electroactive step: Oxidation or reduction of Fe

$$Na_2Ni[Fe^{II}(CN)_6] - e^- \rightleftharpoons Na_2Ni[Fe^{III}(CN)_6]^+$$

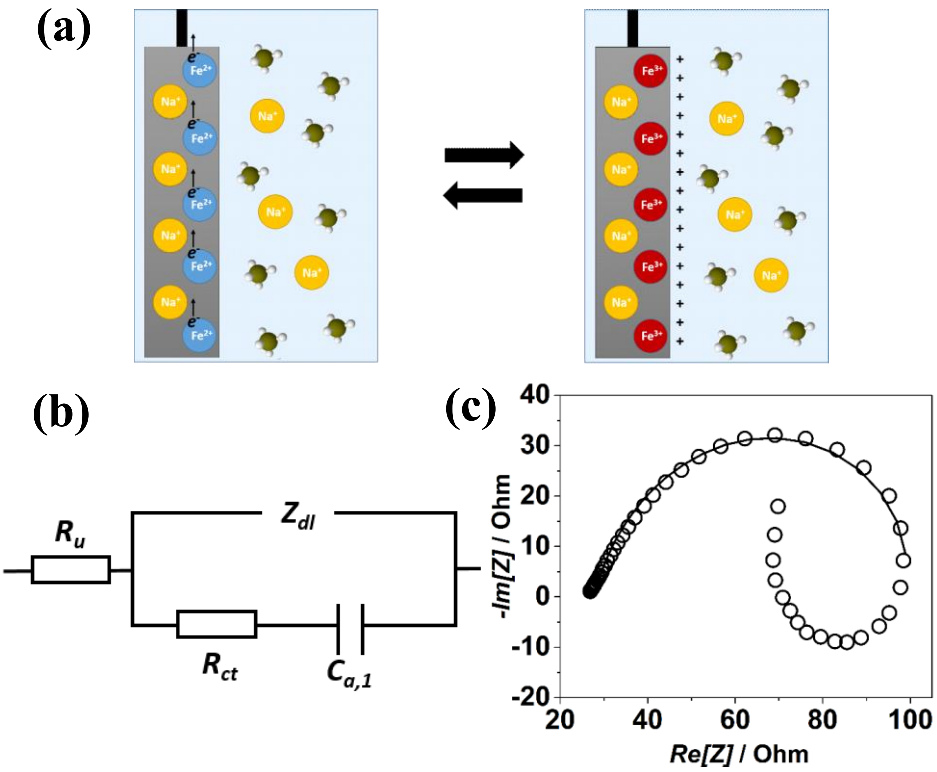

Figure 6.5. The first step of the proposed Na-intercalation and -deintercalation process. (a) Graphical illustration of the oxidation and reduction of Fe in the $Na_2Ni[Fe(CN)_6]$ films. (b) The corresponding equivalent electric circuit for this stage that can be often found in the literature (R_u – uncompensated resistance, Z_{dl} – double-layer impedance, R_{ct} – charge transfer resistance, and $C_{a,1}$ – adsorption capacitance). (c) A representative “loop-shaped” impedance spectra (open symbols) with the partial fitting (solid line) using the EEC model present in (a).

Figure 6.5 (a) shows the graphical illustration of the oxidation and reduction of Fe in the $Na_2Ni[Fe(CN)_6]$ films. **Figure 6.5 (b)** represents the EEC model describing the one-stage surface-limited reversible redox process. This model can, however, solely account for the upper-semicircle of the impedance spectra as shown in **Figure 6.5 (c)**. The EEC model failed for the fitting of full spectra, which disproves the appropriateness of the simplified model in interpreting the obtained data. The imperfection of the fitting using the four-element model indicates the possibility of the existence of other steps in the Na-intercalation mechanism. Therefore, a more complicated model with additional circuit elements is needed. The excess positive charge may temporarily remain at the NiHCF films before the Na-deintercalation is complete. This excess charge could be effectively compensated by the adsorption of negative ions from the electrolytes (step 2). For instance, in the studied system, the positively charged interface might be temporarily neutralized by specifically adsorbing anions (*e.g.*, SO_4^{2-}) from the electrolyte. Here, sulfate ions represent adsorption species present in the electrolyte. This adsorption process is distinguishable via the EIS analysis. Thus, the second step can be written as:

(2) Specific adsorption or desorption step (temporary compensation of the excess charge)

$$2\,Na_2Ni[Fe^{III}(CN)_6]^+ + SO_4^{2-} \rightleftharpoons (Na_2Ni[Fe^{III}(CN)_6])_2SO_4$$

Figure 6.6 (a) shows the illustration of the two-step mechanism: the oxidation and reduction of Fe in the NiHCF films and the adsorption and desorption of anions for the charge compensation. The EEC model accounting for the two-step mechanism can be constructed as shown in **Figure 6.6 (b)**. This EEC model can explain the impedance spectra at higher frequencies, but the fitting result is, nevertheless, incomplete over the whole frequency range (see **Figure 6.6 (c)**). Significant residual errors were observed in the low frequencies in an attempt to the fitting of the full spectra.

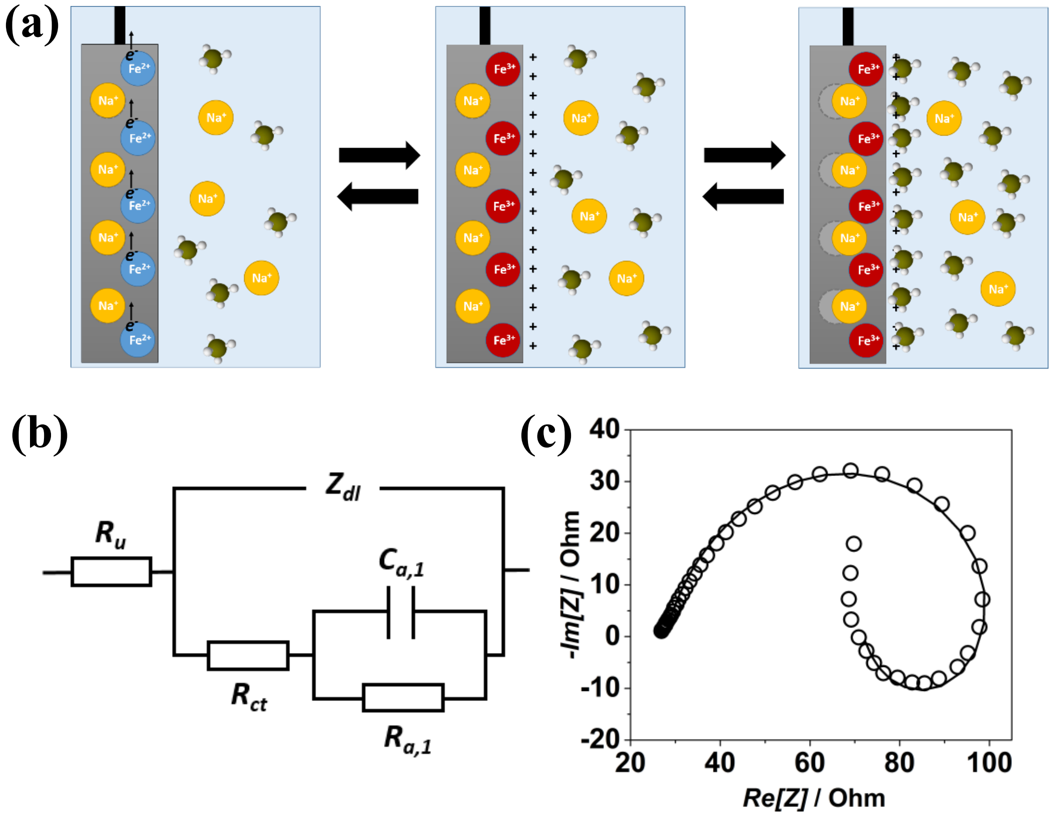

Figure 6.6. Two-step process consisting of a charge-transfer and a specific adsorption reaction. (a) Scheme of the first and second steps of Na-intercalation and -deintercalation. The two steps are quasi-reversible and interconnected with each other. (b) An equivalent electric circuit that can describe two intrinsically-connected reversible redox processes (R_u – uncompensated resistance, Z_{dl} – double-layer impedance, R_{ct} – charge transfer resistance, $R_{a,1}$ – adsorption resistance, and $C_{a,1}$ – adsorption capacitance). Note, that within this physical model $R_{a,1}$ and $C_{a,1}$ can be formally negative due to the properties of the physicochemical equations describing the system. (c) The loop-shaped impedance spectra with the partial fitting result using the EEC model presented in (b). Note that the fitting of full spectra is not possible yet using the model shown in (b).

When the intercalation and deintercalation of Na-ions are completed, the adsorbed species will leave the surface of the NiHCF films (step 3). Therefore, the last step can be described as:

(3) A process without a net charge-transfer involving the Na-deintercalation in conjunction with the desorption of anions:

$$(Na_2Ni[Fe^{III}(CN)_6])_2SO_4 \rightleftharpoons 2\,Na^+ + SO_4^{2-} + 2\,NaNi[Fe^{III}(CN)_6]$$

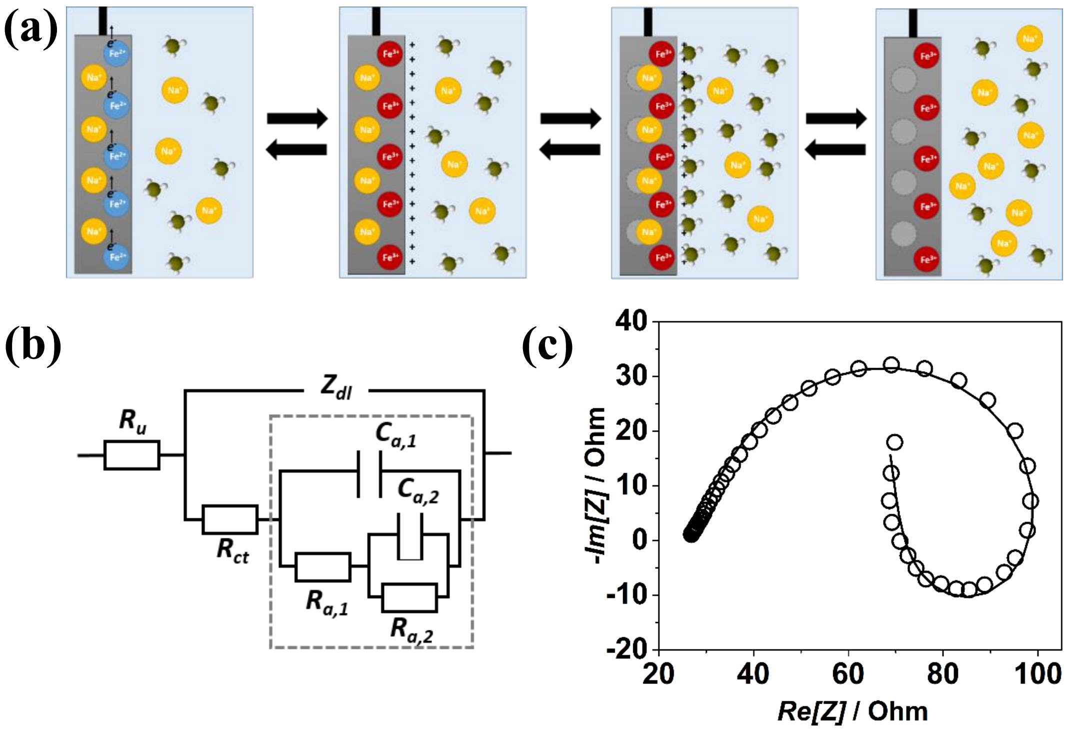

Figure 6.7. Three interconnected reversible steps of Na-intercalation and -deintercalation. (a) Scheme of the "three-stage mechanism" and (b) the corresponding equivalent electric circuit capable to explain the "loop-shaped" spectra (R_u – uncompensated resistance, Z_{dl} – double-layer impedance, R_{ct} – charge transfer resistance, and the other resistance and capacitance elements in the dashed-square are pseudo-resistance and capacitance). Note, that within this physical model $R_{a,1}$ and $C_{a,1}$ as well as $R_{a,2}$ and $C_{a,2}$ can be formally negative due to the properties of the physicochemical equations describing the system (c) The loop-shaped spectra with the fitting using the EEC model in (b).

Including the two above-discussed steps, it can be concluded that the mechanism of the Na-intercalation (and -deintercalation) has *at least* three quasi-reversible steps: (1) the alteration of the oxidation state of Fe in the NiHCF thin films, (2) temporary adsorption (or desorption) of anions, and (3) Na-intercalation and -deintercalation with the subsequent desorption (or adsorption) of the temporarily adsorbed (or desorbed) species.

Figure 6.7 (a) shows a schematic illustration of the proposed three-stage mechanism. An EEC model representing the three-stage mechanism is shown in **Figure 6.7 (b)**. It should be noted that the four elements in the selected part are solely formal parameters which describe the adsorption and desorption processes; their value can be either positive or negative, and they must be considered as a group, not individual elements.[171] **Figure 6.7(c)** shows a representative impedance spectrum with an excellent fitting result. By using this EEC model presented in **Figure 6.7 (b)** to fit the recorded impedance spectra, one can obtain excellent fitting results for all the impedance spectra measured at different potentials (see **Figure 6.4**).

The conducted assessment of the fitting results ensured the validity of the proposed model. This further indicates that the acquired spectra are not associated with the artifacts or experimental errors, such as contamination, non-stationarity, or non-linearity effects. The detailed mathematical derivation of this model and its unique relationship with electrochemical processes involving three steps are described in **Appendix A** in more detail. The unique relationship of the impedance spectra and other EEC models presented below can be found in the literature.[171]

If anions indeed participate in the Na-intercalation and -deintercalation process, the change in the electrolyte composition should influence some kinetic parameters of Na-intercalation. In order to find another support for the hypothesis of the three-stage mechanism, cyclic voltammetry study of the NiHCF thin films in various aqueous electrolytes was performed.

6.1.3 Correlation of the Nature of Anions with Na-Intercalation Properties

Under the assumption of the three-stage mechanism that involves the anion adsorption and desorption, the change of the anion component of the electrolytes would influence the kinetics of Na-intercalation and -deintercalation. In order to study the change of the kinetic parameters, five different Na-salts with different conjugate base anions were selected: Na_2SO_4, NaCl, $NaNO_3$, $NaClO_4$, and NaOAc (sodium acetate). The chosen anions have different electronic structures or net charge densities. The concentrations of the anions in all five electrolytes were equally set to 0.25 M. Besides, different concentrations of Na_2SO_4 electrolytes were used to study the concentration-effect: 0.25 M, 0.5 M, and 1 M Na_2SO_4. $Na_2Ni[Fe(CN)_6]$ thin films were prepared as described in **Chapter 6.1.1**. For the Na_2SO_4, $NaNO_3$, $NaClO_4$, and NaOAc systems, electrode potentials were cycled from 0.05 V to 0.85 V vs Ag/AgCl at a scan rate of 50 mV s^{-1}, whereas in the case of 0.25 M NaCl the potential range was reduced to 0.8 V to avoid evolution of chlorine gas occurring at 0.85 V. While recording the CVs of the NiHCF, the frequency changes of the quartz crystals were also measured using an EQCM to monitor the mass changes of the NiHCF films. Although different potential ranges were applied in the case of 0.25 M NaCl, the recorded EQCM curves do not show significant mass deviations between all the studied systems: the frequency deviation between the intercalated and deintercalated states o**f all studied films was calculated as *ca* 60 Hz (~1 µg cm^{-1}) as shown in **Appendix B**.

Figures 6.8 shows the CVs (solid lines) and the charge-discharge curves (dotted lines) for the $Na_2Ni[Fe(CN)_6]$ thin films in (a) 0.25 M Na_2SO_4, (b) 0.25 M NaCl, (c) 0.25 M $NaNO_3$, (d) 0.25 M $NaClO_4$ and (e) 0.25 M NaOAc electrolytes, respectively. The recorded CVs of the NiHCF films using the different electrolytes resemble each other as summarized in **Figure 6.8 (f)**. This result shows that the change of the anions present in the electrolyte does not alter Na-intercalation and -deintercalation *per se*. The amount of charge consumed for Na-intercalation and -deintercalation is nearly equal to each other: The mass alteration due to intercalation and deintercalation are almost the same in all five cases as can be seen in **Figure A3** of **Appendix B**. However, the recorded charge-discharge curves result in significantly different values of the so-called "voltammetric reversibility" which can be associated with the kinetics of the Na-intercalation and -deintercalation processes (see the dotted lines in **Figure 6.8 (a-e)**).

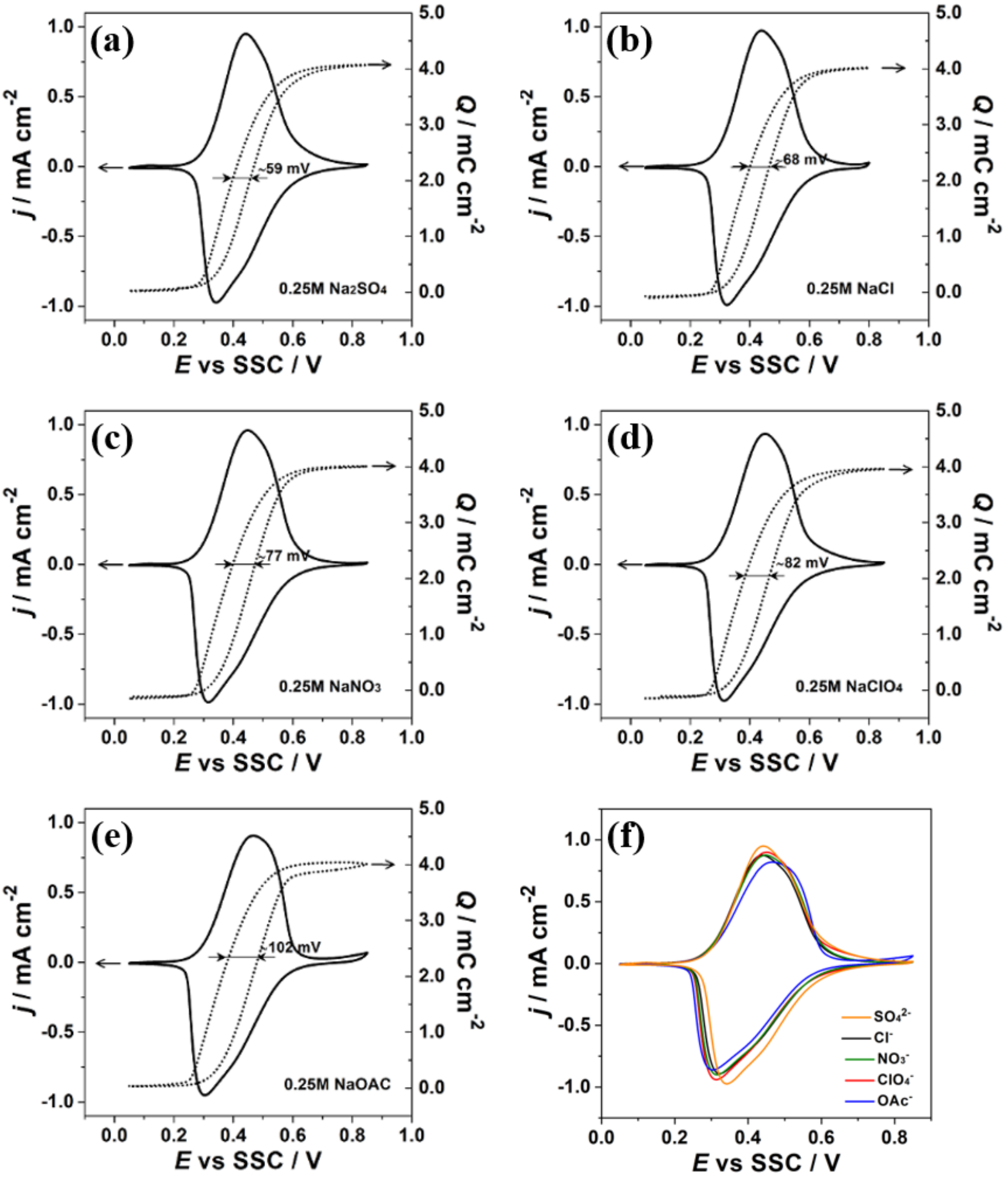

Figure 6.8. Typical CVs of $Na_2Ni[Fe(CN)_6]$ thin films with the charge-discharge curves recorded in different electrolytes: (a) 0.25 M Na_2SO_4, (b) 0.25 M NaCl, (c) 0.25 M $NaNO_3$, (d) 0.25 M $NaClO_4$, and (e) 0.25 M NaOAc as well as (f) the collection of the five CVs. The scan rate was set to 50 mV s^{-1}.

The relationship between the reversibility and the electrolyte composition cannot be simply explained with the electrolyte conductivity since the conductivities of aqueous electrolytes of Na_2SO_4, NaCl and $NaNO_3$ are primarily similar considering the given concentration.[235, 236] The analysis of the voltammetric reversibility further supports the hypothesis of the "three-stage mechanism" and also suggests the importance of the choice of the electrolytes.

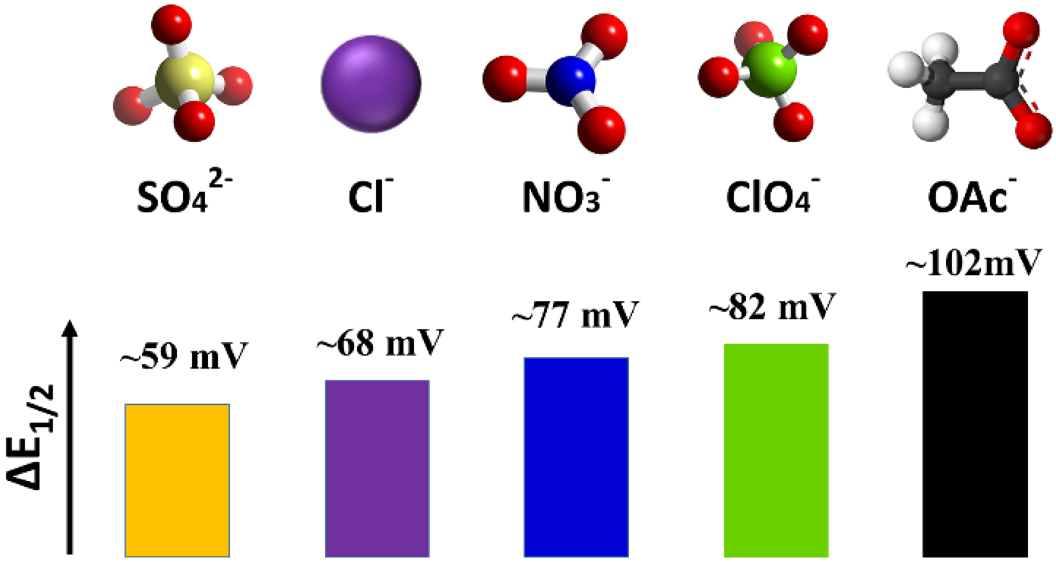

Figure 6.9. "Voltammetric reversibility" ($\Delta E_{1/2}$) in the case of different anions present in the electrolyte during Na-intercalation and -deintercalation.

The voltammetric reversibility can be quantified for instance with the potential deviation ($\Delta E_{1/2}$) between the "half-charged" and the "half-discharged" states. The potentials of the half-charged and -discharged states were defined as the mean value of the integrated charges of the anodic and cathodic branches of the CVs. Interestingly, the voltammetric reversibility seemed to depend on the nature of the anions: The more "asymmetric" anion or with a lower net charge density is used, the larger the value of the voltammetric reversibility is observed ($\Delta E_{1/2}$: $SO_4^{2-} < Cl^- < NO_3^- < ClO_4^- < OAc^-$). This trend is schematically illustrated in **Figure 6.9**.

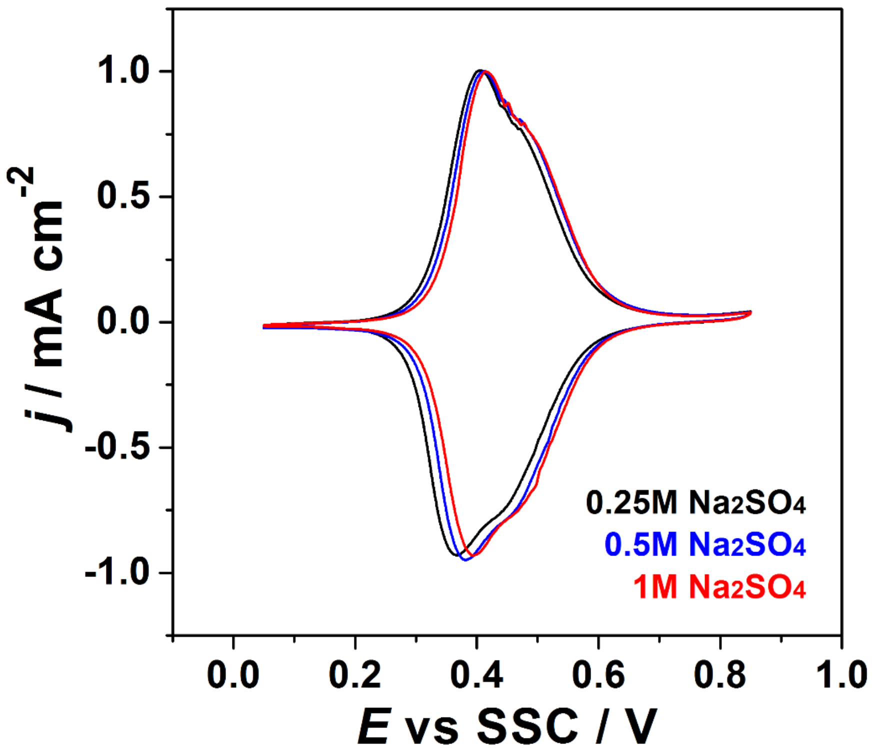

Figure 6.10. CVs of $Na_2Ni[Fe(CN)_6]$ films in Na_2SO_4 electrolytes with different concentrations of 0.25 M (black), 0.5 M (blue), and 1 M (red) (scan rate: 50 mV s^{-1}).

Furthermore, another evidence of the significance of the electrolyte composition was found in the investigation using Na_2SO_4 electrolytes of different concentrations. The increase in the concentration of sodium sulfate in the aqueous solution shifts the potentials of Na-intercalation and -deintercalation towards more positive values as shown in **Figure 6.10**. Moreover, the irreversibility of the charging and discharging is significantly decreased in the electrolyte with higher concentrations. For instance, $\Delta E_{1/2}$ in the 1 M Na_2SO_4 electrolyte is approximately 15 mV, which is roughly four times smaller than that for 0.25 M Na_2SO_4. It is not merely explained with the conductivity of the electrolytes as the conductivity of the Na_2SO_4 solution does not proportionally increase in the given concentration range.

The EIS studies of $Na_2Ni[Fe(CN)_6]$ films were additionally performed in other electrolytes containing different alkali metal cations or anions to show that the loop-shaped spectra appeared not only at specific electrolyte compositions. As shown in **Appendix C**, the loop-shaped EIS spectra were also observed in various electrolytes with different compositions revealing that it is not the experimental artifacts, or it is not limited to particular electrolyte compositions.

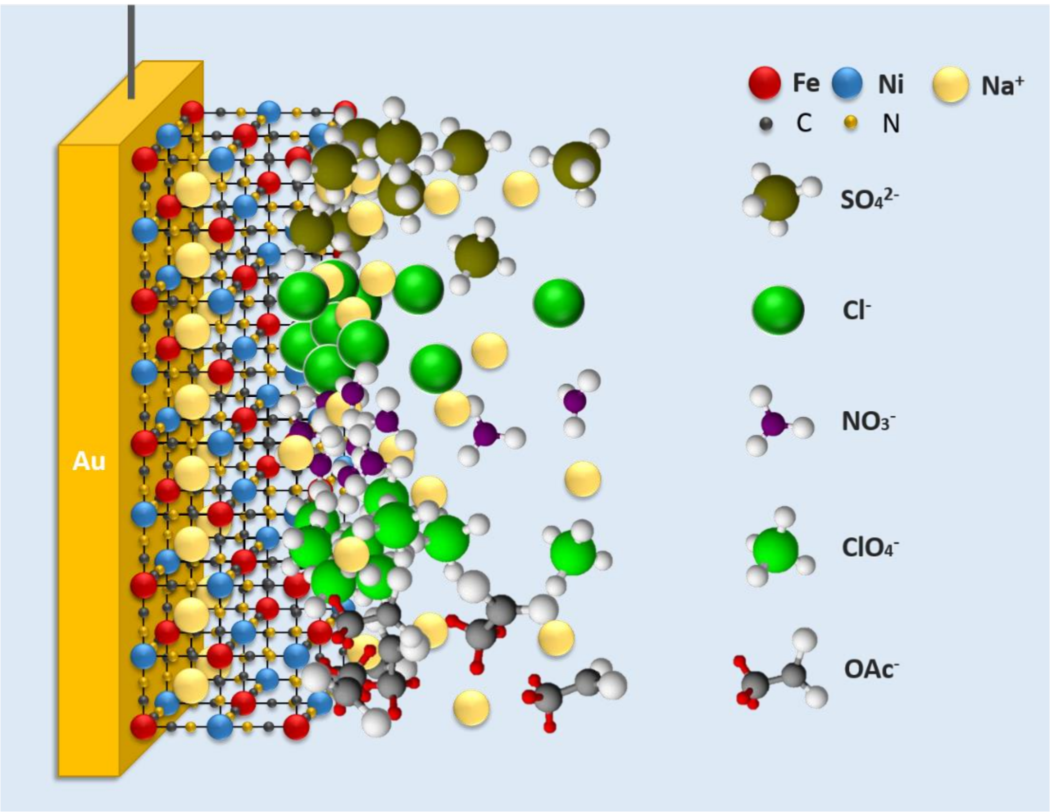

Figure 6.11. Schematic illustration of the situation in the case of Na-intercalation and -deintercalation using NiHCF thin films. During the intercalation (and deintercalation) processes, the anions are adsorbed (desorbed) at the interface of the NiHCF to compensate the excess charges. Different anions (SO_4^{2-}, Cl^-, NO_3^-, ClO_4^- and OAc^-) graphically demonstrate the effectiveness of the charge compensation depending on their geometry and effective charge density.

Figure 6.11 graphically illustrates the situation for the Na-intercalation and -deintercalation. The cubic frameworks with different sizes of spheres schematically represent the $Na_2Ni[Fe(CN)_6]$ films. In the course of Na-intercalation, Na-ions travel through the interfacial layer and diffuse into the films.

Summarizing the abovementioned findings, Na-intercalation into the $Na_2Ni[Fe(CN)_6]$ film in aqueous media seems to have *at least* three quasi-reversible steps involving intermediate steps of anion adsorption and desorption. Participation of the anions in

Na-intercalation and -deintercalation emphasizes the importance of the choice of the electrolyte composition in designing the battery systems. A slight modification in the electrolyte composition causes the change in the kinetics of the interfacial charge transfer.

6.1.4 Battery Performance Tests for NiHCF Electrodes

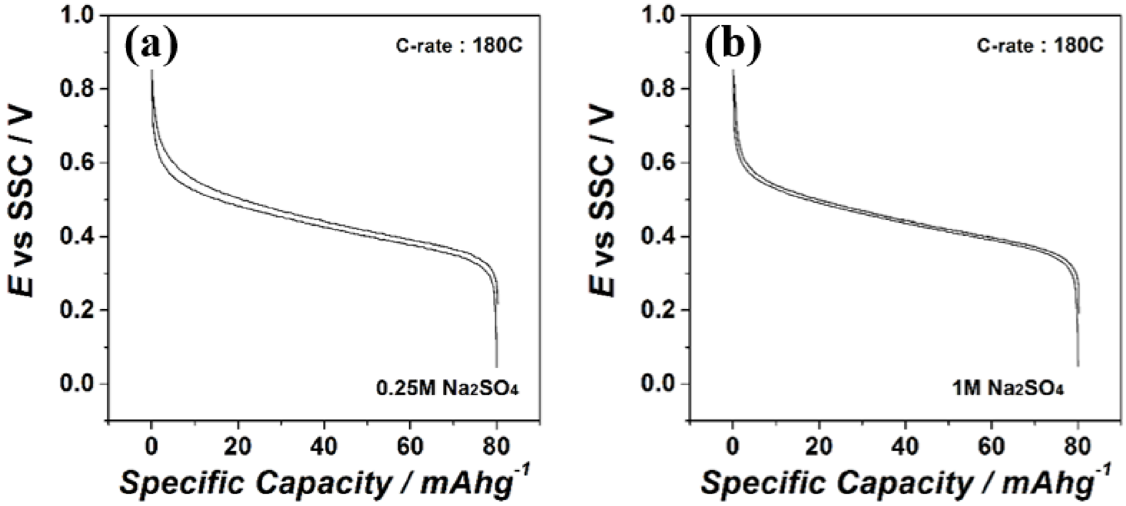

Figure 6.12. Galvanostatic charge/discharge profiles for $Na_2Ni[Fe(CN)_6]$ films in (a) 0.25 M Na_2SO_4 and (b) 1 M Na_2SO_4 electrolytes.

The charge and discharge profiles for an optimized half-cell using $Na_2Ni[Fe(CN)_6]$ films were recorded in 0.25 M Na_2SO_4 and 1 M Na_2SO_4 aqueous electrolytes as shown in **Figure 6.12 (a)** and **6.12 (b)**, respectively. In the optimized systems, $Na_2Ni[Fe(CN)_6]$ films exhibit a specific capacity of ~80 mAh g^{-1} even at 180 C (20 seconds for the full charge).[4] This capacity value is only 5% less compared to the theoretical specific capacity of the $Na_2Ni[Fe(CN)_6]$. Compared to the reported value in the literature, the specific capacity of the electrodeposited NiHCF exhibited *ca* 25% enhancement.[102] Moreover, virtually symmetric shape of the charging and discharging curves was observed in 1 M Na_2SO_4 electrolyte.

---

[4] 1C is defined as the rate at which the battery is fully charged in one hour.

6.1.5 Cation Effect on Intercalation Properties of NiHCF

As the nature of the anions in electrolytes influences the voltammetric reversibility, it can be foreseen that the replacement of intercalating species having different electrochemical properties would also change the properties of the intercalation system. Considering the crystal structure, NiHCF has enough space to accommodate all alkali metal cations of different sizes, from Li^+ to Cs^+ (see **Figure 6.13**).[237] In order to investigate these effects, cyclic voltammetry and EQCM study of NiHCF films were performed in 0.25 M of aqueous electrolytes of $AMNO_3$ (AM = Li, Na, K, Rb, or Cs).

Mere speculation was proposed in the literature that the capability of the insertion of alkali metal cations and the resulting changes in the electrochemical properties of the host materials are involved with the size of intercalating species.[238-240] Considering the size of alkali metal cations, one can expect that the bigger cations need to overcome the larger energy barrier to be intercalated into the structure. According to this argument, Cs-ions should be intercalated at the more negative potential compared to that of smaller ions such as Li^+ or Na^+ ions.

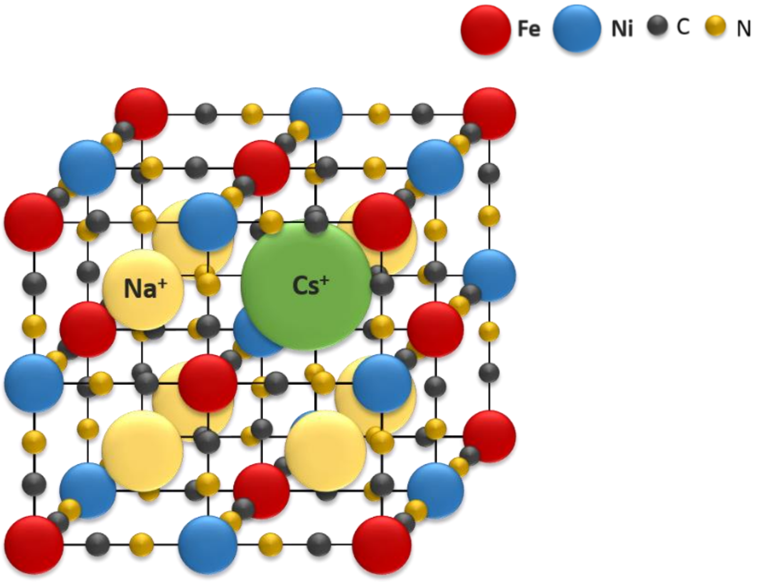

Figure 6.13. Schematics of the crystal structure of NiHCF accommodating Na- and Cs-ions. The sizes of all atoms in the drawing are proportional to their relative size difference.

In contrast to the abovementioned hypothesis, an exactly opposite situation was observed. The intercalation of the cations with bigger sizes was observed at the more positive potential. **Figure 6.14 (a)** shows the collection of typical CVs of NiHCF thin films in aqueous electrolytes containing $AMNO_3$, where AM is Li, Na, K, Rb, or Cs. Cleary, apart from the cation size, other physicochemical parameters might be crucial in the determination of the potential for the intercalation. Assuming that the solvation shells of the hydrated cations will be lost before intercalation, the ionic hydration energy might be one of the parameters determining the intercalation potential. **Figure 6.14 (b)** displays the plot of the electrode potential at the "half-charged" state, $E_{1/2}$, as a function of the hydration energy of the cations. In the plot, one can observe a quasi-linear correlation of the potential and hydration energy.

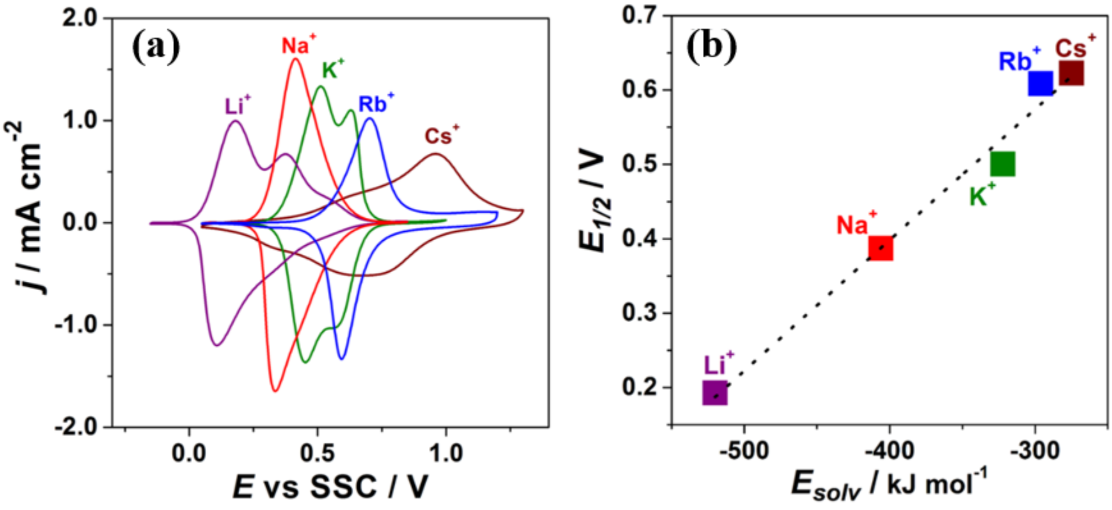

Figure 6.14. (a) Typical CVs of $Na_2Ni[Fe(CN)_6]$ in 0.25 M aqueous solutions of MNO_3 where M = Li, Na, K, Rb, or Cs (scan rate: 50 mV s^{-1}). (b) Correlation of the hydration energy of alkali metal cations and the potential at the "half-charged" state ($E_{1/2}$).

The observed mass alteration during the charging and discharging (see **Appendix D**) suggested that approximately half of Na-ions is replaced with other alkali metal cations. The net reaction can be thus formulated as below:

$$NaNi[Fe^{III}(CN)_6] + AM^+ + e^- \rightleftharpoons AMNaNi[Fe^{II}(CN)_6]$$

6.2 Vanadium Hexacyanoferrate

The study of vanadium hexacyanoferrates has been rarely reported compared to other PBAs.[139, 141, 241-246] To the best of my knowledge, the first electrochemical investigation of vanadium hexacyanoferrates was reported in 1986 by Dong and Li.[141] In their study, it was revealed that a relatively high concentration of H_2SO_4 is necessary for the supporting electrolyte for reversible redox reactions of vanadium hexacyanoferrates. They claimed that the mechanism of the redox reaction of vanadium hexacyanoferrate is attributed to the change of the oxidation states of both V and Fe atoms with the participation of protons and alkali metal cations present in the aqueous solution. In a later study, however, Carpenter *et al*. reported the controversial result disclosing the origin of the redox processes in vanadium hexacyanoferrate.[139] From the XPS and electrochemical studies, they concluded that V-atoms of vanadium hexacyanoferrate were not involved in the redox reaction, but Fe atoms were the electroactive ones. Another issue of vanadium hexacyanoferrates is their poor stability in neutral or basic electrolytes.[242] Albeit vanadium hexacyanoferrates show comparatively good stability in very acidic media, the acidic environment is not preferred in the battery applications.[85] For large-scale applications, the stability of the films in pH-neutral aqueous solutions should be improved.

In this work, vanadium hexacyanoferrates were prepared by electrochemical deposition using Dong *et al*.'s method with slight modifications.[246] The physicochemical properties of vanadium hexacyanoferrate thin films were investigated in different aqueous electrolytes composed of various alkali metal cations and anions. To verify the validity and applicability of the previously discussed three-stage mechanism to this system, the thin films were investigated using electrochemical impedance spectroscopy combined with cyclic voltammetry and XPS measurements. The electroactive centers of vanadium hexacyanoferrates were disclosed from the XPS. A feasible solution to the stability issue of vanadium hexacyanoferrate in nearly neutral media was proposed. Finally, the performance of the vanadium hexacyanoferrates as battery electrode materials was tested in different electrolytes.

6.2.1 Preparation of $Na_2VO_x[Fe(CN)_6]$ Electrodes

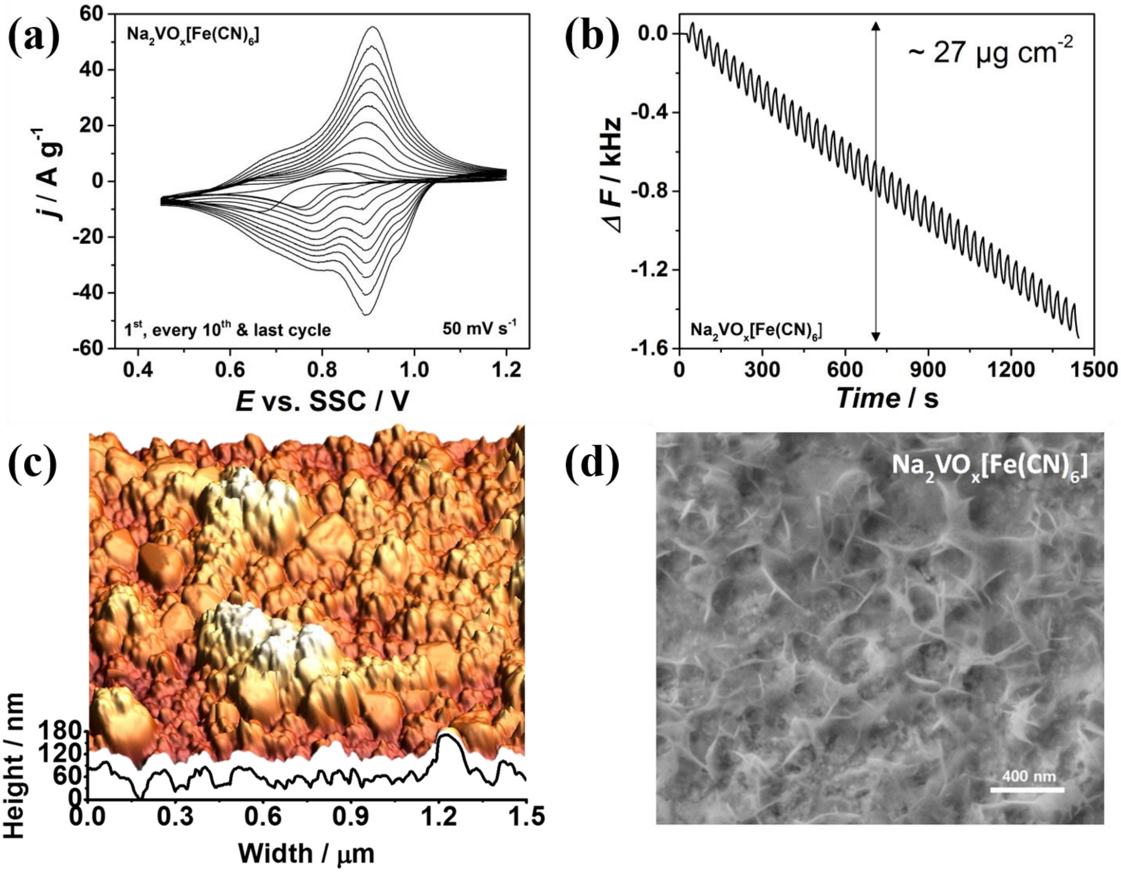

Figure 6.15. Preparation of $Na_2VO_x[Fe(CN)_6]$ thin films. (a) Representative CVs of the electrodeposition of $Na_2VO_x[Fe(CN)_6]$ and (b) the corresponding EQCM profile monitoring the frequency changes due to the deposition. (c) Typical AFM and (d) SEM image of $Na_2VO_x[Fe(CN)_6]$ thin film.

The preparation protocol of $Na_2VO_x[Fe(CN)_6]$ (VO_xHCF) thin films was adopted by modifying the method of Dong *et al* to some extent. The electrochemical deposition of $Na_2VO_x[Fe(CN)_6]$ was carried out in the glass cells with a three-electrode configuration as shown in **Figure 5.1**. AT-cut gold QCM wafers, a gold single crystal and sputtered gold on glass chips (arrandee^{TM}) were used as the substrates for the deposition. A Pt wire and an Ag/AgCl electrodes were used as the counter electrode and the reference electrode, respectively. The aqueous deposition solution was prepared by mixing 3.6 M H_2SO_4, 5 mM $NaVO_3$ and 5 mM $K_3Fe(CN)_6$ in ultrapure water. For the VO_xHCF deposition, the electrode was cycled in the potential range from 0.45 V to 1.2 V vs Ag/AgCl for *ca* 110 cycles at a scan rate of 50 mV s^{-1}. Electrode mass change was simultaneously measured with the EQCM to determine the deposited mass.

The electrochemical deposition of $Na_2VO_x[Fe(CN)_6]$ thin films was conducted under the potentiodynamic condition using the following tentative net reaction scheme:

$$2Na^+ + VO_3^- + [Fe(CN)_6]^{3-} + (6 – 2x)H^+ \rightarrow Na_2VO_x[Fe(CN)_6] + (3 – x)\ H_2O$$

Figure 6.15 (a) displays representative CVs of the deposition of $Na_2VO_x[Fe(CN)_6]$ thin films. For better visualization, only the first and every 10th cycles are presented in **Figure 6.15 (a)**. The obtained anodic and cathodic peak currents of the CVs were originated from the change of the oxidation number of Fe atoms of $Na_2VO_x[Fe(CN)_6]$ thin films, which results in the intercalation and deintercalation of Na ions. The increase in the peak currents indicates the successful growth of the $Na_2VO_x[Fe(CN)_6]$ thin films: As the amount of the films increases, the larger number of Fe atoms of the VO_xHCF films are oxidized and reduced, *i.e.*, the higher current flow is observed. The net mass changes due to the VO_xHCF deposition were monitored using the EQCM as shown in **Figure 6.15 (b)**. The resulting mass of the deposited $Na_2VO_x[Fe(CN)_6]$ thin films was calculated to be ~27 µg cm^{-2}. The fluctuation of the electrode mass during the deposition is associated with the reversible Na-intercalation and -deintercalation, which are caused by the redox reactions of Fe atoms during the $Na_2VO_x[Fe(CN)_6]$ deposition. From the comparison of the measured mass by the EQCM and the calculated value from the integrated charge, the stoichiometric number of oxygen, x, is estimated to be slightly lower than 2. The number of oxygen (x) is lower compared to that of metavanadate anions (VO_3^-) used in the deposition solution. The lower x value is presumably attributed to the conversion of the metavanadate ions into other forms, namely, VO_2^+ and VO^{2+} in the acidic aqueous solution.[141] The morphology of the electrodeposited $Na_2VO_x[Fe(CN)_6]$ thin films was studied using AFM and SEM. **Figure 6.15 (c)** shows a typical AFM image of the $Na_2VO_x[Fe(CN)_6]$ thin films, and the surface structure with the mean height of roughly 90 nm is seen from the image. An SEM image of $Na_2VO_x[Fe(CN)_6]$ films is displayed in **Figure 6.15(d)**. Although these two images showed the different surface structures, it can be concluded from both images that the $Na_2VO_x[Fe(CN)_6]$ thin films fully cover the electrode surface without pores.

6.2.2 Mechanism of Na-Intercalation into VO_xHCF

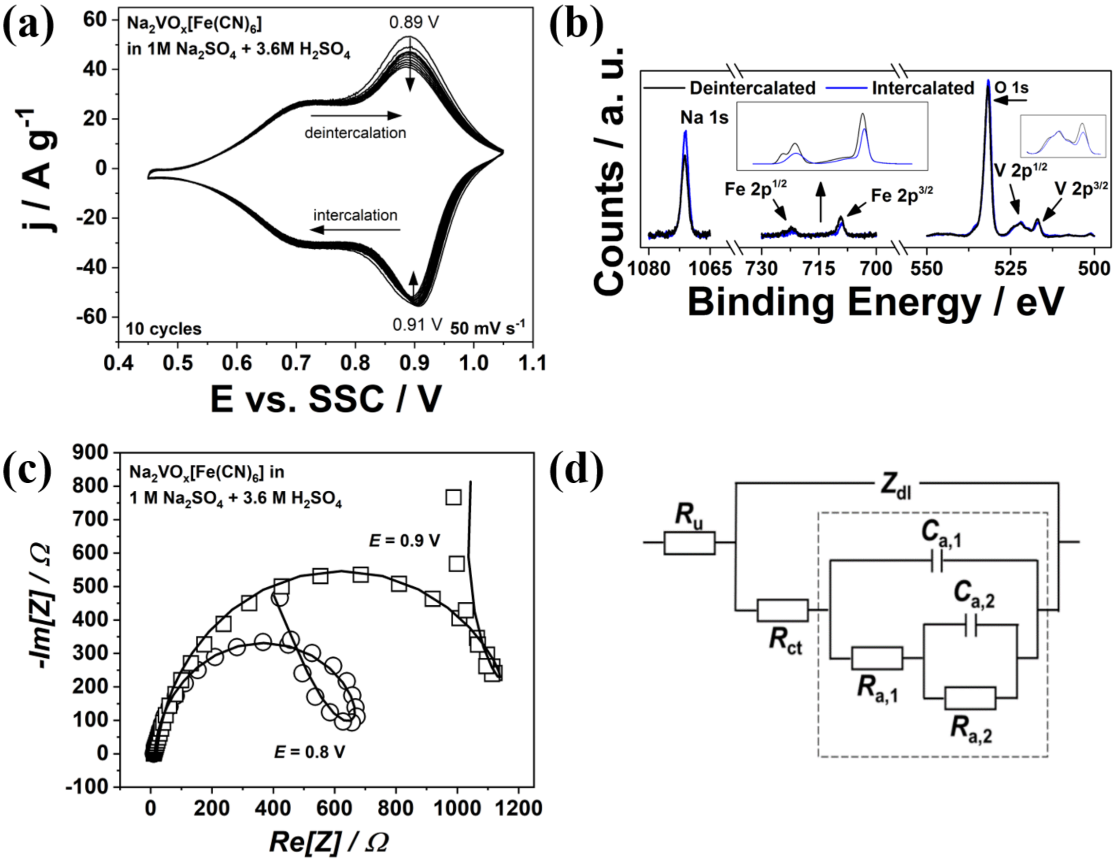

Figure 6.16. Characterization of the $Na_2VO_x[Fe(CN)_6]$ thin films. (a) Typical CVs of the VO_xHCF thin films measured in 1 M Na_2SO_4 + 3.6 M H_2SO_4 electrolyte (scan rate: 50 mV s^{-1}). The electrode potential was cycled from 0.45 V to 1.05 V vs Ag/AgCl. (b) XPS data of the VO_xHCF thin films. Black and blue lines represent the obtained XPS data from the Na-deintercalated and the Na-intercalated VO_xHCF thin films, respectively. (c) Impedance spectra of the VO_xHCF thin films measured in 1 M Na_2SO_4 + 3.6 M H_2SO_4 electrolytes at 0.8 V and 0.9 V vs Ag/AgCl. (d) EEC describing the three-stage mechanism.

From the FT-IR analysis, Dong *et al* claimed that the origin of Na-intercalation and -deintercalation at the vanadium hexacyanoferrate thin films is attributed to the redox reaction of both V and Fe atoms in the structure.[141, 243] However, Carpenter *et al*. argued that only Fe atoms in vanadium hexacyanoferrate are electroactive and involved in the electrochemical reaction.[139] In order to shed light on the Na-intercalation mechanism of VO_xHCF, cyclic voltammetric, EIS, and XPS measurements were performed.

Figure 6.16(a) shows ten consecutive CV cycles of VO_xHCF thin films in an aqueous electrolyte containing 1 M Na_2SO_4 and 3.6 M H_2SO_4. Characteristic anodic and cathodic peaks of Na-intercalation and -deintercalation were observed at ~0.91 V and ~0.89 V vs SSC. The current density of the anodic and cathodic peaks has slightly decreased during cycling within the given potential range (degradation of the films). The comparison of the XPS spectra of the charged VO_xHCF (black) and the discharged VO_xHCF (blue) is displayed in **Figure 6.16(b)**. From the XPS spectra, the presence of the main constituent elements (Na, V, Fe, and O) of VO_xHCF was confirmed. Each XPS peak was identified with the respective elements in comparison to the literature.[247] Notably, one can see a relatively reduced Na 1s peak at the Na-deintercalated VO_xHCF when compared to that of the Na-intercalated sample, which suggests that not all Na-ions were fully released from the VO_xHCF films, but some Na-ions remained in the structure. From the XPS spectra analysis, Fe atoms in the VO_xHCF films were identified to be electroactive. The binding energies of both Fe $2p^{1/2}$ and Fe $2p^{3/2}$ slightly differ between the Na-intercalated and -deintercalated samples. This observation is in good agreement with the literature, supporting the argument that Fe atoms are involved in the redox reaction for the Na-intercalation and -deintercalation processes.[139, 141, 243] However, the binding energy shift of V or O between the two samples is barely detectable, which is in good accordance with Carpenter *et al*'s claims.[139]

As previously discussed in **Chapter 6.1.2**, if the Na-intercalation and -deintercalation processes involve more than three stages, the impedance responses of the investigated system will display the “loop-shaped" spectra in the Nyquist plots. EIS measurements were carried out in the potential range from 0.55 V to 1.05 V using ac signals of a 10 mV amplitude with varying frequencies from 50 kHz to 0.1 Hz. As shown in **Figure 6.16 (c)**, indeed, the “loop-shaped” impedance spectra were obtained at 0.8 V and 0.9 V, where the Na-intercalation and -deintercalation occurred. The reliability of the acquired impedance data was confirmed with the K-K test revealing no significant issues with the data quality. Using the EEC shown in **Figure 6.16(d)**, excellent fitting results were obtained, which suggest the existence of the three-stage mechanism for Na-intercalation in this system. Note that the generally-accepted EEC with Warburg elements cannot explain the loop-shaped spectra, as the Warburg element accounts for a linear behavior at low frequency (typically 45 ° with respect to the X-axis in a Nyquist plot). However, the EEC of the three-stage mechanism can successfully fit the complex impedance spectra with a minimum number of the circuit elements possible. In a similar way to the case of NiHCF thin films, Na-intercalation and -deintercalation mechanisms can be described with the following three stages:

i) Redox reaction of $Fe^{II/III}$, which is kinetically quicker compared to the other processes

$$Na_2VO_x[Fe^{II}(CN)_6] \rightleftharpoons Na_2VO_x[Fe^{III}(CN)_6]^+ + e^-$$

ii) Specific adsorption of charge-compensating species, for instance anions (A^-)

$$Na_2VO_x[Fe^{III}(CN)_6]^+ + A^- \rightleftharpoons Na_2VO_x[Fe^{III}(CN)_6]A$$

iii) Na-intercalation or deintercalation with the adsorption or desorption of the anions

$$Na_2VO_x[Fe^{III}(CN)_6]A \rightleftharpoons NaVO_x[Fe^{III}(CN)_6] + Na^+ + A^-$$

The detailed interpretation of how the “loop-shaped” impedance spectra account for the three-stage mechanism is described in the previous section in **Chapter 6.1.2**. It should be noted that the hypothesis of the three-stage mechanism argues that the Na-intercalation process involves *at least* three stages. In other words, in more complex systems, for instance, $Na_2VO_x[Fe^{II}(CN)_6]$ that was investigated in this work, the number of intermediate steps in the reaction scheme can exceed three.

PBAs are constituted with various transition metals that are interconnected with cyanide bonds. In the literature, a large number of PBA materials have been investigated mostly by replacing the nitrogen-linked Fe elements with other transition metals. From the study of NiHCF thin films, the change in intercalating cations, which are also constituent elements, significantly alters the $E_{1/2}$ potential of the NiHCF thin films (see **Chapter 6.1.5**). Thus, when making a straightforward prediction, changing the intercalating species shifts the $E_{1/2}$ potentials of PBA materials.

6.2.3 Cation Effect on Intercalation Properties of VO$_x$HCF

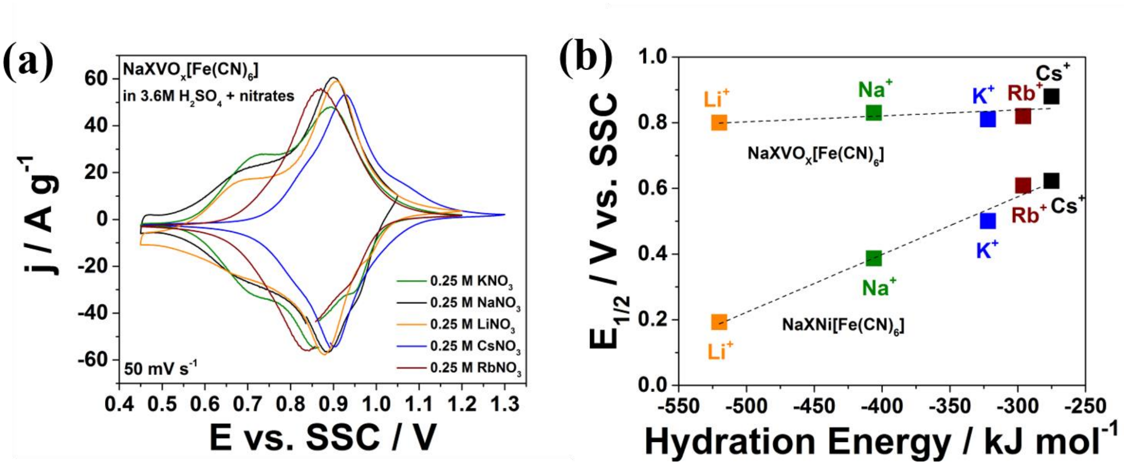

Figure 6.17. (a) Characteristic CVs of NaXVO$_x$[Fe(CN)$_6$] thin films in aqueous electrolytes containing 3.6 M H_2SO_4 + 0.25 M XNO$_3$, where X = Li, Na, K, Rb, or Cs. (b) The comparison of the $E_{1/2}$ potentials of NiHCF and VO$_x$HCF thin films for the intercalation of the different alkali metal cations. The $E_{1/2}$ potentials are plotted as a function of the hydration energies of the intercalating cations.

Figure 6.17(a) shows representative CVs of VO$_x$HCF thin films in aqueous solutions containing 0.25 M XNO$_3$, where X = Li, Na, K, Rb, or Cs, with the addition of 3.6 M H_2SO_4. In the case of the NiHCF thin films, the $E_{1/2}$ potentials significantly vary depending on the hydration energies of intercalating alkali metal cations. However, the "solvation effect" in the case of VO$_x$HCF is not remarkable compared to that of NiHCF thin films: The $E_{1/2}$ potentials of VO$_x$HCF thin films do not exhibit the noticeable dependence on the intercalating cations as shown in **Figure 6.17(b)**. The intercalation potentials only slightly shifted in the different electrolytes. This contrary result to the previous study might be related to the complex redox reaction of vanadium in VO$_x$HCF with protons in the electrolyte, but it is skeptical to explain the reason for the different behavior of the NiHCF and VO$_x$HCF with the single parameter. Therefore, further profound investigations are necessary to reveal the observed difference between the NiHCF and the VO$_x$HCF.

6.2.4 Electrode Compositions and Intercalation Potentials of PBAs

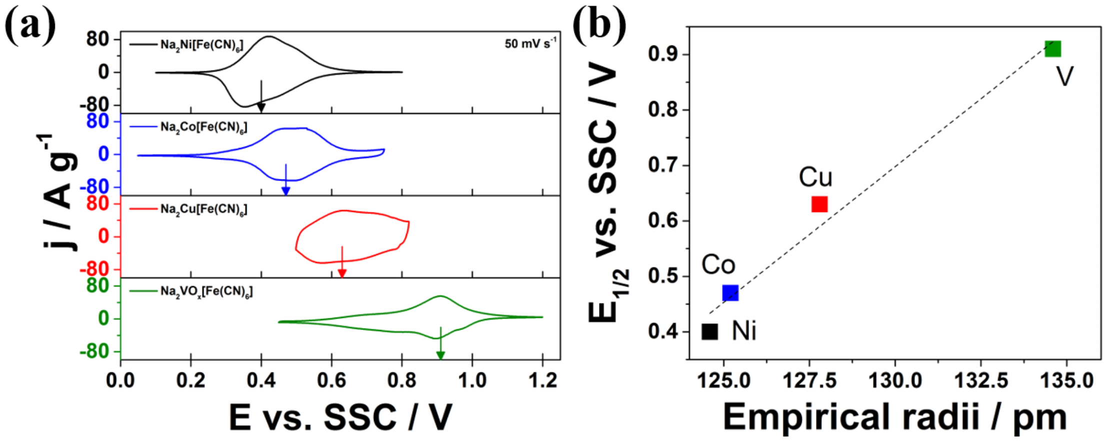

Figure 6.18. (a) Characteristic CVs of $Na_2Ni[Fe(CN)_6]$, $Na_2Co[Fe(CN)_6]$, $Na_2Cu[Fe(CN)_6]$, and $Na_2VO_x[Fe(CN)_6]$ and (b) the corresponding $E_{1/2}$ potentials as a function of the empirical radii of the N-coordinated transition metal elements (Ni, Co, Cu, and V) of the PBAs.

As seen in **Figure 6.18(a)**, Na-intercalation and -deintercalation using different PBA electrodes took place in different potential ranges. When their $E_{1/2}$ potentials are plotted as a function of the empirical radii of the replaced transition metals in PBA thin films, one can view an interesting correlation. As displayed in **Figure 6.18(b)**, the correlation between the $E_{1/2}$ potentials and the size of the empirical radii of the transition metals seems to be roughly linear: the $E_{1/2}$potentials exhibit the more positive at the PBAs with the bigger empirical radii of the key transition metals. The obtained $E_{1/2}$potentials of the studied PBAs are ~0.91 V for VO_xHCF, whereas NiHCF, CoHCF, CuHCF for ~0.44 V, ~0.51 V, and ~0.67 V, respectively.

6.2.5 Battery Tests and Stabilization of VO_xHCF Electrodes

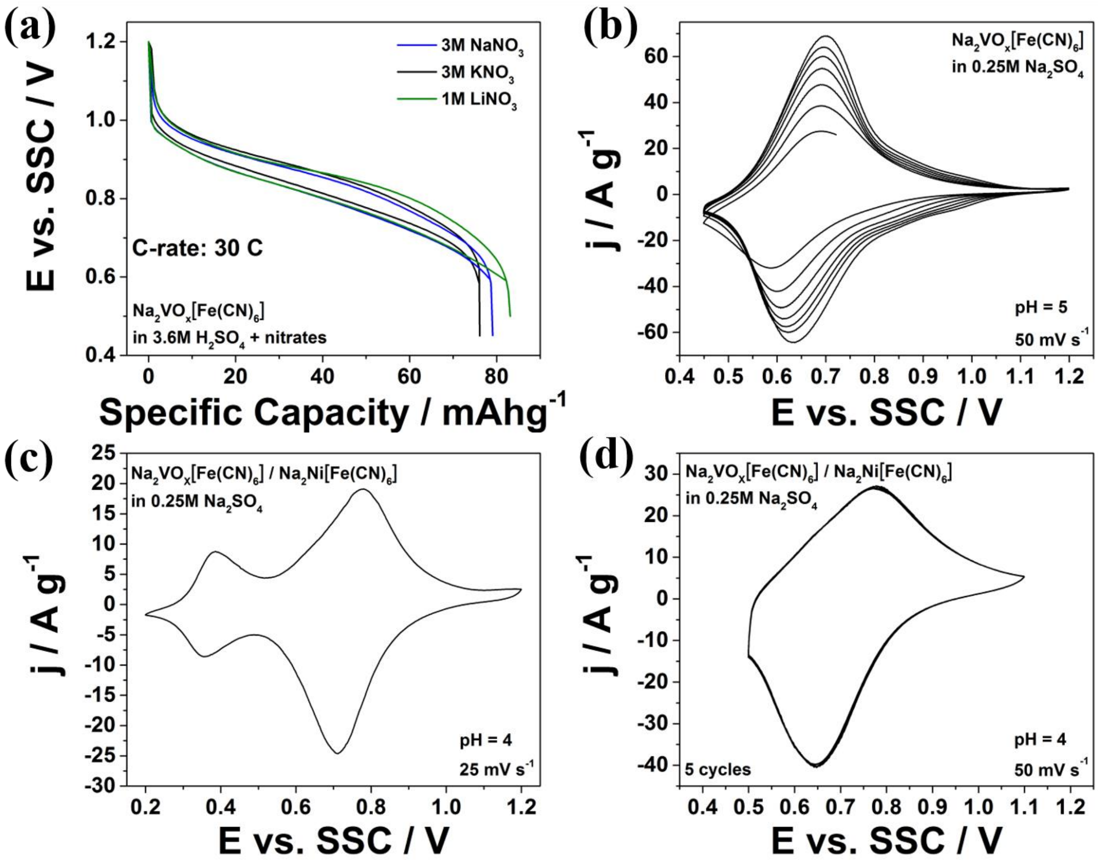

Figure 6.19. (a) Galvanostatic profiles (C-rate: 30 C) of the $Na_2VO_x[Fe(CN)_6]$ thin films in aqueous electrolytes of 3 M $NaNO_3$ (blue), 3 M KNO_3 (black) and 1 M $LiNO_3$ (green). 3.6 M H_2SO_4 was added in all the three electrolytes. (b) CVs of the VO_xHCF thin films in 0.25 M Na_2SO_4 aqueous electrolyte (pH = 5) at a scan rate of 50 mV s^{-1}. (c) CVs of the VO_xHCF films coated with the NiHCF films in 0.25 M Na_2SO_4 electrolyte (pH = 4) at a scan rate of 25 mV s^{-1}. (d) Five CV cycles of the VO_xHCF thin film protected with the NiHCF coating in 0.25 M Na_2SO_4 (pH = 4) (scan rate of 25 mV s^{-1}). The cycling stability of the VO_xHCF thin films was greatly improved. The acidity of the aqueous electrolytes was adjusted by adding H_2SO_4.

Figure 6.19 (a) displays the charge and discharge curves of the $Na_2VO_x[Fe(CN)_6]$ thin-film electrodes in a galvanostatic condition (C-rate: 30 C) in three different aqueous electrolytes of 3.6 M H_2SO_4 with 3 M $NaNO_3$ (blue), 3 M KNO_3 (black) and 1 M $LiNO_3$ (green), respectively. The $Na_2VO_x[Fe(CN)_6]$ thin films showed the potential plateau around 0.9 V vs SSC in all the cases. The specific capacities of the VO_xHCF electrodes were obtained as ~83, ~79, and ~76 mAh g^{-1} in the 1 M $LiNO_3$, 3 M $NaNO_3$, and 3 M

KNO_3 electrolytes, respectively. The obtained capacities are very close to the theoretical values. Interestingly, the change of the intercalating cations changed the specific capacities of the VO_xHCF to a little extent. Presumably, because of the large channels of the VO_xHCF for Li-, Na- and K-intercalation, the number of the intercalating cations is virtually the same (equal total charge), which results in the difference in only total mass due to the mass difference of the Li-, Na- and K-ions. Note that the specific capacity is equivalent to a measure of the stored charge per unit weight.

It has been reported in the literature that VO_xHCF electrodes exhibited severe stability issues in neutral media. In many cases, PBA materials showed rapid degradation typically in basic or neutral media.[248] In this work, the VO_xHCF electrodes also suffered from severe degradation even in less acidic media (at pH 5) as shown in **Figure 6.19 (b)**. The use of extremely high acidic aqueous electrolytes in the battery is not desired due to the following issues: (i) The high acidity raises concerns regarding environmental and safety issues of the accidental leakage of the electrolytes. (ii) The increase in the acidity shifts the stability window of aqueous electrolyte towards more positive potential, which in return reduces the operating electrochemical window for anode materials. It should be stressed that the choice of the anode materials for aqueous batteries are even more restricted compared to the cathode materials. Therefore, for facilitating the deployment of VO_xHCF electrodes in aqueous battery systems, the improvement of the stability in less acidic media is crucial.

One viable solution to address the stability issues of the VO_xHCF electrode is to coat the surface with the protective layers, which do not deteriorate the battery performance of the VO_xHCF at the same time. For this purpose, NiHCF thin films were chosen as protective layers due to several beneficial characteristics of NiHCF: (i) NiHCF exhibits the excellent cycling stability at neutral pH.[102] (ii) Particularly, less strain effect between VO_xHCF and NiHCF-coating was expected due to the similarity in the crystal structure and the lattice parameters of the NiHCF to those of the VO_xHCF.[237, 244, 245, 249-252] (iii) The potential range for Na-intercalation and deintercalation in the case of the NiHCF does not fairly overlap (0.2 V – 0.6 V) of those of the VO_xHCF (0.55 V – 0.95 V).[22, 246]

The protective layers of $Na_2Ni[Fe(CN)_6]$ were electrochemically deposited on the VO_xHCF thin films by applying a constant potential (0.37 V vs SSC) in the aqueous deposition solution consisting of 0.5 mM $NiCl_2$ and 0.5 mM $K_3Fe(CN)_6$ and 0.1 M H_2SO_4. **Figure 6.19 (c)** displays the resulting CVs of a $Na_2VO_x[Fe(CN)_6]/Na_2Ni[Fe(CN)_6]$ electrode in a 0.25 M Na_2SO_4 aqueous electrolyte (pH = 4). In comparison to the CVs of pure $Na_2VO_x[Fe(CN)_6]$ electrodes, the NiHCF-coated VO_xHCF electrode shows additional redox peaks around ~0.37 V. Interestingly, the Na-intercalation and -deintercalation peaks (*ca* 0.71 V/0.78 V) are shifted to more cathodic potentials compared to those (*ca* 0.63 V/ 0.7 V) of the uncoated VO_xHCF thin films. The cathodic shifts of the Na-intercalation and deintercalation peaks might be caused by the protective layers of the NiHCF thin films. In the reduced potential range, the optimized VO_xHCF/NiHCF system exhibit significantly enhanced cycling stability, showing redox peaks at ~0.65 V and ~0.78 V as can be seen in **Figure 6.19 (d)**.

6.3 Chromium Hexacyanoferrate

In the development of next-generation battery materials for large-scale applications, the availability and the price of raw materials should be particularly taken into account. Considering the statistics of the global production of battery materials (especially inexpensive metals), it seems reasonable to develop electrodes based on Fe or Cr due to their abundance in the Earth's crust (see **Figure 6.20**).

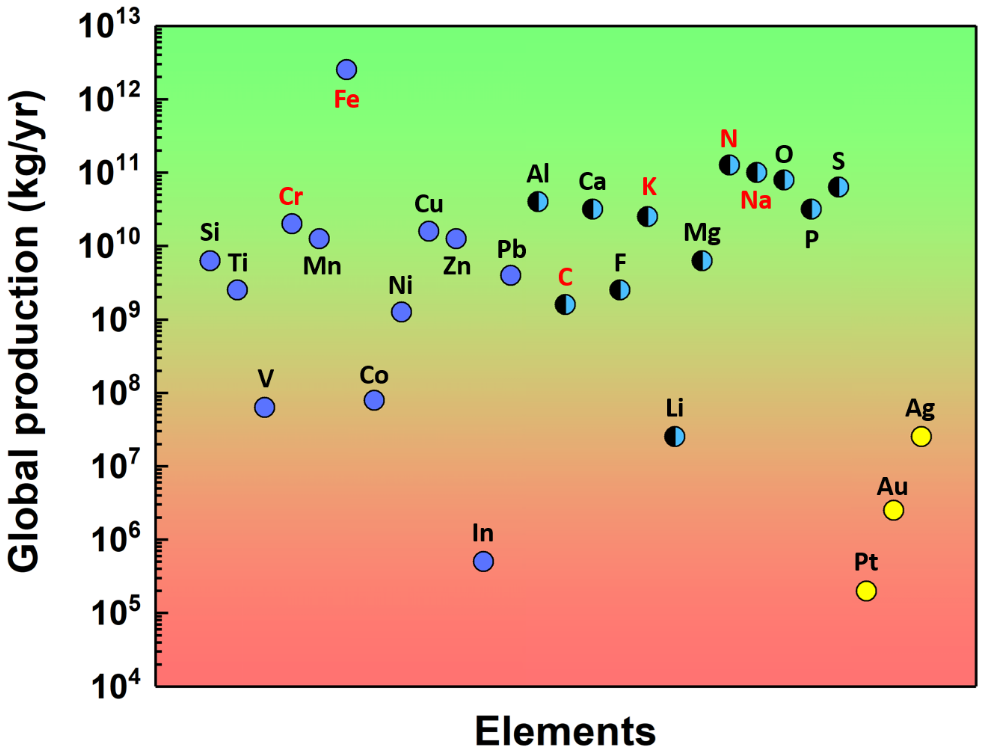

Figure 6.20. Annual global production of the elements that are often found in battery materials: Elements that are often used for electrodes are represented with the full circles, and those with half-black circles represent the elements that can be either electrode or electrolyte components. Reproduced from the reference [253] with permission from the American Chemical Society.

The excellent tunability of PBA composition facilitates the replacement of expensive or rare constituent elements with inexpensive and abundant ones. For instance, chromium hexacyanoferrates (CrHCFs) seem to be a promising candidate as the electrode materials for aqueous Na-ion batteries due to the high occurrence of Cr and Fe. Furthermore, it was reported that the formal potential of CrHCF for K-intercalation in aqueous media exhibited

1.005 V vs SHE, which is a relatively high value for aqueous alkali metal-ion batteries.[254] However, the main requirement for the utilization of CrHCF as battery material is that the intercalation potential for Na-ions does not significantly differ from that of K-intercalation. In the literature, the majority of studies on CrHCF focused on its electrochemical properties,[255, 256] usage as an ion exchanger,[257-259] chemical sensor,[260-262] biosensor, [263-267] and (electro)catalyst.[268, 269] However, research on CrHCF for battery applications is scarce. In detail, only one study is available in the literature to the best of my knowledge.[270] Hence, this chapter addresses the successful preparation of CrHCF thin films on 3D-graphene foam and the evaluation of their performance as an electrode material.

6.3.1 Preparation of $Na_2Cr[Fe(CN)_6]$ Electrodes

According to the literature, electrochemical deposition of chromium hexacyanoferrate (CrHCF) films requires the reduction of Cr^{3+} in the deposition solution.[255, 256, 271] The standard reduction potentials of Cr^{3+} are reported to be -0.41 V vs SHE for $Cr^{3+/2+}$ and -0.74 V vs SHE for $Cr^{3+/0}$, respectively.[272] For the electrodeposition of CrHCF thin films on a gold electrode, the electrode potential should be cycled from -0.85 V to 1.00 V vs SSC. Unfortunately, gold QCM working electrodes could not be used as a substrate for the deposition of CrHCF thin films since no proper CrHCF film deposition could be achieved (even with the extended deposition time).

Moreover, gas evolution (H_2 evolution) was observed around -0.7 V vs Ag/AgCl (3 M KCl) as shown in **Appendix E**. Thus, less electrocatalytically active substrates for the hydrogen evolution had to be identified for the CrHCF deposition. In the literature, glassy carbon electrodes were often utilized as the substrate for CrHCF deposition, but the amount of the deposited CrHCF was not large enough to serve as an electrode material.[255, 260, 262, 265, 267, 269, 273] Herein, Graphene/thermoplastic polyurethane flexible foams (Graphene Supermarket, USA), namely 3D graphene foams, were identified to be served as substrates for the CrHCF deposition. In this work, a Pt wire and silver/silver chloride (SSC, Schott) filled with 3 M KCl were utilized as the counter and reference electrodes, respectively. For the CrHCF deposition, the Luggin capillary of the reference electrode was filled with a saturated aqueous KCl solution.

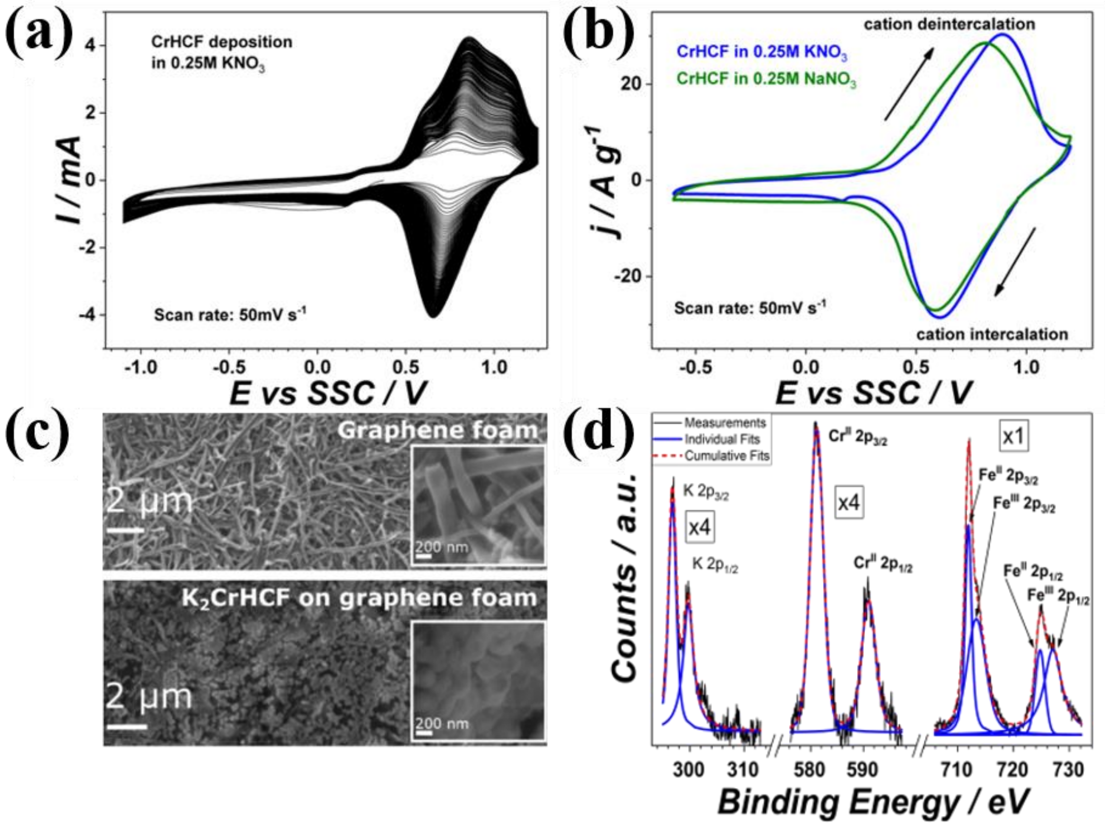

Figure 6.21. (a) Representative CVs of the electrochemical deposition of CrHCF thin films on graphene foams. (b) Representative CVs of the CrHCF thin films in 0.25 M KNO_3 (blue) and 0.25 M $NaNO_3$ (green) aqueous electrolytes, respectively. (c) SEM images of the graphene-foam before (top) and after the CrHCF deposition (bottom). (d) XPS analysis of the deposited CrHCF thin films using a polycrystalline Pt QCM electrode as the substrate.

The deposition and electrochemical characterization of CrHCF thin films were carried out in the setup shown in **Figure 5.1 (b)**. The deposition solutions for CrHCF thin films were prepared by dissolving 0.25 M KNO_3, 10 mM $CrCl_3$, and 5 mM $K_3Fe(CN)_6$ in ultrapure water. The electrode potential was cycled between -1.1 V and 1.25 V vs SSC at a scan rate of 50 mV s^{-1} for ~100 cycles. **Figure 6.21 (a)** displays typical CVs, which characterize the growth of chromium (II) hexacyanoferrates. In detail, the growth of CrHCF thin films is verified by monitoring the increase in cathodic and anodic current peaks upon cycling. In contrast to the NiHCF or VO_xHCF deposition, a very negative potential of *ca* -1.1 V is needed to reduce Cr^{3+} species.[253] This finding is in good agreement with the findings of Gao, Jiang, and Karyakin.[255, 256, 271] Subsequently, the intercalation and deintercalation of Na- and K-ions were assessed by cyclic voltammetry. **Figure 6.21 (b)** shows typical CVs of CrHCF thin films recorded in aqueous 0.25 M KNO_3 (blue) and 0.25 M $NaNO_3$ (green) electrolytes, respectively. The recorded anodic and cathodic peaks can be attributed to the change of the oxidation number of Fe in CrHCF, which shows the occurrence of the intercalation and deintercalation of the alkali metal cations. The morphological analysis of the deposited CrHCF thin films was performed using SEM. **Figure 6.21 (c)** displays typical SEM images of the 3D graphene foam before (top) and after (bottom) the CrHCF deposition. The pure graphene foams show a complex structure consisting of nano-sized rods. Interestingly, the substrate is not visible after CrHCF deposition. Instead, it is homogeneously covered with CrHCF films (see magnified image). The deposited CrHCF thin films showed an adequately smooth topography of CrHCF aggregates with a mean size of roughly 166 nm.

The chemical composition of the CrHCF thin films was revealed using XPS. To acquire better XPS spectra, flat QCM Pt electrodes were used as substrates for the CrHCF deposition. After the deposition, the CrHCF thin films were “fully charged” (the deintercalated state) for XPS analysis. As displayed in **Figure 6.21 (d)**, all expected elements (K, Fe, and Cr) of CrHCF were identified from the XPS spectra. Interestingly, K peaks were still observed in the XPS data even after the deintercalation. The XPS peaks of Fe seem to overlap with at least two peaks. The characteristic peaks of Fe^{2+} for $2p_{3/2}$ and $2p_{1/2}$ were observed at ~711.99 and ~724.91 eV, respectively, and those of Fe^{3+} for $2p_{3/2}$ and $2p_{1/2}$ appeared at ~713.39 and ~727.13 eV, respectively.[274] The ratio of the Fe^{2+}- and Fe^{3+}-peak areas suggests that 3+ is the dominant oxidation state in the charged CrHCF thin films. The divergence of the XPS peaks of Fe can be attributed to the oxidation and reduction reactions during charging and discharging, which is good agreement with the literature.[253] Hence, considering the redox reaction of Fe, a tentative reaction formula can be suggested as following:

$$KCr^{II}[Fe^{III}(CN)_6] + K^+ + e^- \rightleftharpoons K_2Cr^{II}[Fe^{II}(CN)_6]$$

6.3.2 Influence of Electrolyte Compositions on Capacity Retention of CrHCF

In the previous studies of NiHCF and VO_xHCF thin films, it was found that anion species present in the electrolyte take part in the intercalation and deintercalation processes. The change of the electrolyte composition has significant effects on battery performance, namely voltammetric reversibility and cycling stability. To identify the optimal electrolyte composition for the maximization of the battery performance, various electrolytes were utilized to investigate the cycling performance of the CrHCF thin films as following: i) 0.25 M of K-containing electrolytes with different anions, namely NO_3^-, Cl^-, OAc^- (acetate) and SO_4^{2-} and ii) 0.25 M of NO_3-based aqueous electrolytes with different alkali metal cations such as Li^+, Na^+, K^+, Rb^+, and Cs^+. The CrHCF thin films were cycled over 1000 cycles in all the corresponding electrolytes.

The CVs of CrHCF thin films exhibit a similar shape, independent on the anions present in the electrolyte (see **Figure 6.22(a)**). However, the K-intercalation and -deintercalation potentials vary in different electrolytes. Similarly to the case of NiHCF, improved reversibility was observed in the electrolytes containing anions with more symmetric shapes or higher net electric charges (*i.e.*, the less peak separation: $SO_4^{2-} < Cl^- < NO_3^- < CH_3COO^-$). An interesting trend is also observable at the electrode potentials of the K-intercalation and -deintercalation. The intercalation potentials (cathodic peaks) shift towards more positive values in the order of K_2SO_4 (red), KCl (green), KNO_3 (blue), and KCH_3COO (black). Notably, in the case of KCH_3COO, not only the potential shift is significant, but also the CVs exhibit a more asymmetric shape compared to the others. This surprising result explicitly demonstrates the significance of the electrolyte composition for the battery performance of CrHCF. The long-term stability tests of CrHCF thin films further supports the importance of the electrolyte composition. If the anions are not associated with the charging and discharging processes, the capacity retentions should not deviate from each other. However, the capacity retention of the CrHCFs over 1000 cycles varied to a larger degree, depending on the electrolyte composition (see **Figure 6.22B)**. For instance, in the case of 0.25 M KCH_3COO, the capacity dropped to *ca* 10 % of its initial value within 100 cycles, whereas *ca* 57 % of the initial capacity was retained in the case of 0.25 M KNO_3 even after 1000 cycles.

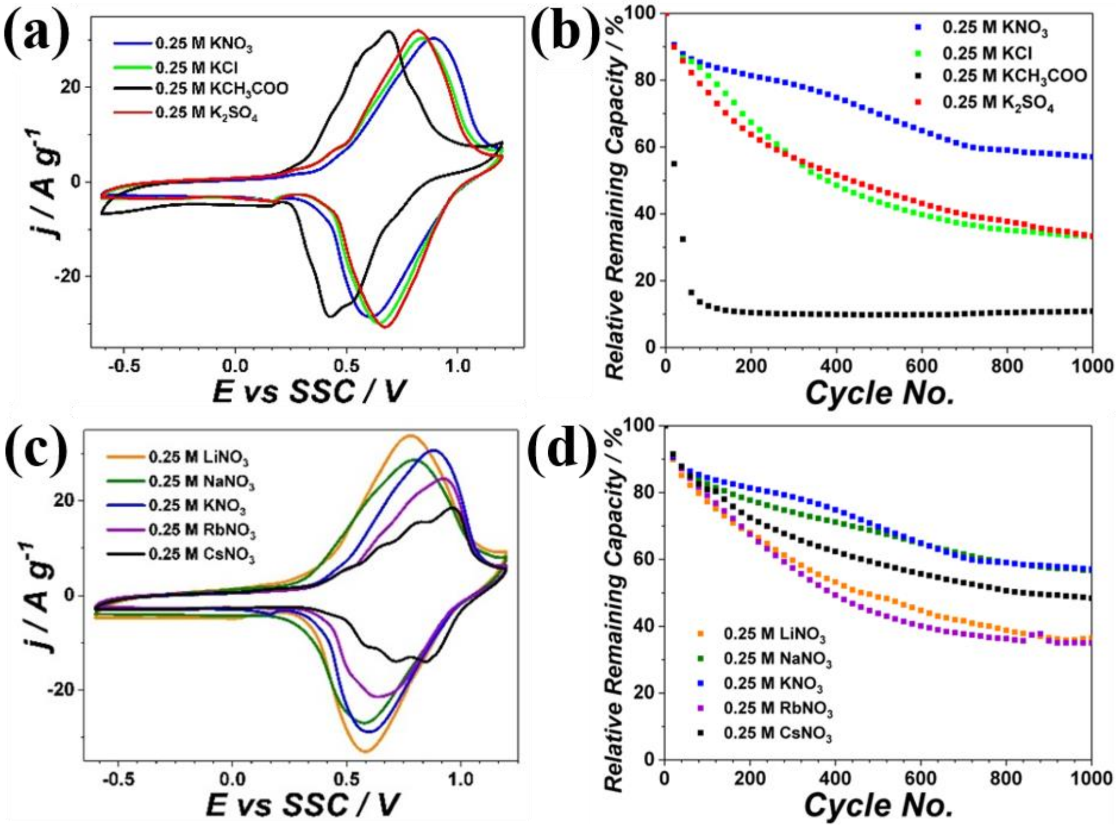

Figure 6.22. Electrochemical measurements of CrHCF thin films in four different electrolytes with different compositions. (a) CVs of CrHCF thin films and (b) corresponding long-term stability tests in 0.25 M of K-containing aqueous electrolytes: KNO_3 (blue), KCl (green), KCH_3COO (black) and K_2SO_4 (red). (c) CVs of CrHCF thin films and (d) corresponding long-term stability tests in 0.25 M of nitrate-based aqueous electrolytes with different alkali metal cations: $LiNO_3$ (yellow), $NaNO_3$ (olive), KNO_3 (blue), $RbNO_3$ (purple) and $CsNO_3$ (black).

Many PBAs are known to be capable of accommodating different sizes of cations because of their large channels.[22, 101-103, 275] As discussed in the previous chapters, the CVs of NiHCF thin films significantly differed depending on the intercalating species, whereas the shape of the CVs for the VO_xHCF thin films appeared to be similar regardless of the nature of the intercalating cations present in the electrolyte. As can be seen in **Figure 6.22 (c)**, the CVs of CrHCF thin films in 0.25 M $AMNO_3$ electrolytes (AM = Li, Na, K, Rb, or Cs) displayed a similar shape except for the case of 0.25 M $CsNO_3$. Since Cs-ions are bigger and heavier than Li-ions, one can anticipate that the cycling stability of the CrHCF will be better in the Li-containing electrolyte compared to that in the Cs-containing one.

Moreover, the more symmetric CV shape of the CrHCF in the Li-electrolyte compared to that in the Cs-electrolyte could support that simple expectation. Surprisingly, the long-term stability tests of CrHCF thin films showed a counterintuitive result. After 1000 cycles, the CrHCF thin films demonstrated higher capacity retention in 0.25 M $CsNO_3$ than in 0.25 M $LiNO_3$ or 0.25 M $RbNO_3$ as seen in **Figure 6.22 (d)**. The cycling stability of the CrHCF thin films was the highest in $NaNO_3$ and KNO_3 electrolyte, which resulted in ~56 % and ~57 % capacity retention with respect to the initial value, respectively. These results suggest that neither size nor mass of the intercalating cations is the sole factor determining the battery performance.

6.3.3 Electrode Compositions and Intercalation Potentials of CrHCF

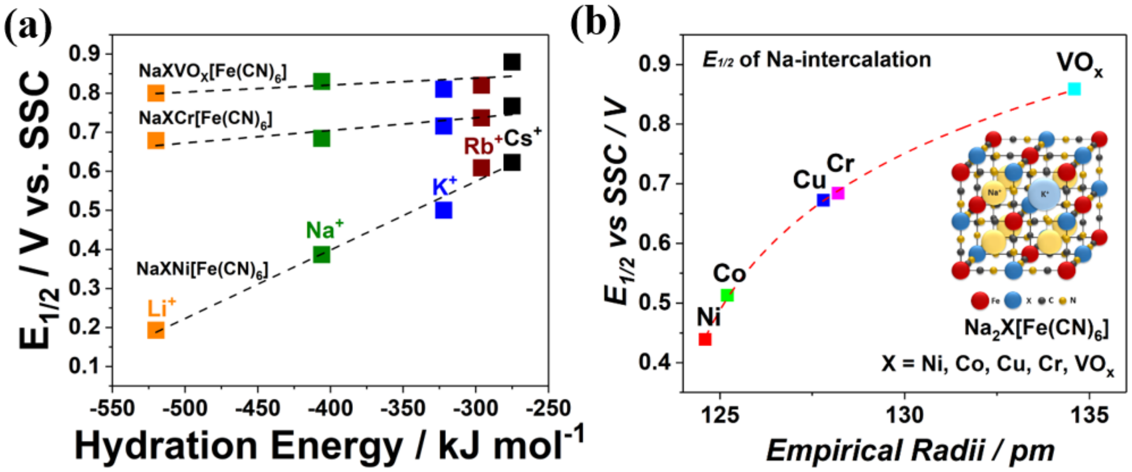

Figure 6.23. Electrode compositions of different PBAs and their intercalation potentials for different alkali metal cations. (a) $E_{1/2}$ potentials for NiHCF, VO_xHCF, and CrHCF electrodes as a function of the hydration energies of intercalating alkali metal cations (Li^+, Na^+, K^+, Rb^+, and Cs^+). (b) Comparison of the $E_{1/2}$ of PBA electrodes ($Na_2X[Fe(CN)_6]$ where X = Ni, Co, Cu, Cr, VO_x]) as a function of the empirical radii of the transition metals that are linked to the nitrogen.

Figure 6.23 (a) shows the $E_{1/2}$ potentials of the NiHCF, VO_xHCF, and CrHCF electrodes as a function of the hydration energies of intercalating alkali metal cations. The $E_{1/2}$ potentials of the CrHCF electrode do show a dependence on the hydration energies of the intercalating cations, however, similarly to the case of the VO_xHCF electrode it is less pronounced than in the case of NiHCF. On the other hand, an interesting correlation of the $E_{1/2}$ potentials with the electrode composition is observed, as shown in **Figure 6.23 (b)**. The $E_{1/2}$ potentials of PBA electrodes tend to shift toward more positive values, at which the PBAs consist of the N-connected transition metals with bigger empirical radii. Finally, a model symmetric cell was built using two identical CrHCF electrodes and 0.25 M $NaNO_3$ aqueous electrolytes.

6.3.4 Battery and Supercapacitor Performance of CrHCF

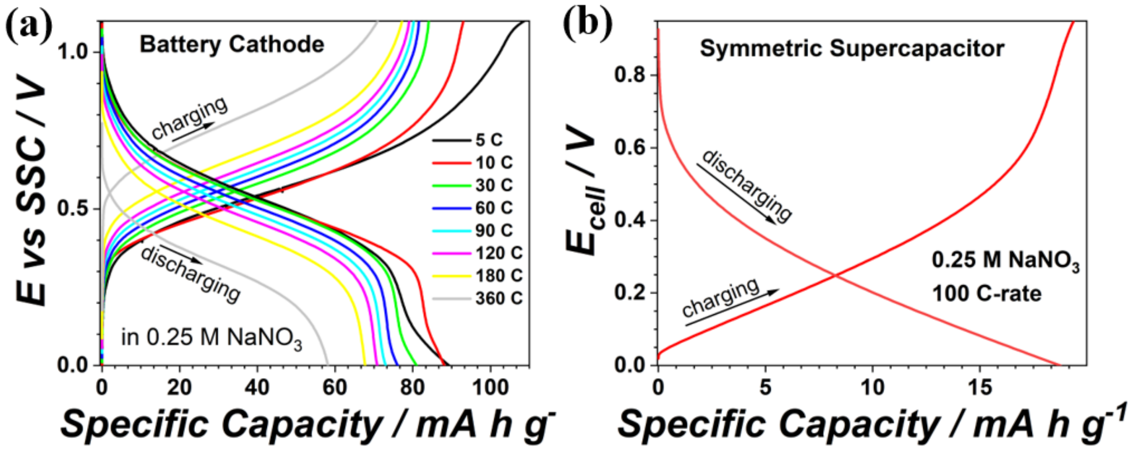

Figure 6.24. The performance of CrHCF as a battery cathode and in a supercapacitor. (a) Charge-discharge profiles of the CrHCF electrode in 0.25 M $NaNO_3$ electrolytes at different C-rates. (b) Galvanostatic charge-discharge curves of the symmetric cell composed of two identical CrHCF electrodes at a C-rate of 100 C in the 0.25 M $NaNO_3$ aqueous electrolyte.

The charge/discharge rate capability of CrHCF thin films was investigated using a 0.25 M $NaNO_3$ electrolyte. The specific capacities of the CrHCF electrodes were measured at different C-rates (from 5 C to 360 C). **Figure 6.24 (a)** displays the resulting charge-discharge curves. The obtained specific capacities were highly dependent on the C-rates. The higher specific capacities were obtained at the slower charging rates. For instance, the CrHCF electrode showed specific capacities of *ca* 88 mAh g^{-1} at 10 C and *ca* 58 mAh g^{-1} at 360 C, respectively. The correlation between the hydration energies of the intercalating alkali metal cations and their intercalation potentials were investigated. **Figure 6.24 (b)** shows the charge-discharge curves of the symmetric CrHCF cell. The resulting specific capacities of the symmetric cell were *ca* 19 mAh g^{-1} at 100 C with the maximum operation voltage of 0.95 V; the specific energy density was calculated to be ca 4.6 Wh kg^{-1}. The obtained feature is comparable to the commercial supercapacitors based on non-aqueous electrolytes, which are already available for power grids and industrial applications.[276, 277]

6.4 Manganese Hexacyanomanganate

Whereas various sorts of cathode materials for Na-ion batteries operating in organic electrolytes have been evaluated as to be compatible with aqueous systems, identification of suitable anode materials remains the major bottleneck in realization of high energy aqueous Na-ion battery systems. The main reason for the difficulty in developing of anode materials is due to the limited electrochemical stability windows of aqueous electrolytes. The redox potential of many cathode materials for Na-intercalation and -deintercalation lies within the stable potential window of aqueous electrolytes. On the other hand, conventional anode materials, namely graphites, do not exhibit Na-intercalation and -deintercalation in the given potential ranges (-0.414 V and 0.817 V vs SHE at pH 7).[85, 196, 278, 279] Therefore, it is crucial to develop new anode materials operating in the stable potential window of aqueous electrolytes without triggering any side reactions, such as hydrogen evolution reaction (HER). Further requirements of advanced anode materials for aqueous Na-ion batteries can be listed: (i) Na-intercalation and -deintercalation should take place at the electrode potential as low as possible for achieving higher energy density. (ii) The electrode materials should be physically and chemically stable during the battery operation. (iii) The anode materials should be compatible with the corresponding cathode materials.[280]

Many anode materials have been reported in the literature. Probably NASICON (Na superionic conductor) is the most intensively studied class of anode materials for aqueous Na-ion batteries. Park *et al.* firstly reported the applicability of $NaTi_2(PO_4)_3$ as an anode material in the aqueous system.[281] The theoretical specific capacity of $NaTi_2(PO_4)_3$ was calculated to be *ca* 133 mAh g^{-1}, and the plateau potential was observed at 2.1 V vs Na/Na^+ (-0.61 V vs SHE). However, $NaTi_2(PO_4)_3$ exhibited a quick capacity fading in aqueous media mainly due to its low electronic conductivity, dissolution of the active material and side reactions with the electrolytes.[89] Various approaches have been made to address the abovementioned issues, for instance coating with conductive materials,[86, 93, 105, 282-291] nano-structuring[292] and replacing Ti with heteroatoms.[293-296] Albeit NASICON-type anode materials might exhibit a high specific capacity with low working potentials, the high price of Ti and poor cyclability will be more costly over their high energy density in the case of large-scale applications.

Organic compounds are another type of anode materials for aqueous Na-ion batteries. For instance, polyimide,[297] quinone,[298] alloxazine[299] and polypyrrole[300] were reported as anode materials in the literature. Qin *et al*. proposed 1,4,5,8-Naphthalenetetracarboxylic dianhydride (NTCDA)-derived polyimide as an anode material.[297] Unlike intercalation compounds, the NTCDA-derived polyimide undergoes an enolization process that captures cations with +1 charge. The polyimide anodes demonstrated a high discharge capacity of *ca* 184 mAh g^{-1}, but it suffered from the rapid capacity fading. Although further enhancements of polyimide-based anodes have been achieved by tailoring the molecular structures,[301, 302] a fast capacity decay is yet questionable for practical applications.

Some transition metal oxides show the functionality of anode materials for aqueous Na-ion batteries. Liu *et al*. reported polypyrrole coated-MoO_3 with the argument of its amazingly high theoretical capacity of *ca* 1111 mAh g^{-1}, but the actual capacity that they obtained was only 33 mAh g^{-1}.[303] 1D nanostructured $Na_2V_6O_{16}\cdot nH_2O$ was reported by Deng *et al*. and showed a high initial discharge capacity of 123 mAh g^{-1}, but it significantly decreased to 42 mAh g^{-1} in the subsequent cycle.[304]

Another remarkable family of anode materials is Prussian blue analogs (PBAs). Cui *et al*. showed a new approach to the well-known PBAs as electrode materials for aqueous media.[102, 103] They reported manganese hexacyanomanganate (MnHCMn) as an anode material for this type of batteries.[101] The MnHCMn was prepared by a coprecipitation method and exhibited a specific capacity of 57 mAh g^{-1} with the working potential of around 0.052 V vs SHE, which is, however, still high as an anode material. The most promising feature of the MnHCMn is that it is not only composed of very abundant and cheap elements but also displays excellent cyclability over thousand cycles with high stability and rate capability.

Despite the remarkable progress in improving the cathode materials for aqueous Na-ion batteries, identification and development of the anode materials is the stagnant point at the current stage. In the following subchapter, electrochemically prepared MnHCMn thin-film electrodes are demonstrated as an excellent anode material for aqueous Na-ion batteries.

Subsequently, MnHCMn thin films are characterized by different techniques to investigate the fundamentals and practices.

6.4.1 Preparation of $Na_xMn[Mn(CN)_6]$ Electrodes

Electrochemical deposition and characterization including battery tests of $Na_xMn[Mn(CN)_6]$ thin-film electrodes were conducted in the glass cell using a three-electrode configuration under Ar-atmosphere. The schematics of the used glass cells are shown in **Figure 5.1 (a)** and **5.1(b)**. AT-cut gold quartz crystals or gold arrandee™ were utilized as substrates for the deposition. As the reference and counter electrodes, an Ag/AgCl (SSC) electrode and a Pt wire were used, respectively.

Electrochemical deposition of the MnHCMn thin films was performed by cycling the electrode potential from -0.6 V to -1.18 V vs SSC at a scan rate of 50 mV s^{-1}. The deposition solution consisted of 7 mM $MnSO_4$ and 11 mM $K_4[Mn(CN)_6]$ in a 0.25 M Na_2SO_4 aqueous solution. The synthesis of $K_4[Mn(CN)_6]$ was conducted at the Department of Chemistry of Technical University of Munich. The detailed synthesis procedure is provided in **Appendix F**. In the course of the deposition process, the frequency changes of the QCM electrode, which can be computed to the mass changes, were simultaneously monitored.

The net reaction scheme for the electrodeposition of MnHCMn thin films can be tentatively described with two-steps as[101, 280]

Reduction process

$$3Na^+_{(aq.)} + Mn^{2+}_{(aq.)} + [Mn^{II}(CN)_6]^{4-}_{(aq.)} + e^- \rightarrow Na_3Mn[Mn^I(CN)_6]_{(s.)}$$

Oxidation process

$$Na_3Mn[Mn^I(CN)_6]_{(s.)} \rightarrow Na^+_{(aq.)} + e^- + Na_2Mn[Mn^{II}(CN)_6]_{(s.)}$$

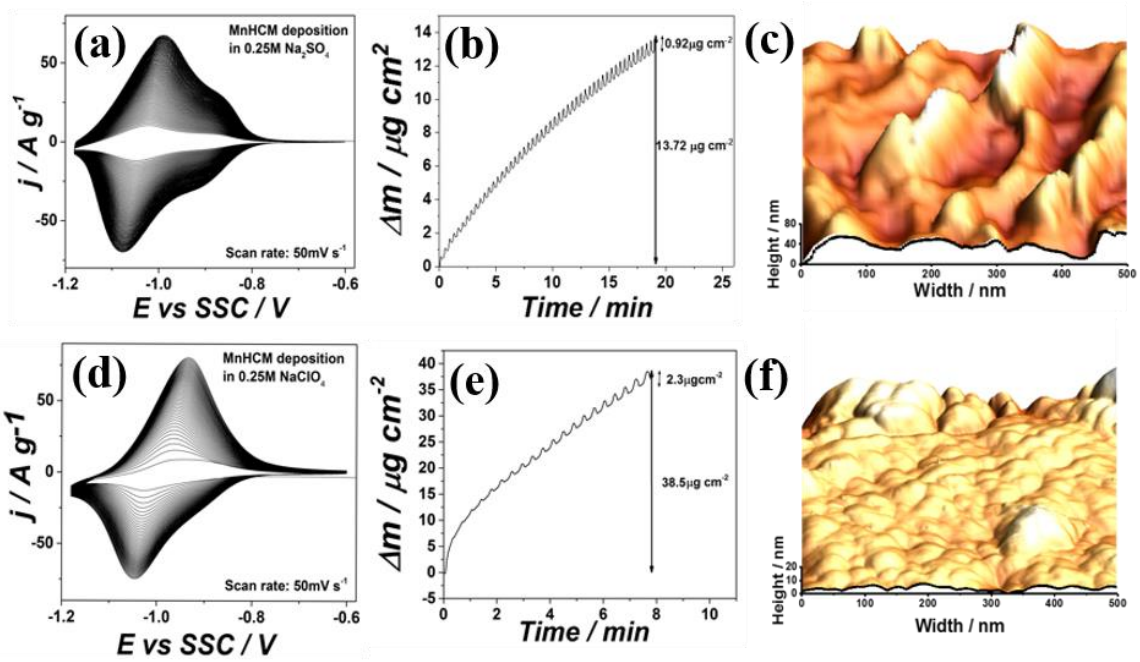

Figure 6.25. Electrochemical deposition and AFM images of $Na_xMn[Mn(CN)_6]$ (MnHCMn) thin films. (a, d) Representative CVs for the electrochemical deposition of MnHCMn from an aqueous solution consisting of 7 mM $MnSO_4$ and 11 mM $K_4[Mn(CN)_6]$ in conjunction with (a) 0.25 M Na_2SO_4 and (d) 0.25 M $NaClO_4$. (b, e) The corresponding EQCM curves disclosing the mass changes during the deposition. The AFM image of the deposited MnHCMn thin films from (c) the Na_2SO_4-based and (f) the $NaClO_4$-based solutions.

Figures 6.25 (a) and **6.25 (d)** show the characteristic CVs of the electrochemical deposition of MnHCMn thin films on AT-cut quartz crystal substrates from aqueous deposition solutions consisting of 7 mM $MnSO_4$ and 11 mM $K_4[Mn(CN)_6]$ together with (a) 0.25 M Na_2SO_4 and (d) 0.25 M $NaClO_4$, respectively. As can be seen from the CVs, the increase in current density of cathodic and anodic peaks reveals the growth of MnHCMn thin films along with potential cycling. While the MnHCMn thin films showed a gradual growth in both of the deposition solutions, surprisingly, the MnHCMn thin films from 0.25 M $NaClO_4$-based deposition solution resulted in a quicker growth rate compared to that of the 0.25 M Na_2SO_4-based solution.

The corresponding EQCM curves display the mass changes due to the MnHCMn thin film growth in real-time (see **Figure 6.25(b)** and **6.25 (e)**). ~13.72 μg cm^{-2} and ~38.5 μg cm^{-2}

of the mass changes were observed (b) from the MnHCMn thin film deposition from the Na_2SO_4-based solution and (d) from the $NaClO_4$-based solution, respectively. The mass oscillations during the growth of MnHCMn thin films explicitly show the occurrence of Na-intercalation and -deintercalation in the course of the deposition. Interestingly, the deposition rate of the MnHCMn films in the $NaClO_4$-based solution was roughly six times faster compared to that of the use of the Na_2SO_4-based solution. Taking into account the hypothesis of the three-stage mechanism that anions present in the electrolyte participate in Na-intercalation and -deintercalation, it can be concluded that the growth rate of the films is significantly increased by changing the anions (*i.e.*, replacing SO_4^{2-} with ClO_4^-).[22, 280]

However, the MnHCMn films that were deposited from the perchlorate-containing solutions exhibited an inferior Na-storage property. The MnHCMn thin films that were deposited from the Na_2SO_4-based solutions exhibited approximately 6.70 % of mass change after Na-intercalation. This value is virtually equal to the theoretical one (~6.88%) with the assumption that one Na-ion (*ca* 23 g mol^{-1}) is involved in the Na-intercalation into $Na_3Mn[Mn(CN)_6]$ (*ca* 334 g mol^{-1}) within the given potential range. The little deviation of 0.18 % is probably related to the capacitive charge stored at the MnHCMn films. On the other hand, the MnHCMn thin films that were prepared from the $NaClO_4$-based solutions showed merely ~5.97 % of the Na-utilization. The reduced proportion was presumably caused by the fast growth of the films, which resulted in the deposition of a remarkable amount of inactive materials. Therefore, throughout the experiments, 0.25 M of Na_2SO_4 was chosen as a supporting electrolyte for the deposition solution in the subsequent experiments.

Figure 6.25 (c) and **6.25 (f)** display the AFM images of the deposited MnHCMn thin films from (c) the Na_2SO_4-based and (f) the $NaClO_4$-based solutions, respectively. More uneven surface morphology can be observed in (c), which is related to the MnHCMn thin films deposited at a slower rate. This result is counterintuitive to the commonly-believed fact that faster deposition produces more uneven surfaces. Considering that the sole difference in the deposition solution is the type of the anion species present in the supporting electrolytes, this can be another evidence of the three-stage mechanism: Anions take part not only in the Na-intercalation and -deintercalation but also in the deposition process.[280]

6.4.2 Mechanism of Na-Intercalation into MnHCMn

In order to examine the Na-intercalation mechanism, the deposited MnHCMn thin films were cycled in a 0.25 M Na_2SO_4 aqueous electrolyte between -0.6 V and -1.18 V with respect to the Ag/AgCl reference electrode (scan rate: 50 mV s^{-1}). A typical CV of MnHCMn thin films in the 0.25 M Na_2SO_4 electrolyte is shown in **Figure 6.26 (a)**. The obtained CVs display an anodic peak at around -1.0 V and a cathodic peak at around -1.08 V. According to the literature, the redox reaction of $Mn^{I/II}$ of MnHCMn occurs at the potential of ~0.7 V vs SHE (-0.91 V vs SSC).[101, 254] However, it was observed in this study that the potentials are shifted towards more negative ones. This discrepancy is probably due to the use of the different electrolytes (1 M K-electrolyte) in the literature.[254] The pronounced characteristic peaks of $Mn^{I/II}$ are the evidence of the occurrence of Na-intercalation and -deintercalation at the MnHCMn thin films.

A tentative net reaction of Na-intercalation and -deintercalation in MnHCMn in the aqueous Na-electrolyte within the given potential range can be formulated as:

$$Na_2Mn^{II}[Mn^{II}(CN)_6] + Na^+ + e^- \rightleftharpoons Na_3Mn^{II}[Mn^{I}(CN)_6]$$

To verify the aforementioned reaction scheme, XPS measurements using the MnHCMn thin films in the Na-intercalated and Na-deintercalated states were performed. **Figure 6.26 (b)** exhibits the obtained XPS peaks for Na and Mn of the MnHCMn thin films. The reduced intensity of Na 1s peak (red-line) was observed at the Na-deintercalated MnHCMn compared to that of the Na-intercalated MnHCMn. As can be expected from the reaction formula, not all Na ions were extracted from the MnHCMn thin films. According to the literature, the MnHCMn should be charged to 4.0 V vs Na/Na^+ to fully deintercalate Na-ions (equivalent to 1.29 V vs SHE).[156] However, this is not practical because the redox reaction of Mn in the P-site, *i.e.*, the N-linked Mn, is not reversible since the $Mn^{III}[Mn^{III}(CN)_6]$ is highly soluble and thus unstable in aqueous electrolyte.[101] The binding energy shifts of Mn $2p^{1/2}$ and Mn $2p^{3/2}$ were revealed between the Na-intercalated and Na-deintercalated MnHCMn, which shows the redox activity of Mn. For instance, the binding energies of Mn $2p^{3/2}$ peaks of Mn^+ (Na-intercalated) and Mn^{2+} (Na-deintercalated) were obtained as 641.15 eV and 642.19 eV, respectively. Compared to those values from the literature,[156] the binding energy of Mn^+ showed a deviation of 0.05 eV, but that of

Mn^{2+} was 0.59 eV. The relatively noticeable deviation of the binding energies of Mn^{2+} between the obtained and the literature values might be related to the overlap of several possible valence states of Mn, which could have different intensities. Generally, distinguishing the valance states of Mn is not straightforward, thus it would need more advanced experimental techniques to determine the exact valance states of Mn.

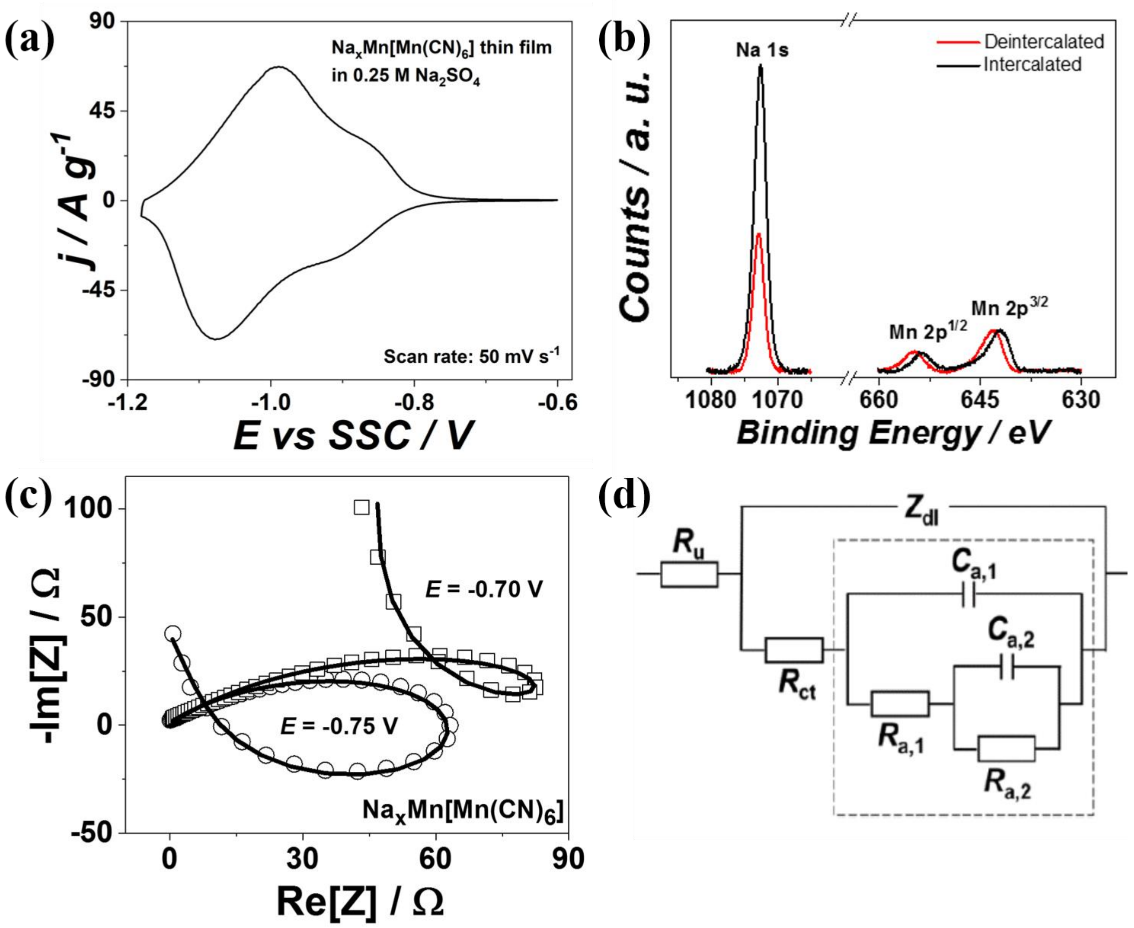

Figure 6.26. Identification of the Na-intercalation and -deintercalation mechanism for the $Na_xMn[Mn(CN)_6]$ (MnHCMn) thin films. (a) The characteristic CV of MnHCMn thin films in a 0.25 M Na_2SO_4 aqueous electrolyte. (b) XPS analysis for the MnHCMn thin films in the Na-intercalated (black) and Na-deintercalated (red) states, respectively. (c) The EIS spectra (open symbols) of MnHCMn thin films in a 0.25 M Na_2SO_4 electrolyte measured at the potential of –0.7 V (squares) and -0.75 V (circles) vs SSC together with the fittings (solid lines). The other EIS data collected at different electrode potentials and the corresponding fittings are presented in **Appendix G**. (d) The equivalent electric circuit used for the fitting. The description of the circuit elements is given in **Chapter 6.1.2**.

The impedance study of the MnHCMn thin films was conducted by applying ac probing signals with 10 mV amplitude and various frequencies between 10 kHz and 0.5 Hz. The impedance data were acquired in the potential region from -0.6 V to -1.18 V with 70 steps. **Figure 6.26 (c)** shows the EIS spectra collected at the potentials where Na-intercalation and -deintercalation take place. The other impedance spectra recorded at different potentials are presented in **Appendix G**. Similarly to the case of the previous studies of the NiHCF and VO_xHCF, the "loop-shaped" spectra were also observed.

On the other hand, the measured impedance spectra exhibited a typical shape of the combination of a semi-circle and a line at the potentials (*e.g.*, - 0.6 V and – 0.65V), where neither Na-intercalation nor -deintercalation is expected to occur (See **Figure A8A** and **A8F)**. The Kramers-Kronig check did not reveal any quality issues for the obtained impedance data. **Figure 6.26 (d)** displays the equivalent electric circuit used to fit the measured spectra. The good fitting results using this EEC suggest the presence of at least three intermediate steps during Na-intercalation and -deintercalation in this system as well. As previously discussed, the three-stage mechanism involves participation of anions present in the electrolyte in the course of the intercalation and deintercalation. As a result, the voltammetric reversibility can be influenced by replacing anions in the electrolytes. Similarly to the NiHCF and VO_xHCF, a tentative model of the Na-deintercalation mechanism can be proposed for the case of sulfate-ions present in the electrolytes as:

$$Na_3Mn[Mn^{I}(CN)_6] \leftrightarrow Na_3Mn[Mn^{II}(CN)_6]^{+} + e^{-} \tag{1}$$

$$2Na_3Mn[Mn^{II}(CN)_6]^{+} + SO_4^{2-} \leftrightarrow (Na_3Mn[Mn^{II}(CN)_6])_2SO_4 \tag{2}$$

$$(Na_3Mn[Mn^{II}(CN)_6])_2SO_4 \leftrightarrow 2Na^{+} + SO_4^{2-} + 2\,Na_2Mn[Mn^{II}(CN)_6] \tag{3}$$

6.4.3 Electrolyte Compositions and Intercalation Properties of MnHCMn

In order to verify how anions influence the voltammetric reversibility, CV measurements of MnHCMn thin films were performed in different aqueous Na-electrolytes. **Figure 6.27 (a)** shows typical CVs of the MnHCMn thin films in 0.25 M Na_2SO_4 (black), 0.25 M $NaNO_3$ (blue), and 0.25 M $NaClO_4$ (red). The recorded CVs exhibit not only different shapes but also a different degree of reversibility depending on the electrolytes. Interestingly, a similar trend was observed in the case of the NiHCF films. The CVs of MnHCMn films in the electrolyte having the anions with a higher net effective charge density or a more symmetric structure resulted in less cathodic-anodic peak separations (*i.e.*, better voltammetric reversibility): $\Delta E_{1/2,SO_4^{-2}} < \Delta E_{1/2,NO_3^-} < \Delta E_{1/2,ClO_4^-}$.

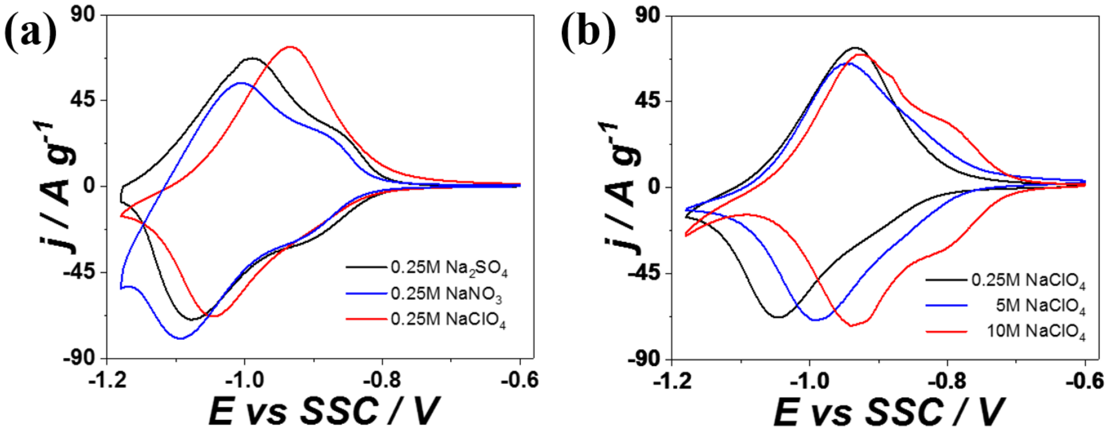

Figure 6.27. (a) Characteristic CVs of MnHCMn thin films in aqueous Na-electrolytes containing different anions: 0.25 M Na_2SO_4 (black), 0.25 M $NaNO_3$ (blue), and 0.25 M $NaClO_4$ (red). (b) CVs of MnHCMn thin films in $NaClO_4$ electrolytes with different concentrations: 0.25 M (black), 5 M (blue) and 10 M (red). The scan rate was set as 50 mV s^{-1} for all the cases.

Recently, the concentration of the electrolyte is considered a crucial element for improving the performance of aqueous battery systems.[305-309] For the study of concentration effects on the voltammetric-reversibility, $NaClO_4$ was chosen because of its high solubility in water. **Figure 6.27 (b)** displays representative CVs of MnHCMn in 0.25 M $NaClO_4$ (black), 5 M $NaClO_4$ (blue), and 10 M $NaClO_4$ (red). The cathodic current peaks shifted to more positive potentials as the concentration of $NaClO_4$ electrolytes increases, whereas the position of the anodic current peaks does not significantly change. In other words, the voltammetric reversibility of the MnHCMn was considerably improved in the more concentrated $NaClO_4$ solutions. Notably, the CV of MnHCMn recorded in 10 M $NaClO_4$ exhibited a virtually symmetric shape. The cathodic-anodic peak separations for the MnHCMn films greatly diminished in the ascending order of the concentration: $\Delta E_{0.25\ M\ NaClO_4}$ = ~100 mV, $\Delta E_{5\ M\ NaClO_4}$ = ~50 mV, and $\Delta E_{10\ M\ NaClO_4}$ = ~1 mV. The observed improvement of the reversibility cannot be simply ascribed to the ionic conductivity of the electrolyte, as the conductivity of $NaClO_4$ aqueous solution does not always increase upon the concentration increase. For instance, the conductivity increases until 5 M, but then decreases as the concentration increases.[310] Hence, the rational choice of the electrolyte composition is crucial to improve the battery system's efficiency further.

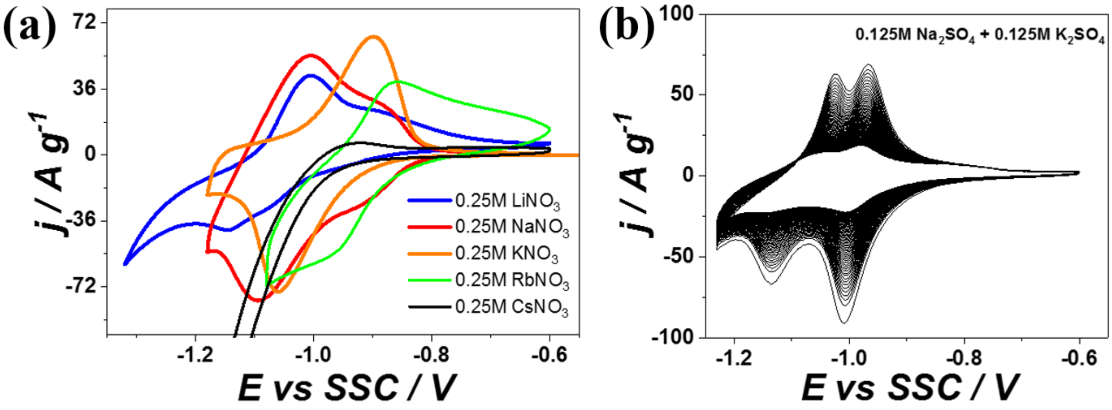

Figure 6.28. (a) Characteristic CVs of the MnHCMn thin films in 0.25 M nitrate-based aqueous electrolytes containing different alkali metal cations (Li^+, Na^+, K^+, Rb^+, and Cs^+). (b) CVs of the MnHCMn thin films characterizing co-intercalation of Na^+ and K^+.

Many PBA compounds showed the ability to intercalate various-size alkali metal cations.[22, 101-103, 275] In the literature, a few of them, namely NiHCF or CoHCF, exhibited the alteration of intercalation potentials for different alkali metal cations, which can be related to the solvation energy of the cations.[22, 311] In order to investigate the intercalation properties of different cations at MnHCMn thin films, 0.25 M $AMNO_3$ aqueous electrolytes (AM = Li, Na, K, Rb, or Cs) were utilized. From the study of intercalation of alkali metal cations at MnHCMn thin films, a surprising result was obtained.

As shown in **Figure 6.28 (a)**, it was revealed that not all kinds of alkali metal cations could be intercalated into the MnHCMn thin films. While well-pronounced cathodic and anodic peaks were observed in the 0.25 M $NaNO_3$ and 0.25 M KNO_3 electrolytes, Rb-ions did not appear to effectively intercalate into the MnHCMn. Moreover, the intercalation of Li-ions into the MnHCMn does not seem to practically occur (see the cathodic peak of blue CV in **Figure 6.28 (a)**), but one can see higher anodic current, which can be related to the deintercalation of Na-ions. The CV of MnHCMn thin films in 0.25 M $CsNO_3$ does not show characteristic features of the intercalation but instead reveals a side reaction, *e.g.*, hydrogen evolution, at the potential of the intercalation to be foreseen to occur. Considering that the channel size of the MnHCMn (~10.5 Å) is large enough to accommodate Cs-ions, it is an unanticipated result.[156] This can be associated with the fact that the properties of the alkali metal cations probably have a vast influence on the HER catalytic activity of different electrodes.[182, 312-319] These consequences show that neither the size of the intercalating species nor their hydration energy are the only determining factors controlling the intercalation in this specific case.[22] **Figure 6.28 (b)** exhibits CVs of MnHCMn films in an aqueous solution containing both of 0.125 M Na_2SO_4 and 0.125 M K_2SO_4. The co-intercalation of both ions into the MnHCMn films was observed. However, serious degradation of the films occurred at a comparably quick rate.

XPS measurements of the MnHCMn films were conducted to confirm the occurrence of Na- and K-intercalation and the poor intercalation property of Li-ions. **Figure 6.29** shows the XPS peaks of Li, Na, and K collected from the K-intercalated, the Li-intercalated, and both of Na- and K-intercalated MnHCMn thin films, respectively. As expected, a substantially low-intensity XPS peak for Li was seen, verifying the poor Li-intercalation into the MnHCMn in the 0.25 M $LiNO_3$ aqueous electrolyte. Contrarily, distinct XPS peaks for K were observed at both K-intercalated and Na- and K-co-intercalated MnHCMn films. This shows the successful intercalation of K^+ into the MnHCMn films. Especially in the case of the co-intercalated sample, the relative intensity changes of Na and K peaks were found. Here, the intensity of the Na peak increased, whereas that of the K peak decreased. This might be due to the fact that both Na- and K-ions shared the intercalation channels in the MnHCMn films. The XPS peaks of Mn appeared to be virtually overlapped, showing that the MnHCMn thin films were "fully charged" in all the cases.

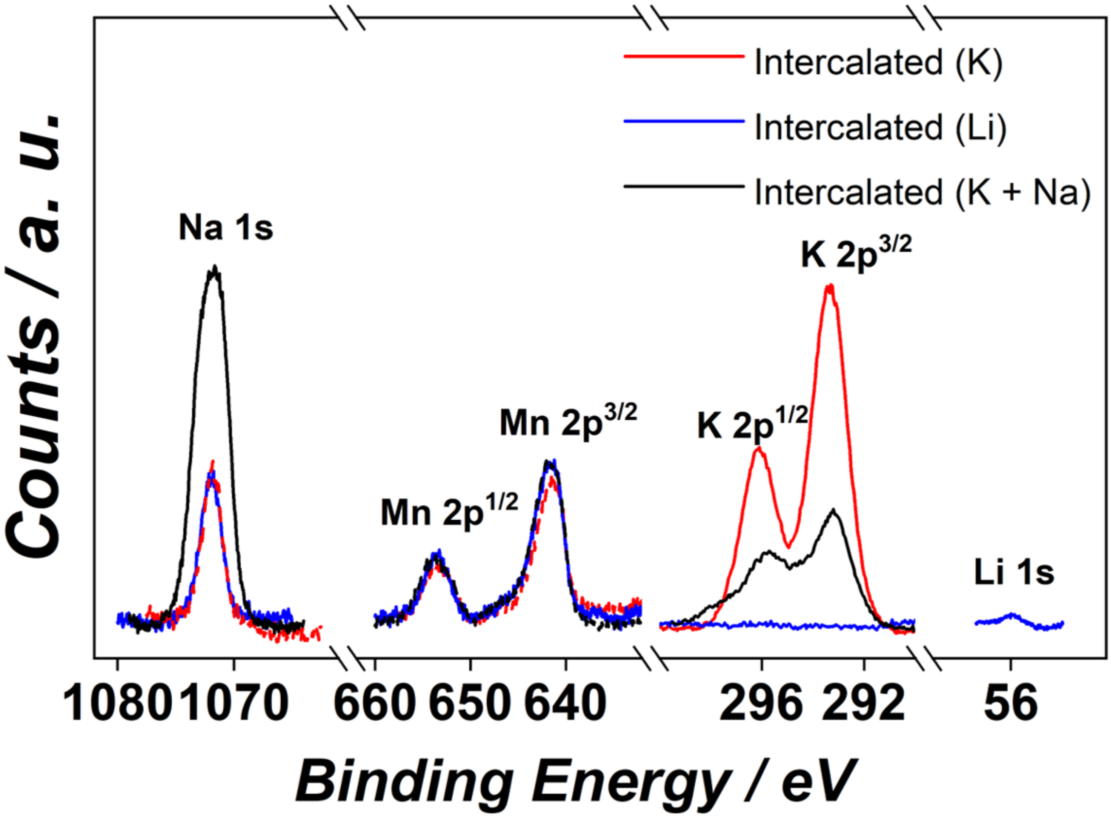

Figure 6.29. XPS analysis of the MnHCMn thin films in the K-intercalated (red), Li-intercalated (blue), and K- and Na-co-intercalated (black) states, respectively.

6.4.4 Battery Performance Tests for MnHCMn

Grounded on the discovery of the influence of the electrolyte composition on cycling efficiency, an optimized battery system using an MnHCMn electrode was built to investigate the battery performances. As revealed from the previous studies, the effect of highly concentrated $NaClO_4$ electrolyte outperforms the anion effect of Na_2SO_4 due to the high solubility of $NaClO_4$ (10 M) in comparison with that of Na_2SO_4 (less than 2 M). Highly-concentrated aqueous electrolytes have been deemed superior in aqueous battery systems in the literature.[305-309] Thus, a 10 M $NaClO_4$ aqueous electrolyte was utilized instead of Na_2SO_4 based electrolytes.

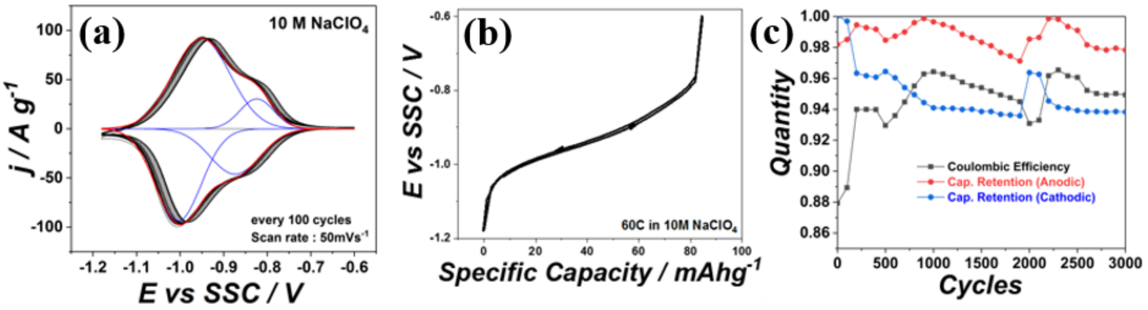

Figure 6.30. Battery tests of MnHCMn electrodes. (a) Representative CVs for the MnHCMn electrodes in a 10 M $NaClO_4$ electrolyte (3000 cycles). For better visualization, every 100 cycles are displayed. (b) Charge and discharge profiles of the MnHCMn electrode in a 10 M $NaClO_4$ electrolyte (C-rate: 60 C). (c) A long-term battery performance test of the MnHCMn electrode. The capacity retentions of anodic and cathodic processes together with Coulombic efficiency is provided.

The MnHCMn electrode was cycled in the potential range of from -1.18 V to -0.6 V at 50 mV s^{-1} for 3000 cycles. **Figure 6.30 (a)** exhibits the resulting CVs of the MnHCMn electrode in 10 M $NaClO_4$. After 100 cycles, the $E_{1/2}$ potentials for the cathodic and anodic scans were calculated as -0.958 V and -0.930 V vs SSC, respectively. At such negative potentials, the hydrogen evolution reaction was not observed. Those working potentials of the MnHCMn are surprisingly low in pH-neutral aqueous media considering the equilibrium potential of hydrogen reduction to be -0.413 V vs SHE (-0.610 V vs SSC).[101] After 3000 cycles, the CVs of the MnHCMn electrode showed solely negligible degradation. Interestingly, the $E_{1/2}$ potentials seemed to shift towards more positive values to a small extent (*ca* -0.937 V and *ca* -0.910 V, respectively) after the completion of 3000 cycles. The optimized system delivered a specific capacity of *ca* 85 mAh g^{-1} at 60 C as displayed in **Figure 6.30 (b)**. This is roughly 50 % enhancement compared to the value in the literature.[101] **Figure 6.30(c)** shows the obtained capacity retentions and Coulombic efficiency. The MnHCMn electrode exhibited very low capacity drop over 3000 cycles. Only approximately 6 % drop in the discharge capacity was observed. The Coulombic efficiency was maintained between 94 and 96 % in average.[101]

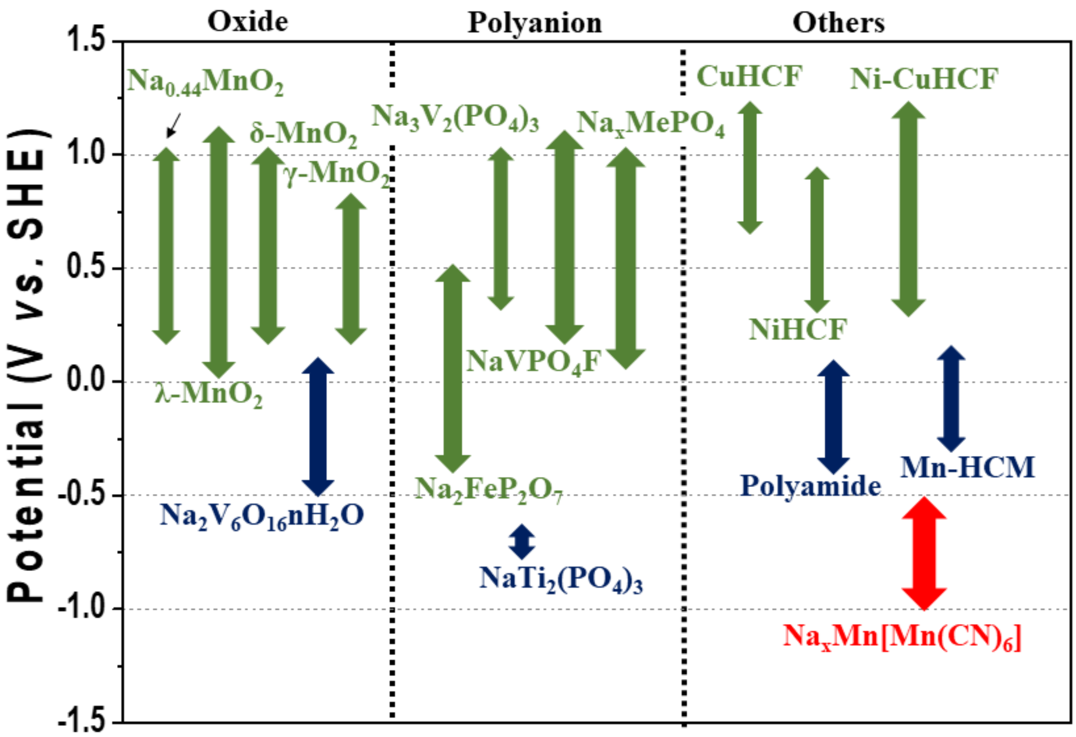

Figure 6.31. Operating potential ranges of the $Na_xMn[Mn(CN)_6]$ thin films in comparison with various types of electrode compounds for aqueous Na-ion batteries. Reproduced from reference [85] with permission from the American Chemical Society.

Figure 6.31 summarizes various electrode compounds for Na-ion batteries in aqueous media with pH 7. The electrodeposited $Na_xMn[Mn(CN)_6]$ thin films display the lowest operating potentials among the reported materials to the best of my knowledge. Remarkably, no HER was seen in neutral aqueous electrolytes containing Na^+ and K^+ even at such a negative potential.

7. Conclusions

The main aim of this thesis was identification of suitable electrode materials for aqueous Na-ions batteries for grid-scale applications as well as investigation of their physicochemical and electrochemical properties to find parameters that influence their battery performance. In this work, four different Prussian blue analogs, namely nickel hexacyanoferrate (NiHCF), vanadium hexacyanoferrate (VO_xHCF), chromium hexacyanoferrate, and manganese hexacyanomangante (MnHCMn), were successfully synthesized via electrochemical deposition. They demonstrated excellent features as promising candidates for aqueous Na-ion batteries and enabled interesting fundamental findings which allow predictable manipulation of battery performance.

In **Chapter 6.1**, widely-accepted simple models of a one-stage Na-intercalation mechanism were challenged to examine the correctness of the model. Using impedance measurements and careful analysis, the Na-intercalation seemed to proceed via at least three reaction steps, involving participation of anions present in the electrolyte. The appearance of the “loop-shaped” impedance spectra recorded within the operating potentials was deemed as the indicator of the presence of the so-called “three-stage mechanism” of Na-intercalation. The involvement of anions in the Na-intercalation was evidenced by the observation that the voltammetric reversibility is significantly influenced by the nature of the anions present in the electrolyte. The better voltammetric reversibility was obtained from the NiHCF thin films immersed in the electrolyte containing anions with higher net-charge density or a more symmetric ionic structure. The significance of the three-stage mechanism lies in the fact is that the battery performance can be further enhanced by a rational choice of the composition of the electrolytes. With the gained knowledge, NiHCF thin films exhibited the $E_{1/2}$ potential of ~0.38 V vs SSC and a specific capacity of approximately 80 mAh g^{-1} at an extremely high charge rate (180 C). Furthermore, the recorded charge-discharge profiles in 1 M Na_2SO_4 were virtually overlapped for the NiHCF system showing excellent energy efficiency during charging and discharging. Last but certainly not least, the nature of the alkali metal cations has shown a substantial effect on determining the intercalation potential in the studied system. It is assumed that the $E_{1/2}$ potential of NiHCF is quasi-linearly related to the hydration energy of alkali metal cations.

Chapter 6.2 discusses the study of $Na_2VO_x[Fe(CN)_6]$ (VO_xHCF) thin films. The electrochemically deposited VO_xHCF thin films showed the highest $E_{1/2}$ potential ($E_{1/2}$: ~0.90 V vs SSC) in acidic media without recognizable side reactions compared to those of $Na_2Ni[Fe(CN)_6]$, $Na_2Co[Fe(CN)_6]$ and $Na_2Cu[Fe(CN)_6]$ studied in this work. The obtained specific capacities of VO_xHCF electrodes exhibited ~83, ~79 and ~76 mAh g^{-1} at a high charge-discharge rate (30 C) in aqueous electrolytes of 1 M $LiNO_3$, 3 M $NaNO_3$, and 3 M KNO_3 with the addition of 3.6 M H_2SO_4, respectively. Despite the high operating potential and high specific capacity, the requirement of high acidity for ensuring the stability of VO_xHCF was needed to be mediated. As the protective layer, the NiHCF coating was suggested to be used at the VO_xHCF electrode. The NiHCF-coated VO_xHCF electrodes displayed a significantly improved cyclability in a 0.25 M Na_2SO_4 aqueous electrolyte at pH=4. Interestingly, the operating potential of the coated VO_xHCF electrode has shown negative shifts of approximately 0.2 V. The validity of the three-stage intercalation mechanism was confirmed for all four investigated PBAs. The fact that the "loop-shaped" spectra appear at different systems suggests that it is neither a material-specific nor experimental artifact. The XPS study revealed that vanadium is not associated with the redox reaction in VO_xHCF, but it was mainly ascribed to the change of the oxidation state of Fe. The intercalation potentials of VO_xHCF did not show a strong dependence on the nature of the alkali metal cations; the solvation effects were not well-pronounced compared to the NiHCF system. An empirical trend was found from the summary of the intercalation potentials for the NiHCF, CoHCF, CuHCF, and VO_xHCF electrodes. It was seen that the size of the transition metal is highly relevant to the working potential of the PBA electrodes.

Chapter 6.3 summarizes the results on identification and development of $Na_2Cr[Fe(CN)_6]$ electrodes for aqueous Na- and K-ion batteries. It was revealed that the electrochemical deposition of CrHCF thin films required a very negative potential (-1.1 V vs SSC) to be applied. Gold electrodes were not appropriate for the CrHCF deposition because of vast side reactions at the potential of -0.7 V vs SSC, which was still too positive compared to the required potential for the effective CrHCF deposition. Instead, 3D-graphene foams were identified to be good substrates for the CrHCF deposition since they did not show any side reactions until -1.1 V vs SSC. The long-term cyclability tests of the CrHCF electrodes showed that they perform better in NO_3-based aqueous electrolytes compared to other electrolytes. The optimized CrHCF electrode displayed $E_{1/2}$ of 0.69 V vs SSC (in 0.25 M $NaNO_3$) and 0.72 V vs SSC (in 0.25 M KNO_3) and a specific capacity of 88 mAh g^{-1} at 10 C in 0.25 M $NaNO_3$. After 1000 cycles, the CrHCF electrode retained more than 60 % of the initial capacity revealing its long cycle life. The constructed model cell using two identical CrHCF electrodes exhibited an open-circuit voltage of 0.95 V with an energy density of approximately 4.6 Wh kg^{-1} at 100 C. Similar to the VO_xHCF, the solvation effects of alkali metal cations did not show a remarkable influence on their intercalation potentials for the case of CrHCF. The empirical studies of five different PBA electrodes hinted that the size of the transition metal is important to tune the working potentials for this material.

In **Chapter 6.4**, $Na_xMn[Mn(CN)_6]$ thin films were introduced as an excellent anode material for aqueous Na-ion batteries. The extremely low working potential of the electrodeposited MnHCMn was recorded to be -0.93 V vs SSC, which is the lowest value for aqueous Na-ion batteries ever reported to the best of my knowledge. A great emphasis should be placed on the fact that hydrogen evolution reaction was not observed at MnHCMn thin films even at -1.15 V vs SSC in 0.25 M of aqueous Na-electrolytes. The obtained specific capacity of the MnHCMn thin films exhibited ~85 mAh g^{-1} (C-rate: 60 C) with exceptionally high capacity retention over 3000 cycles in 10 M $NaClO_4$ aqueous electrolytes. The "loop-shaped" impedance spectra can also be seen in this system, which indicates that the three-stage mechanism is also valid for the MnHCMn system. Interestingly, the participation of anions was additionally found in the course of the deposition process in which the deposition rate and resulting morphology of the MnHCMn thin films significantly changed depending on the anions present in the deposition solutions. The reason for the changes might be attributed to specific adsorption and desorption of anions in Na-intercalation and -deintercalation, which simultaneously accompanied by the deposition processes. Surprisingly, Cs-ions nor Li-ions were not intercalated into MnHCMn thin films within the given potential ranges. What is worse, the hydrogen evolution reaction was seen in the case of a 0.25 M $CsNO_3$ electrolyte. This result explicitly suggests that the electrolyte composition substantially affects not only the intercalation properties but also catalytic reactions at the MnHCMn electrode surface.

To sum up, this dissertation presented three different cathode and one anode compounds based on Prussian blue analogs and discussed on their Na-intercalation mechanisms and battery performances in different electrolytes. The excellent features of the demonstrated PBA electrodes are the abundance of raw materials, high operating potential both positive and negative electrodes and long cycle life. In the course of the work, it was found that the intercalation mechanism of alkali metal cations has more than three steps, which involve anion adsorption and desorption to compensate for the excess charge at the electrode surface. The discussed “three-stage mechanism” is found to be valid not only for the particular systems presented in this dissertation but it can also be applied to different aqueous and non-aqueous battery systems. Another impact of this work is put on the discovery of the importance of electrolyte compositions on battery performances.

8. Appendix

A. Three-Stage Mechanism

The theoretical background of the “three-stage mechanism” for Na-intercalation and -deintercalation at Prussian blue analog electrodes is mathematically explained here. This part is based on Chapter 5 of *Electrochemical Impedance Spectroscopy and its Applications* by Andrzej Lasia.[171]

Faradaic Reaction Involving Two Adsorbed Species with Subsequent Potential-Independent Desorption

Supposing an electrochemical process involves two adsorbed species and the exchange of two electrons without diffusion of redox species. Then, their chemical reaction can be described as below[166]:

$$A_{sol} + e \underset{\overleftarrow{k}_{-1}}{\overset{\overrightarrow{k}_1}{\rightleftarrows}} B_{ads} \qquad \textbf{Eq}.\ \text{A1.1}$$

$$B_{ads} + e \underset{\overleftarrow{k}_{-2}}{\overset{\overrightarrow{k}_2}{\rightleftarrows}} C_{ads} \qquad \textbf{Eq}.\ \text{A1.2}$$

$$C_{ads} \underset{k_{-3}}{\overset{k_3}{\rightleftarrows}} D_{sol} \qquad \textbf{Eq}.\ \text{A1.3}$$

Eq. A1.1 and **Eq. A1.2** are the electrochemical reactions that involve charge transfer between reactants and products. **Eq. A1.3** is a pure chemical desorption reaction which is not necessarily potential-dependent. A_{sol} and D_{sol} are the species present in the electrolyte, and B_{ads} and C_{ads} are the adsorbed species at the surface of the electrode. $\overrightarrow{k_i}$ and $\overleftarrow{k}_{-i}$ (i = 1, 2) are the potential-dependent forward and backward rate constants, respectively. k_3 and k_{-3} are the forward and backward rate constants, respectively. Here, it should be noted that the arrow signs over the rate constants indicate the potential dependent reactions where electron-transfer is involved. These three reactions can be formulated into kinetic equations:

$$v_1 = \overrightarrow{k}_1 (1 - \theta_B - \theta_C) - \overleftarrow{k}_{-1}\theta_B \qquad \textbf{Eq}.\ \text{A1.4}$$

$$v_2 = \overrightarrow{k}_2\, \theta_B - \overleftarrow{k}_{-2}\theta_C \qquad \textbf{Eq}.\ \text{A1.5}$$

$$v_3 = k_3\theta_C - k_{-3}(1 - \theta_B - \theta_C) \qquad \textbf{Eq}.\ \text{A1.6}$$

where v_i is the reaction rate of the process *i* with units of flux, mol cm^{-2} s^{-1} and θ_B and θ_C are the coverage fraction of the active sites by the adsorbed species B and C, respectively. **Eq. A1.4** - **A1.6** can be further expanded with the assumption of the Langmuir adsorption isotherm as below:

$$\begin{aligned} v_1 = k_1^0 \Gamma_\infty C_A(0)(1 - \theta_B - \theta_C) \exp[-\beta_1 f(E - E_1^0)] \\ - k_{-1}^0 \Gamma_\infty \theta_B \exp[(1 - \beta_1) f(E - E_1^0)] \end{aligned}$$

Eq. A1.7

$$v_2 = k_2^0 \Gamma_\infty \theta_B \exp[-\beta_2 f(E - E_2^0)] - k_{-2}^0 \Gamma_\infty \theta_C \exp[(1 - \beta_2) f(E - E_2^0)] \qquad \textbf{Eq}.\ \text{A1.8}$$

$$v_3 = k_3^0 \Gamma_\infty \theta_C - k_{-3}^0 \Gamma_\infty C_D(0)(1 - \theta_B - \theta_C) \qquad \textbf{Eq}.\ \text{A1.9}$$

where k_i^0 is the standard heterogeneous rate constant at the standard potential (k_1^0 and k_{-3}^0 are in the unit of cm^3 s^{-1} mol^{-1}, and the other rate constants are in the unit of s^{-1}). $C_A(0)$ and $C_D(0)$ are the surface concentration of species A_{sol} and D_{sol}. Γ_∞ is the total surface concentration of the active sites in the unit of mol cm^{-2}. β_i is the charge transfer coefficient ($0 < \beta_i < 1$). $f = F/RT$, where *F*, *R*, and *T* are the Faraday constant, the gas constant, and the absolute temperature in Kelvin, respectively. E_i^0 is the standard potential of redox process *i*.

At the equilibrium potential E_{eq}, the reaction rates (v_1, v_2, and v_3) are zero, and the surface concentrations become equal to the bulk concentration, $C_A(0) = C_A^*$ and $C_D(0) = C_D^*$. Here, * denotes the equilibrium. The introduction of these parameters results in the following equations:

$$v_1^* = k_1^0 C_A^* \Gamma_\infty^* (1 - \theta_B^* - \theta_C^*) \exp\left[-\beta_1 f\left(E_{eq} - E_1^0\right)\right]$$
$$- k_{-1}^0 \Gamma_\infty^* \theta_B^* \exp\left[(1 - \beta_1) f\left(E_{eq} - E_1^0\right)\right] \quad \textbf{Eq}.\ \text{A1.10}$$

$$v_2^* = k_2^0 \Gamma_\infty^* \theta_B^* \exp\left[-\beta_2 f\left(E_{eq} - E_2^0\right)\right] - k_{-2}^0 \Gamma_\infty^* \theta_C^* \exp\left[(1 - \beta_2) f\left(E_{eq} - E_2^0\right)\right] \quad \textbf{Eq}.\ \text{A1.11}$$

$$v_3^* = k_3^0 \Gamma_\infty^* \theta_C^* - k_{-3}^0 C_D^* \Gamma_\infty^* (1 - \theta_B^* - \theta_C^*) \quad \textbf{Eq}.\ \text{A1.12}$$

By reformulating **Eq**. A1.10 and **Eq**. A1.11, the deviation of the equilibrium potentials (E_{eq}) from the standard redox potentials (E_1^0 and E_2^0) can be written as below:

$$E_{eq} - E_1^0 = \frac{1}{f} \ln \frac{k_1^0}{k_{-1}^0} C_A^* \frac{1-\theta_B^*-\theta_C^*}{\theta_B^*} \quad \textbf{Eq}.\ \text{A1.13}$$

$$E_{eq} - E_2^0 = \frac{1}{f} \ln \frac{k_2^0}{k_{-2}^0} \frac{\theta_B^*}{\theta_C^*} \quad \textbf{Eq}.\ \text{A1.14}$$

By introducing the overpotential, $\eta = E - E_{eq}$, the deviation between the applied potential and the standard redox potential can be expressed as $E - E_i^0 = E - E_{eq} + E_{eq} - E_i^0 = \eta + E_{eq} - E_i^0$ (i = 1 or 2). With some lengthy calculations, the forward and backward rate constants ($\vec{k}_1$, $\overleftarrow{k}_{-1}$, $\vec{k}_2$, $\overleftarrow{k}_{-2}$, k_3 and k_{-3}) can be expressed with the heterogenous rate constants as:

$$\vec{k}_1 = k_1 \exp(-\beta_1 f \eta) \quad \textbf{Eq}.\ \text{A1.15} \qquad \overleftarrow{k}_{-1} = k_{-1} \exp[(1 - \beta_1) f \eta] \quad \textbf{Eq}.\ \text{A1.16}$$

$$\vec{k}_2 = k_2 \exp(-\beta_2 f \eta) \quad \textbf{Eq}.\ \text{A1.17} \qquad \overleftarrow{k}_{-2} = k_{-2} \exp[(1 - \beta_2) f \eta] \quad \textbf{Eq}.\ \text{A1.18}$$

$$k_3 = k_3^0 \, \Gamma_\infty \quad \textbf{Eq}.\ \text{A1.19} \qquad k_{-3} = k_{-3}^0 \Gamma_\infty C_D(0) \quad \textbf{Eq}.\ \text{A1.20}$$

where $k_1 = {k_1^0}^{(1-\beta_1)} {k_{-1}^0}^{\beta_1} {C_A^*}^{-\beta_1} C_A(0) \Gamma_\infty (\frac{1-\theta_B^*-\theta_C^*}{\theta_B^*})^{-\beta_1}$ **Eq**. A1.21

$$k_{-1} = {k_1^0}^{(1-\beta_1)} {k_{-1}^0}^{\beta_1} C_A^{*(1-\beta_1)} \Gamma_\infty (\frac{1-\theta_B^*-\theta_C^*}{\theta_B^*})^{1-\beta_1} \quad \textbf{Eq}.\ \text{A1.22}$$

$$k_2 = {k_2^0}^{(1-\beta_2)} {k_{-2}^0}^{\beta_2} \Gamma_\infty (\frac{\theta_B^*}{\theta_C^*})^{-\beta_2} \quad \textbf{Eq}.\ \text{A1.23}$$

$$k_{-2} = {k_2^0}^{(1-\beta_1)} {k_{-2}^0}^{\beta_2} \Gamma_\infty (\frac{\theta_B^*}{\theta_C^*})^{1-\beta_2} \quad \textbf{Eq}.\ \text{A1.24}$$

Since the reaction rates v_1 and v_2 are involved with the exchange of electrons between the electrode and the redox species, the equation of the total current flow can be expressed by summing up the reaction rates v_1 and v_2: $i = -F(v_1 + v_2) = -Fr_0$, where $r_0 = v_1 + v_2$. Therefore, the current is also a function of η, θ_B and θ_C. The phasor of the current (Δi) can be described with a partial equation as below:

$$\Delta i = \left(\frac{\partial i}{\partial \eta}\right)_{\theta_B,\theta_C} \Delta \eta + \left(\frac{\partial i}{\partial \theta_B}\right)_{\eta,\theta_C} \Delta \theta_B + \left(\frac{\partial i}{\partial \theta_C}\right)_{\eta,\theta_B} \Delta \theta_C \qquad \textbf{Eq}.\ \text{A1.25}$$

by substituting i with $-Fr_0$, **Eq**. A1.25 is rewritten as:

$$\Delta i = -F[\left(\frac{\partial r_0}{\partial \eta}\right)_{\theta_B,\theta_C} \Delta \eta + \left(\frac{\partial r_0}{\partial \theta_B}\right)_{\eta,\theta_C} \Delta \theta_B + \left(\frac{\partial r_0}{\partial \theta_C}\right)_{\eta,\theta_B} \Delta \theta_C] \qquad \textbf{Eq}.\ \text{A1.26}$$

The changes in the surface coverage of species B and C (Γ_B and Γ_C) can be described as:

$$\frac{d\Gamma_B}{dt} = \Gamma_\infty \frac{d\theta_B}{dt} = \frac{\sigma_1}{F}\frac{d\theta_B}{dt} = v_1 - v_2 = \Delta r_1 \qquad \textbf{Eq}.\ \text{A1.27}$$

$$\frac{d\Gamma_C}{dt} = \Gamma_\infty \frac{d\theta_C}{dt} = \frac{\sigma_2}{F}\frac{d\theta_C}{dt} = v_2 - v_3 = \Delta r_2 \qquad \textbf{Eq}.\ \text{A1.28}$$

here $\Gamma_B = \Gamma_\infty \theta_B$, $\Gamma_C = \Gamma_\infty \theta_C$, and $\sigma_i = F\Gamma_\infty$ (i = 1 or 2). σ_1 and σ_2 are the total charge to fully cover the electrode surface with species B and C, respectively. The changes in the surface coverage of the species B and C are also the function of η, θ_B and θ_C. Similarly to **Eq. A1.25**, Δr_1 and Δr_2 can be described as:

$$\Delta r_1 = \frac{\sigma_1}{F}\frac{d\theta_B}{dt} = \left(\frac{\partial r_1}{\partial \eta}\right)_{\theta_B,\theta_C} \Delta \eta + \left(\frac{\partial r_1}{\partial \theta_B}\right)_{\eta,\theta_C} \Delta \theta_B + \left(\frac{\partial r_1}{\partial \theta_C}\right)_{\eta,\theta_B} \Delta \theta_C \qquad \textbf{Eq}.\ \text{A1.29}$$

$$\Delta r_2 = \frac{\sigma_2}{F}\frac{d\theta_C}{dt} = \left(\frac{\partial r_2}{\partial \eta}\right)_{\theta_B,\theta_C} \Delta \eta + \left(\frac{\partial r_2}{\partial \theta_B}\right)_{\eta,\theta_C} \Delta \theta_B + \left(\frac{\partial r_2}{\partial \theta_C}\right)_{\eta,\theta_B} \Delta \theta_C \qquad \textbf{Eq}.\ \text{A1.30}$$

By introducing of the phasors ($\Delta i = \tilde{\imath} e^{i\omega t}$, $\Delta \eta = \tilde{\eta} e^{i\omega t}$, $\Delta \theta = \tilde{\theta} e^{i\omega t}$, and, $\Delta r = \tilde{r} e^{i\omega t}$) and by dividing both sides by the time term ($e^{i\omega t}$), the following equations can be obtained:

$$\tilde{\imath} = -F[\left(\frac{\partial r_0}{\partial \eta}\right)_{\theta_B,\theta_C} \tilde{\eta} + \left(\frac{\partial r_0}{\partial \theta_B}\right)_{\eta,\theta_C} \widetilde{\theta_B} + \left(\frac{\partial r_0}{\partial \theta_C}\right)_{\eta,\theta_B} \widetilde{\theta_C}] \qquad \textbf{Eq}.\ \text{A1.31}$$

$$\widetilde{r_1} = j\omega \frac{\sigma_1}{F} \widetilde{\theta_B} = \left(\frac{\partial r_1}{\partial \eta}\right)_{\theta_B,\theta_C} \tilde{\eta} + \left(\frac{\partial r_1}{\partial \theta_B}\right)_{\eta,\theta_C} \widetilde{\theta_B} + \left(\frac{\partial r_1}{\partial \theta_C}\right)_{\eta,\theta_B} \widetilde{\theta_C} \qquad \textbf{Eq}.\ \text{A1.32}$$

$$\widetilde{r_2} = j\omega \frac{\sigma_2}{F} \widetilde{\theta_C} = \left(\frac{\partial r_2}{\partial \eta}\right)_{\theta_B,\theta_C} \tilde{\eta} + \left(\frac{\partial r_2}{\partial \theta_B}\right)_{\eta,\theta_C} \widetilde{\theta_B} + \left(\frac{\partial r_2}{\partial \theta_C}\right)_{\eta,\theta_B} \widetilde{\theta_C} \qquad \textbf{Eq}.\ \text{A1.33}$$

By dividing **Eq. A1.31 - A.133** by $\tilde{\eta}$, the following equations can be obtained:

$$\frac{\tilde{\imath}}{\tilde{\eta}} = -F[\left(\frac{\partial r_0}{\partial \eta}\right)_{\theta_B,\theta_C} + \left(\frac{\partial r_0}{\partial \theta_B}\right)_{\eta,\theta_C} \frac{\widetilde{\theta_B}}{\tilde{\eta}} + \left(\frac{\partial r_0}{\partial \theta_C}\right)_{\eta,\theta_B} \frac{\widetilde{\theta_C}}{\tilde{\eta}}] \qquad \textbf{Eq}.\ \text{A1.34}$$

$$j\omega \frac{\sigma_1}{F} \frac{\widetilde{\theta_B}}{\tilde{\eta}} = \left(\frac{\partial r_1}{\partial \eta}\right)_{\theta_B,\theta_C} + \left(\frac{\partial r_1}{\partial \theta_B}\right)_{\eta,\theta_C} \frac{\widetilde{\theta_B}}{\tilde{\eta}} + \left(\frac{\partial r_1}{\partial \theta_C}\right)_{\eta,\theta_B} \frac{\widetilde{\theta_C}}{\tilde{\eta}} \qquad \textbf{Eq}.\ \text{A1.35}$$

$$j\omega \frac{\sigma_2}{F} \frac{\widetilde{\theta_C}}{\tilde{\eta}} = \left(\frac{\partial r_2}{\partial \eta}\right)_{\theta_B,\theta_C} + \left(\frac{\partial r_2}{\partial \theta_B}\right)_{\eta,\theta_C} \frac{\widetilde{\theta_B}}{\tilde{\eta}} + \left(\frac{\partial r_2}{\partial \theta_C}\right)_{\eta,\theta_B} \frac{\widetilde{\theta_C}}{\tilde{\eta}} \qquad \textbf{Eq}.\ \text{A1.36}$$

By solving the above equations, the Faradaic admittance $\tilde{Y} = \frac{\tilde{\imath}}{\tilde{\eta}}$ can be described as:

$$\tilde{Y} = \frac{\tilde{\imath}}{\tilde{\eta}} = -F\left(\frac{\partial r_0}{\partial \eta}\right)_{\theta_B,\theta_C} + \left\{-\frac{F^3}{\sigma_1\sigma_2}\left[\left(\frac{\partial r_0}{\partial \theta_B}\right)\left(\frac{\partial r_1}{\partial \theta_C}\right)\left(\frac{\partial r_2}{\partial \eta}\right) - \left(\frac{\partial r_0}{\partial \theta_B}\right)\left(\frac{\partial r_1}{\partial \eta}\right)\left(\frac{\partial r_2}{\partial \theta_C}\right) + \left(\frac{\partial r_0}{\partial \theta_B}\right)\left(\frac{\partial r_1}{\partial \eta}\right)\left(\frac{\partial r_2}{\partial \theta_B}\right) - \right.\right.$$
$$\left.\left(\frac{\partial r_0}{\partial \theta_B}\right)\left(\frac{\partial r_1}{\partial \theta_B}\right)\left(\frac{\partial r_2}{\partial \eta}\right)\right] + j\omega F^2\left[-\frac{1}{\sigma_1}\left(\frac{\partial r_0}{\partial \theta_B}\right)\left(\frac{\partial r_1}{\partial \eta}\right) - \frac{1}{\sigma_2}\left(\frac{\partial r_0}{\partial \theta_C}\right)\left(\frac{\partial r_2}{\partial \eta}\right)\right]\Big\}\Big\{j\omega\Big[-F\Big\{\frac{1}{\sigma_1}\left(\frac{\partial r_1}{\partial \theta_B}\right) +$$
$$\frac{1}{\sigma_2}\left(\frac{\partial r_2}{\partial \theta_C}\right)\Big\}\Big] + \omega^2 + \frac{F^2}{\sigma_1\sigma_2}\left[\left(\frac{\partial r_1}{\partial \theta_B}\right)\left(\frac{\partial r_2}{\partial \theta_C}\right) - \left(\frac{\partial r_1}{\partial \theta_C}\right)\left(\frac{\partial r_2}{\partial \theta_B}\right)\right]\Big\}^{-1} \qquad \textbf{Eq}.\ \text{A1.37}$$

As the impedance is measured at different frequencies, it is convenient to organize the equation with respect to the frequency (ω) and to consider the other components in constants. Then, **Eq. A1.37** can be written as:

$$\tilde{Y} = \frac{\tilde{\imath}}{\tilde{\eta}} = A + \frac{B + j\omega C}{j\omega D - \omega^2 + E} \qquad \textbf{Eq}.\ \text{A.1.38}$$

where

$A = -F\left(\frac{\partial r_0}{\partial \eta}\right)_{\theta_B,\theta_C}$

$B = -\frac{F^3}{\sigma_1\sigma_2}\left[\left(\frac{\partial r_0}{\partial \theta_B}\right)\left(\frac{\partial r_1}{\partial \theta_C}\right)\left(\frac{\partial r_2}{\partial \eta}\right) - \left(\frac{\partial r_0}{\partial \theta_B}\right)\left(\frac{\partial r_1}{\partial \eta}\right)\left(\frac{\partial r_2}{\partial \theta_C}\right) + \left(\frac{\partial r_0}{\partial \theta_B}\right)\left(\frac{\partial r_1}{\partial \eta}\right)\left(\frac{\partial r_2}{\partial \theta_B}\right) - \left(\frac{\partial r_0}{\partial \theta_B}\right)\left(\frac{\partial r_1}{\partial \theta_B}\right)\left(\frac{\partial r_2}{\partial \eta}\right)\right]$

$C = -F^2\left[-\frac{1}{\sigma_1}\left(\frac{\partial r_0}{\partial \theta_B}\right)\left(\frac{\partial r_1}{\partial \eta}\right) - \frac{1}{\sigma_2}\left(\frac{\partial r_0}{\partial \theta_C}\right)\left(\frac{\partial r_2}{\partial \eta}\right)\right]$

$$D = -F\left\{\frac{1}{\sigma_1}\left(\frac{\partial r_1}{\partial \theta_B}\right) + \frac{1}{\sigma_2}\left(\frac{\partial r_2}{\partial \theta_C}\right)\right\}$$

$$E = \frac{F^2}{\sigma_1\sigma_2}\left[\left(\frac{\partial r_1}{\partial \theta_B}\right)\left(\frac{\partial r_2}{\partial \theta_C}\right) - \left(\frac{\partial r_1}{\partial \theta_C}\right)\left(\frac{\partial r_2}{\partial \theta_B}\right)\right]$$

Here, parameters A, C, are always positive, but B and D can be either positive or negative. As the Faradaic impedance ($\tilde{Z}$) is the reverse of the admittance, it can be written as:

$$\tilde{Z} = \frac{1}{\tilde{Y}} = \left[A + \frac{B+j\omega C}{j\omega D-\omega^2+E}\right]^{-1} = \frac{1}{A} - \frac{B+j\omega C}{A^2[\omega^2+j\omega\left(D+\frac{C}{A}\right)-\left(E+\frac{B}{A}\right)]} \qquad \textbf{Eq}.\ \mathrm{A1.39}$$

$\frac{1}{A}$ corresponds to the charge transfer resistance (R_{ct}), and the polarization resistance can be obtained at zero frequency ($\omega = 0$) as $R_{pol} = R_{ct} + \frac{B}{A^2(E+B/A)}$. **Eq A1.39** can be reformulated as:

$$\tilde{Z} = R_{ct} + \frac{1}{j\omega C_{a,1} + \frac{1}{R_{a,1} + \frac{1}{j\omega C_{a,2} + \frac{1}{R_{a,2}}}}} \qquad \textbf{Eq}.\ \mathrm{A1.40}$$

where $C_{a,1} = -\frac{A^2}{C}$, $R_{a,1} = \frac{C}{A^2E+AB}$, $C_{a,2} = \frac{(AB-ADC-C^2)^2}{C(C^2E+B^2-BCD)}$, and $R_{a,2} = -\frac{A(C^2E+B^2-BCD)}{ACE+BC}$.

Eq. A1.39 can be represented as, for instance, a ladder-type electric circuit as illustrated in **Figure A1**.

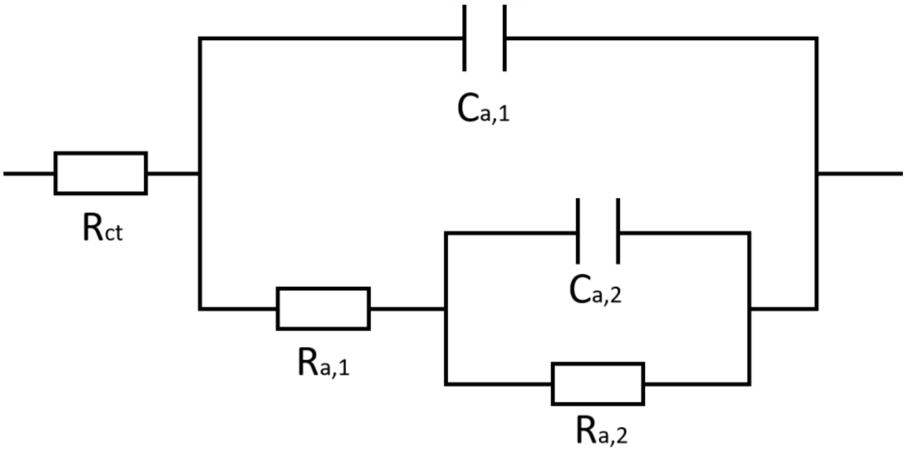

Figure A1. Equivalent electric circuit describing a Faradaic reaction involving two reversibly adsorbed species with their subsequent desorption.

Notably, the parameters $C_{a,1}$, $R_{a,1}$, $C_{a,2}$ and $R_{a,2}$ can be either positive or negative in contrast to real electric circuit elements that have positive values. The reason is that they are not present in the real system, but they theoretically deducted from the mathematical derivation (see above). By taking the double layer response into account, the whole EEC can be drawn as in **Figure A2**.

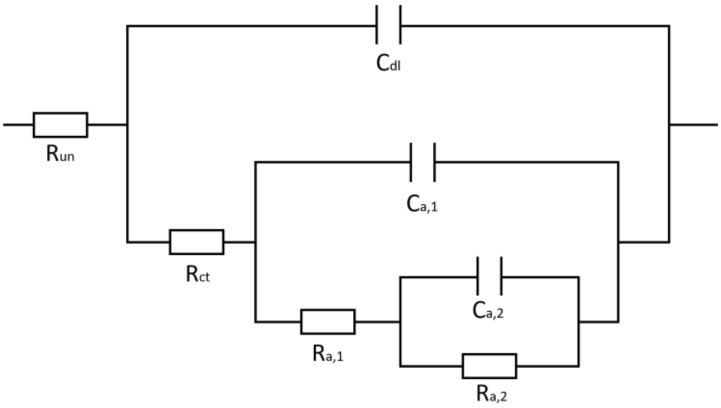

Figure A2. Equivalent electric circuit describing the double layer response and the response of the Faradaic reaction involving two reversibly adsorbed species. R_{un} and C_{dl} represent uncompensated resistance and the double layer capacitance, respectively.

This model was used to perform the fitting of the acquired impedance spectra from Na-intercalation and -deintercalation measurements.

B. EQCM curves of NiHCF in 0.25 M Na-Electrolytes (Na_2SO_4, NaCl, $NaNO_3$, $NaClO_4$, and NaOAc)

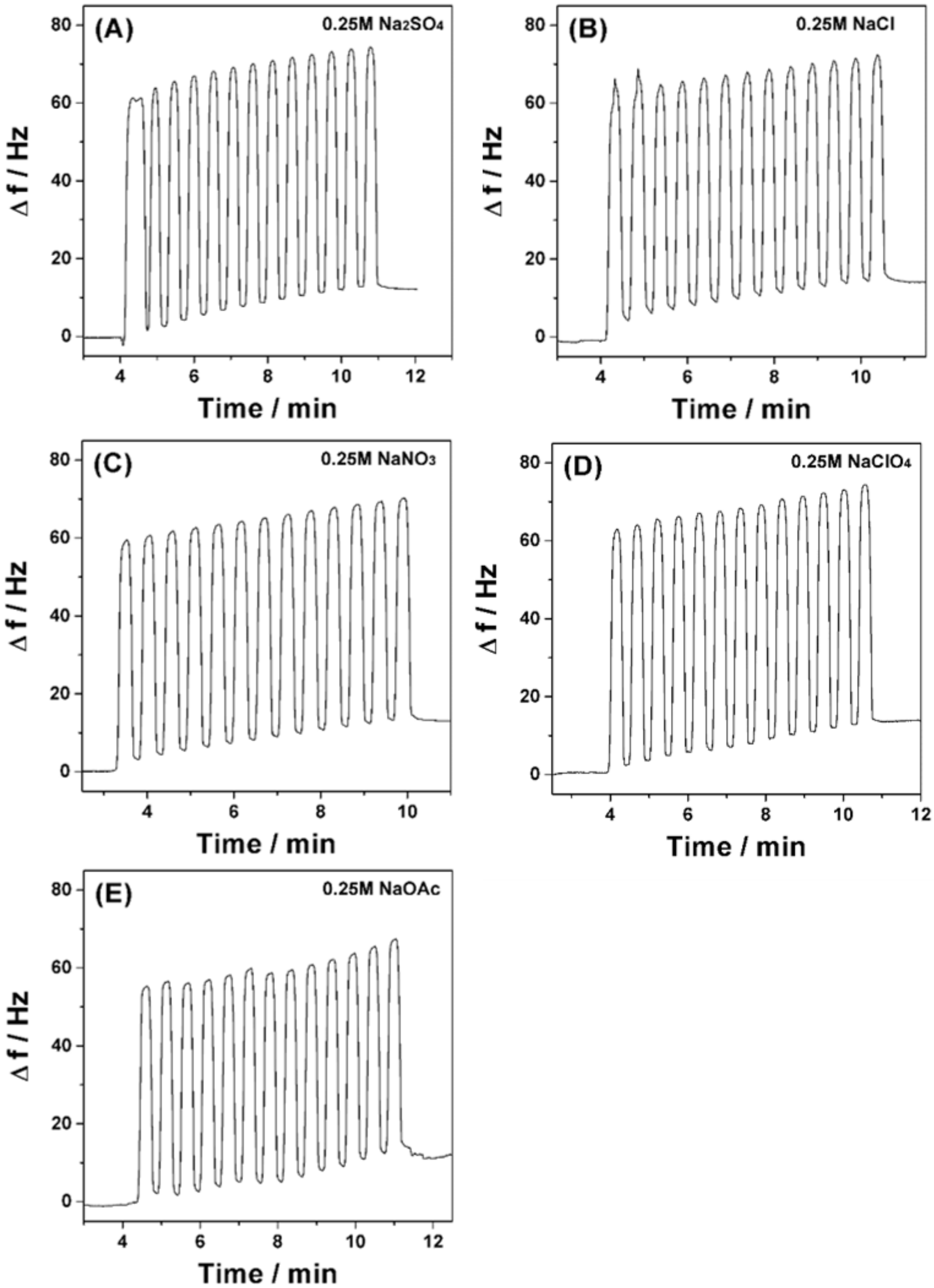

Figure A3. EQCM-curves of $Na_2Ni[Fe(CN)_6]$ electrodes in different electrolytes: (A) 0.25 M Na_2SO_4 (B) 0.25 M NaCl (C) 0.25 M $NaNO_3$ (D) 0.25 M $NaClO_4$, and (E) 0.25 M NaOAc.

C. EIS of NiHCF in 0.25 M K_2SO_4 and 0.25 M KNO_3

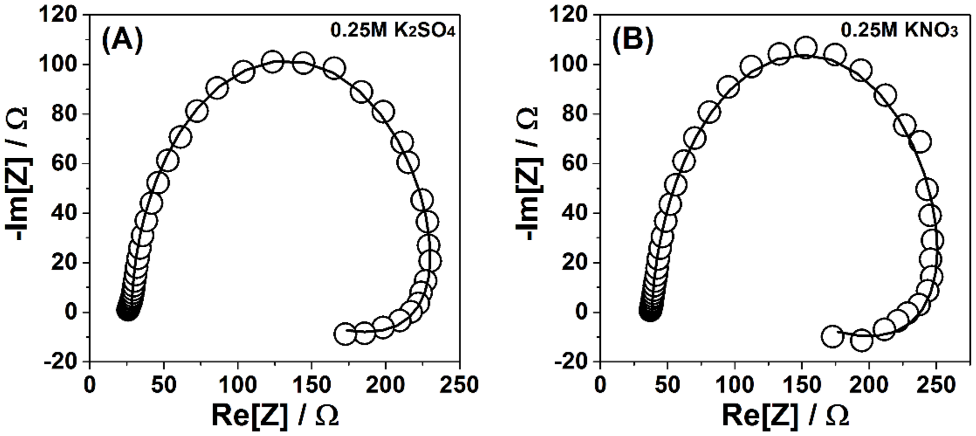

Figure A4. Impedance spectra (open symbols) and the corresponding fitting results (solid lines) of NiHCF measured (A) at 0.6 V in 0.25 M KNO_3 and at (B) at 0.5 V in 0.25 M K_2SO_4.

D. EQCM Curves of NiHCF in 0.25 M AMNO$_3$, (AM = Li, Na, K, Rb, or Cs)

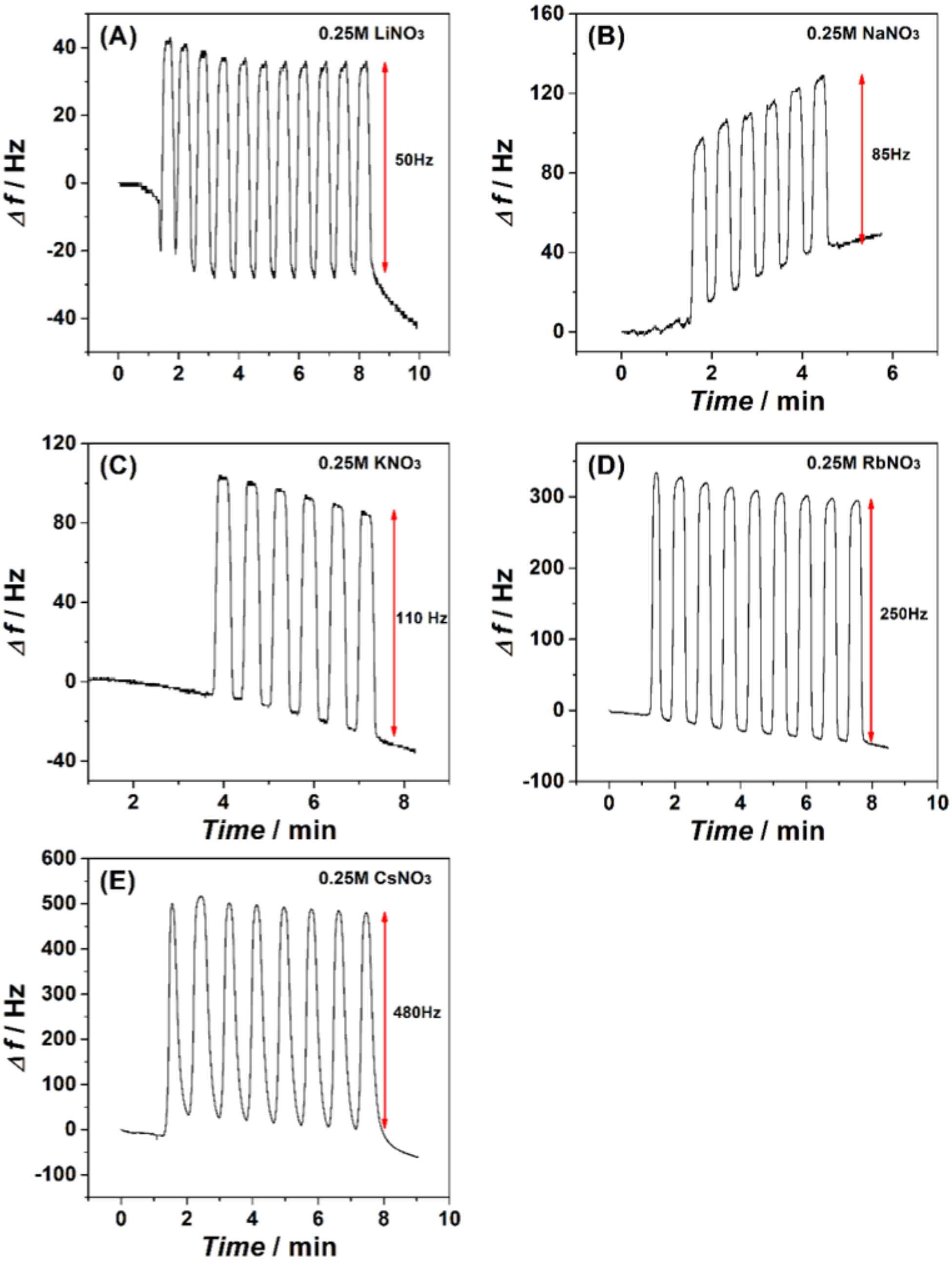

Figure A5. EQCM curves of $Na_2Ni[Fe(CN)_6]$ films characterizing Na intercalation and -deintercalation in different electrolytes: (A) 0.25 M $LiNO_3$ (B) 0.25 M $NaNO_3$ (C) 0.25 M KNO_3 (D) 0.25 M $RbNO_3$, and (E) 0.25 M $CsNO_3$.

E. CV of Gold Electrode in Deposition Solution

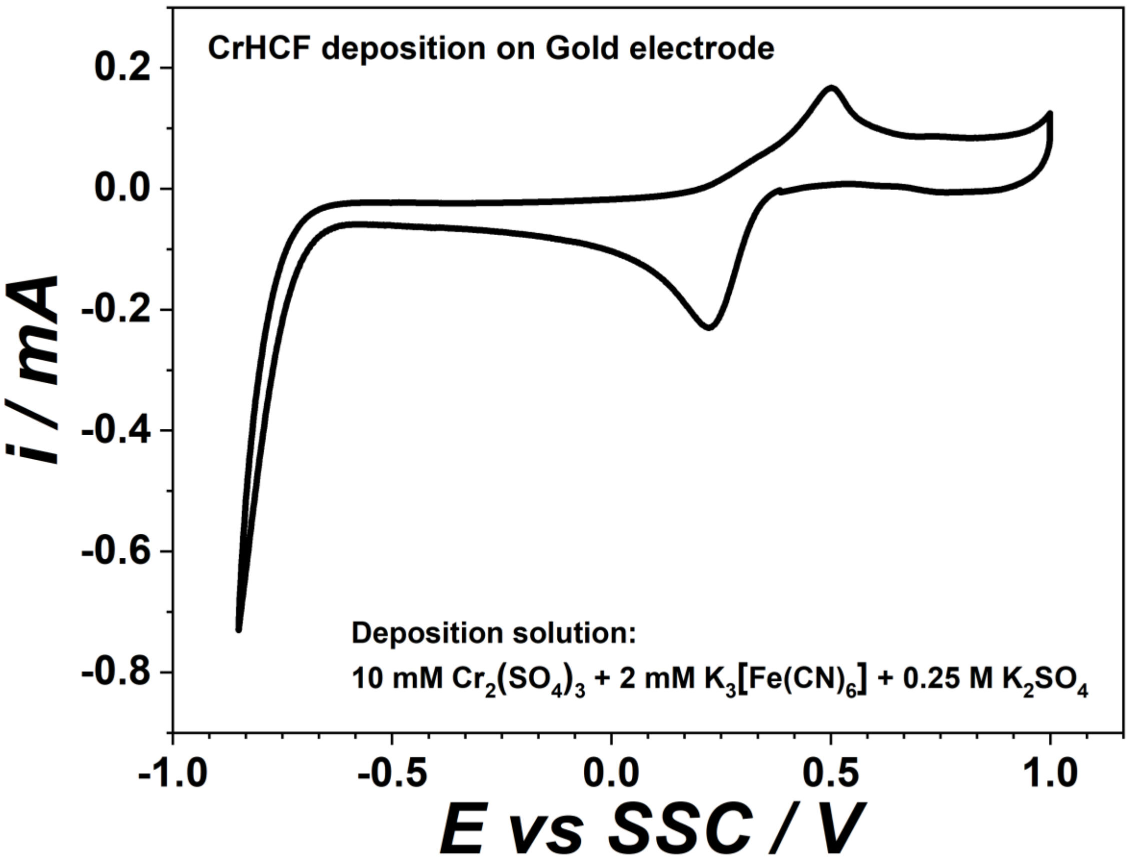

Figure A6. A typical CV of a gold electrode in an aqueous solution containing 10 mM $Cr_2(SO_4)_3$ + 2 mM $K_3[Fe(CN)_6]$ + 0.25 M K_2SO_4 in the potential range from – 0.9 V to 1.0 V vs Ag/AgCl.

F. Synthesis of Potassium Hexacyanomanganate(III) Trihydrate, $K_3[Mn(CN)_6]\cdot 3H_2O$

Potassium hexacyanomanganate(III) was synthesized using the methods of Grube, Brause, and Meyer with a slight modification.[320] An aqueous solution of $MnSO_4$ (150 g, 1 mol, 1.0 eq., 360 mL H_2O) was slowly added to a stirred solution of $NaHCO_3$ (215 g, 2.55 mol, 2.6 eq.) in 1 L water. The resulting precipitate of $MnCO_3$ was stirred for another 15 min, retrieved by suction filtration and thoroughly washed with water until the filtrate was free of excess of sulfate and carbonate.

The moist $MnCO_3$ was divided into three portions of 50g, which were subsequently treated equally. The $MnCO_3$ was added to a vigorously stirred aqueous solution of KCN (135 g, 2.07 mol, 6.3 eq., 270 mL H_2O). During the exothermic reaction, the temperature of the suspension was controlled not to exceed 50°C. After the color had turned from pale yellow to dark violet, it was cooled externally to 10°C, and diluted hydrogen peroxide solution (3%, 50 mL) was added. After the suspension had turned dark brown formed manganese oxides were removed by suction filtration.

The resulting dark red solution from each portion was stored at 4-7°C for about a week. Precipitated $K_3Mn(CN)_6$ was recovered by suction filtration, thoroughly washed with ethanol and dried in a vacuum desiccator over solid KOH. The retrieved portions of the product were combined to yield 157 g (0.411 mol, 0.41 eq., 41 %) $K_3Mn(CN)_6\cdot 3H_2O$ as micro-crystalline, dark red-brownish powder. Elemental analysis of the synthesized $K_3Mn(CN)_6\cdot 3H_2O$ revealed the composition of C 18.44%, H 0.18%, N 21.40% which exhibits a good agreement with the theoretical values (C 18.84 %, N 21.98 %, H 1.58 %).

This page is reproduced from the reference [280] with permission from the American Chemical Society.

G. EIS Spectra of MnHCMn in 10 M NaClO$_4$

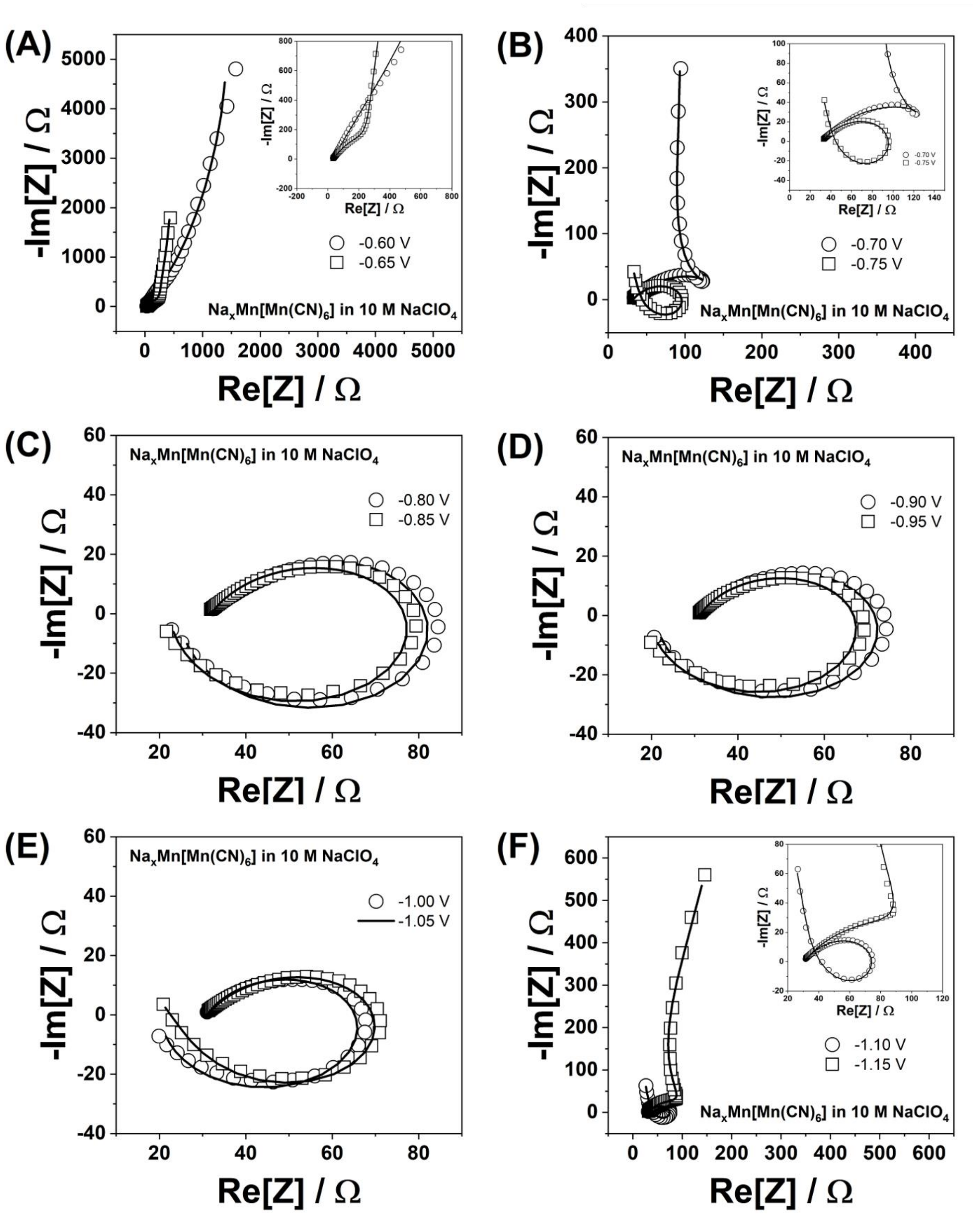

Figure A7. (A-F) EIS spectra of MnHCMn measured at different potentials in 10 M NaClO$_4$ electrolytes. The open symbols are the obtained experimental data, and the solid lines are fitting results.

9. Related Publications

Energy &
Environmental
Science

ROYAL SOCIETY
OF CHEMISTRY

PAPER

View Article Online
View Journal | View Issue

Cite this: *Energy Environ. Sci.*, 2016, 9, 955

How simple are the models of Na intercalation in aqueous media?†

Jeongsik Yun,[a] Jonas Pfisterer[a] and Aliaksandr S. Bandarenka*[ab]

Intercalation is among interesting phenomena changing everyday life with a remarkable speed. Numerous generations of modern batteries use it and markedly contribute to the portfolio of energy materials for future sustainable energy provision. Na-ion batteries operating in aqueous media, being presumably the "number two" compared to other alternatives for portable and automotive applications, are probably among potential leaders in the case of future larger-scale energy storage schemes, specifically because of safety and sustainability issues. However, there is a certain lack of detailed understanding of such systems. In this work, using model electrodes we further emphasise that it is not only the electrode materials themselves that determine the performance of intercalation electrodes. Surprisingly, comparatively slight changes in the electrolyte composition and solvation effects can very radically control intercalation of alkali metal cations. Therefore, it would be stimulating to adjust existing strategies in designing future aqueous battery systems. Several examples are given using one of the state-of-the-art cathode materials, $Na_2Ni[Fe(CN)_6]$, with model electrodes prepared as quasi-uniform thin films.

Received 18th October 2015,
Accepted 16th December 2015

DOI: 10.1039/c5ee03197d

www.rsc.org/ees

Broader context

Na-ion batteries operating in aqueous media are among the most promising candidates to contribute to the solution of the so-called generation *vs.* consumption problem in future sustainable energy provision schemes, perhaps even at the "TW-level". However, in order to improve existing electrode materials in these devices, deeper fundamental understanding of processes governing their performance is necessary. In this work, it is shown that the interfacial transfer of sodium between one of the best cathode materials and aqueous electrolytes likely involves at least three stages. These stages are significantly influenced by the electrolyte properties and composition. The findings of this work can be used to design ever better Na-ion aqueous batteries, taking into account that the specific capacity of the optimised cathode systems in this work is just 5% lower compared to the theoretical one at a C-rate as high as 180 C. Additionally, the role of solvation effects is emphasized.

Introduction

Solar and wind energy systems already significantly contribute to energy provision schemes nowadays.[1–4] However, more effective solutions of the so-called "generation *versus* consumption" problem are required to facilitate their further development. Rechargeable batteries are a part of the answer to this challenge as they are, in general, very convenient means for energy storage thanks to their relative affordability, flexibility, high energy conversion efficiency and simple maintenance.[5,6]

Intercalation materials for lithium ion batteries remain probably among the most attractive ones for portable devices and automotive applications.[7–9] Nevertheless, for larger-scale stationary energy storage systems, several key issues should be additionally considered. For instance, one of them is related to sustainability factors.[10] It has been roughly estimated that in order to address the so-called "TW-challenge" using just Li-ion batteries, ~160 years of current lithium production would be necessary.[11] While there is a certain capability to increase the rate of production of this metal substantially, it is nowadays clear that its fast accumulation for various stationary applications might be problematic. A second issue is associated with the current use of flammable organic electrolytes in Li-ion batteries. Safety problems upon scaling up are often of non-trivial complexity, increasing the maintenance costs and the total system price in this case.[12–16]

A viable alternative for stationary large-scale storage applications is to use Na-ion batteries, where electrode materials operate in aqueous media.[17–24] These types of devices have attracted great attention with an increasing amount of publications,

---

[a] *Physik-Department ECS, Technische Universität München, James-Franck-Straße 1, 85748 Garching, Germany. E-mail: bandarenka@ph.tum.de; Tel: +49(0) 89289 12531*

[b] *Nanosystems Initiative Munich (NIM), Schellingstraße 4, 80799 Munich, Germany*

† Electronic supplementary information (ESI) available: Experimental details, additional experimental data and data analysis. See DOI: 10.1039/c5ee03197d

as thoroughly reviewed recently by Kim *et al.*[25] Accumulation of Na in amounts necessary to address the TW-challenge seems to be more than one order of magnitude faster compared with lithium.[11] Additionally, aqueous electrolytes would gradually minimise safety risks. However, further development and optimisation of functional electrode materials in this area require detailed understanding of processes which control Na intercalation and de-intercalation, including interfacial charge transfer. For this, model systems and electrodes as well as their comprehensive *in situ* characterisation are necessary.

In this work, using model electrodes consisting of electrochemically deposited thin films of one of the state-of-the-art cathode materials, namely $Na_2Ni[Fe(CN)_6]$ (a typical representative of so-called Prussian blue analogues),[26,27] we demonstrate that intercalation of Na and its reversibility in cathodic and anodic cycles are largely influenced by the nature of anions present in the electrolytes. On the other hand, the electrode potential required for intercalation is determined not only by the electrode material itself: it is directly proportional to the hydration (solvation) energy of cations. Implications for the development of new Na-ion battery systems are briefly discussed.

Experimental

$Na_2Ni[Fe(CN)_6]$ thin films were deposited onto AT-cut Au quartz crystal wafers (Stanford Research Systems) from a solution of 0.25 M Na_2SO_4 containing 0.5 mM $K_3Ni[Fe(CN)_6]$ and 0.5 mM $NiCl_2 \cdot 6H_2O$ by cycling the potential in the range from 0.05 V to 0.85 V at a scan rate of 50 mV s^{-1} for ~60 cycles, as shown in Fig. 1A and B. All chemicals and solvents utilised in this work were used without further treatments and are listed with full details in the ESI.† The experiments were performed in a typical glass cell exploiting a three-electrode setup using a Bio-Logic VSP-300 potentiostat and a QCM 200 (Stanford Research Systems) electrochemical quartz crystal microbalance (EQCM). Electrode potentials were referred to an Ag/AgCl (SSC) reference electrode. A Pt wire was used as a counter electrode.

Cyclic voltammetry, EQCM measurements and common battery tests were performed using different electrolytes including

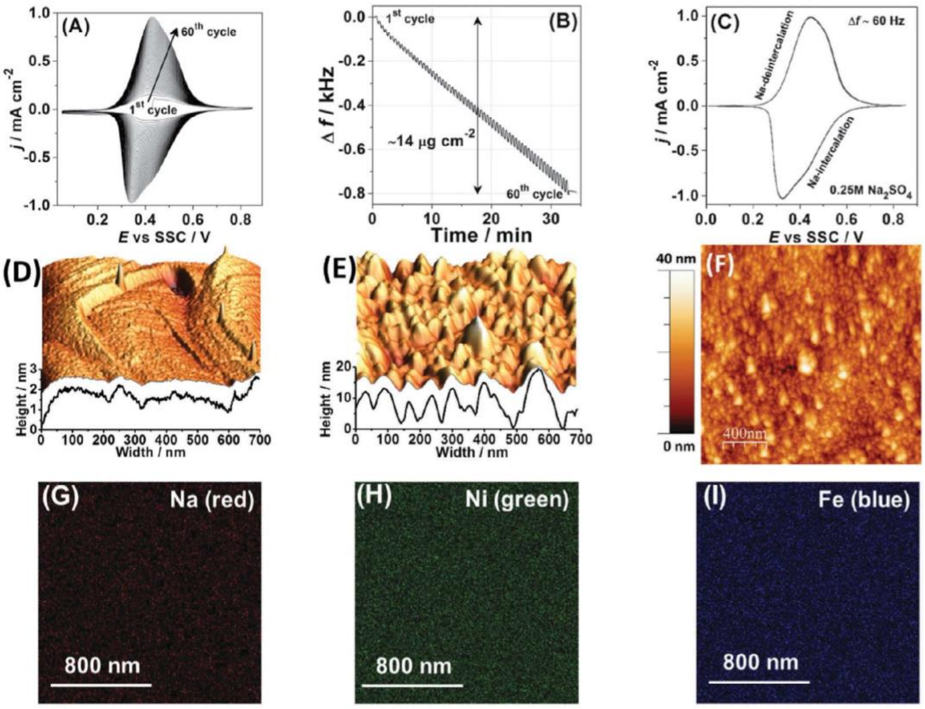

Fig. 1 Characterisation of the $Na_2Ni[Fe(CN)_6]$ thin films. (A) A typical cyclic voltammogram obtained during film deposition and (B) the corresponding electrode mass change, d*E*/d*t* = 50 mV s^{-1}. (C) A typical cyclic voltammogram characterising Na intercalation/de-intercalation in aqueous 0.25 M Na_2SO_4 electrolyte. (D–F) AFM images comparing a reference metal single-crystal surface (D) before and (E and F) after deposition of the $Na_2Ni[Fe(CN)_6]$ thin films. (G–I) Distribution of (G) Na, (H) Ni and (I) Fe in the resulting film (see ESI† for further details).

1 M Na_2SO_4, 0.25 M Na_2SO_4, 0.25 M NaCl, 0.25 M $NaNO_3$, 0.25 M $NaClO_4$ and 0.25 M NaOAc (sodium acetate). Moreover, in order to determine the onset potential for intercalation of various alkali metal cations, further experiments also involved different 0.25 M aqueous solutions of MNO_3 (where M = Li, Na, K, Rb, or Cs) at a scan rate of 50 mV s^{-1}. Electrochemical impedance spectroscopy (EIS) characterisation of the $Na_2Ni[Fe(CN)_6]$ thin films in 0.25 M Na_2SO_4 electrolytes was conducted using AC probing frequencies between 10 kHz and 0.5 Hz with a 10 mV amplitude of the probing signals in the potential range between 0.1 V and 0.8 V. The output of the fitting procedure was controlled by root-mean-square deviations and estimated individual parameter errors using home-made "EIS Data Analysis 1.0" software to ensure the validity of the model and correctness of the fitting, as described in detail elsewhere.[28,29]

The morphology and uniformity of the deposited thin films were investigated by SEM, electron microprobe and AFM. The atomic force microscope, utilised in this work, was a multimode EC-STM/AFM instrument (Veeco VI) with a Nanoscope IIID controller using the Nanoscope 5.31r1 software. All measurements were conducted in tapping mode (AFM tips, Bruker RTESP-300). SEM and electron microprobe images were obtained with a 20 kV beam using "Mira" from Tescan, Czech Republic, with an "INCA Energy 350" electron microprobe from Oxford Instruments Analytical, UK.

Further detailed information on experimental procedures, instrumentation and chemicals is available in the ESI.†

Results and discussion

The following electrochemical reaction was used to form thin films of $Na_2Ni[Fe(CN)_6]$ under potentiodynamic conditions, as additionally described in detail in the ESI:†

$$2Na^+_{(aq)} + Ni^{2+}_{(aq)} + [Fe^{III}(CN)_6]^{3-}_{(aq)} + 1e^- \rightarrow Na_2Ni[Fe^{II}(CN)_6]_{(solid)}$$

Fig. 1A shows a typical cyclic voltammogram (CV), which characterises the deposition process. It should be noted here that CVs in each subsequent figure, related to the same type of experiments (for instance CVs of Na intercalation in 0.25 M Na_2SO_4 solutions), are shown for different sets of experiments intentionally in order to demonstrate a good reproducibility; however, some possible stability issues are not taken into account, as they are outside of the scope of this work. Anodic and cathodic peaks in the CV shown in Fig. 1A are due to the changes in the oxidation state of Fe in the forming $Na_2Ni[Fe(CN)_6]$ film. It can be seen from Fig. 1A that the peak current increases with the potential cycles. The associated net electrode mass change measured using a quartz crystal microbalance is shown in Fig. 1B. A comparison of the resulting mass change at the end of the deposition process (~14 μg cm^{-2}) and the integrated charge from the CV (~4.6 mC cm^{-2}) gives, within ~5% accuracy, the expected molar weight for $Na_2Ni[Fe(CN)_6]$ (note that oscillations seen in Fig. 1B are due to intercalation and de-intercalation of sodium during the film formation). Fig. 1C shows a typical CV of the $Na_2Ni[Fe(CN)_6]$ film in a pure aqueous 0.25 M Na_2SO_4 electrolyte characterising Na intercalation/de-intercalation (corresponding net electrode mass change is ~1 μg cm^{-2}, which is close to that expected, considering that only 50% of sodium is exchanged in the complete cycle). The resulting electrodes are relatively smooth (see the morphology and topology in Fig. 1D–F and the ESI†), with uniform distribution of the key elements, Na, Ni and Fe, as revealed by the electron microprobe technique (Fig. 1G–I).

A generally accepted scheme of Na intercalation and de-intercalation in aqueous systems in the case of $Na_2Ni[Fe(CN)_6]$ cathode material is as follows:[25]

$$NaNi[Fe^{III}(CN)_6] + Na^+ + e^- \leftrightarrow Na_2Ni[Fe^{II}(CN)_6] \quad (1)$$

This scheme describes Na intercalation as a very simple one-stage process, in which neither solvent nor other electrolyte components play an essential role. In order to explore the validity of the mechanism presented above in more detail, we have performed an EIS study combined with nano-gravimetry. The latter was used to particularly ensure the required quasi-stationarity of the system during the measurements. Fig. 2A shows a typical electrode mass change during voltammetric cycling and subsequent potentiostatic modes (the latter is referred to as being rather convenient for the further comparison situation when only ~50% of the intercalated sodium is exchanged, *i.e.* a "half-charged"/"half-discharged" state). As can be seen from Fig. 2A, after the electrode potential had been fixed, the electrode mass remained practically unchanged during the time required to obtain an impedance spectrum (~1 min). Additionally, Kramers–Kronig tests did not reveal significant problems with spectral quality.

Surprisingly, impedance spectra recorded at different electrode potentials at which Faradaic processes take place do not support the hypothesis about the simple one-stage mechanism of the interfacial process. Typical "loops" which can be seen in the spectra (Fig. 2C–F) suggest at least a three-stage mechanism involving two reversible "intermediate steps" with interfacial charge transfer, followed by a step which does not contribute to the net charge transfer through the interface (see ESI† for further details). The unique relation of the spectral shapes and the multi-stage mechanisms is well known and protocolled for various systems, as summarised in ref. 30. Furthermore, a relatively simple physical model which reflects the above-mentioned three-stage mechanism (Fig. 2B) fits well all the spectra for all the measured potentials, additionally verifying that the observed spectral shapes are not an experimental artifact due to, for example, contaminations, non-stationarity or non-linearity effects. Thus, a more complex model should be taken into account.

As a first approximation we propose the following three-stage mechanism capable of explaining the impedance data (for simplicity only de-intercalation is formally discussed, while all three steps are quasi-reversible):

(1) Electroactive step, *i.e.* oxidation of Fe^{II}, which proceeds comparatively fast due to the good electronic conductivity of the film (we use some arbitrary schematic designations in the equations below):

$$Na_2Ni[Fe^{II}(CN)_6] - e^- \leftrightarrow Na_2Ni[Fe^{III}(CN)_6]^+ \quad (2)$$

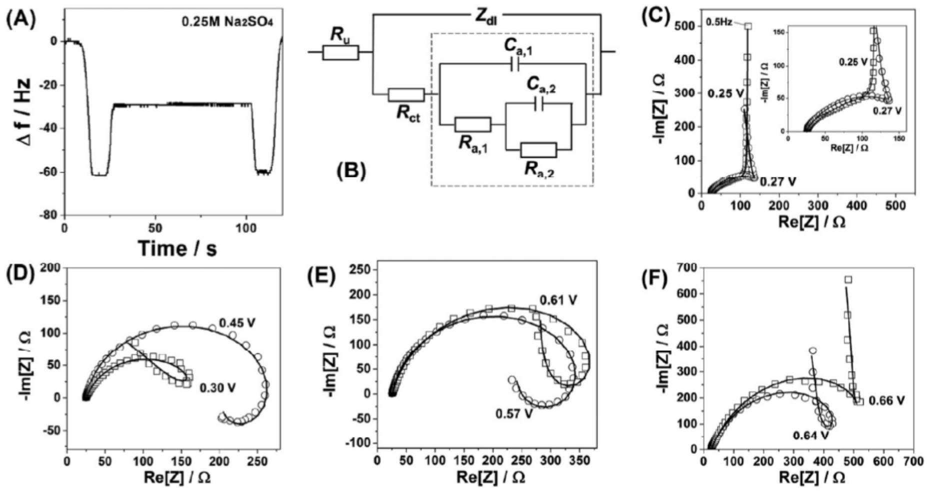

Fig. 2 Characterisation of the $Na_2Ni[Fe(CN)_6]$ thin films using impedance spectroscopy. (A) A typical electrode mass change curve confirming quasi-stationarity of the system within the time necessary to record one impedance spectrum. (B) Equivalent electric circuit reflecting the 3-stage mechanism (R_u, uncompensated resistance; Z_{dl}, impedance of the double layer; R_{ct}, charge transfer resistance; other R and C elements are adsorption (pseudo)resistances and (pseudo)capacitances, respectively, which are given by complex combinations of physicochemical parameters of adsorption/desorption (see text for details)). (C–F) Examples of impedance spectra (open symbols) at different electrode potentials together with the fitting (solid curves) to the model shown in (B). Inset in (C) shows the high frequency part of the same spectrum.

(2) Specific adsorption step, which can be considered as temporary compensation of the excess positive electrode charge due to relatively slow Na^+ de-intercalation (this step is likely to be distinguished as a separate one in EIS, as the mass transport in solids is relatively slow compared to that in liquids, and the change in the oxidation state of Fe in the film is in turn faster than the mentioned compensation from the electrolyte side):

$$2Na_2Ni[Fe^{III}(CN)_6]^+ + SO_4^{2-} \leftrightarrow (Na_2Ni[Fe^{III}(CN)_6])_2SO_4 \quad (3)$$

(3) "Non-electroactive step" (no net interfacial charge transfer), in which Na^+ and SO_4^{2-} ions leave the surface:

$$(Na_2Ni[Fe^{III}(CN)_6])_2SO_4 \leftrightarrow 2Na^+ + SO_4^{2-} + 2NaNi[Fe^{III}(CN)_6] \quad (4)$$

Importantly, the suggested mechanism involves the electrolyte components, namely anions. If sodium intercalation and de-intercalation indeed depend on the electrolyte composition, some key kinetic properties should be affected by changing the nature of the anions or their concentrations accordingly. Indeed, Fig. 3A further supports this hypothesis.

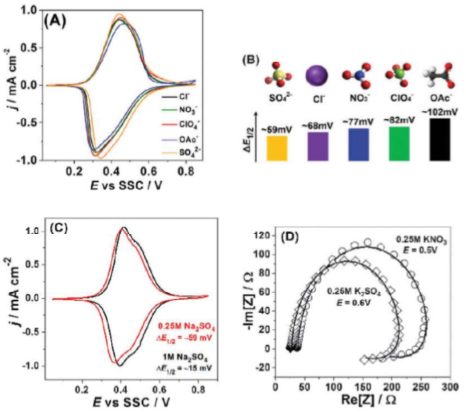

Fig. 3 Influence of the nature of anions and their concentration on reversibility and mechanism of sodium intercalation to $Na_2Ni[Fe(CN)_6]$. (A) Typical CVs in the presence of different anions, $dE/dt = 50$ mV s^{-1}. (B) Qualitative correlations between $\Delta E_{1/2}$ and the net charge density as well as the "symmetry" of the anions. (C) Effect of the sulfate-anion concentration on the voltammetric reversibility. (D) Impedance spectra (open symbols) and corresponding fitting results (solid curves, model is shown in Fig. 2B) in the presence of KNO_3 and K_2SO_4.

Fig. 3A shows how the nature of anions influences the peak shapes and so-called voltammetric reversibility, *i.e.* it reveals how fast intercalation and de-intercalation of sodium are as a function of the electrolyte composition. Noticeably, the corresponding peak separation becomes more and more evident if more "asymmetric" anions and/or anions with a lower net negative charge density are used, *i.e.* $SO_4^{2-} < Cl^- < NO_3^- < ClO_4^- < OAc^-$. This trend cannot be easily explained by some electrolyte conductivity issues, as, for example, aqueous solutions of Na_2SO_4, NaCl and $NaNO_3$ of these concentrations have very similar (within 2–3%) conductivities. However, the above-elucidated trend is in qualitative accordance with eqn (3), where efficient compensation of the excess "electrode charge" is necessary for the fast sodium exchange at the interface. Fig. 3B additionally illustrates this effect, in which the differences between the potentials of the "half-charged" and "half-discharged" states, $\Delta E_{1/2}$, are given for each anion used in this study.

Further evidence supporting the importance of the electrolyte composition for sodium interfacial transfer is given in Fig. 3C. The increase in the concentration of Na_2SO_4 not only shifts the potentials of Na intercalation/de-intercalation, as expected from the common rules; it also decreases the degree of CV-irreversibility between the "charging" and "discharging" cycles. Again, this effect cannot be easily explained by, for example, some electrolyte conductivity issues. It is even not proportional to the increase in the electrolyte conductivity ($\sim$2 times). However, it is well in accordance with the requirement of fast and effective compensation of the effective charge at the interface (eqn (3)) and questioning the simple mechanism represented by eqn (1).

Moreover, Fig. 3D demonstrates that the observed shapes of the impedance spectra are not because of some specific electrolyte composition: changing the anions or cations does seem to be critical for the mechanism of the interfacial charge transfer itself in this case, further reducing the probability of misinterpretation of the CVs shown in Fig. 3A and C. Therefore, even relatively small changes in the electrolyte composition can play a very essential role in the interfacial charge transfer. Fig. 4A schematically illustrates the importance of the intermediate interfacial charge compensation from the electrolyte side during intercalation/de-intercalation. Additionally, Fig. 4B shows that the performance of an optimised system, even at a high C-rate (180 C), is very good, with the specific capacity ($\sim$80 mA h g^{-1}) being only $\sim$5% lower than the theoretically possible value for this material (see more experimental data in Fig. S8–S10 of the ESI†).

Another important parameter controlling the performance of secondary intercalation batteries is the potential at which intercalation starts. Very straightforward expectations about the

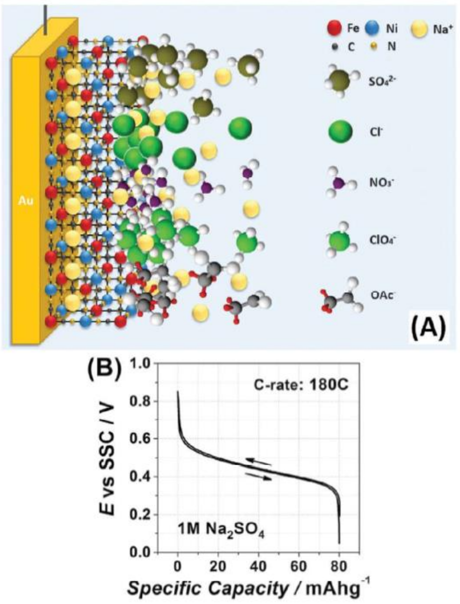

Fig. 4 (A) Schematic representation of the situation when the temporal and spatial charge compensation is critical to enhance the interfacial charge transfer (see text for details). Due to a slower diffusion of alkali metal cations in the solid with respect to the liquid electrolyte side (illustrated as a deficiency of Na ions in the solid thin film), the comparatively immediate change in the oxidation state of Fe atoms in the film requires a fast response from the electrolyte side. The latter would depend on the concentration, effective charge density and geometry of, for example, anions. (B) Galvanostatic charge and discharge curves at 180 C for $Na_2Ni[Fe(CN)_6]$ electrodes in 1 M Na_2SO_4. The galvanostatic cycling even at this very high C-rate shows a very low hysteresis resulting in high energy efficiencies.

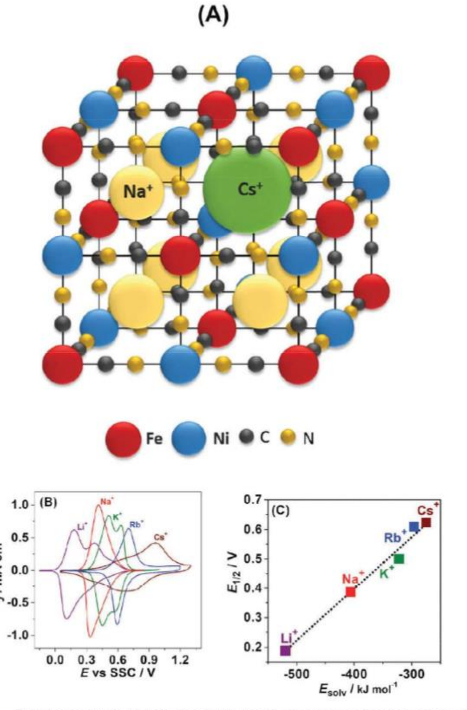

Fig. 5 Cation size *versus* cation solvation effect on intercalation of alkali metal cations into $Na_2Ni[Fe(CN)_6]$. (A) Schematics of the $Na_2Ni[Fe(CN)_6]$ crystal structure demonstrating that even Cs^+ can be inserted (all atoms have approximately realistic relative sizes). (B) Typical cyclic voltammograms for $Na_2Ni[Fe(CN)_6]$ in 0.25 M aqueous solutions of MNO_3 (where M = Li, Na, K, Rb, or Cs), dE/dt = 50 mV s^{-1}. (C) The potential of the "half-charged" state as a function of the alkali metal cation hydration energy.

capability of alkali metal cations to insert into the $Na_2Ni[Fe(CN)_6]$-like structures from the electrolyte side are associated with the size of the intercalating cations.[31–33] According to these expectations, the larger the cation, the more difficult it is to be intercalated into the solid state structure; though it is still possible for all the cations from Li^+ to Cs^+ to do so in the case of $Na_2Ni[Fe(CN)_6]$ (see schematics in Fig. 5A). Corresponding to this model, Cs^+ should intercalate at much more negative potentials compared to *e.g.* Li^+. However, what is observed experimentally is exactly the opposite, as was partially reported previously.[34,35]

Fig. 5B displays typical CVs for $Na_2Ni[Fe(CN)_6]$ in 0.25 M aqueous solutions of MNO_3 (where M = Li, Na, K, Rb, or Cs). It can be seen that intercalation is possible for all five alkali metal cations. Moreover, our quartz crystal microbalance data (not shown here) suggest that even after tens of initial cycles the net reaction can be fairly described as follows:

$$NaNi[Fe^{III}(CN)_6] + M^+ + e^- \leftrightarrow MNaNi[Fe^{II}(CN)_6]$$

(where M = Li, K, Rb, Cs), *i.e.* only approximately half of the sodium is replaced by the other alkali metal cations.

Surprisingly, despite the biggest cation radius of Cs^+, its insertion starts at the most positive electrode potentials followed by Rb^+, K^+, Na^+, and Li^+. Evidently, not only the cation size but other physicochemical parameters control the potential of their insertion. One of these parameters might be the ion hydration energy. Indeed if the potential of the half-charged state is plotted as a function of the alkali metal cation hydration energy, a statistically relevant linear correlation is observed (Fig. 5C).

Conclusions

In summary, we have further emphasised the importance of the electrolyte composition for the kinetics and mechanisms of interfacial charge transfer during intercalation/de-intercalation of sodium in the cathode materials for Na-ion batteries. Answering the question stated in the title of this paper, the commonly accepted models of Na intercalation in aqueous media, including a variety of theoretical ones, are likely to be too oversimplified affecting the strategies of the development of new materials for large-scale energy storage schemes. In particular, the nature of the anions present in the electrolyte significantly influences the intercalation/de-intercalation. On the other hand, solvation effects are probably among the main parameters governing the potential of alkali metal intercalation.

Consequently, more sophisticated models for Na intercalation in aqueous media need to be further elaborated to account for the observed trends. This will enhance our fundamental understanding and thus the performance of such Na-ion battery systems in the future.

Acknowledgements

Financial support from SFB 749, the cluster of excellence Nanosystems Initiative Munich (NIM) is gratefully acknowledged.

References

1 V. S. Arunachalam and E. L. Fleischer, *MRS Bull.*, 2008, **33**, 264–276.

2 J. P. Holdren, *Science*, 2007, **315**, 737.

3 D. Ginley, M. A. Green and R. Collins, *MRS Bull.*, 2008, **33**, 355–364.

4 Z. G. Yang, J. L. Zhang, M. C. W. Kintner-Meyer, X. C. Lu, D. W. Choi, J. P. Lemmon and J. Liu, *Chem. Rev.*, 2011, **111**, 3577–3613.

5 B. Dunn, H. Kamath and J. M. Tarascon, *Science*, 2011, **334**, 928–935.

6 G. L. Soloveichik, *Annu. Rev. Chem. Biomol. Eng.*, 2011, **2**, 503–527.

7 M. Armand and J. M. Tarascon, *Nature*, 2008, **451**, 652–657.

8 J. M. Tarascon and M. Armand, *Nature*, 2001, **414**, 359–367.

9 V. Etacheri, R. Marom, R. Elazari, G. Salitra and D. Aurbach, *Energy Environ. Sci.*, 2011, **4**, 3243–3262.

10 J. Y. Luo and Y. Y. Xia, *Adv. Funct. Mater.*, 2007, **17**, 3877–3884.

11 P. C. K. Vesborg and T. F. Jaramillo, *RSC Adv.*, 2012, **2**, 7933–7947.

12 Y. Wu, X. Dai, J. Ma and Y. Chen, *Lithium Ion Batteries: Practice and Applications*, Chemical Industry Press, Beijing, 2004.

13 W. Tang, Y. S. Zhu, Y. Y. Hou, L. L. Liu, Y. P. Wu, K. P. Loh, H. P. Zhang and K. Zhu, *Energy Environ. Sci.*, 2013, **6**, 2093–2104.

14 Z. Chang, Y. Q. Yang, M. X. Li, X. W. Wang and Y. P. Wu, *J. Mater. Chem. A*, 2014, **2**, 10739–10755.

15 W. Tang, L. L. Liu, Y. S. Zhu, H. Sun, Y. P. Wu and K. Zhu, *Energy Environ. Sci.*, 2012, **5**, 6909–6913.

16 Y. G. Wang, J. Yi and Y. Y. Xia, *Adv. Energy Mater.*, 2012, **2**, 830–840.

17 H. L. Pan, Y. S. Hu and L. Q. Chen, *Energy Environ. Sci.*, 2013, **6**, 2338–2360.

18 S. Ferlay, T. Mallah, R. Ouahes, P. Veillet and M. Verdaguer, *Nature*, 1995, **378**, 701–703.

19 Y. H. Lu, L. Wang, J. G. Cheng and J. B. Goodenough, *Chem. Commun.*, 2012, **48**, 6544–6546.

20 L. Wang, Y. H. Lu, J. Liu, M. W. Xu, J. G. Cheng, D. W. Zhang and J. B. Goodenough, *Angew. Chem., Int. Ed.*, 2013, **52**, 1964–1967.

21 H. W. Lee, R. Y. Wang, M. Pasta, S. W. Lee, N. Liu and Y. Cui, *Nat. Commun.*, 2014, **5**, 5280.

22 C. D. Wessells, R. A. Huggins and Y. Cui, *Nat. Commun.*, 2011, **2**, 550.

23 M. Pasta, C. D. Wessells, R. A. Huggins and Y. Cui, *Nat. Commun.*, 2012, **3**, 1149.

24 M. Pasta, C. D. Wessells, N. Liu, J. Nelson, M. T. McDowell, R. A. Huggins, M. F. Toney and Y. Cui, *Nat. Commun.*, 2014, **5**, 3007.

25 H. Kim, J. Hong, K.-Y. Park, H. Kim, S.-W. Kim and K. Kang, *Chem. Rev.*, 2014, **114**, 11788–11827.

26 C. D. Wessells, S. V. Peddada, R. A. Huggins and Y. Cui, *Nano Lett.*, 2011, **11**, 5421–5425.

27 X. Y. Wu, Y. L. Cao, X. P. Ai, J. F. Qian and H. X. Yang, *Electrochem. Commun.*, 2013, **31**, 145–148.

28 A. S. Bondarenko, *Anal. Chim. Acta*, 2012, **743**, 41.

29 A. S. Bondarenko and G. A. Ragoisha, in *Progress in Chemometrics Research*, ed. A. L. Pomerantsev, 2005, pp. 89–102.

30 A. Lasia, *Electrochemical Impedance Spectroscopy and its Applications*, Springer-Verlag, New York, 2014, p. 367.

31 K. Itaya, I. Uchida and V. D. Neff, Electrochemistry of polynuclear transition metal cyanides: prussian blue and its analogues, *Acc. Chem. Res.*, 1986, **19**(6), 162–168.

32 N. Bagkar, C. A. Betty, P. A. Hassan, K. Kahali, J. R. Bellare and J. V. Yakhmi, *Thin Solid Films*, 2006, **497**(1–2), 259–266.

33 W. Jin, A. Toutianoush and M. Pyrasch, *et al.*, *J. Phys. Chem. B*, 2003, **107**(44), 12062–12070.

34 M. A. Malik, P. J. Kuelsza and R. Marrassi, *Electrochim. Acta*, 2004, **49**, 4253–4258.

35 W. Chen, J. Tang and X.-H. Xia, *J. Phys. Chem. C*, 2009, **113**, 21577–21581.

ACS APPLIED MATERIALS & INTERFACES
Research Article
www.acsami.org

Electrodeposited $Na_2VO_x[Fe(CN)_6]$ films As a Cathode Material for Aqueous Na-Ion Batteries

Bianca Paulitsch,[†] Jeongsik Yun,[†,‡] and Aliaksandr S. Bandarenka*[,†,‡]

[†]Physik-Department ECS, Technische Universität München, James-Franck-Straße 1, 85748 Garching, Germany
[‡]Nanosystems Initiative Munich (NIM), Schellingstraße 4, 80799 Munich, Germany

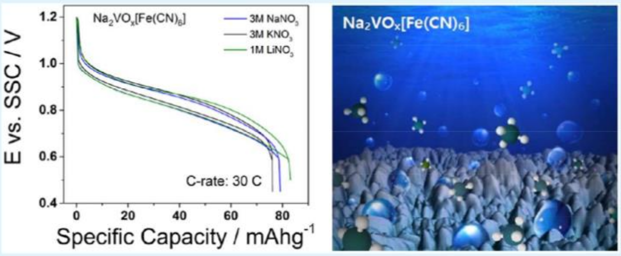

ABSTRACT: The so-called Prussian blue analogues (PBAs) are spotlighted as promising cathode materials for aqueous Na-ion batteries regarding their good performance for the application in future large-scale energy storage systems. In this work, we demonstrate that one of the PBA representatives, namely $Na_2VO_x[Fe(CN)_6]$ thin films (VHCFs), is a promising cathode material for aqueous Na-ion batteries with very positive intercalation/deintercalation potentials, which might likely designate a new benchmark in the field. To maximize the material utilization, we have formed VHCF thin films on model current collectors from aqueous solutions. The resulting films demonstrated a very positive half-charge potential ($\Delta E_{1/2} \approx 0.91$ V vs Ag/AgCl reference electrode) in acidic media with a specific capacity of ~80 mAh g^{-1} recorded at high C-rates (30 C) in 1 M $LiNO_3$, 3 M $NaNO_3$ and 3 M KNO_3 electrolytes in the presence of 3.6 M H_2SO_4. It is also shown that well-known solvation effects related to the nature of the alkali metal cations during intercalation and deintercalation are surprisingly not pronounced in the case of VHCFs.

KEYWORDS: *Na-ion battery, cathode battery materials, vanadium hexacyanoferrate, Prussian blue analogues, intercalation*

1. INTRODUCTION

An efficient and sustainable solution of the so-called generation versus consumption problem will most probably enable further and wider application of "clean" energy provision schemes. It is nowadays widely accepted that battery systems will significantly contribute to such a solution, for instance in the case of stationary energy storage systems.[1] However, to upscale the battery-based schemes to the TW-level,[2] abundant materials, safe systems, and easy production processes are required.[3] From the portfolio of the devices, aqueous Na-ion batteries are a suitable choice taking into account the above-mentioned issues:[4−6] although Li-ion batteries are currently the "number one" in automotive applications, aqueous Na-ion batteries have clear benefits for stationary systems. For example, accumulation of sodium is nowadays at least 1 order of magnitude faster compared to lithium.[7] Aqueous electrolytes are safer compared to those used in the state of the art nonaqueous Li-ion batteries. Finally, the electrode materials for these batteries normally contain abundant elements. However, the major issue related to the intercalation materials for the aqueous Na-ion batteries is that they should simultaneously enable a wide operational window and prohibit side reactions, such as oxygen and hydrogen evolution reactions.[8] For instance, cathode materials should enable reversible intercalation and deintercalation of sodium at the electrode potentials, which are as positive as possible, and simultaneously should not catalyze the oxygen evolution reaction. As for the anodes, the electrode materials should enable sodium intercalation and deintercalation at the potentials, which are as negative as possible, and should prohibit the hydrogen evolution reaction. These "anti-electrocatalytic" requirements significantly restrict the choice of the materials for the efficient Na-ion batteries operating in aqueous media.

The Prussian blue analogues (PBAs) with a general formula $A_xB_y[M(CN)_6]$ (where A is, for example, an alkali metal cation, B is a transition metal cation or oxy-cation, and M is some transition metal like Fe or Mn) are a class of compounds that are recently of great interest to use at both cathodes and anodes in Na-ion aqueous batteries.[9−11] Lately, a screening among some PBA materials led to the development of battery systems

Received: December 6, 2016
Accepted: February 16, 2017
Published: February 16, 2017

DOI: 10.1021/acsami.6b15666
ACS Appl. Mater. Interfaces 2017, 9, 8107−8112

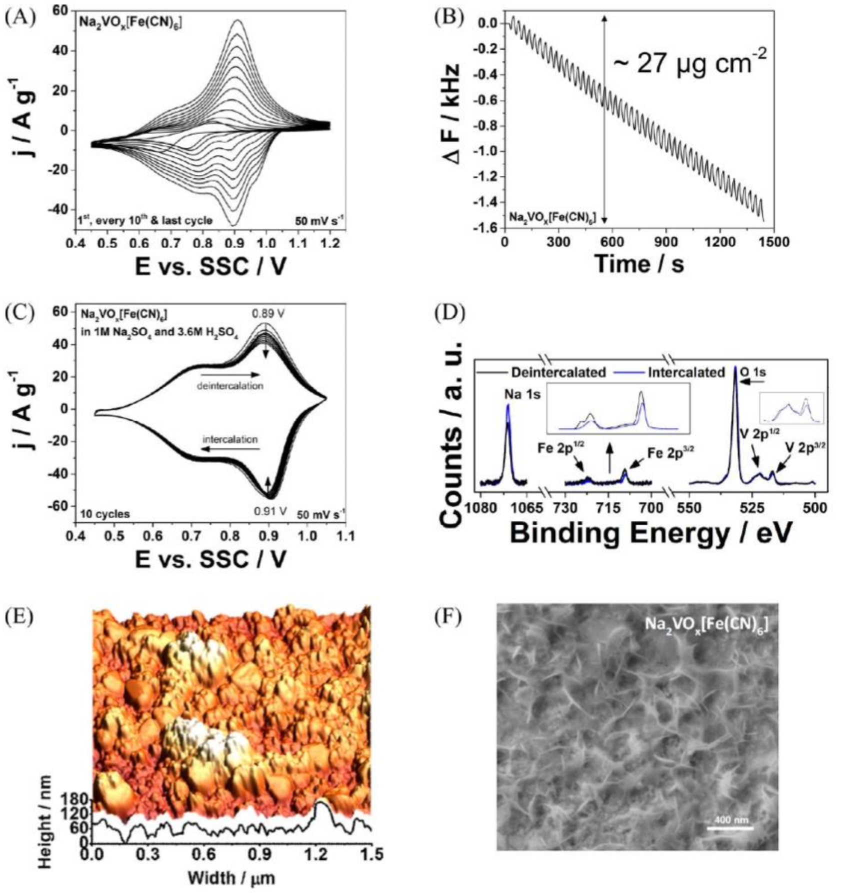

Figure 1. Na$_2$VO$_x$[Fe(CN)$_6$] thin film growth and characterization. (A) A typical CV of Na$_2$VO$_x$[Fe(CN)$_6$] film deposition from the aqueous solution containing 3.6 M H$_2$SO$_4$, 5 mM NaVO$_3$ and 5 mM K$_3$Fe(CN)$_6$ by cycling the electorde potential in the range of 0.45 to 1.2 V at a scan rate of 50 mV/s and (B) its corresponding QCM curves revealing the resulting electrode mass change of ~27 μg cm^{-2}. (C) Sodium intercalation/deintercalation for the deposited film in 1 M Na$_2$SO$_4$ + 3.6 M H$_2$SO$_4$, dE/dt = 50 mV/s. (D) XPS spectra of key elements (Na, Fe, O, and V) for the deposited VHCF thin films comparing the deintercalated (black) and intercalated (blue) states. (E) AFM and (F) SEM images of the resulting film.

with operating voltage between 1.0 and ca. 1.4 V.[12,13] However, a further significant increase in the operating voltage is necessary motivating to a further screening for better cathode and anode materials.

In this work, we demonstrate that electrodeposited films of Na$_2$VO$_x$[Fe(CN)$_6$] are a promising cathode material for Na-ion batteries operating in acidic aqueous media. With its positive half-charge potential as high as ca. 0.91 V vs Ag/AgCl reference electrode and reversible intercalation/deintercalation of alkali metal cations, it outperforms the state of the art PBA materials like Na$_2$Ni[Fe(CN)$_6$] or Na$_2$Cu[Fe(CN)$_6$] even at high C-rates. Surprisingly, although the mechanism of the mass and charge transfer involves electrolyte components, namely anions, the influence of the nature of the alkali metal cations present in the electrolytes on the potential of the intercalation/deintercalation is of much less importance, if compared with other PBA materials.[14,15]

2. EXPERIMENTAL SECTION

Electrochemical deposition and characterization of Na$_2$VO$_x$[Fe(CN)$_6$] thin films were performed in a glass cell with a three-electrode configuration using a VSP-300 potentiostat (Bio-Logic, France) and a QCM 200 (Standford Research Systems, USA). A Au single crystal, a sputtered Au on glass arrandee or an AT-cut Au quartz crystal wafer (5 MHz, 1″ diameter) were used as working electrodes. A Pt wire was used as a counter electrode. All electrode potentials in this work are referred to the Ag/AgCl (SSC) reference electrode. The thin film deposition procedure was adapted from Dong et al.[16] with modifications. Namely, Na$_2$VO$_x$[Fe(CN)$_6$] thin films were electrochemically deposited by cycling the potential between 0.45 to 1.2 V in a solution containing 3.6 M H$_2$SO$_4$, 5 mM NaVO$_3$ and 5 mM K$_3$Fe(CN)$_6$ at a scan rate of 50 mV/s for ~110 cycles as shown in Figure 1A. Characterization of the intercalation was performed using

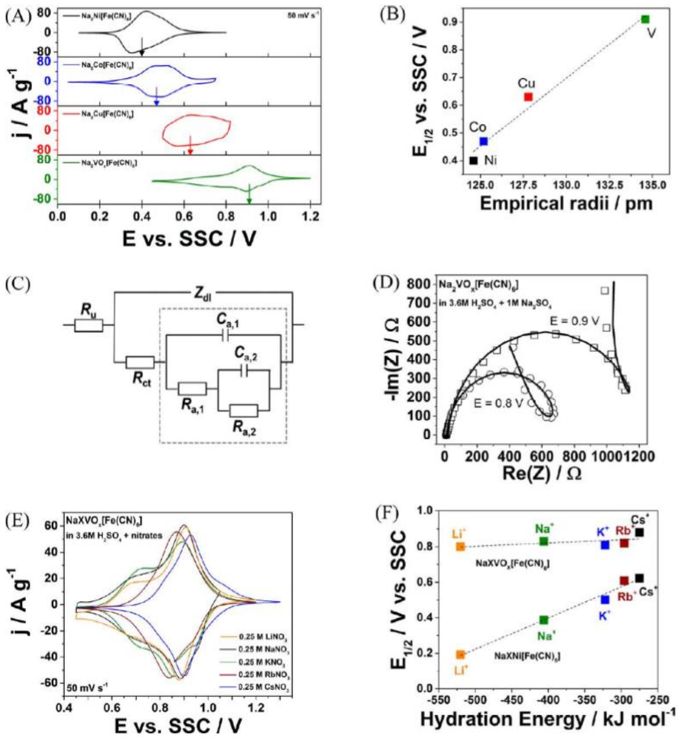

Figure 2. (A) Typical CVs for sodium intercalation/deintercalation in the case of $Na_2B[Fe(CN)_6]$ (B = Ni, Co, Cu and VO_x) in 0.25 M Na_2SO_4 aqueous electrolytes. In the VHCF film, 3.6 M H_2SO_4 was added to stabilize the film. (B) The half-charge potentials as a function of empirical radii of transition metal elements that are linked to the N-coordinates in the PBA crystal structure. (C) The equivalent circuit (R_u, uncompensated resistance; Z_{dl}, impedance of the double layer; R_{ct}, charge transfer resistance, other R and C elements are adsorption (pseudo)resistances and (pseudo)capacitances, respectively). (D) Impedance spectra (open circles) with fitting results (lines, see refs[14,15] for further details regarding the model and fitting) for two different potentials. (E) Typical CVs of the $Na_2VO_x[Fe(CN)_6]$ films in 3.6 M H_2SO_4 and 0.25 M XNO_3 aqueous electrolytes (X = Li, Na, K, Rb and Cs) with (F) the comparison of the effect of cations (half-charge state vs cation hydration energies) in the case of VHCF and NiHCF electrodes.

cyclic voltammetry (CV) in different electrolytes containing 0.25 M $LiNO_3$, 0.25 M $NaNO_3$, 0.25 M KNO_3, 0.25 M $RbNO_3$, 0.25 M $CsNO_3$ in 3.6 M H_2SO_4 and 0.25 M Na_2SO_4 in ultrapure water (Evoqua, Germany). Common battery tests were performed using 1 M $LiNO_3$, 3 M $NaNO_3$ and 3 M KNO_3 in 3.6 M H_2SO_4 as electrolytes. The protective $Na_2Ni[Fe(CN)_6]$ (NiHCF) thin coating layer was formed by depositing NiHCF at a constant potential (0.37 V) for 10 min from a solution containing 0.5 mM $NiCl_2 \cdot 6H_2O$ and 0.5 mM $K_3Fe(CN)_6$ and 0.1 M H_2SO_4 onto the predeposited VHCF thin films. The preparation of $Na_2Co[Fe(CN)_6]$, $Na_2Cu[Fe(CN)_6]$ and $Na_2Ni[Fe(CN)_6]$ thin films has been performed according to the procedure described in detail elsewhere.[15]

The sample morphology was investigated using atomic force microscopy (AFM) and scanning electron microscopy (SEM). For the AFM measurements a multimode EC-STM/AFM instrument (Veeco VI) with a Nanoscope IIID controller was used with the Nanoscope 5.31r1 software. All measurements were performed in tapping mode with AFM tips (Bruker REESP-300). For SEM investigations the NVision 40 (Zeiss) was used. X-ray photoelectron spectroscopy (XPS) was performed using a SPECS XPS spectrometer (SPECS, Germany). The X-ray beam was generated in a XR50 X-ray tube by an Al anode (12 kV, 200W) with photon energy of 1486.61 eV and beam focus of 1.4 mm × 4 mm on the sample. The kinetic energy of the electrons was detected by a semispherical electron energy analyzer (PHOIBOS 150 2D CCD), operating with a pass energy of 20 eV to ensure a high resolution of the spectra.

Electrochemical impedance spectroscopy (EIS) measurements were performed in the potential range between 0.55 and 1.05 V using *ac*-probing frequencies from 50 kHz to 0.1 Hz with a 10 mV amplitude. The impedance data were analyzed using homemade software.[17,18]

3. RESULTS AND DISCUSSION

The following general scheme was used to deposit $Na_2VO_x[Fe(CN)_6]$ thin films under potentiodynamic electrochemical conditions:

$$2Na^+ + VO_3^- + [Fe(CN)_6]^{3-} + (6-2x)H^+ \rightarrow Na_2VO_x[Fe(CN)_6] + (3-x)H_2O$$

Figure 1A demonstrates a typical CV characterizing VHCF thin film deposition, where only the first and every 10th cycles are shown. Anodic and cathodic peaks are associated with the

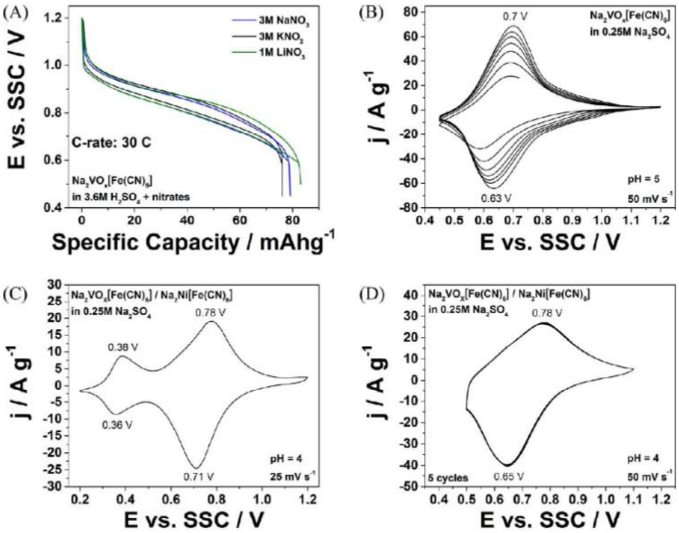

Figure 3. (A) Galvanostatic charge and discharge curves at the 30C rate for the $Na_2VO_x[Fe(CN)_6]$ films in 1 M $LiNO_3$, 3 M $NaNO_3$, and 3 M KNO_3 with 3.6 M H_2SO_4 electrolytes with specific capacities of ~83, ~79, and ~76 mAh g^{-1}, respectively. (B) Typical CVs of the VHCF film in 0.25 M Na_2SO_4 (pH 5) with peak potentials of 0.7 V/0.63 V. (C) CVs of the VHCF electrodes coated with NiHCF thin films (25 mV s^{-1} scan rate in 0.25 M Na_2SO_4 (pH 4, with H_2SO_4 pH correction) with peak potentials of 0.38 V/0.36 V showing the impact of NiHCF and 0.78 V/0.71 V belonging to VHCF. (D) Improved stability of VHCF/NiHCF "protected" thin film in 0.25 M Na_2SO_4 with peak potentials of 0.78 V/0.65 V.

change of the oxidation state of Fe inside the subsequently growing thin film followed by alkali metal cation intercalation and deintercalation. The associated net mass change of the electrode was measured during the deposition process using the electrochemical quartz crystal microbalance (EQCM) as shown in Figure 1B.

The resulting mass change of the working electrode was calculated to be ~27 μg cm^{-2} (fluctuations in the mass, which can be also seen in Figure 1B, are due to alkali metal cation intercalation and deintercalation during the film growth). Considering the results of XPS in combination with EQCM and CV results and Faraday's law, it was possible to calculate the composition of the thin film. Using the corresponding integrated charge obtained from the voltammograms, we obtain the values x in $Na_2VO_x[Fe(CN)_6]$ of slightly below 2. The lower than expected x values are likely due to conversion of VO_3^- not only to VO_2^+ but also to some extent to VO^{2+} in acidic aqueous media.[16]

Figure 1C shows 10 subsequent CV cycles characterizing Na intercalation and deintercalation with main peaks at ~0.9 V demonstrating slightly decreasing current densities. XPS spectra analysis confirms the presence of key elements (Na, V, O, and Fe) in the VHCF thin films (Figure 1D). All XPS-peaks were identified by comparing the experimental binding energies to the references of the binding energies from ref 19. From the comparison of the XPS peaks of the intercalated and deintercalated states, it is clearly seen that the intensity of the Na 1s peak is decreased for the deintercalated state, indicating that Na ions leave the structure in the anodic scan. The shift of the binding energies for Fe $2p^{1/2}$ and Fe $2p^{3/2}$ results from different oxidation states of Fe in the VHCF thin films after the intercalation and deintercalation of sodium. The double peak of Fe $2p^{1/2}$ for the deintercalated state suggests that both Fe^{III} and Fe^{II} are present in the film. In the intercalated state, Fe^{III} is reduced to Fe^{II} resulting in a single peak. For the Fe $2p^{3/2}$ peak, the change in oxidation state can be seen in a slight binding energy shift to higher values for the intercalated state. The XPS peaks for O and V seem not to be affected by the insertion of Na, as expected.[20] From the XPS analysis it can be concluded that only Fe is contributing to the capacity behavior of VHCF. Figure 1E shows an AFM image of $Na_2VO_x[Fe(CN_6)]$ thin film, where structures of over 180 nm are seen. SEM image of the $Na_2VO_x[Fe(CN_6)]$ sample is shown in Figure 1F. The comparison of these two images reveals different aspects; however, suggesting that the resulting films are not porous, and the geometric electrode surface area can (as the first approximation) be considered as the real electroactive one.

Figure 2A compares CVs of some state-of-the art cathode materials, namely PBA-containing Ni, Co, and Cu, as well as VHCF electrodes in a 0.25 M Na_2SO_4 aqueous electrolyte (3.6 M H_2SO_4 was added in VHCF to stabilize the films). Among different PBAs, $Na_2VO_x[Fe(CN)_6]$ demonstrates the most positive electrode potential for Na intercalation in 0.25 M Na_2SO_4 aqueous electrolyte. The half-charge potential of $Na_2VO_x[Fe(CN)_6]$ reaches ~0.91 V, whereas Ni-, Co-, and Cu-HCF films show the half wave potential at 0.44, 0.51, and 0.67 V, respectively. Interestingly, a roughly linear correlation between the half-charge potentials and the empirical radii of the key transition metal elements[21,22] can be seen in Figure 2B.

The interfacial charge and mass transfer process at the VHCF thin films during quasi-reversible Na intercalation/deintercalation was also investigated using electrochemical impedance spectroscopy. The used equivalent electric circuit model and the resulting impedance spectra[14] are shown in Figure 2C, D, respectively. The "loop-shaped" impedance spectra, similar to refs 14 and 15, reveal that Na intercalation of VHCF follows at least a three-stage mechanism involving anions in the electrolyte.

It should be noticed here that the difference in the impedance spectra in Figure 2D is due to changes in the kinetics of the interfacial charge and mass transport at different electrode potentials. Normally, the kinetic parameters are exponential functions of the potential, resulting in very significant changes even if the potential is changed slightly.

Na intercalation in the case of the VHCF thin films involves specific adsorption of anions from the electrolyte because of the different kinetic rate of a faster oxidation/reduction of Fe and a slower diffusion of Na in the electrolyte and electrode. If the three-stage mechanism could be represented using simplified terms, the first step is the change in the oxidation state of Fe in the VHCF thin film, which could be represented as follows:

$$Na_2VO_x[Fe^{II}(CN)_6] - 1e^- \leftrightarrow Na_2VO_x[Fe^{III}(CN)_6]^+ \tag{1}$$

Because of a good conductivity of the VHCF thin film, this oxidation/reduction rate of Fe is much faster than diffusion rate of the Na ions in the solid electrode and the electrolytes. Thus, the surface of the thin film would temporarily show the excess positive charge and attract anions in the electrolyte to compensate the excess charge (we assume the specific adsorption in this case).

$$Na_2VO_x[Fe^{III}(CN)_6]^+ + A^- \leftrightarrow Na_2VO_x[Fe^{III}(CN)_6]A \tag{2}$$

where A is anion in the electrolyte. Finally, Na ions and the anions leave the thin film:

$$Na_2VO_x[Fe^{III}(CN)_6] \leftrightarrow Na^+ + A^- + NaVO_x[Fe^{III}(CN)_6] \tag{3}$$

Further details regarding the mechanism and the interpretation of EIS spectra are demonstrated in refs14 and15.

Figure 2E displays typical CVs for VHCF electrodes in different 0.25 M XNO_3 aqueous electrolytes (where X = Li, Na, K, Rb and Cs) with the addition of 3.6 M H_2SO_4. It is known that solvation effects during intercalation of different alkali metal cations might be one of the key parameters to determine the electrode potential of NiHCF.[14] However, in the case of VHCF the "solvation effect" is not as pronounced as compared to NiHCF as shown in Figure 2F, where the intercalation potential only slightly depend on the nature of the alkali metal cation. This effect is very surprising but detailed explanation of it is outside of the scope of this manuscript, where phenomenological effects are intended to be primarily described. Further investigations are necessary to address the above-mentioned issues.

Common battery tests for $Na_2VO_x[Fe(CN)_6]$ thin films were also performed. Specific capacities of $Na_2VO_x[Fe(CN)_6]$ electrodes in 1 M $LiNO_3$, 3 M $NaNO_3$, and 3 M KNO_3 electrolytes with 3.6 M H_2SO_4 at the 30 C rate show values close to the theoretical ones with ~83, ~79, and ~76 mAh g^{-1}, respectively, as can be seen in Figure 3A. Similar behavior of the different cations further underlines the already mentioned low impact of cations on the performance of VHCF.

It should be noted that some PBAs are unstable in basic and neutral media, because CN^- ligands can likely be exchanged by OH^-, which results in degradation of PBAs battery performance.[23] The cycle stability of the VHCF thin film is poor in electrolytes only containing 0.25 M Na_2SO_4 showing fast degradation as can be seen in Figure 3B. To address instability of VHCF thin films in neutral solutions, we propose that other, more stable thin films, e.g., NiHCF layers, could be electrochemically deposited as protecting layers onto VHCF. NiHCF was selected as protective layer, because NiHCF has a similar crystal structure to VHCF, which will introduce less strain to the VHCF structure and the electroactive potential range of NiHCF lays outside of the electroactive potential range of VHCF and therefore a deposition with constant potential is not affecting the performance of VHCF. Figure 3C shows one example of CV characterization of such a layered electrode when $Na_2Ni[Fe(CN)_6]$ thin protective layer was deposited on much thicker $Na_2VO_x[Fe(CN)_6]$ film. As can be seen from Figures 3C, the protection causes some cathodic shift in the potentials of intercalation and deintercalation of sodium compared to the pure $Na_2VO_x[Fe(CN)_6]$ films in the acidic media with peak potentials of 0.78 V/0.71 V. This is likely due to the influence of the $Na_2Ni[Fe(CN)_6]$ material on the resulting film properties (notice also a pair of smaller peaks at approximately 0.38 V/0.36). On the other hand, the protective coating indeed can stabilize the system as shown in Figure 3D, where 5 stable cycles are shown with peak potentials of 0.78 V/0.65 V.

■ CONCLUSIONS

The very positive half-charge potential for intercalation/deintercalation of sodium reveals the electrodeposited VHCF material as a promising candidate for the cathodes in acidic aqueous Na-ion batteries, outperforming in that respect Ni-, Co-, and Cu- HCFs even at high C-rates. In fact, the VHCF-films exhibit the highest anodic potential for the Na intercalation without noticeably catalyzing side reactions among PBA-based materials. The issue regarding the stability of the VHCF film in neutral or basic media can be addressed by coating the VCHF films with very thin protective layers, for instance, NiHCF.

Interestingly, the intercalation electrode potential for PBA-based cathode materials seems to be determined by the choice of transition metal elements that are largely linked to the N atoms in the PBA structures.

As for the VHCFs, Na intercalation into the VHCF follows a three stage mechanism involving anions present in the electrolytes. However, the well-known solvation effects associated with the alkali-metal cations in the intercalation process was not pronounced in the case of VHCF compared to those known for, for example, NiHCF. This surprising result should be further studied to deepen the understanding of intercalation processes.

■ AUTHOR INFORMATION

Corresponding Author

*E-mail: bandarenka@ph.tum.de. Tel. +49 (0) 89 289 12531.

ORCID

Aliaksandr S. Bandarenka: 0000-0002-5970-4315

Notes

The authors declare no competing financial interest.

■ ACKNOWLEDGMENTS

Financial support from the cluster of excellence Nanosystems Initiative Munich (NIM) is gratefully acknowledged. We thank Dr. Faheem Butt and Siegfried Schreier for SEM imaging and Yunchang Liang for AFM imaging.

DOI: 10.1021/acsami.6b15666
ACS Appl. Mater. Interfaces 2017, 9, 8107–8112

■ REFERENCES

(1) Dunn, B.; Kamath, H.; Tarascon, J. M. Electrical Energy Storage for the Grid: A Battery of Choices. *Science* **2011**, *334* (6058), 928−935.

(2) Smalley, R. E. Future Global Energy Prosperity: The Terawatt Challenge. *MRS Bull.* **2005**, *30* (06), 412−417.

(3) Palomares, V.; Serras, P.; Villaluenga, I.; Hueso, K. B.; Carretero-Gonzalez, J.; Rojo, T. Na-Ion Batteries, Recent Advances and Present Challenges to Become Low Cost Energy Storage Systems. *Energy Environ. Sci.* **2012**, *5* (3), 5884−5901.

(4) Kim, S.-W.; Seo, D.-H.; Ma, X.; Ceder, G.; Kang, K. Electrode Materials for Rechargeable Sodium-Ion Batteries: Potential Alternatives to Current Lithium-Ion Batteries. *Adv. Energy Mater.* **2012**, *2* (7), 710−721.

(5) Ellis, B. L.; Nazar, L. F. Sodium and Sodium-Ion Energy Storage Batteries. *Curr. Opin. Solid State Mater. Sci.* **2012**, *16* (4), 168−177.

(6) Kim, H.; Hong, J.; Park, K.-Y.; Kim, H.; Kim, S.-W.; Kang, K. Aqueous Rechargeable Li and Na Ion Batteries. *Chem. Rev.* **2014**, *114* (23), 11788−11827.

(7) Vesborg, P. C.; Jaramillo, T. F. Addressing the Terawatt Challenge: Scalability in the Supply of Chemical Elements for Renewable Energy. *RSC Adv.* **2012**, *2* (21), 7933−7947.

(8) Luo, J.-Y.; Cui, W.-J.; He, P.; Xia, Y.-Y. Raising the Cycling Stability of Aqueous Lithium-Ion Batteries by Eliminating Oxygen in the Electrolyte. *Nat. Chem.* **2010**, *2* (9), 760−765.

(9) Lu, Y.; Wang, L.; Cheng, J.; Goodenough, J. B. Prussian Blue: A New Framework of Electrode Materials for Sodium Batteries. *Chem. Commun.* **2012**, *48* (52), 6544−6546.

(10) Wessells, C. D.; Peddada, S. V.; Huggins, R. A.; Cui, Y. Nickel Hexacyanoferrate Nanoparticle Electrodes For Aqueous Sodium and Potassium Ion Batteries. *Nano Lett.* **2011**, *11* (12), 5421−5425.

(11) Wessells, C. D.; Huggins, R. A.; Cui, Y. Copper Hexacyanoferrate Battery Electrodes with Long Cycle Life and High power. *Nat. Commun.* **2011**, *2*, 550.

(12) Pasta, M.; Wessells, C. D.; Liu, N.; Nelson, J.; McDowell, M. T.; Huggins, R. A.; Toney, M. F.; Cui, Y. Full Open-Framework Batteries for Stationary Energy Storage. *Nat. Commun.* **2014**, *5*, DOI: 10.1038/ncomms4007.

(13) Wu, X. Y.; Sun, M. Y.; Shen, Y. F.; Qian, J. F.; Cao, Y. L.; Ai, X. P.; Yang, H. X. Energetic Aqueous Rechargeable Sodium-Ion Battery Based on $Na_2CuFe(CN)_6$-$NaTi_2(PO_4)_3$ Intercalation Chemistry. *ChemSusChem* **2014**, *7* (2), 407−411.

(14) Yun, J.; Pfisterer, J.; Bandarenka, A. S. How Simple Are the Models of Na Intercalation in Aqueous Media? *Energy Environ. Sci.* **2016**, *9*, 955−961.

(15) Ventosa, E.; Paulitsch, B.; Marzak, P.; Yun, J.; Schiegg, F.; Quast, T.; Bandarenka, A. S. The Mechanism of the Interfacial Charge and Mass Transfer During Intercalation of Alkali Metal Cations. *Adv. Sci.* **2016**, *3*, 1600211.

(16) Shaojun, D.; Fengbin, L. Researches on Chemically Modified Electrodes: Part XV. Preparation and Electrochromism of the Vanadium Hexacyanoferrate Film Modified Electrode. *J. Electroanal. Chem. Interfacial Electrochem.* **1986**, *210* (1), 31−44.

(17) Bondarenko, A. S. Analysis of Large Experimental Datasets in Electrochemical Impedance Spectroscopy. *Anal. Chim. Acta* **2012**, *743*, 41−50.

(18) Bondarenko, A. S.; Ragoisha, G. A. *Progress in Chemometrics Research*; Nova Science Publishers: New York, 2005; pp 89−102.

(19) Wagner, C. D.; Muilenberg, G. E. *Handbook of X-Ray Photoelectron Spectroscopy: A Reference Book of Atandard Data for Use in X-Ray Photoelectron Spectroscopy*. Physical Electronics Division, Perkin-Elmer Corp., 1979.

(20) Carpenter, M. K.; Conell, R. S.; Simko, S. J. Electrochemistry and Electrochromism of Vanadium hexacyanoferrate. *Inorg. Chem.* **1990**, *29* (4), 845−850.

(21) Wessells, C. D.; McDowell, M. T.; Peddada, S. V.; Pasta, M.; Huggins, R. A.; Cui, Y. Tunable Reaction Potentials in Open Framework Nanoparticle Battery Electrodes for Grid-Scale Energy Storage. *ACS Nano* **2012**, *6* (2), 1688−1694.

(22) Teatum, E.; Gschneider, K.; Waber, J. In *Report NoLA-2345*; U.S. Dept. of Commerce: Washington, D.C., 1960; p 45.

(23) Yang, Y.; Brownell, C.; Sadrieh, N.; May, J.; Del Grosso, A.; Place, D.; Leutzinger, E.; Duffy, E.; He, R.; Houn, F.; et al. Quantitative Measurement of Cyanide Released from Prussian Blue. *Clin. Toxicol.* **2007**, *45* (7), 776−781.

ACS OMEGA
Article
Cite This: ACS Omega 2018, 3, 5111−5115

Chromium(II) Hexacyanoferrate-Based Thin Films as a Material for Aqueous Alkali Metal Cation Batteries

Radu Bors,[†] Jeongsik Yun,[†,‡] Philipp Marzak,[†,‡] Johannes Fichtner,[†] Daniel Scieszka,[†,‡]
and Aliaksandr S. Bandarenka*,[†,‡]

[†]Department of Physics, ECS, Technical University of Munich, James-Franck-Straße 1, 85748 Garching, Germany
[‡]Nanosystems Initiative Munich (NIM), Schellingstraße 4, 80799 Munich, Germany

ABSTRACT: Identification and characterization of novel battery electrode materials are key factors in transitioning the grids to renewable energy provision. Given the scale of the challenge, special attention should be paid to safety and availability of resources. This paper presents a new electrode material for aqueous batteries and supercapacitors based on highly available resources: chromium(II) hexacyanoferrate (CrHCF) thin films. Electrodeposited CrHCF exhibited "half-charge" potentials ($E_{1/2}$) of ∼0.69 and ∼0.72 V versus silver/silver chloride (reference electrode) for Na and K intercalation, respectively, a high specific capacity of ∼88 mA h/g (10 C), and a good rate performance at fast C-rate (360 C). The electrolyte composition significantly influences the long-term cycling stability of the CrHCF electrodes and the choice of the intercalating alkali metal cations significantly impacts the $E_{1/2}$ potentials. Finally, a CrHCF-based symmetric cell (quasi-supercapacitor) was constructed and showed high specific energy of ∼4.6 W h/kg at 100 C.

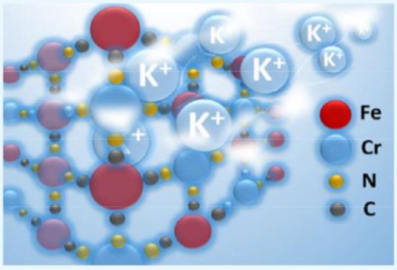

■ INTRODUCTION

The changes in society's perspective on climate change and sustainability have led to global compromises to reduce carbon-based emissions, such as the Paris climate change agreement. In a bid to cut carbon emission, various technologies have been developed for electricity provision from renewable energy sources, as well as for energy consumption, such as fuel cell cars and battery electric vehicles. In research and development of energy technologies, batteries (often combined with super-capacitors) are placed as the key candidates for electricity storage to transfer energy from production to consumption.[1,2] The expectation for the huge growth in the electric vehicle market has opened explosive increase of investments on battery development from both public and private institutions, leading to already successful commercialization.[3]

However, the development of appropriate electrochemical energy storage systems (ESSs) for grid ESSs is still at an early stage because of different requirements from mobile applications.[4] For large-scale applications, safety and costs should be considered to be equal to or even more important than energy density. The global energy demand is predicted to increase to ca. 30 TW_{avg} by 2050.[5] To achieve sustainable energy provision using new schemes, the availability and the abundance of materials should be taken into consideration as one of the main factors for upscaling. Figure 1 provides a visual comparison of the annual global production of common elements for battery materials. It suggests that the direct application of current Li-ion batteries onto grid-scale storage systems might not be achievable within a reasonable time scale,[5] despite their high energy density and well-developed technology. The limited availability and increasing demand of Li will further increase the price, which makes it more difficult to address the "Terawatt Challenge" in time.[6,7] Furthermore, flammable organic electrolytes of Li-ion batteries largely increase safety risks in large-scale applications.

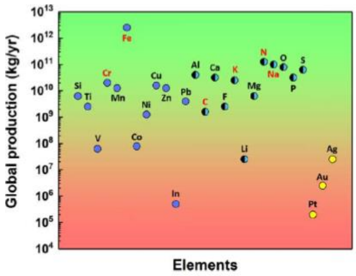

Figure 1. Annual global production of common elements for battery applications. The full circles represent the elements mainly used for electrode materials and the half-black circles represent those for either electrodes or electrolytes, partly adapted from ref 5.

Received: February 14, 2018
Accepted: April 5, 2018
Published: May 10, 2018

DOI: 10.1021/acsomega.8b00273
ACS Omega 2018, 3, 5111−5115

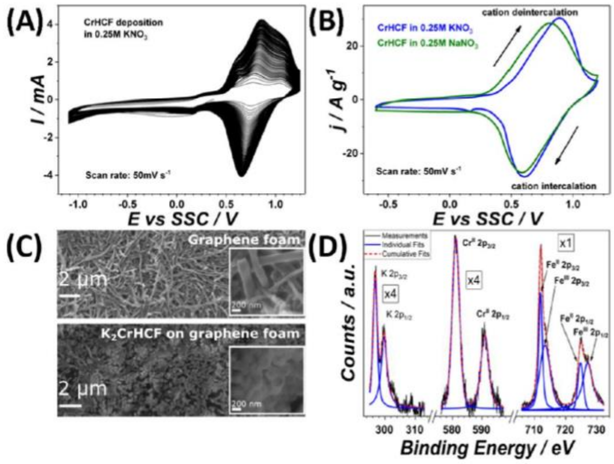

Figure 2. (A) Typical CVs characterizing the electrodeposition of CrHCF thin films. (B) Typical CVs of CrHCF thin film in aqueous 0.25 M KNO_3 (blue curve) and 0.25 M $NaNO_3$ (green curve) electrolytes. (C) SEM images of graphene foam before CrHCF deposition (top) and electrodeposited CrHCF thin films on graphene foam, showing the film morphology (bottom). (D) Typical XPS spectrum of electrodeposited CrHCF thin films. To improve the signal intensity, the CrHCF thin film was electrodeposited onto a Pt/Ti quartz crystal substrate.

Aqueous batteries using different alkali metal cations for grid-scale energy storage have drawn a considerable attention, thanks to safety and the high rate capability of aqueous electrolytes compared to organic electrolytes.[8] Among various classes of electrode materials for aqueous batteries, Prussian blue analogues (PBAs) are particularly interesting owing to their superior cycle life, low price, and abundant raw materials for building electrodes.[9−11] PBAs have fcc structure based on the two transition metals that are coordinated with sixfold carbon or nitrogen. The representative chemical formula of PBAs can be written as $X_yTM^1[TM^2(CN)_6]$ (where X represents the intercalating cations, TM^1 and TM^2 are the transition metals, and y is frequently 1 or 2). Many different PBAs have been studied for aqueous and nonaqueous batteries such as $Na_2Ni[Fe(CN)_6]$ (NiHCF),[12−14] $Na_{1.54}Co[Fe(CN)_6]_{0.86}\cdot\gamma_{0.14}\cdot2.16H_2O$ (CoHCF),[15] $K_{0.71}Cu\ [Fe(CN)_6]_{0.72}\cdot3.7H_2O$ (CuHCF),[16] $Na_2VO_x[Fe(CN)_6]$ (VHCF),[17] and $Na_xMn[Mn(CN)_6]$ (MnHCM).[18,19] However, considering utilization for large-scale applications and the availability of raw materials, it would be ideal to use the most abundant and light TM^1 and TM^2, namely, Cr and Fe (see Figure 1).

■ RESULTS AND DISCUSSION

Figure 2A shows a typical cyclic voltammogram (CV) characterizing the electrochemical deposition of chromium(II) hexacyanoferrate (CrHCF) thin films: the increase in cathodic and anodic current peaks reveals the growth of the film. Electrodeposition on graphene foam using a smaller potential range, for example, from −0.7 to 1.1 V versus silver/silver chloride (SSC), could not be achieved. Only when the lower potential was extended to −1.1 V versus SSC, CrHCF electrodeposition occurred. This is in good accordance with the claims of Gao and Jiang et al.[20,21] that reduction of Cr^{3+} (−0.95 V vs SSC)[22] is a mandatory condition for electrodeposition. Further insight into the CrHCF electrodeposition mechanism is beyond the scope of this manuscript.

Representative CVs of CrHCF thin films in aqueous 0.25 M $NaNO_3$ (green curves) and 0.25 M KNO_3 (blue curves) electrolytes characterizing intercalation and deintercalation of K^+ are depicted in Figure 2B. The cathodic and anodic peaks result from the change of the oxidation state of Fe in CrHCF, which in turn induces the intercalation and deintercalation of Na or K cations, respectively. Figure 2C shows typical scanning electron microscopy (SEM) images of graphene foam before (top) and after (bottom) CrHCF thin-film deposition. The substrate shows a branch-like structure, but after the deposition of CrHCF thin films, the structure appears to be homogeneously covered with the deposit and shows a smooth topology with an average feature size of about 166 nm. X-ray photoelectron spectroscopy (XPS) analysis of CrHCF thin films deposited on flat Pt electrodes (see Figure 2D) indicates the presence of all key elements, Fe, K, and Cr.

The presence of K-related peaks in the XPS data suggests that not all K^+ cations are removed from the CrHCF thin films during deintercalation (CrHCF is in the deintercalated state, Figure 2D). The investigation of Fe $2p_{1/2}$ and Fe $2p_{3/2}$ peaks reveals that the main oxidation state of iron after deintercalation is +3 (at ∼713.39 and ∼727.13 eV for Fe $2p_{3/2}$ and Fe $2p_{1/2}$, respectively); also, the peaks with less peak area and reduced binding energy can be observed alongside these peaks (at ∼711.99 and ∼724.91 eV for Fe $2p_{3/2}$ and Fe $2p_{1/2}$, respectively).

According to Yamashita and Hayes,[23] these peaks can be assigned to Fe^{II}, caused by partially divergent oxidation of Fe during the K deintercalation process. Therefore, the tentative reaction scheme for intercalation/deintercalation of K ions in CrHCF thin films can be proposed as following

$$KCr^{II}[Fe^{III}(CN)_6] + K^+ + e^- \leftrightarrow K_2Cr^{II}[Fe^{II}(CN)_6] \qquad (1)$$

According to recent studies,[13,18,24] anions participate in the intercalation/deintercalation processes and affect the reversibility and stability of the electrode materials. The influence of

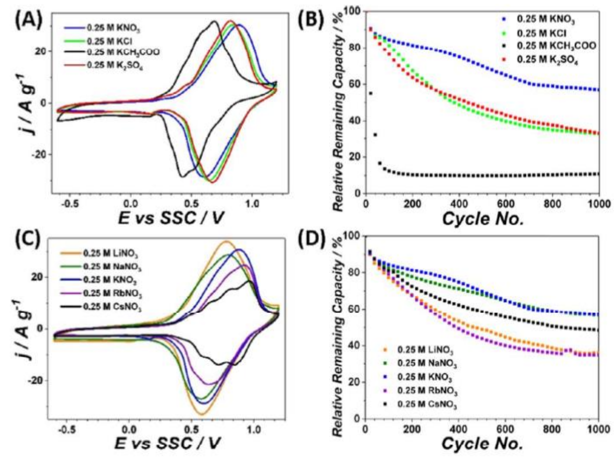

Figure 3. Characterization of the CrHCF electrodes in aqueous electrolytes containing different anions and/or alkali metal cations. (A) Typical CVs of CrHCF electrodes and (B) their long-term cycling tests in 0.25 M KNO_3 (blue), 0.25 M KCl (green), 0.25 M KOAc (black), and 0.25 M K_2SO_4 (red). (C) Typical CVs of CrHCF thin films and (D) their long-term cycling tests in 0.25 M $LiNO_3$ (yellow), 0.25 M $NaNO_3$ (olive), 0.25 M KNO_3 (blue), 0.25 M $RbNO_3$ (purple), and 0.25 M $CsNO_3$ (black).

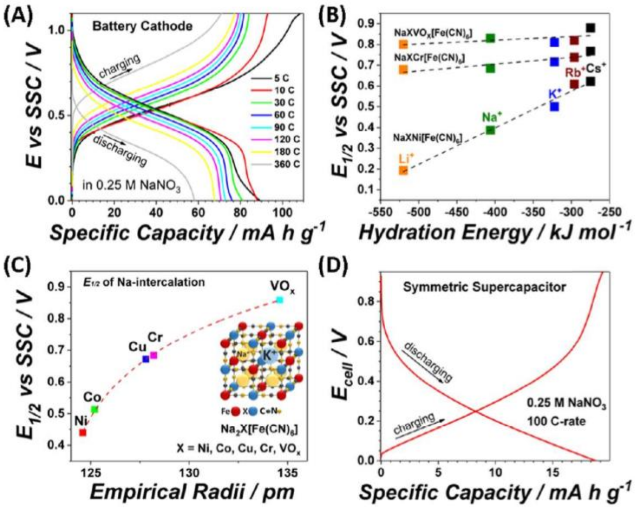

Figure 4. (A) Galvanostatic charge−discharge test of the CrHCF electrodes in 0.25 M $NaNO_3$ electrolytes at different C rates. (B) Comparison of the $E_{1/2}$ potentials for the CrHCF, VHCF, and NiCHF electrodes as a function of the hydration energy of the intercalating alkali metal cations. (C) $E_{1/2}$ potentials of NiHCF, CoHCF, CuHCF, VHCF, and CrHCF electrodes for Na intercalation/deintercalation as a function of empirical radii of transition metals.[17,26] (D) Charge−discharge characteristic curves for a CrHCF symmetric cell (quasi-supercapacitor) at 100 C using a 0.25 M $NaNO_3$ aqueous electrolyte.

the electrolyte composition on the reversibility and stability of CrHCF thin films was investigated using 0.25 M K-containing electrolytes, namely KNO_3, KCl, KOAc (potassium acetate), and K_2SO_4.

The shapes of CVs look similar regardless of the anions present in the electrolytes, whereas the potential of K intercalation/deintercalation varies (see Figure 3A). Among the studied electrolytes, the long-term stability tests of CrHCF electrodes showed the highest cycle stability in 0.25 M KNO_3 solutions (ca. 57% of the initial capacity), as shown in Figure 3B. The worst stability was observed for the sample in 0.25 M KOAc, which retained only ∼21% of its initial charge capacity

Table 1. Specific Capacities for CrHCF Electrodes in 0.25 M $NaNO_3$ at Different C-Rates

C-rate	5 C	10 C	30 C	60 C	90 C	120 C	180 C	360 C
specific capacity (mA h/g)	~89	~88	~81	~76	~73	~71	~68	~58

after only 50 cycles. The large channels of PBAs have been shown to be able to host different cations.[13,25] Figure 3C shows the CVs of CrHCF thin films in 0.25 M XNO_3 electrolytes (X = Li, Na, K, Rb, and Cs) characterizing quasi-reversible intercalation/deintercalation of different alkali metal cations into/from CrHCF. The shapes of CVs in different electrolytes appear similar except for the case of 0.25 M $CsNO_3$, but the positions of the CVs are slightly different. Subsequently, the long-term cycling tests of CrHCF thin films were performed in different electrolytes for 1000 cycles (see Figure 3D). CrHCF thin films cycled in $NaNO_3$ and KNO_3 showed the best stabilities after 1000 cycles, reaching ~56 and ~57% of the initial capacity, respectively.

The specific capacity of a CrHCF electrode in 0.25 M $NaNO_3$ was measured at multiple C rates to investigate the rate performance (see Figure 4A). The resulting specific capacities strongly depended on the applied C rate (summarized in Table 1). At 10 C, the electrode showed a specific capacity of ~88 mA h/g, and the specific capacities tend to be lower at higher C rates. The half-charge potential ($E_{1/2}$) of CrHCF thin films slightly varies depending on the nature of the alkali metal cations in different electrolytes as shown in Figure 4B.

In contrast to the case of NiHCF,[13] the half-charge potentials of CrHCF only slightly depend on the hydration energy of alkali metal cations, similar to VHCF.[17] Figure 4C shows a good correlation between the $E_{1/2}$ potentials for different PBAs (NiHCF, CoHCF, CuHCF, VHCF, and CrHCF) and the empirical radii of the key TM^1 elements of PBAs. The larger the empirical radii of the transition metals TM^1 in PBAs, the higher the $E_{1/2}$ potentials are.

Using CrHCF, we have also constructed a symmetric cell (quasi-supercapacitor with two identical CrHCF electrodes) operating at 100 C, with the maximum initial operational voltage of 0.95 V (see Figure 4D). It demonstrated a specific capacity of ~19 mA h/g and a specific energy density of ~4.6 W h/kg. At 120 C, the Coulombic efficiency exhibited ~99.6%. These values slightly outperform those of commercially available nonaqueous supercapacitor systems for power grids and industrial applications (energy density of ~3−4 W h/kg and maximum efficiency at nominal power of 98.6%).[27,28]

The good rate performance of CrHCF electrodes would position them between battery and supercapacitor materials, opening the possibility of future application of this material in hybrid ESSs. If the CrHCF electrode is combined with an appropriate Na battery anode, such as a phosphorene−graphene anode,[29] the recently reported high-rate TiO_2 anode,[30] or MnHCM,[18] it would result in a full cell with excellent voltage and rate capability.

■ CONCLUSIONS

In summary, we have demonstrated electrodeposited CrHCF thin films as an affordable cathode material for aqueous Na^+ and K^+ ion batteries. CrHCF electrodes exhibited the $E_{1/2}$ potential of ~0.69 and ~0.72 V versus SSC for Na and K intercalation, respectively, and a high specific capacity of ~88 mA h/g at 10 C, with excellent cycling stability and capacity retention of ~60% after 1000 cycles. Surprisingly, the choice of electrolytes has a significant influence on the cycle life. The electrode potential of PBAs appears to be adjustable by replacing N-coordinated transition metals with others. The symmetric cell using two CrHCF electrodes showed a high voltage of 0.95 V and an energy density of ~4.6 W h/kg at 100 C. The high availability of raw resources for the fabrication of CrHCF electrodes should enable the use of this material in large-scale ESSs.

■ EXPERIMENTAL SECTION

Electrochemical measurements were carried out in an electrochemical glass cell in Ar-saturated electrolytes (Argon 5.0 Westfalen AG) using a three-electrode configuration and a VSP-300 potentiostat (Bio-Logic, France) to control the experiments. Graphene/thermoplastic polyurethane flexible foam (Graphene Supermarket, USA) and AT-cut Pt quartz crystals (Standford Research Systems, USA) served as working electrodes and substrates, respectively, for the electrochemical deposition of CrHCF thin films. A Pt wire and 3 M KCl Ag/AgCl (SSC, Schott) were used as a counter and a reference electrode, respectively. The electrochemical deposition of CrHCF thin films was performed using a deposition solution containing 0.25 M KNO_3, 10 mM $CrCl_3$ (prepared from $CrCl_3 \cdot 6H_2O$, 95%, Sigma-Aldrich, Germany), and 5 mM $K_3Fe[(CN)_6]$ (~99%, ReagentPlus, Sigma-Aldrich, Germany) in ultrapure water (Evoqua, Germany) by cycling electrode potential between −1.1 and 1.25 V versus SSC at a scan rate of 50 mV s^{-1}. Cyclic voltammetry analysis of the resulting CrHCF thin films was performed in different electrolytes (0.25 M KNO_3, 0.25 M KCl, 0.25 M K_2SO_4, 0.25 M KCH_3COO, 0.25 M $LiNO_3$, 0.25 M $NaNO_3$, 0.25 M KNO_3, 0.25 M $RbNO_3$, and 0.25 M $CsNO_3$, all ReagentPlus, Sigma-Aldrich, Germany) to investigate the electrochemical characteristics and battery performance. For that, the electrode potential was cycled from −0.6 to 1.2 V versus SSC for 1000 cycles at a rate of 50 mV s^{-1}. Battery capacitance determination tests of CrHCF thin films were carried out in the 0.25 M $NaNO_3$ electrolyte at different C rates (5, 10, 30, 60, 90, 120, 180, and 360 C). A 0.95 V symmetric cell (a quasi-supercapacitor) was constructed using two CrHCF thin-film electrodes and the 0.25 M $NaNO_3$ aqueous electrolyte; and its charge−discharge test was performed at 100 C. Prior to the XPS measurements, the electrochemically deposited CrHCF thin films were rinsed with pure water several times to remove possible residues of still-adsorbed chemicals and then dried in ambient conditions. It should be noted here that the drying procedure in ambient conditions did not introduce any functional changes of the CrHCF thin films, neither in electrochemical nor XPS measurements. The XPS setup included SPECS GmbH XR50 X-ray source with Al anode (Kα line at 1486.61 eV), a SPECS GmbH spectrometer, and SPECS GmbH PHOIBOS 150 hemispherical energy analyzer. High-resolution field emission SEM analysis of the deposited films was performed on Zeiss NVision 40, operated at 3 kV.

■ AUTHOR INFORMATION

Corresponding Author

*E-mail: bandarenka@ph.tum.de. Phone: +49 (0) 89 289 12531 (A.S.B.).

ORCID

Philipp Marzak: 0000-0003-3372-0816
Aliaksandr S. Bandarenka: 0000-0002-5970-4315

Notes

The authors declare no competing financial interest.

■ ACKNOWLEDGMENTS

Financial support from the cluster of excellence Nanosystems Initiative Munich (NIM) and the TUM-IGSSE project 11.01 is gratefully acknowledged. J.Y. is thankful for the financial support from Nagelschneider Stiftung. This work was supported by the German Research Foundation (DFG) and the Technical University of Munich within the Open Access Publishing Funding Programme.

■ REFERENCES

(1) Nykvist, B.; Nilsson, M. Rapidly Falling Costs of Battery Packs for Electric Vehicles. *Nat. Clim. Change* **2015**, *5*, 329−332.

(2) Béguin, F.; Presser, V.; Balducci, A.; Frackowiak, E. Carbons and Electrolytes for Advanced Supercapacitors. *Adv. Mater.* **2014**, *26*, 2219−2251.

(3) Block, D.; Harrison, J. *Electric Vehicle Sales and Future Projections*; Electric Vehicle Transportation Center: Cocoa, FL, Jan 2014.

(4) Malhotra, A.; Battke, B.; Beuse, M.; Stephan, A.; Schmidt, T. Use Cases for Stationary Battery Technologies: A Review of the Literature and Existing Projects. *Renewable Sustainable Energy Rev.* **2016**, *56*, 705−721.

(5) Vesborg, P. C. K.; Jaramillo, T. F. Addressing the Terawatt Challenge: Scalability in the Supply of Chemical Elements for Renewable Energy. *RSC Adv.* **2012**, *2*, 7933−7947.

(6) Dunn, B.; Kamath, H.; Tarascon, J.-M. Electrical Energy Storage for the Grid: A Battery of Choices. *Science* **2011**, *334*, 928−935.

(7) Sonoc, A.; Jeswiet, J. A Review of Lithium Supply and Demand and a Preliminary Investigation of a Room Temperature Method to Recycle Lithium Ion Batteries to Recover Lithium and Other Materials. *Procedia CIRP* **2014**, *15*, 289−293.

(8) Kim, H.; Hong, J.; Park, K.-Y.; Kim, H.; Kim, S.-W.; Kang, K. Aqueous Rechargeable Li and Na Ion Batteries. *Chem. Rev.* **2014**, *114*, 11788−11827.

(9) Lu, Y.; Wang, L.; Cheng, J.; Goodenough, J. B. Prussian Blue: a New Framework of Electrode Materials for Sodium Batteries. *Chem. Commun.* **2012**, *48*, 6544−6546.

(10) Xue, L.; Li, Y.; Gao, H.; Zhou, W.; Lü, X.; Kaveevivitchai, W.; Manthiram, A.; Goodenough, J. B. Low-Cost High-Energy Potassium Cathode. *J. Am. Chem. Soc.* **2017**, *139*, 2164−2167.

(11) Pasta, M.; Wessells, C. D.; Huggins, R. A.; Cui, Y. A High-rate and Long Cycle Life Aqueous Electrolyte Battery for Grid-scale Energy Storage. *Nat. Commun.* **2012**, *3*, 1149.

(12) Wessells, C. D.; Peddada, S. V.; Huggins, R. A.; Cui, Y. Nickel Hexacyanoferrate Nanoparticle Electrodes for Aqueous Sodium and Potassium Ion Batteries. *Nano Lett.* **2011**, *11*, 5421−5425.

(13) Yun, J.; Pfisterer, J.; Bandarenka, A. S. How Simple Are the Models of Na Intercalation in Aqueous Media? *Energy Environ. Sci.* **2016**, *9*, 955−961.

(14) Senthilkumar, S. T.; Abirami, M.; Kim, J.; Go, W.; Hwang, S. M.; Kim, Y. Sodium-ion Hybrid Electrolyte Battery for Sustainable Energy Storage Applications. *J. Power Sources* **2017**, *341*, 404−410.

(15) Pasta, M.; Wang, R. Y.; Ruffo, R.; Qiao, R.; Lee, H.-W.; Shyam, B.; Guo, M.; Wang, Y.; Wray, L. A.; Yang, W.; Toney, M. F.; Cui, Y. Manganese−Cobalt Hexacyanoferrate Cathodes for Sodium-Ion Batteries. *J. Mater. Chem. A* **2016**, *4*, 4211−4223.

(16) Wessells, C. D.; Huggins, R. A.; Cui, Y. Copper Hexacyanoferrate Battery Electrodes with Long Cycle Life and High Power. *Nat. Commun.* **2011**, *2*, 550.

(17) Paulitsch, B.; Yun, J.; Bandarenka, A. S. Electrodeposited $Na_2VO_x[Fe(CN)_6]$ Films as a Cathode Material for Aqueous Na-Ion Batteries. *ACS Appl. Mater. Interfaces* **2017**, *9*, 8107−8112.

(18) Yun, J.; Schiegg, F. A.; Liang, Y.; Scieszka, D.; Garlyyev, B.; Kwiatkowski, A.; Wagner, T.; Bandarenka, A. S. Electrochemically Formed Na_xMn $[Mn (CN)_6]$ Thin Film Anodes Demonstrate Sodium Intercalation and De-Intercalation at Extremely Negative Electrode Potentials in Aqueous Media. *ACS Appl. Energy Mater.* **2018**, *1*, 123−128.

(19) Lee, H.-W.; Wang, R. Y.; Pasta, M.; Lee, S. W.; Liu, N.; Cui, Y. Manganese Hexacyanomanganate Open Framework as a High-Capacity Positive Electrode Material for Sodium-Ion Batteries. *Nat. Commun.* **2014**, *5*, 5280.

(20) Gao, Z. Electrochemical Behavior of Chromium(III)-Hexacyanoferrate Film Modified Electrodes: Voltammetric and Electrochemical Impedance Studies. *J. Electroanal. Chem.* **1994**, *370*, 95−102.

(21) Jiang, M.; Zhou, X.; Zhao, Z. A New Zeolitic Thin Film Based on Chromium Hexacyanoferrate on Conducting Substrates. *J. Electroanal. Chem. Interfacial Electrochem.* **1990**, *287*, 389−394.

(22) Bratsch, S. G. Standard Electrode Potentials and Temperature Coefficients in Water at 298.15 K. *J. Phys. Chem. Ref. Data* **1989**, *18*, 1−21.

(23) Yamashita, T.; Hayes, P. Analysis of XPS Spectra of Fe^{2+} and Fe^{3+} Ions in Oxide Materials. *Appl. Surf. Sci.* **2008**, *254*, 2441−2449.

(24) Ventosa, E.; Paulitsch, B.; Marzak, P.; Yun, J.; Schiegg, F.; Quast, T.; Bandarenka, A. S. The Mechanism of the Interfacial Charge and Mass Transfer during Intercalation of Alkali Metal Cations. *Adv. Sci.* **2016**, *3*, 1600211.

(25) Wang, R. Y.; Wessells, C. D.; Huggins, R. A.; Cui, Y. Highly Reversible Open Framework Nanoscale Electrodes for Divalent Ion Batteries. *Nano Lett.* **2013**, *13*, 5748−5752.

(26) Teatum, E.; Gschneider, K.; Waber, J. *Report NoLA-2345*; U.S. Dept. of Commerce: Washington, D.C., 1960; p 45.

(27) Grid-Scale Energy Storage System for Back-Up Power and Power Quality Applications. https://www.skeletontech.com/skelgrid (accessed March 30, 2018).

(28) Skeleton Module 170V SMOD170V53F Datasheet, 2016. https://www.skeletontech.com/hubfs/Skeleton-170Vmodule_datasheet.pdf (accessed Mar 30, 2018), Skeleton Technologies GmbH.

(29) Sun, J.; Lee, H.-W.; Pasta, M.; Yuan, H.; Zheng, G.; Sun, Y.; Li, Y.; Cui, Y. A Phosphorene−Graphene Hybrid Material as a High-Capacity Anode for Sodium-Ion Batteries. *Nat. Nanotechnol.* **2015**, *10*, 980−985.

(30) Zhou, M.; Xu, Y.; Wang, C.; Li, Q.; Xiang, J.; Liang, L.; Wu, M.; Zhao, H.; Lei, Y. Amorphous TiO_2 Inverse Opal Anode For High-Rate Sodium Ion Batteries. *Nano Energy* **2017**, *31*, 514−524.

ACS APPLIED ENERGY MATERIALS

Article

Cite This: *ACS Appl. Energy Mater.* 2018, 1, 123−128

www.acsaem.org

Electrochemically Formed $Na_xMn[Mn(CN)_6]$ Thin Film Anodes Demonstrate Sodium Intercalation and Deintercalation at Extremely Negative Electrode Potentials in Aqueous Media

Jeongsik Yun,[†,‡,∥] Florian A. Schiegg,[†,‡,∥] Yunchang Liang,[†,‡] Daniel Scieszka,[†,‡] Batyr Garlyyev,[†]
Anika Kwiatkowski,[§] Thomas Wagner,[§] and Aliaksandr S. Bandarenka*[,†,‡]

[†]Physik-Department ECS, Technische Universität München, James-Franck-Straße 1, 85748 Garching bei München, Germany
[‡]Nanosystems Initiative Munich (NIM), Schellingstraße 4, 80799 Münich, Germany
[§]Department of Chemistry, Technische Universität München, Lichtenbergstrasse 4, 85747 Garching bei München, Germany

Supporting Information

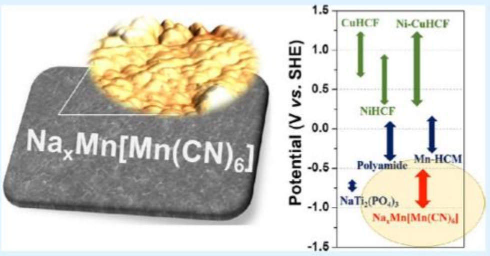

ABSTRACT: The development of electrode materials for Na-ion batteries has been substantially accelerated recently with respect to application in grid energy storage systems. Specifically, development of Na-ion batteries operating in aqueous media is considered more promising for this application due to safety issues. Many different types of cathode materials for aqueous Na-ion batteries have been proposed; however, the number and performance of contemporary anode materials are still insufficient for practical deployment. In this work, we demonstrate that electrochemically deposited $Na_xMn[Mn(CN)_6]$ thin films are very promising anode materials for aqueous Na-ion batteries. $Na_xMn[Mn(CN)_6]$ films exhibit (i) very low half-charge potential ca. −0.73 V vs SHE (ca. −0.93 V vs SSC) being one of the lowest among those reported in the literature for the electrode materials, which also inhibit hydrogen evolution reaction; (ii) a specific capacity of ca. 85 mA h g^{-1}; and (iii) only ~3% loss of capacity and high round-trip efficiency (99.6%) after 3,000 cycles. Surprisingly, the choice of the electrolyte composition has a very strong influence not only on the intercalation process but also on the long-term performance of battery anodes and their electrode surface morphology.

KEYWORDS: *aqueous Na-ion batteries, Na intercalation, $Na_xMn[Mn(CN)_6]$, Na-ion battery anodes, electrochemical impedance spectroscopy*

1. INTRODUCTION

Over the past years, the need for decentralized integration of so-called large energy storage systems (ESSs) as buffers to smoothen power fluctuation generated by less flexible renewable energy sources has risen in importance.[1−6] Aqueous rechargeable alkali-metal-ion batteries and especially aqueous rechargeable sodium-ion batteries have positioned themselves as promising alternatives to conventional lithium-ion batteries (LIBs) to cope with these needs.[7,8] From a kinetic point of view, aqueous sodium-ion batteries profit from a favorable transport of Na^+ over Li^+ in both electrodes and electrolyte, enhancing the performance of the system.[9−11] Moreover, their electrolyte inherent safety and environmental friendliness coupled to the cost-efficiency due to extremely abundant constituents are major arguments to implement them in large-scale ESSs. However, the bigger atomic radius and mass of Na^+ ions compared to Li^+ ions implying poorer volumetric and gravimetric energy densities, as well as the smaller operating voltage window arising from the electrolysis of the aqueous electrolyte together with the lack of suitable anode materials in aqueous media, are among the biggest drawbacks that have to be balanced. Thus, for aqueous Na-ion batteries to become competitive in ESS applications, new materials that effectively overcome these limitations have to be found.

Many cathode materials for LIB such as $LiCoO_2$, $LiMn_2O_4$, and $LiFePO_4$ are applicable to sodium-ion batteries, but commonly used anode materials for LIB such as graphite are not suitable for them due to their instability in the Na^+-intercalated state in aqueous electrolytes.[12] The anode materials for aqueous Na-ion batteries should fulfill various requirements. (i) They should exhibit the lowest possible electrode potentials for sodium intercalation and deintercalation to achieve high full cell voltages and high energy densities, but, at the same time, (ii) they should not trigger any side reactions such as hydrogen evolution reaction (HER). Furthermore, the anode materials have to be chemically and

Received: October 11, 2017
Accepted: December 18, 2017
Published: December 18, 2017

DOI: 10.1021/acsaem.7b00022
ACS Appl. Energy Mater. 2018, 1, 123−128

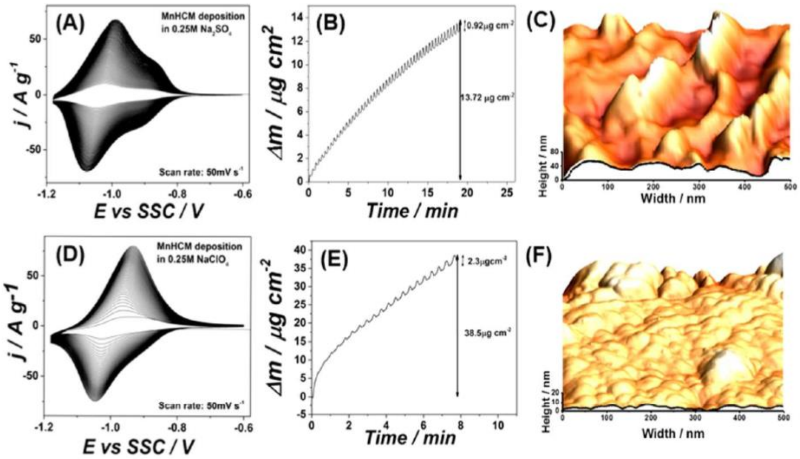

Figure 1. Electrochemical and AFM characterization of $Na_xMn[Mn(CN)_6]$ thin films. The films were deposited from aqueous solutions containing 7 mM $MnSO_4$ and 11 mM $K_4[Mn(CN)_6]$ together with (A–C) 0.25 M Na_2SO_4 and (D, E) 0.25 M $NaClO_4$. The panels show characteristic cyclic voltammograms of $Na_xMn[Mn(CN)_6]$ thin films during deposition from the aqueous solution containing (A) 0.25 M Na_2SO_4 and (D) 0.25 M $NaClO_4$, respectively. Corresponding EQCM curves (B, E) show the mass changes of the deposited $Na_xMn[Mn(CN)_6]$ thin films as (B) ca. 14 μg cm^{-2} and (E) ca. 38.5 μg cm^{-2}, respectively. AFM images of $Na_xMn[Mn(CN)_6]$ thin films from the deposition solution containing (C) 0.25 M Na_2SO_4 and (F) 0.25 M $NaClO_4$ reveal drastically different surface roughness. Note the different scale of the z-axis of the profile line across the bottom of each AFM image in panels C and F.

mechanically stable at the operating pHs of the electrolyte to prevent dissolution and deformation of the active material. Correspondingly, the anode materials have to operate in the same media (be compatible) with the state-of-the-art cathodes.[13]

Several types of anode materials have been proposed to meet the above-mentioned requirements. For instance, NASICON-type anodes were first proposed by Park et al., and their specific capacity exhibited 100 mA h g^{-1} at 2 C with the plateau voltage at ca. −0.61 V vs SHE and a cycle retention of 95% over 100 cycles.[14−16] Qu et al. reported intercalation properties of the nanostructured vanadium oxide $V_2O_5 \cdot 0.6H_2O$, presenting a reversible capacity of 43 mA h g^{-1} in a 0.5 M Na_2SO_4 aqueous electrolyte.[17] Further improvements led to the one-dimensional nanostructured $Na_2V_6O_{16} \cdot nH_2O$ with a lower redox potential and a high initial charge capacity of ca. 123 mA h g^{-1}.[18] However, it suffers from irreversible structural changes upon Na^+ insertion, deteriorating its intercalation properties resulting in a specific capacity of 42 mA h g^{-1} in subsequent cycles. Recently, a 1,4,5,8-naphthalenetetracarboxylic dianhydride (NTCDA)-derived polyimide was reported by Qin et al., presenting a discharge potential of *ca* −0.19 V vs SHE when operated in a highly concentrated 5 M $NaNO_3$ aqueous electrolyte.[19] It showed an extremely high discharge capacity of 165 mA h g^{-1} at a discharge rate of 1/3 C. However, its stability is rather questionable, with a capacity decay of 17% after 20 cycles; and the Na^+ storage mechanism is still not fully understood. Pasta et al. showed another approach using coprecipitation of the Prussian blue analogue (PBA)-based $Mn^{II}{-}N{\equiv}C{-}Mn^{III/II}$, also operating in aqueous electrolytes.[13,20] Its working potential was found to be ca. 0.052 V vs SHE, with a specific capacity of 57 mA h g^{-1} and a high rate capability at C rates between 1 and 10 C. When combining the manganese hexacyanomanganate (MnHCM) anode with the well-known copper hexacyanoferrate (CuHCF) cathode, it showed an almost negligible capacity loss over 1,000 cycles, presenting a Coulombic efficiency of 99.8% at 10 C. Despite the various approaches, it is evident that further research is necessary to come up with an anode material to achieve significantly higher energy density, specific capacity, and good stability.

In this work, we demonstrate that electrochemically deposited MnHCM thin films show an extremely low half-charge intercalation potential of ca. −0.73 V vs SHE, which is one of the lowest potentials ever reported for the anode material for aqueous Na-ion batteries, to the best of our knowledge. The electrochemically deposited thin film furthermore showed a specific capacity of 85 mA h g^{-1} with retention of 97% over 3,000 cycles and a high round-trip efficiency of ∼99.6%, thus presenting a significant improvement compared to the previously reported systems. The inhibition of HER at the potentials of charging/discharging allows, in principle, achieving the operating potential over 2 V if combined with state-of-the-art cathode materials for aqueous Na-ion batteries. Interestingly, not only ions in the electrolyte involved in the intercalation processes but also different anions species, which are present in the deposition solutions, drastically change the morphology and the performance of the resulting electrode material.[21−25]

2. RESULTS AND DISCUSSION

The electrochemical deposition of $Na_xMn[Mn(CN)_6]$ thin films was conducted making use of the following tentative redox schemes, which manifest themselves in Figure 1A,D.

DOI: 10.1021/acsaem.7b00022
ACS Appl. Energy Mater. 2018, 1, 123−128

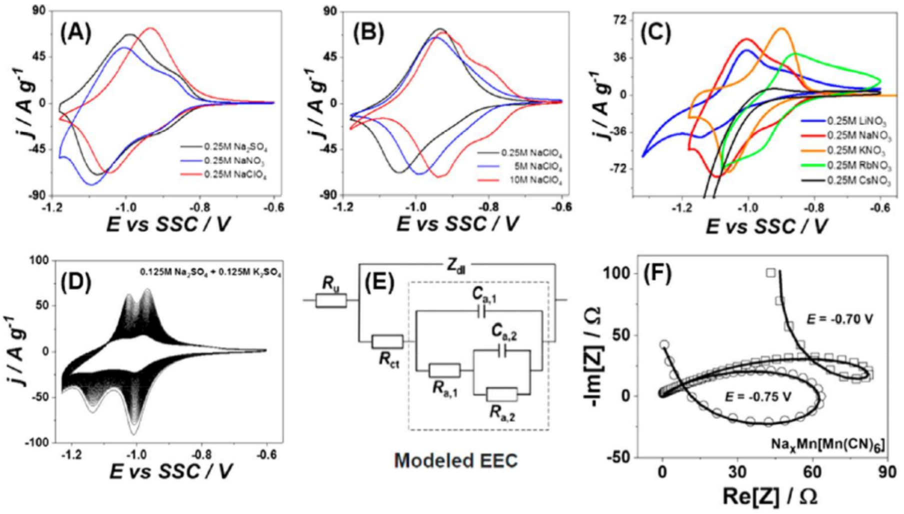

Figure 2. Characterization of the MnHCM thin films. (A) CVs of MnHCM thin films in 0.25 M Na_2SO_4 (black), 0.25 M $NaNO_3$ (blue), and 0.25 M $NaClO_4$ (red), respectively. (B) CVs of MnHCM thin films in $NaClO_4$ electrolytes of different concentrations: 0.25 M (black), 5 M (blue), and 10 M (red). (C) Intercalation/deintercalation of different alkali metal cations (Li^+, Na^+, K^+, Rb^+, and Cs^+) into MnHCM thin films. (D) CVs of MnHCM thin films in the mixture of 0.125 M Na_2SO_4 and 0.125 M K_2SO_4 electrolytes (scan rate in all the cases is 50 mV s^{-1}). (E) The equivalent electric circuit proposed to model the intercalation mechanism (see the SI) and (F) the collected EIS data (open symbols) of MnHCM thin films in 0.25 M Na_2SO_4 electrolyte and their fitting data (solid lines) are shown, respectively.

reduction of the redox active species:

$$3Na^+(aq) + Mn^{2+}(aq) + [Mn^{II}(CN)_6]^{4-}(aq) + e^- \rightarrow Na_3Mn[Mn^I(CN)_6](s) \quad (1)$$

oxidation of the redox active species:

$$Na_3Mn[Mn^I(CN)_6](s) \rightarrow Na_2Mn[Mn^{II}(CN)_6](s) + Na^+(aq) + e^- \quad (2)$$

Panels A and D of Figure 1 show the characteristic cyclic voltammograms (CVs) for electrochemical deposition of $Na_xMn[Mn(CN)_6]$ thin films from deposition solutions containing 7 mM $MnSO_4$ and 11 mM $K_3[Mn(CN)_6]$ based on (A) 0.25 M Na_2SO_4 and (D) 0.25 M $NaClO_4$ electrolytes, respectively. The deposition from the 0.25 M $NaClO_4$-based solution results in a faster growth of the $Na_xMn[Mn(CN)_6]$ thin films compared to that from the 0.25 M Na_2SO_4-based solution. Panels B and E of Figure 1 demonstrate typical electrochemical quartz crystal microbalance (EQCM) curves describing the mass changes of the Au quartz crystal electrodes during electrochemical deposition of $Na_xMn[Mn(CN)_6]$ thin films from the 0.25 M Na_2SO_4-based and the 0.25 M $NaClO_4$-based deposition solutions, respectively. Resulting mass changes due to the thin film depositions result in ~14 μg cm^{-2} from the 0.25 M Na_2SO_4-based solution and ~38 μg cm^{-2} from the 0.25 M $NaClO_4$-based solution, respectively. The "oscillations" of the mass seen in Figure 1B,E characterize intercalation/deintercalation of Na ions during the film deposition.

Interestingly, different practically pH-neutral electrolytes (i.e., Na_2SO_4 and $NaClO_4$) not only change the rate of the deposition but also influence the surface morphology of the deposited films (Figure 1C,F). Counterintuitively in this case, the faster deposition results in a much smoother and uniform surface than the slower deposition, indicating different modes of deposition. This can be closely related to the nature of the anions species that are present in the deposition solutions; anions should likely participate in the deposition process through specific adsorption at the surface. Recent studies on the intercalation mechanism support this hypothesis.[21−25]

The studies found that anion species participate in the intercalation processes and have a significant influence on the intercalation. In order to further investigate the influence of electrolyte composition on the intercalation, cyclic voltammetry of $Na_xMn[Mn(CN)_6]$ thin films was performed in different electrolytes. Figure 2A shows representative CVs of $Na_xMn[Mn(CN)_6]$ thin films in 0.25 M Na_2SO_4, 0.25 M $NaNO_3$, and 0.25 M $NaClO_4$ electrolytes. As already found in the previous research, the "irreversibility" of intercalation varies depending on the anions in the electrolytes, exhibiting different shapes of CVs.[21−25] Figure 2B shows CVs of $Na_xMn[Mn(CN)_6]$ in $NaClO_4$ electrolytes of different concentrations (0.25, 5, and 10 M). As can be seen in Figure 2B, the voltammetric behavior of the film is more reversible in electrolytes with higher ionic strength.

Since Na_2SO_4 shows only limited solubility in water (lower than 2 M), $NaClO_4$ was chosen due to its extremely high solubility. The higher the concentration is of $NaClO_4$ electrolytes, the more intercalation/deintercalation reversibility can be achieved. Especially, at 10 M $NaClO_4$, the CV shows almost symmetric shape. The peak separations were reduced from $\Delta E_{0.25M}$ = 100 mV at a 0.25 M $NaClO_4$ electrolyte over ΔE_{5M} = 50 mV to ΔE_{10M} = 1 mV, significantly improving the systems' efficiency, and this cannot be explained just with the changes in the ionic conductivity of the electrolyte. Some PBAs

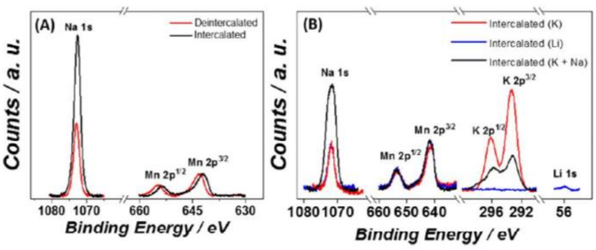

Figure 3. (A) XPS data for MnHCM thin films in "Na-intercalated" and "Na-deintercalated" states. (B) XPS data for MnHCM thin films at intercalated states with different alkali metal cations (Li, Na, and K). All XPS peaks confirmed the presence of intercalated species in the MnHCM thin films. The intensity of the Na peaks is different according to the state of the intercalation, but their positions are the same, while Mn peaks were shifted according to the intercalation/deintercalation of Na ions.

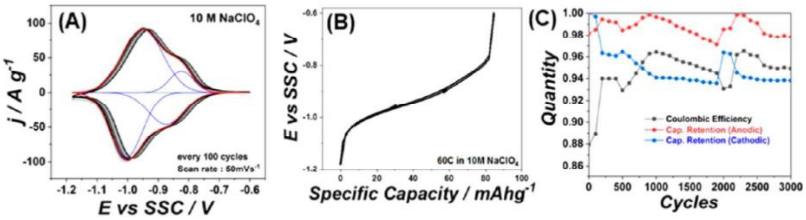

Figure 4. Battery tests of MnHCM thin films. (A) CVs of MnHCM thin films in 10 M $NaClO_4$ for over 3,000 cycles (only every 100th cycle is shown; deconvolution of the peaks is also presented). (B) Battery capacity determination of MnHCM thin films at 60 C (ca 5 A g^{-1}). The resulting specific capacity was ca. 85 mA h g^{-1} with almost overlapped hysteresis of charge/discharge. (C) Anodic and cathodic capacity retention and Coulombic efficiency of the deposited thin film.

such as nickel hexacyanoferrate (NiHCF) and cobalt hexacyanoferrate (CoHCF) have different electrode potentials for intercalation of alkali metal cations, which can be associated with different hydration energies of alkali metal cations.[21,24] However, MnHCM thin films show very poor intercalation properties for Li^+, Rb^+, and Cs^+ ions (see Figure 2C). Considering the ionic radius of Li^+, this can be found as a rather surprising fact, which, however, can be explained by taking into account the influence of alkali metal cations on the HER catalytic activity of various electrodes.[26]

In the case of Cs intercalation, only HER takes place at the potential where Na or K intercalation occurs, showing that the nature of the cations drastically influences the HER catalytic activity of electrodes.[26] A simple assumption that the size of the intercalating species or the related hydration energy would determine the nature of the intercalation process is not true in this particular case; the catalytic properties of the whole system likely influence the interfacial process.[21] Figure 2D shows CVs of co-intercalation of Na^+ and K^+ ions, which are simultaneously present in the electrolyte, into the MnHCM thin films. The CVs show that co-intercalation of both ions is possible, but the films suffer from severe degradation in a number of cycles. Panels E and F of Figure 2 are the equivalent electric circuit (EEC) model used for fitting and collected EIS spectra for MnHCM thin films, respectively. As shown in Figure 2F, the "loop-shaped" EIS spectra indicate at least three stages during the intercalation processes.[21−25] The Krammer–Kronig test did not reveal any problem with the quality of the fittings. Detailed explanation and interpretation for the physical meaning of the EEC model and its corresponding fittings are given in the Supporting Information (SI).

All key elements for MnHCM thin films were found from the XPS analysis. The comparison of MnHCM thin films in the Na-intercalated state and the Na-deintercalated state confirmed that not all Na ions are expelled from the films as expected from eq 2 as evident from Figure 3A. Figure 3B shows XPS peaks regarding different elements. Interestingly, characteristic XPS peaks for Na were seen at all MnHCM thin films, which shows that some amount of Na is present in the MnHCM thin films regardless of the intercalation of different alkali metal cations from the corresponding solutions containing Li or K ions. These Na ions are the ones of the main composition of the MnHCM structure. Mn peaks are clearly shown in all of the XPS measurements. Characteristic XPS peaks for lithium were very small, verifying the analysis of the CV of MnHCM thin films in 0.25 M $LiNO_3$ and the limited, negligible intercalation of Li ions into the MnHCM thin films. On the other hand, XPS peaks related to potassium prove that intercalation of K ions had taken place not only in 0.25 M K_2SO_4 but also in the mixture of 0.125 M Na_2SO_4 and 0.125 M K_2SO_4 electrolytes. The comparison of MnHCM thin films in the Na-intercalated state and the Na-deintercalated state confirmed that not all Na ions are expelled from the films. The shift of the binding energy of Mn elements between Mn $2p^{1/2}$ and Mn $2p^{3/2}$ peaks of the Na-intercalated/-deintercalated films suggests that the intercalation of sodium is accompanied by the change of the oxidation state of Mn. The binding energies of Mn $2p^{3/2}$ of $Na_xMn[Mn(CN)_6]$ are 641.15 eV for Mn^{2+} (Na-intercalated film) and 642.19 eV for Mn^{3+} (Na-deintercalated film). Compared to the binding energies of Mn $2p^{3/2}$ of $Na_2Mn[Mn(CN)_6]$, the difference of the binding energy shows only 0.05 eV for Mn^{2+} and 0.09 eV for Mn^{3+}, respectively.[20] Those values are in good agreement with the other literature values.[30]

Based on the above-discussed findings, an optimized system was set up and its properties were analyzed. A 10 M amount of $NaClO_4$ was chosen as an electrolyte to provide the charge carrier of the system due to its considerably higher solubility limit compared to Na_2SO_4 and the fact that the investigated concentration effect outweighs the anion effect. The system was cycled 3,000 times with a scan rate of 50 mV s^{-1} between −1.18 and −0.6 V. Figure 4A displays CVs of MnHCM thin films in 10 M $NaClO_4$, where every 100th cycle is shown. Other than that postulated so far, no HER was observed in this range. The cathodic and anodic half-charged potentials were found to be as low as −0.958 and −0.930 V, after 100 cycles, respectively. After the full 3,000 cycles, they had slightly shifted toward less negative values (ca. −0.937 and −0.910 V, respectively), thus showing a superior cycling stability. The system presented a specific discharge capacity of ~85 mA h g^{-1} at a high C rate (60 C, i.e., ca. 5A g^{-1}) as shown in Figure 4B. The capacity retention over the 3,000 cycles was as high as 97.0%, and the Coulombic efficiency improved from 95.1% in the first cycle to 99.6% in the last cycle (shown in Figure 4C). Figure 5 shows the different classes of the electrode materials for aqueous sodium-ion batteries. Electrochemically deposited $Na_xMn[Mn(CN)_6]$ thin films exhibit one of the lowest electrode potentials among different types of electrode materials for aqueous Na-ion batteries. Notably, no HER was observed (in the presence of Na^+ and K^+) even at such a low potential.

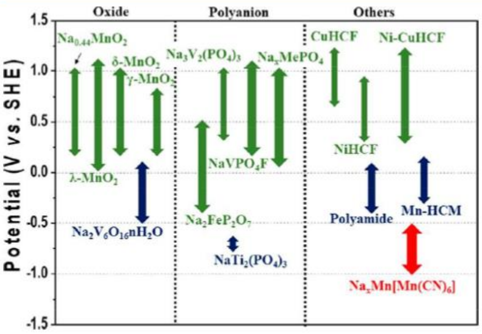

Figure 5. Working electrode potentials of $Na_xMn[Mn(CN)_6]$ in comparison with different classes of electrode materials for aqueous Na-ion batteries. Adapted with permission from ref 12. Copyright 2014 American Chemical Society.

3. CONCLUSION

An extremely low electrode potential for Na-intercalation/-deintercalation in aqueous media was achieved with electrochemically deposited sodium manganese hexacyanomanganate thin films, which at the same time do not catalyze the hydrogen evolution reaction. The half-charged potential of $Na_xMn[Mn(CN)_6]$ thin films in a 10 M $NaClO_4$ aqueous electrolyte exhibited −0.93 V vs SSC with a high Coulombic efficiency and a good specific capacity of 85 mA h g^{-1} showing only marginal losses over 3,000 cycles. Interestingly, electrolyte composition and its concentration have an influence not only on the battery performance but also on the morphology of the $Na_xMn[Mn(CN)_6]$ thin film during the deposition. Intercalation of Li^+ and Rb^+ into $Na_xMn[Mn(CN)_6]$ thin film triggered severe degradation of the films upon cycling, and Cs^+ does not intercalate into the films at all. Notably, hydrogen evolution reaction does not take place at the $Na_xMn[Mn(CN)_6]$ thin films at the potentials even lower than −1.15 V vs SSC in 0.25 M $NaNO_3$ and 0.25 M KNO_3 electrolytes, but, surprisingly, hydrogen evolution reaction takes place at the $Na_xMn[Mn(CN)_6]$ thin films in 0.25 M $CsNO_3$, which suggests the electrolyte composition has a strong influence not only on the intercalation properties but also on side reactions at the electrode. For the optimization of the aqueous Na-ion batteries for future applications, the role of the electrolytes composition should be comprehensively studied.

4. EXPERIMENTAL SECTION

Deposition, in situ characterization, and battery performance tests of $Na_xMn[Mn(CN)_6]$ thin films were performed in an argon-flooded three-electrode setup consisting of an AT-cut Au quartz crystal wafer (5 MHz, 1 in. diameter) or an Au-sputtered glass arrandee as working electrode, a Pt wire as counter electrode, and an Ag/AgCl (SSC) reference electrode, against which all the potentials are referred to (unless others are indicated explicitly), with the exception of Figure 5, summarizing the data from the literature and that obtained in this work. Potentials and currents were controlled with a VSP-300 potentiostat (Bio-Logic, France). A QCM 200 (Stanford Research Systems, USA) electrochemical quartz crystal microbalance (EQCM) was used to monitor the mass changes related to the deposited film. The schematics of the experimental setup are provided in Figure S4.

For the deposition of MnHCM thin films, an aqueous solution containing 0.25 M Na_2SO_4, 7 mM $MnSO_4$, and 11 mM $K_4[Mn(CN)_6]$ (see the SI) was prepared, and the potential of the working electrode was cycled at a scan rate of 50 mV s^{-1} in the range between −1.18 and −0.6 V. The same deposition procedure was modified by replacing 0.25 M Na_2SO_4 with 0.25 M $NaClO_4$ in the preparation of the deposition solution. Potassium hexacyanomanganate(III) was synthesized following a slight alternation of the methods of Grube, Brause, and Meyer, respectively.[27] All other chemicals used are referred to in more detail in the SI.

The reaction mechanism was analyzed using electrochemical impedance spectroscopy (EIS) using a 10 mV ac perturbation with probing frequencies between 10 kHz and 0.5 Hz in the potential range described above. The fitting quality was controlled by the normalized root-mean-square deviations, and the fitting was performed with the homemade "EIS Data Analysis 1.1" software.[28] The morphology of the synthesized film was investigated using a multimode atomic force microscopy (AFM) instrument (Veeco Instruments Inc.) with a Nanoscope IIID controller using the Nanoscope 5.31r1 software. All measurements were performed in tapping mode making use of Bruker REESP-300 AFM tips. All microscopy data were analyzed by the WSxM 5.0 Develop 8.0 software.[29]

The MnHCM thin film chemical composition was investigated by means of X-ray photoelectron spectroscopy (XPS) using a SPECS XPS spectrometer (SPECS, Germany) employing an Al anode (12 kV, 200 W) and setting the pass energy to 20 eV to ensure a high resolution of the spectra. Due to the high vulnerability of the film in the presence of oxygen, water, and possibly light, special precautions, such as the use of an Ar-purged preconditioning cell and the shielding from light had to be taken.[20] Further details on experimental procedures, instrumentation, and chemicals are given in the SI.

■ ASSOCIATED CONTENT

Ⓢ Supporting Information

The Supporting Information is available free of charge on the ACS Publications website at DOI: 10.1021/acsaem.7b00022.

Synthesis of potassium hexacyanomanganate(III) trihydrate, chemicals used, fitting of EIS spectra and their interpretation, experimental setup, and scanning electron microscope measurement (PDF)

■ AUTHOR INFORMATION

Corresponding Author

*E-mail: bandarenka@ph.tum.de.

ORCID

Aliaksandr S. Bandarenka: 0000-0002-5970-4315

Author Contributions

[∥]J.Y. and F.A.S. contributed equally to this work.

Notes

The authors declare no competing financial interest.

■ ACKNOWLEDGMENTS

Financial support from the cluster of excellence Nanosystems Initiative Munich (NIM) is gratefully acknowledged. J.Y. is thankful for the financial support from Nagelschneider Stiftung. T.W. and A.K. thank the Department of Chemistry TUM for courtesy granting access to laboratory space and equipment.

■ REFERENCES

(1) Obama, B. The irreversible Momentum of Clean Energy. *Science* **2017**, *355*, 126−129.

(2) Drechsler, M.; Egerer, J.; Lange, M.; Masurowski, F.; Meyerhoff, J.; Oehlmann, M. Efficient and Equitable Spatial Allocation of Renewable Power Plants at the Country Scale. *Nat. Energy* **2017**, *2*, 17124.

(3) Dunn, B.; Kamath, H.; Tarascon, J. M. Electrical Energy Storage for the Grid: A Battery of Choices. *Science* **2011**, *334*, 928−935.

(4) Smalley, R. E. Future Global Energy Prosperity: The Terawatt Challenge. *MRS Bull.* **2005**, *30*, 412−417.

(5) Vesborg, P. C.; Jaramillo, T. F. Addressing the Terawatt Challenge: Scalability in the Supply of Chemical Elements for Renewable Energy. *RSC Adv.* **2012**, *2*, 7933−7947.

(6) Alstone, P.; Gershenson, G.; Kammen, D. M. Decentralized Energy Systems for Clean Electricity Access. *Nat. Clim. Change* **2015**, *5*, 305−314.

(7) Wang, Y.; Yi, J.; Xia, Y. Recent Progress in Aqueous Lithium-Ion Batteries. *Adv. Energy Mater.* **2012**, *2*, 830−840.

(8) Hwang, J. Y.; Myung, S. T.; Sun, Y. K. Sodium-Ion Batteries: Present and Future. *Chem. Soc. Rev.* **2017**, *46*, 3529−3614.

(9) Yamada, Y.; Koyama, Y.; Abe, T.; Ogumi, Z. Correlation between Charge− Discharge Behavior of Graphite and Solvation Structure of the Lithium Ion in Propylene Carbonate-Containing Electrolytes. *J. Phys. Chem. C* **2009**, *113*, 8948−8953.

(10) Yamada, Y.; Iriyama, Y.; Abe, T.; Ogumi, Z. Kinetics of Lithium Ion Transfer at the Interface between Graphite and Liquid Electrolytes: Effects of Solvent and Surface Film. *Langmuir* **2009**, *25*, 12766−12770.

(11) Ong, S. P.; Chevrier, V. L.; Hautier, G.; Jain, A.; Moore, C.; Kim, S.; Ma, X.; Ceder, G. Voltage, Stability and Diffusion Barrier Differences between Sodium-Ion and Lithium-Ion Intercalation Materials. *Energy Environ. Sci.* **2011**, *4*, 3680−3688.

(12) Kim, H.; Hong, J.; Park, K. Y.; Kim, H.; Kim, S. W.; Kang, K. Aqueous Rechargeable Li and Na Ion Batteries. *Chem. Rev.* **2014**, *114*, 11788−11827.

(13) Pasta, M.; Wessells, C. D.; Liu, N.; Nelson, J.; McDowell, M. T.; Huggins, R. A.; Toney, M. F.; Cui, Y. Full Open-Framework Batteries for Stationary Energy Storage. *Nat. Commun.* **2014**, *5*, 3007.

(14) Park, S. I.; Gocheva, I.; Okada, S.; Yamaki, J. Electrochemical Properties of $NaTi_2(PO_4)_3$ Anode for Rechargeable Aqueous Sodium-Ion Batteries. *J. Electrochem. Soc.* **2011**, *158*, A1067−A1070.

(15) Delmas, C.; Cherkaoui, F.; Nadiri, A.; Hagenmuller, P. A Nasicon-Type Phase as Intercalation Electrode: $NaTi_2(PO_4)_3$. *Mater. Res. Bull.* **1987**, *22*, 631−639.

(16) Pang, G.; Yuan, C.; Nie, P.; Ding, B.; Zhu, J.; Zhang, X. Synthesis of NASICON-Type Structured $NaTi_2(PO_4)_3$−Graphene Nanocomposite as an Anode for Aqueous Rechargeable Na-Ion Batteries. *Nanoscale* **2014**, *6*, 6328−6334.

(17) Qu, Q.; Liu, L.; Wu, Y.; Holze, R. Electrochemical Behavior of $V_2O_5 \cdot 0.6\,H_2O$ Nanoribbons in Neutral Aqueous Electrolyte Solution. *Electrochim. Acta* **2013**, *96*, 8−12.

(18) Deng, C.; Zhang, S.; Dong, Z.; Shang, Y. 1D Nanostructured Sodium Vanadium Oxide as a Novel Anode Material for Aqueous Sodium Ion Batteries. *Nano Energy* **2014**, *4*, 49−55.

(19) Qin, H.; Song, Z.; Zhan, H.; Zhou, Y. Aqueous Rechargeable Alkali-Ion Batteries with Polyimide Anode. *J. Power Sources* **2014**, *249*, 367−372.

(20) Lee, H.-W.; Wang, R. Y.; Pasta, M.; Lee, S. W.; Liu, N.; Cui, Y. Manganese hexacyanomanganate open framework as a high-capacity positive electrode material for sodium-ion batteries. *Nat. Commun.* **2014**, *5*, 5280.

(21) Yun, J.; Pfisterer, J.; Bandarenka, A. S. How Simple are the Models of Na Intercalation in Aqueous Media? *Energy Environ. Sci.* **2016**, *9*, 955−961.

(22) Ventosa, E.; Paulitsch, B.; Marzak, P.; Yun, J.; Schiegg, F.; Quast, T.; Bandarenka, A. S. The Mechanism of the Interfacial Charge and Mass Transfer during Intercalation of Alkali Metal Cations. *Adv. Sci.* **2016**, *3*, 1600211.

(23) Pham-Cong, D.; Choi, J. H.; Yun, J.; Bandarenka, A. S.; Kim, J.; Braun, P. V.; Jeong, S. Y.; Cho, C. R. Synergistically Enhanced Electrochemical Performance of Hierarchical $MoS_2/TiNb_2O_7$ Heteronanostructures as Anode Materials for Li-Ion Batteries. *ACS Nano* **2017**, *11*, 1026−1033.

(24) Paulitsch, B.; Yun, J.; Bandarenka, A. S. Electrodeposited $Na_2VO_x[Fe(CN)_6]$ Films as a Cathode Material for Aqueous Na-Ion Batteries. *ACS Appl. Mater. Interfaces* **2017**, *9*, 8107−8112.

(25) Scieszka, D.; Yun, J.; Bandarenka, A. S. What Do Laser-Induced Transient Techniques Reveal for Batteries? Na- and K-Intercalation from Aqueous Electrolytes as an Example. *ACS Appl. Mater. Interfaces* **2017**, *9*, 20213−20222.

(26) Colic, V.; Pohl, M. D.; Scieszka, D.; Bandarenka, A. S. Influence of the Electrolyte Composition on the Activity and Selectivity of Electrocatalytic Centers. *Catal. Today* **2016**, *262*, 24−35.

(27) Brauer, G., Ed. *Handbuch der Präparativen Anorganischen Chemie*, 2nd ed., Vol. *1*; Ferdinand Enke Verlag: Stuttgart, Germany, 1960.

(28) Bondarenko, A. S. Analysis of large experimental datasets in electrochemical impedance spectroscopy. *Anal. Chim. Acta* **2012**, *743*, 41−50.

(29) Horcas, I.; Fernandez, R.; Gomez-Rodriguez, J. M.; Colchero, J.; Gomez-Herrero, J.; Baro, A. M. WSXM: A Software for Scanning Probe Microscopy and a Tool for Nanotechnology. *Rev. Sci. Instrum.* **2007**, *78*, 013705.

(30) Nesbitt, H. W.; Banerjee, D. Interpretation of XPS Mn(2p) spectra of Mn oxyhydroxides and constraints on the mechanism of MnO2 precipitation. *Am. Mineral.* **1998**, *83*, 305−315.

10. References

[1] Schwieterman, E. W., Reinhard, C. T., Olson, S. L., Harman, C. E., Lyons, T. W. *Astrophys. J.* **2019**, *878* (1), 19.

[2] Habitable Exoplanets Catalog. http://phl.upr.edu/projects/habitable-exoplanets-catalog, (Accessed online December 2019)

[3] The Solar System and Beyond is Awash in Water. https://www.nasa.gov/jpl/the-solar-system-and-beyond-is-awash-in-water, (Accessed online December 2019)

[4] Blöschl, G., Hall, J., Parajka, J., Perdigão, R. A., Merz, B., Arheimer, B., Aronica, G. T., Bilibashi, A., Bonacci, O., Borga, M. *Science* **2017**, *357* (6351), 588-590.

[5] Diffenbaugh, N. S., Trapp, R. J., Brooks, H. *Trans., Am. Geophys. Union* **2008**, *89* (53), 553-554.

[6] Figueres, C., Le Quéré, C., Mahindra, A., Bäte, O., Whiteman, G., Peters, G., Guan, D. *Nature* **2018**, *564* 27-30.

[7] V. Masson-Delmotte, P. Zhai, H. O. Pörtner, D. Roberts, J. Skea, P.R. Shukla, A. Pirani, W. Moufouma-Okia, C. Péan, R. Pidcock, S. Connors, J. B. R. Matthews, Y. Chen, X. Zhou, M. I. Gomis, E. Lonnoy, T. Maycock, M. Tignor, T. Waterfield (eds.) *Global Warming of 1.5°C. An IPCC Special Report on the Impacts of Global Warming of 1.5 C Above Pre-Industrial Levels and Related Global Greenhouse Gas Emission Pathways, in the Context of Strengthening the Global Response to the Threat of Climate Change. Sustainable Development, and Efforts to Eradicate Poverty*, 2018.

[8] Watson, R. T., *Climate Change 2001: Synthesis Report. A Contribution of Working Groups I, II and III to the Third Assessment Report of the Integovernmental Panel on Climate Change*, Cambridge University Press, Cambridge, United Kingdom, and New York, NY, USA, 2001, 398p.

[9] Victor, D. G., Akimoto, K., Kaya, Y., Yamaguchi, M., Cullenward, D., Hepburn, C. *Nature* **2017**, *548* (7665), 25-27.

[10] Albert, S., Bronen, R., Tooler, N., Leon, J., Yee, D., Ash, J., Boseto, D., Grinham, A. *Reg. Environ. Change* **2018**, *18* (8), 2261-2272.

[11] Birkmann, J., Welle, T., Solecki, W., Lwasa, S., Garschagen, M. *Nature* **2016**, *537* (7622), 605-608.

[12] Peters, G. P., Geden, O. *Nat. Clim. Change* **2017**, *7* (9), 619.

[13] Peters, G. P., Andrew, R. M., Canadell, J. G., Fuss, S., Jackson, R. B., Korsbakken, J. I., Le Quéré, C., Nakicenovic, N. *Nat. Clim. Change* **2017**, *7* (2), 118.

[14] Cabeza, L. F., Palacios, A., Serrano, S., Ürge-Vorsatz, D., Barreneche, C. *Renewable*

Sustainable Energy Rev. **2018**, *82* 681-688.

[15] Tollefson, J. *Nature* **2018**, *562* (7726), 172-173.

[16] Tollefson, J. *Nature* **2019**, *573* 324-327.

[17] Zervos, A. *Renewables 2018 Global Status Report*, 2018.

[18] Fraunhofer ISE. https://www.energy-charts.de/power.htm?source=solar-wind&year=2019&month=2, (Accessed online December 2019)

[19] Zervos, A. *Renewables 2019 Global Status Report*, 2019.

[20] Lewis, N. S., Nocera, D. G. *Proc. Natl. Acad. Sci. U.S.A.* **2006**, *103* (43), 15729-15735.

[21] Lewis, N. S. *MRS Bull.* **2007**, *32* (10), 808-820.

[22] Yun, J., Pfisterer, J., Bandarenka, A. S. *Energy Environ. Sci.* **2016**, *9* (3), 955-961.

[23] Chen, H., Cong, T. N., Yang, W., Tan, C., Li, Y., Ding, Y. *Prog. Nat. Sci.* **2009**, *19* (3), 291-312.

[24] Rekioua, D., Matagne, E., *Optimization of Photovoltaic Power Systems: Modelization, Simulation and Control*, Springer Science & Business Media, New York, USA, 2012.

[25] Świerczyński, M., Teodorescu, R., Rasmussen, C. N., Rodriguez, P., Vikelgaard, H., In *Overview of the Energy Storage Systems for Wind Power Integration Enhancement*, 2010 IEEE International Symposium on Industrial Electronics, Bari, Italy, 2010, 3749-3756.

[26] Divya, K., Østergaard, J. *Electr. Power Syst. Res.* **2009**, *79* (4), 511-520.

[27] Rekioua, D., Bensmail, S., Bettar, N. *Int. J. Hydrogen Energy* **2014**, *39* (3), 1604-1611.

[28] Aissou, S., Rekioua, D., Mezzai, N., Rekioua, T., Bacha, S. *Energy Convers. Manage.* **2015**, *89* 615-625.

[29] Rekioua, D., *Wind power electric systems: Modelization, Simulation and Control*, Springer Science & Business Media, New York, USA, 2014.

[30] Idjdarene, K., Rekioua, D., Rekioua, T., Tounzi, A. *Analog Integr. Circuits Signal Process.* **2011**, *69* (1), 67-73.

[31] Mohammedi, A., Rekioua, D., Rekioua, T., Bacha, S. *Int. J. Hydrogen Energy* **2016**, *41* (45), 20928-20938.

[32] Dürr, M., Cruden, A., Gair, S., McDonald, J. *J. Power Sources* **2006**, *161* (2), 1400-1411.

[33] Prasad, A. R., Natarajan, E. *Energy* **2006**, *31* (12), 1943-1954.

[34] Bernard, N., Ahmed, H. B., Multon, B., Kerzreho, C., Delamare, J., Faure, F., In *Flywheel Energy Storage Systems in Hybrid and Distributed Electricity Generation*, PCIM 2003, Nuremberg, Germany May 2003, 9p hal-00674687.

[35] Ibrahim, H., Ilinca, A., Perron, J. *Renewable Sustainable Energy Rev.* **2008**, *12* (5), 1221-1250.

[36] Zakeri, B., Syri, S. *Renewable Sustainable Energy Rev.* **2015**, *42* 569-596.

[37] Zafirakis, D., Chalvatzis, K. J., Baiocchi, G., Daskalakis, G. *Appl. Energy* **2013**, *105* 138-154.

[38] Larcher, D., Tarascon, J.-M. *Nat. Chem.* **2015**, *7* (1), 19.

[39] Multon, B., Ruer, J., *Stocker l'électricité: oui, c'est indispensable et c'est possible. Pourquoi, où, comment?*, ECRIN, Paris, France, 2003.

[40] Zhao, H., Wu, Q., Hu, S., Xu, H., Rasmussen, C. N. *Appl. Energy* **2015**, *137* 545-553.

[41] Auer, J., Keil, J. *State-of-the-art electricity storage systems: indispensable elements of the energy revolution: Indispensable elements of the energy revolution*, Deutsche Bank Research, Frankfurt, Germany, 2012.

[42] Sebastián, R., Alzola, R. P. *Renewable Sustainable Energy Rev.* **2012**, *16* (9), 6803-6813.

[43] Inage, S.-i. *IEA* **2009**, *3* (4), 125.

[44] Kempener, R., Borden, E. *Battery Storage for Renewables: Market Status and Technology Outlook*, International Renewable Energy Agency, Abu Dhabi, 2015.

[45] Poullikkas, A. *Renewable Sustainable Energy Rev.* **2013**, *27* 778-788.

[46] Demirocak, D. E., Srinivasan, S. S., Stefanakos, E. K. *Applied Sciences* **2017**, *7* (7), 731.

[47] Amrouche, S. O., Rekioua, D., Rekioua, T., Bacha, S. *Int. J. Hydrogen Energy* **2016**, *41* (45), 20914-20927.

[48] Connolly, D., *An Investigation into the Energy Storage Technologies Available for the Integration of Alternative Generation Techniques*, 2007, Limerick, Ireland, University of Limerick.

[49] Tarascon, J.-M. *Nat. Chem.* **2010**, *2* (6), 510.

[50] Vesborg, P. C., Jaramillo, T. F. *RSC Adv.* **2012**, *2* (21), 7933-7947.

[51] Palizban, O., Kauhaniemi, K. *J. Energy Storage* **2016**, *6* 248-259.

[52] Cavanagh, K., Ward, J., Behrens, S., Bhatt, A., Ratnam, E., Oliver, E., Hayward, J.,

Electrical energy storage: technology overview and applications, CSIRO, Australia, 2015.

[53] Oberhofer, A., Meisen, P., *Energy Storage Technologies & Their Role in Renewable Integration*, Vol. 1, Global Energy Network Institute (GENI), 2012.

[54] Guney, M. S., Tepe, Y. *Renewable Sustainable Energy Rev.* **2017**, *75* 1187-1197.

[55] Kiehne, H. A., *Battery Technology Handbook*, Vol. 118, CRC Press, Florida, FL, 2003.

[56] *Electrical Energy Storage*, International Electrotechnical Commission (IEC), Geneva, Switzerland, 2011.

[57] Cabeza, L., Martorell, I., Miró, L., Fernández, A., Barreneche, C., *Introduction to thermal energy storage (TES) systems*, (Ed: Cabeza, L. F.), Woodhead Publishing, Cambridge, UK, 2015.

[58] Wagner, L. *Overview of Energy Storage Methods*, Mora Associates Ltd, 2007. http://moraassociates.com/reports/0712%20Energy%20storage.pdf

[59] Dunn, B., Kamath, H., Tarascon, J.-M. *Science* **2011**, *334* (6058), 928-935.

[60] Soloveichik, G. L. *Annu. Rev. Chem. Biomol. Eng.* **2011**, *2* 503-527.

[61] Jaiswal, A. *Renewable Sustainable Energy Rev.* **2017**, *72* 922-934.

[62] Armand, M., Tarascon, J.-M. *Nature* **2008**, *451* (7179), 652.

[63] Posada, J. O. G., Rennie, A. J., Villar, S. P., Martins, V. L., Marinaccio, J., Barnes, A., Glover, C. F., Worsley, D. A., Hall, P. J. *Renewable Sustainable Energy Rev.* **2017**, *68* 1174-1182.

[64] Palomares, V., Serras, P., Villaluenga, I., Hueso, K. B., Carretero-González, J., Rojo, T. *Energy Environ. Sci.* **2012**, *5* (3), 5884-5901.

[65] *Tesla investigates video of model s car exploding, https://www.theguardian.com/technology/2019/apr/22/tesla-investigates-video-of-model-s-car-exploding, (Accessed online December 2019).*

[66] Why those Samsung batteries exploded. https://www.washingtonpost.com/news/the-switch/wp/2016/09/12/why-those-samsung-batteries-exploded/, (Accessed online December 2019)

[67] ESS Equipped with LG Chem's Battery Produced from South Korea Causes Another Fire. http://english.etnews.com/20191023200001, (Accessed online December 2019)

[68] Pehlken, A., Albach, S., Vogt, T. *Int. J. Life Cycle Assess.* **2017**, *22* (1), 40-53.

[69] Grosjean, C., Miranda, P. H., Perrin, M., Poggi, P. *Renewable Sustainable Energy Rev.* **2012**, *16* (3), 1735-1744.

[70] Sterba, J., Krzemień, A., Fernández, P. R., García-Miranda, C. E., Valverde, G. F. *Resour. Policy* **2019**, *62* 416-426.

[71] Martin, G., Rentsch, L., Höck, M., Bertau, M. *Energy Storage Mater.* **2017**, *6* 171-179.

[72] Mohr, S. H., Mudd, G. M., Giurco, D. *Minerals* **2012**, *2* (1), 65-84.

[73] Habib, K., Wenzel, H. *J. Clean. Prod.* **2014**, *84* 348-359.

[74] Sverdrup, H. U. *Resour., Conserv. Recycl.* **2016**, *114* 112-129.

[75] Sonoc, A., Jeswiet, J. *Procedia Cirp* **2014**, *15* 289-293.

[76] McCormick, M. *Ind. Miner.* **2016**, *585* 18.

[77] Risacher, F., Fritz, B. *Aquat. Geochem.* **2009**, *15* (1-2), 123-157.

[78] Yaksic, A., Tilton, J. E. *Resour. Policy* **2009**, *34* (4), 185-194.

[79] Hsieh, I.-Y. L., Pan, M. S., Chiang, Y.-M., Green, W. H. *Appl. Energy* **2019**, *239* 218-224.

[80] William Clowes, T. W., *Congo May More Than Double Tax on Critical Cobalt Supply, https://www.bloomberg.com/news/articles/2018-01-10/congo-may-more-than-double-tax-on-critical-global-cobalt-supply, (Accessed online December 2019).*

[81] Armaroli, N., Balzani, V. *Angew. Chem. Int. Ed.* **2007**, *46* (1-2), 52-66.

[82] Pan, H., Hu, Y.-S., Chen, L. *Energy Environ. Sci.* **2013**, *6* (8), 2338-2360.

[83] Wu, X., Cao, Y., Ai, X., Qian, J., Yang, H. *Electrochem. Commun.* **2013**, *31* 145-148.

[84] Wu, X., Luo, Y., Sun, M., Qian, J., Cao, Y., Ai, X., Yang, H. *Nano Energy* **2015**, *13* 117-123.

[85] Kim, H., Hong, J., Park, K.-Y., Kim, H., Kim, S.-W., Kang, K. *Chem. Rev.* **2014**, *114* (23), 11788-11827.

[86] Hou, Z., Li, X., Liang, J., Zhu, Y., Qian, Y. *J. Mater. Chem. A* **2015**, *3* (4), 1400-1404.

[87] Ellis, B. L., Nazar, L. F. *Curr. Opin. Solid State Mater. Sci.* **2012**, *16* (4), 168-177.

[88] Whitacre, J., Tevar, A., Sharma, S. *Electrochem. Commun.* **2010**, *12* (3), 463-466.

[89] Li, Z., Young, D., Xiang, K., Carter, W. C., Chiang, Y. M. *Adv. Energy Mater.* **2013**, *3* (3), 290-294.

[90] Dong, X., Chen, L., Liu, J., Haller, S., Wang, Y., Xia, Y. *Sci. Adv.* **2016**, *2* (1), e1501038.

[91] Whitacre, J., Wiley, T., Shanbhag, S., Wenzhuo, Y., Mohamed, A., Chun, S., Weber, E., Blackwood, D., Lynch-Bell, E., Gulakowski, J. *J. Power Sources* **2012**, *213* 255-264.

[92] Pasta, M., Wessells, C. D., Huggins, R. A., Cui, Y. *Nat. Commun.* **2012**, *3* 1149.

[93] Pang, G., Nie, P., Yuan, C., Shen, L., Zhang, X., Zhu, J., Ding, B. *Energy Technol.* **2014**, *2* (8), 705-712.

[94] Haxel, G., *Rare Earth Elements: Critical Resources for High Technology*, Vol. 87, US Department of the Interior, US Geological Survey, 2002.

[95] Cotton, F. A., Wilkinson, G., Murillo, C. A., Bochmann, M., Grimes, R., *Advanced Inorganic Chemistry*, Vol. 6, Wiley New York, USA, 1988.

[96] Qu, Q., Fu, L., Zhan, X., Samuelis, D., Maier, J., Li, L., Tian, S., Li, Z., Wu, Y. *Energy Environ. Sci.* **2011**, *4* (10), 3985-3990.

[97] Tang, W., Zhu, Y., Hou, Y., Liu, L., Wu, Y., Loh, K. P., Zhang, H., Zhu, K. *Energy Environ. Sci.* **2013**, *6* (7), 2093-2104.

[98] Wang, G., Fu, L., Zhao, N., Yang, L., Wu, Y., Wu, H. *Angew. Chem. Int. Ed.* **2007**, *46* (1-2), 295-297.

[99] Wessells, C., Huggins, R. A., Cui, Y. *J. Power Sources* **2011**, *196* (5), 2884-2888.

[100] Chernyak, Y., Clements, J. H. *J. Chem. Eng. Data* **2004**, *49* (5), 1180-1184.

[101] Pasta, M., Wessells, C. D., Liu, N., Nelson, J., McDowell, M. T., Huggins, R. A., Toney, M. F., Cui, Y. *Nat. Commun.* **2014**, *5* 3007.

[102] Wessells, C. D., Peddada, S. V., Huggins, R. A., Cui, Y. *Nano Lett.* **2011**, *11* (12), 5421-5425.

[103] Wessells, C. D., Peddada, S. V., McDowell, M. T., Huggins, R. A., Cui, Y. *J. Electrochem. Soc.* **2011**, *159* (2), A98-A103.

[104] Whittaker, E., *A History of the Theories of Aether and Electricity (London: Nelson)*, Vol. Vol. 1, Thomas Nelson and Sons Ltd., London, UK and New York, USA, 1951.

[105] Yao, X., Luo, Y., Li, Y., Li, W., Fang, M., Shui, M., Shu, J., Ren, Y. *Mater. Res. Bull.* **2018**, *104* 194-201.

[106] Lefrou, C., Fabry, P., Poignet, J.-C., *Electrochemistry: the Basics, with Examples*, Springer Science & Business Media, New York, USA, 2012.

[107] Feiner, A.-S., McEvoy, A. *J. Chem. Educ.* **1994**, *71* (6), 493.

[108] Zhang, L. L., Zhao, X. *Chem. Soc. Rev.* **2009**, *38* (9), 2520-2531.

[109] Krischer, K., Savinova, E. R., *Fundamentals of electrocatalysis* in *Handbook of*

Heterogeneous Catalysis, Wiley-VCH Verlag GmbH & Co. KGaA, Weinheim, Germany 2008, 1873-1905.

[110] Guggenheim, E. *The Journal of Physical Chemistry* **1929**, *33* (6), 842-849.

[111] Guggenheim, E. *The Journal of Physical Chemistry* **1930**, *34* (7), 1540-1543.

[112] Butler, J. A. V. *Proc. R. Soc. London, Ser. A* **1926**, *112* (760), 129-136.

[113] Bagotsky, V. S., *Fundamentals of Electrochemistry*, Vol. 44, John Wiley & Sons, 2005.

[114] Laidler, K. J., *Theories of Chemical Reaction Rates*, McGraw-Hill, New York, USA, 1969.

[115] Gileadi, E. *J. Solid State Electrochem.* **2011**, *15* (7-8), 1359.

[116] Brain, M., Bryant, C. W., Pumphrey, C., How batteries work. http://skol.ca/wp-content/uploads/2012/09/battery.pdf, 1

[117] Arora, P., Zhang, Z. *Chem. Rev.* **2004**, *104* (10), 4419-4462.

[118] Gu, Y., Federici, J. *Batteries* **2018**, *4* (3), 42.

[119] Battery Performance Characteristics. https://www.mpoweruk.com/performance.htm, Woodbank Communications Ltd, South Crescent Road, Chester, CH4 7AU, (United Kingdom), (accessed November, 2019)

[120] Ramasamy, R. P., White, R. E., Popov, B. N. *J. Power Sources* **2005**, *141* (2), 298-306.

[121] Kassem, M., Bernard, J., Revel, R., Pelissier, S., Duclaud, F., Delacourt, C. *J. Power Sources* **2012**, *208* 296-305.

[122] Keil, P., Schuster, S. F., Wilhelm, J., Travi, J., Hauser, A., Karl, R. C., Jossen, A. *J. Electrochem. Soc.* **2016**, *163* (9), A1872-A1880.

[123] Ecker, M., Nieto, N., Käbitz, S., Schmalstieg, J., Blanke, H., Warnecke, A., Sauer, D. U. *J. Power Sources* **2014**, *248* 839-851.

[124] Sauvage, F., Baudrin, E., Tarascon, J.-M. *Sens. Actuators, B* **2007**, *120* (2), 638-644.

[125] Jung, Y. H., Lim, C. H., Kim, J.-H., Kim, D. K. *RSC Adv.* **2014**, *4* (19), 9799-9802.

[126] Song, W., Ji, X., Zhu, Y., Zhu, H., Li, F., Chen, J., Lu, F., Yao, Y., Banks, C. E. *ChemElectroChem* **2014**, *1* (5), 871-876.

[127] Kraft, A., *The History of Prussian Blue* in *Prussian Blue-Type Nanoparticles and Nanocomposites: Synthesis, Devices, and Applications*, Pan Standford Publishing Pte. Ltd., Singapore 2019, 1-26.

[128] Wang, B., Han, Y., Wang, X., Bahlawane, N., Pan, H., Yan, M., Jiang, Y. *iScience* **2018**, *3* 110-133.

[129] Qian, J., Wu, C., Cao, Y., Ma, Z., Huang, Y., Ai, X., Yang, H. *Adv. Energy Mater.* **2018**, *8* (17), 1702619.

[130] Su, D., Cortie, M., Wang, G. *Adv. Energy Mater.* **2017**, *7* (8), 1602014.

[131] Chen, W., Zeng, K., Liu, H., Ouyang, J., Wang, L., Liu, Y., Wang, H., Deng, L., Liu, Y. N. *Adv. Funct. Mater.* **2017**, *27* (11), 1605795.

[132] Han, L., Yu, X. Y., Lou, X. W. *Adv. Mater.* **2016**, *28* (23), 4601-4605.

[133] Zhang, W., Hu, S., Yin, J.-J., He, W., Lu, W., Ma, M., Gu, N., Zhang, Y. *J. Am. Chem. Soc.* **2016**, *138* (18), 5860-5865.

[134] Larionova, J., Guari, Y., Long, J., *Prussian Blue Type Nanoparticles for Biomedical Applications* in *Prussian Blue-Type Nanoparticles and Nanocomposites: Synthesis, Devices, and Applications*, Pan Standford Publishing Pte. Ltd., Singapore 2019, 279.

[135] West, A. R., *Basic Solid State Chemistry*, John Wiley & Sons Inc., 1999.

[136] Giménez-Romero, D., Agrisuelas, J., García-Jareño, J. J., Gregori, J., Gabrielli, C., Perrot, H., Vicente, F. *J. Am. Chem. Soc.* **2007**, *129* (22), 7121-7126.

[137] Yamamoto, T., Umemura, Y., Sato, O., Einaga, Y. *J. Am. Chem. Soc.* **2005**, *127* (46), 16065-16073.

[138] Champion, G., Escax, V., Cartier dit Moulin, C., Bleuzen, A., Villain, F., Baudelet, F., Dartyge, E., Verdaguer, M. *J. Am. Chem. Soc.* **2001**, *123* (50), 12544-12546.

[139] Carpenter, M. K., Conell, R. S., Simko, S. J. *Inorg. Chem.* **1990**, *29* (4), 845-850.

[140] Ostrom, G. S., Buttry, D. A. *J. Electroanal. Chem. Interfacial Electrochem.* **1988**, *256* (2), 411-431.

[141] Shaojun, D., Fengbin, L. *J. Electroanal. Chem. Interfacial Electrochem.* **1986**, *210* (1), 31-44.

[142] Itaya, K., Shibayama, K., Akahoshi, H., Toshima, S. *J. Appl. Phys.* **1982**, *53* (1), 804-805.

[143] Kulesza, P., Malik, M., Miecznikowski, K., Wolkiewicz, A., Zamponi, S., Berrettoni, M., Marassi, R. *J. Electrochem. Soc.* **1996**, *143* (1), L10-L12.

[144] Zamponi, S., Giorgetti, M., Berrettoni, M., Kulesza, P. J., Cox, J. A., Kijak, A. *Electrochim. Acta* **2005**, *51* (1), 118-124.

[145] Hartmann, M., Grabner, E., Bergveld, P. *Sens. Actuators, B* **1991**, *4* (3-4), 333-336.

[146] Nguyen, B. T. T., Ang, J. Q., Toh, C.-S. *Electrochem. Commun.* **2009**, *11* (10), 1861-1864.

[147] Ho, K.-C., Lin, C.-L. *Sens. Actuators, B* **2001**, *76* (1-3), 512-518.

[148] Scharf, U., Grabner, E. W. *Electrochim. Acta* **1996**, *41* (2), 233-239.

[149] Karyakin, A. A., Karyakina, E. E., Gorton, L. *J. Electroanal. Chem.* **1998**, *456* (1-2), 97-104.

[150] Pintado, S., Goberna-Ferrón, S., Escudero-Adán, E. C., Galán-Mascarós, J. R. n. *J. Am. Chem. Soc.* **2013**, *135* (36), 13270-13273.

[151] Lu, Y., Wang, L., Cheng, J., Goodenough, J. B. *Chem. Commun.* **2012**, *48* (52), 6544-6546.

[152] Nie, P., Shen, L., Luo, H., Ding, B., Xu, G., Wang, J., Zhang, X. *J. Mater. Chem. A* **2014**, *2* (16), 5852-5857.

[153] Matsuda, T., Moritomo, Y. *Appl. Phys. Express* **2011**, *4* (4), 047101.

[154] Neff, V. D. *J. Electrochem. Soc.* **1985**, *132* 1382-1384.

[155] Nitta, N., Wu, F., Lee, J. T., Yushin, G. *Mater. Today* **2015**, *18* (5), 252-264.

[156] Lee, H.-W., Wang, R. Y., Pasta, M., Lee, S. W., Liu, N., Cui, Y. *Nat. Commun.* **2014**, *5* 5280.

[157] Xu, Y., Zheng, S., Tang, H., Guo, X., Xue, H., Pang, H. *Energy Storage Mater.* **2017**, *9* 11-30.

[158] Hurlbutt, K., Wheeler, S., Capone, I., Pasta, M. *Joule* **2018**, *2* (10), 1950-1960.

[159] Bond, A. M., Feldberg, S. W. *J. Phys. Chem. B* **1998**, *102* (49), 9966-9974.

[160] DuVall, S. H., McCreery, R. L. *Anal. Chem.* **1999**, *71* (20), 4594-4602.

[161] Eliaz, N., Gileadi, E., *Physical Electrochemistry: Fundamentals, Techniques, and Applications*, Wiley-VCH, Weinheim, Germany, 2019.

[162] Macdonald, D. D. *Electrochim. Acta* **2006**, *51* (8-9), 1376-1388.

[163] Parsons, R., Macdonald, D., *DD Macdonald, Transient Techniques in Electrochemistry,(1977), xii+ 326 pp.,*, Elsevier, Plenum, New York, USA, 1979, 326 pp.

[164] Sluyters-Rehbach, M., Sluyters, J., *Electroanalytical Chemistry*, Vol. 4 (Ed: Bard, A.), Marcel Dekker, New York, USA 1970, 75.

[165] Jüttner, K. *Electrochim. Acta* **1990**, *35* (10), 1501-1508.

[166] Lasia, A., *Electrochemical impedance spectroscopy and its applications* in *Modern Aspects of Electrochemistry*, Vol. 32, Springer, New York, USA 2002, 143-248.

[167] Dolin, P., Ershler, B. *Acta Physicochim. URSS* **1940**, *13* 747.

[168] Randles, J. E. B. *Discuss. Faraday Soc.* **1947**, *1* 11-19.

[169] Lasia, A., Conway, B., Bockris, J., White, R., *Modern Aspects of Electrochemistry, vol. 32*, Springer, New York, USA, 1999.

[170] Tarantola, A., *Inverse Problem Theory and Methods for Model Parameter Estimation*, Vol. 89, SIAM, Philadelphia, USA, 2005.

[171] Lasia, A., *Chapter 5. Faradaic Reaction Involving One Adsorbed Species with Subsequent Desorption* in *Electrochemical Impedance Spectroscopy and its Applications*, Springer, New York, USA 2014, 7-66.

[172] Nomura, T., Okuhara, M. *Anal. Chim. Acta* **1982**, *142* 281-284.

[173] Czanderna, A., Lu, C., *Introduction, history, and overview of applications of piezoelectric quartz crystal microbalances* in *Methods and Phenomena*, Vol. 7, Elsevier, 1984, 1-18.

[174] Bruckenstein, S., Shay, M. *Electrochim. Acta* **1985**, *30* (10), 1295-1300.

[175] Bard, A. J., Faulkner, L. R., *Electrochemical Methods: Fundamentals and applications*, Vol. 2, JOHN WILEY & SONS, INC., New York, USA, 2001.

[176] Shouji, E., Buttry, D. A. *Electrochim. Acta* **2000**, *45* (22-23), 3757-3764.

[177] Jiang, H. F., Chen, C. J., Li, H. H. *Adv. Mater. Res.* **2013**, *791* 581-584.

[178] Deakin, M. R., Buttry, D. A. *Anal. Chem.* **1989**, *61* (20), 1147A-1154A.

[179] Sauerbrey, G. *Z. Phys.* **1959**, *155* (2), 206-222.

[180] Ispas, A., Bund, A., *Electrochemical Quartz Crystal Microbalance* in *Encyclopedia of Applied Electrochemistry*, (Eds: Kreysa, G., Ota, K.-i., Savinell, R. F.), Springer New York, New York, USA 2014, 554-568.

[181] Brown, M. E., Gallagher, P. K., *Handbook of Thermal Analysis and Calorimetry: Recent Advances, Techniques and Applications*, Vol. 5, Elsevier, 2011.

[182] Berkes, B. z. B., Inzelt, G. r., Schuhmann, W., Bondarenko, A. S. *J. Phys. Chem. C* **2012**, *116* (20), 10995-11003.

[183] Schmuki, P., Virtanen, S., *Electrochemistry at the Nanoscale*, Springer Science & Business Media, New York, USA, 2009.

[184] Rugar, D., Hansma, P. *Phys. Today* **1990**, *43* (10), 23-30.

[185] Morris, V. J., Kirby, A. R., Gunning, A. P., *Atomic Force Microscopy for Biologists*, Imperial College Press, London , UK, 1999.

[186] Giessibl, F. J. *Rev. Mod. Phys.* **2003**, *75* (3), 949.

[187] Eaton, P., West, P., *Atomic force microscopy*, Oxford university press, 2010.

[188] Zhong, Q., Inniss, D., Kjoller, K., Elings, V. *Surf. Sci. Lett.* **1993**, *290* (1-2), L688-L692.

[189] Stojilovic, N. *J. Chem. Educ.* **2012**, *89* (10), 1331-1332.

[190] Hüfner, S., *Photoelectron Spectroscopy: Principles and Applications*, Springer Science & Business Media, New York, USA, 2013.

[191] Scieszka, D., *In-Depth Characterization of Electrified Solid/Liquid Interfaces with the Laser- Induced Current Transient Technique*, PhD, 2019, Technische Universität München.

[192] Adams, M. *J. South. Afr. Inst. Min. Metall.* **1992**, *92* (1), 17-25.

[193] Tokuda, K., Gueshi, T., Aoki, K., Matsuda, H. *J. Electrochem. Soc.* **1985**, *132* (10), 2390-2398.

[194] Mansfeld, F., Lin, S., Chen, Y., Shih, H. *J. Electrochem. Soc.* **1988**, *135* (4), 906-907.

[195] GAMRY Instruments, Reference Electrodes. https://www.gamry.com/application-notes/instrumentation/reference-electrodes/, (accessed November, 2019)

[196] Luo, J.-Y., Cui, W.-J., He, P., Xia, Y.-Y. *Nat. Chem.* **2010**, *2* (9), 760.

[197] Marzak, P., Yun, J., Dorsel, A., Kriele, A., Gilles, R., Schneider, O., Bandarenka, A. S. *J. Phys. Chem. C* **2018**, *122* (16), 8760-8768.

[198] Marzak, P., *Influence of the Alkali Metal Cation Solvation on their Intercalation into Battery Cathode Materials*, MSc, 2016, Technische Universität München.

[199] Prabakar, S. R., Narayanan, S. S. *Food Chem.* **2010**, *118* (2), 449-455.

[200] Pham-Cong, D., Choi, J. H., Yun, J., Bandarenka, A. S., Kim, J., Braun, P. V., Jeong, S. Y., Cho, C. R. *ACS Nano* **2017**, *11* (1), 1026-1033.

[201] Ventosa, E., Paulitsch, B., Marzak, P., Yun, J., Schiegg, F., Quast, T., Bandarenka, A. S. *Adv. Sci.* **2016**, *3* (12), 1600211.

[202] Dinkelacker, F., Marzak, P., Yun, J., Liang, Y., Bandarenka, A. S. *ACS Appl. Mater. Interfaces* **2018**, *10* (16), 14063-14069.

[203] Li, X., Du, X., Wang, Z., Hao, X., Guan, G., Zhang, H., Abuliti, A., Ma, G. *J. Electroanal. Chem.* **2014**, *717* 69-77.

[204] LI, Y.-g., HAO, X.-g., MA, X.-l., ZHANG, Z.-l., LIU, S.-b., SUN, Y.-p. *Journal of Functional Materials* **2008**, *6*.

[205] Liao, S., Xue, C., Wang, Y., Zheng, J., Hao, X., Guan, G., Abuliti, A., Zhang, H., Ma, G. *Sep. Purif. Technol.* **2015**, *139* 63-69.

[206] Mao Zuqiu, H. X., Yibin, L., Zhonglin, Z., Zhongde, W., Shibin, L. *Technology of Water Treatment* **2009**, *8*.

[207] Pandey, P. C., Pandey, A. K. *Analyst* **2012**, *137* (14), 3306-3313.

[208] Sophia, S. J., Devi, S., Pandian, K. *Int. J. Electrochem. Sci.* **2012**, *7* 6580-6598.

[209] Liu, M., Li, P., Cheng, Y., Xian, Y., Zhang, C., Jin, L. *Anal. Bioanal. Chem.* **2004**, *380* (5-6), 742-750.

[210] Prabakar, S. R., Narayanan, S. S. *Anal. Bioanal. Chem.* **2006**, *386* (7-8), 2107-2115.

[211] Cheng, W., Dong, S., Wang, E. *Chem. Mater.* **2003**, *15* (13), 2495-2501.

[212] Mayer, M., Dedovets, D., Guari, Y., Larionova, J., Long, J., Causse, J. *J. Colloid Interface Sci.* **2017**, *505* 364-372.

[213] Wang, F., Wang, J., Chen, H., Dong, S. *J. Electroanal. Chem.* **2007**, *600* (2), 265-274.

[214] Bocarsly, A. B., Sinha, S. *J. Electroanal. Chem. Interfacial Electrochem.* **1982**, *140* (1), 167-172.

[215] Sinha, S., Humphrey, B. D., Bocarsly, A. B. *Inorg. Chem.* **1984**, *23* (2), 203-212.

[216] Kalwellis-Mohn, S., Grabner, E. *Electrochim. Acta* **1989**, *34* (8), 1265-1269.

[217] Omarova, M., Koishybay, A., Yesibolati, N., Mentbayeva, A., Umirov, N., Ismailov, K., Adair, D., Babaa, M.-R., Kurmanbayeva, I., Bakenov, Z. *Electrochim. Acta* **2015**, *184* 58-63.

[218] Krishnamoorthy, K., Pazhamalai, P., Sahoo, S., Lim, J. H., Choi, K. H., Kim, S. J. *ChemElectroChem* **2017**, *4* (12), 3302-3308.

[219] Lee, H.-W., Pasta, M., Wang, R. Y., Ruffo, R., Cui, Y. *Faraday Discuss.* **2015**, *176* 69-81.

[220] Jiang, H., Xu, Y.-T., Wang, T., Zhu, P.-L., Yu, S., Yu, Y., Fu, X.-Z., Sun, R., Wong, C.-P. *Electrochim. Acta* **2015**, *166* 157-162.

[221] Ma, X., Du, X., Li, X., Hao, X., Jagadale, A. D., Abudula, A., Guan, G. *J. Alloys Compd.* **2017**, *695* 294-301.

[222] Chen, J., Huang, K., Liu, S. *Electrochem. Commun.* **2008**, *10* (12), 1851-1855.

[223] Zhou, Q., Wei, T., Liu, Z., Zhang, L., Yuan, B., Fan, Z. *Electrochim. Acta* **2019**, *303* 40-48.

[224] Nie, P., Yuan, J., Wang, J., Le, Z., Xu, G., Hao, L., Pang, G., Wu, Y., Dou, H., Yan, X. *ACS Appl. Mater. Interfaces* **2017**, *9* (24), 20306-20312.

[225] Berkes, B. B., Maljusch, A., Schuhmann, W., Bondarenko, A. S. *J. Phys. Chem. C* **2011**, *115* (18), 9122-9130.

[226] Bondarenko, A. S. *Anal. Chim. Acta* **2012**, *743* 41-50.

[227] Bondarenko, A., Ragoisha, G., *Inverse Problem in Potentiodynamic Electrochemical Impedance*, Nova Science Publishers, New York, USA, 2005.

[228] Maddala, J., Sambath, K., Kumar, V., Ramanathan, S. *J. Electroanal. Chem.* **2010**, *638* (2), 183-188.

[229] Brett, C. *J. Appl. Electrochem.* **1990**, *20* (6), 1000-1003.

[230] Aoki, I. V., Bernard, M.-C., De Torresi, S. C., Deslouis, C., de Melo, H. G., Joiret, S., Tribollet, B. *Electrochim. Acta* **2001**, *46* (12), 1871-1878.

[231] Yadav, A., Nishikata, A., Tsuru, T. *Corros. Eng., Sci. Technol.* **2008**, *43* (1), 23-29.

[232] Cachet, C., Ströder, U., Wiart, R. *J. Appl. Electrochem.* **1981**, *11* (5), 613-623.

[233] Baker, B. C., West, A. C. *J. Electrochem. Soc.* **1997**, *144* (1), 164-169.

[234] Baker, B. C., West, A. C. *J. Electrochem. Soc.* **1997**, *144* (1), 169-175.

[235] Haynes, W. M., *CRC Handbook of Chemistry and Physics, 96th Edition*, CRC Press, 2015, p. 5-72.

[236] Wolf, A. V., *Aqueous Solutions and Body fluids; Their Concentrative Properties and Conversion Tables*, Hoeber Medical Division, Harper & Row, New York, USA, 1966.

[237] Steen, W. A., Han, S.-W., Yu, Q., Gordon, R. A., Cross, J. O., Stern, E. A., Seidler, G. T., Jeerage, K. M., Schwartz, D. T. *Langmuir* **2002**, *18* (20), 7714-7721.

[238] Itaya, K., Uchida, I., Neff, V. D. *Acc. Chem. Res.* **1986**, *19* (6), 162-168.

[239] Bagkar, N., Betty, C., Hassan, P., Kahali, K., Bellare, J., Yakhmi, J. *Thin Solid Films* **2006**, *497* (1-2), 259-266.

[240] Jin, W., Toutianoush, A., Pyrasch, M., Schnepf, J., Gottschalk, H., Rammensee, W., Tieke, B. *J. Phys. Chem. B* **2003**, *107* (44), 12062-12070.

[241] Wang, Y., Zhu, G., Wang, E. *J. Electroanal. Chem.* **1997**, *430* (1-2), 127-132.

[242] Tsiafoulis, C. G., Trikalitis, P. N., Prodromidis, M. I. *Electrochem. Commun.* **2005**,

7 (12), 1398-1404.

[243] Liu, C., Dong, S. *Electroanalysis* **1997**, *9* (11), 838-842.

[244] Lee, J. H., Ali, G., Kim, D. H., Chung, K. Y. *Adv. Energy Mater.* **2017**, *7* (2), 1601491.

[245] Jiang, P., Lei, Z., Chen, L., Shao, X., Liang, X., Zhang, J., Wang, Y., Zhang, J., Liu, Z., Feng, J. *ACS Appl. Mater. Interfaces* **2019**, *11* (32), 28762-28768.

[246] Paulitsch, B., Yun, J., Bandarenka, A. S. *ACS Appl. Mater. Interfaces* **2017**, *9* (9), 8107-8112.

[247] Wagner, C. D., Muilenberg, G. E., *Handbook of X-ray Photoelectron Spectroscopy : A Reference Book of Standard Data for Use in X-Ray Photoelectron Spectroscopy*, Physical Electronics Division, Perkin-Elmer Corp., Eden Prairie, Minn., 1979.

[248] Yang, Y., Brownell, C., Sadrieh, N., May, J., Del Grosso, A., Place, D., Leutzinger, E., Duffy, E., He, R., Houn, F. *Clin. Toxicol.* **2007**, *45* (7), 776-781.

[249] Kumar, A. S., Barathi, P., Pillai, K. C. *J. Electroanal. Chem.* **2011**, *654* (1-2), 85-95.

[250] Mimura, H., Lehto, J., Harjula, R. *J. Nucl. Sci. Technol.* **1997**, *34* (6), 582-587.

[251] Wang, L., Lu, Y., Liu, J., Xu, M., Cheng, J., Zhang, D., Goodenough, J. B. *Angew. Chem. Int. Ed.* **2013**, *52* (7), 1964-1967.

[252] Yang, D., Xu, J., Liao, X.-Z., He, Y.-S., Liu, H., Ma, Z.-F. *Chem. Commun.* **2014**, *50* (87), 13377-13380.

[253] Bors, R., Yun, J., Marzak, P., Fichtner, J., Scieszka, D., Bandarenka, A. S. *ACS Omega* **2018**, *3* (5), 5111-5115.

[254] Scholz, F., Dostal, A. *Angew. Chem., Int. Ed. Engl.* **1996**, *34* (23-24), 2685-2687.

[255] Jiang, M., Zhou, X., Zhao, Z. *J. Electroanal. Chem. Interfacial Electrochem.* **1990**, *287* (2), 389-394.

[256] Gao, Z. *J. Electroanal. Chem.* **1994**, *370* (1-2), 95-102.

[257] Singh, R. P., Pambid, E. R. *Analyst* **1990**, *115* (3), 301-304.

[258] Jain, A. K., Agrawal, S., Singh, R. P. *Anal. Chem.* **1980**, *52* (8), 1364-1366.

[259] Zakaria, E. *J. Radioanal. Nucl. Chem.* **2005**, *264* (3), 629-635.

[260] Lin, M., Tseng, T. *Analyst* **1998**, *123* (1), 159-163.

[261] Zhang, W., Wang, G., Zhang, X., Fang, B. *Electroanalysis* **2009**, *21* (2), 179-183.

[262] Fang, B., Shen, R., Zhang, W., Wang, G., Zhang, C. *Microchim. Acta* **2009**, *165* (1-

2), 231-236.

[263] Milardović, S., Grabarić, Z., Tkalčec, M., Rumenjak, V. *J. AOAC Int.* **2000**, *83* (5), 1212-1217.

[264] Tseng, T.-F., Yang, Y.-L., Lou, S.-L., "Chromium Hexacyanoferrate Modified Biosensor Based on PQQ-Dependent Glucose Dehydrogenase", presented at *2007 29th Annual International Conference of the IEEE Engineering in Medicine and Biology Society*, 2007.

[265] Cottica, S. M., Nozaki, J., Nakatani, H. S., Oliveira, C. C., Souza, N. E. d., Visentainer, J. V. *J. Braz. Chem. Soc.* **2009**, *20* (3), 496-501.

[266] Tseng, T.-F., Yang, Y.-L., Lin, Y.-J., Lou, S.-L. *Sensors* **2010**, *10* (7), 6347-6360.

[267] Lin, M. S., Shih, W. C. *Anal. Chim. Acta* **1999**, *381* (2-3), 183-189.

[268] de Lara González, G. L., Kahlert, H., Scholz, F. *Electrochim. Acta* **2007**, *52* (5), 1968-1974.

[269] Shen, R., Li, X., Lium, G., Ji, Y., Wang, G., Fang, B. *Electroanalysis* **2010**, *22* (20), 2383-2388.

[270] Eftekhari, A. *J. Power Sources* **2003**, *117* (1-2), 249-254.

[271] Karyakin, A. A. *Electroanalysis* **2001**, *13* (10), 813-819.

[272] Vanysek, P., *CRC Handbook of Chemistry and Physics* Vol. 8 (Ed: Lide, D. R.), CRC Press LLC, Corporate Blvd., Boca Raton, FL 33431, USA, 2000, 23-33.

[273] Amutha, R., Josiah, J., Jebin, J. A., Jagannathan, P., Berchmans, S. *J. Appl. Electrochem.* **2010**, *40* (11), 1985-1990.

[274] Yamashita, T., Hayes, P. *Appl. Surf. Sci.* **2008**, *254* (8), 2441-2449.

[275] Wang, R. Y., Wessells, C. D., Huggins, R. A., Cui, Y. *Nano Lett.* **2013**, *13* (11), 5748-5752.

[276] Grid-Scale Energy Storage System for Back-Up Power and Power Quality Applications. https://www.skeletontech.com/skelgrid, (accessed November, 2019)

[277] Skeleton Technologies GmbH. https://www.skeletontech.com/hubfs/Skeleton-170Vmodule_datasheet.pdf, (accessed November, 2019)

[278] Tang, W., Zhu, Y., Hou, Y., Liu, L., Wu, Y., Loh, K., Zhang, H., Zhu, K. *Energy Environ. Sci.* **2013**, *6* (7), 2093-2104.

[279] Li, W., Dahn, J. R., Wainwright, D. S. *Science* **1994**, *264* (5162), 1115-1118.

[280] Yun, J., Schiegg, F. A., Liang, Y., Scieszka, D., Garlyyev, B., Kwiatkowski, A.,

Wagner, T., Bandarenka, A. S. *ACS Appl. Energy Mater.* **2018**, *1* (1), 123-128.

[281] Park, S. I., Gocheva, I., Okada, S., Yamaki, J.-i. *J. Electrochem. Soc.* **2011**, *158* (10), A1067-A1070.

[282] Wu, W., Mohamed, A., Whitacre, J. *J. Electrochem. Soc.* **2013**, *160* (3), A497-A504.

[283] Li, Z., Ravnsbæk, D. B., Xiang, K., Chiang, Y.-M. *Electrochem. Commun.* **2014**, *44* 12-15.

[284] Li, X., Zhu, X., Liang, J., Hou, Z., Wang, Y., Lin, N., Zhu, Y., Qian, Y. *J. Electrochem. Soc.* **2014**, *161* (6), A1181-A1187.

[285] Arun, N., Aravindan, V., Ling, W. C., Madhavi, S. *J. Alloys Compd.* **2014**, *603* 48-51.

[286] Mohamed, A. I., Sansone, N. J., Kuei, B., Washburn, N. R., Whitacre, J. *J. Electrochem. Soc.* **2015**, *162* (10), A2201-A2207.

[287] Yunwei, H., Hua, Y., Yuanxin, W., Chi, C., Shi, Y., Changchun, A. *Electrochemistry* **2016**, *84* (9), 705-708.

[288] Cao, X., Yang, Y. *Mater. Lett.* **2018**, *231* 183-186.

[289] Pang, G., Yuan, C., Nie, P., Ding, B., Zhu, J., Zhang, X. *Nanoscale* **2014**, *6* (12), 6328-6334.

[290] Lei, P., Li, S., Luo, D., Huang, Y., Tian, G., Xiang, X. *J. Electroanal. Chem.* **2019**.

[291] Liu, Z., An, Y., Pang, G., Dong, S., Xu, C., Mi, C., Zhang, X. *Chem. Eng. J.* **2018**, *353* 814-823.

[292] Hung, T.-F., Lan, W.-H., Yeh, Y.-W., Chang, W.-S., Yang, C.-C., Lin, J.-C. *ACS Sustainable Chem. Eng.* **2016**, *4* (12), 7074-7079.

[293] Gao, H., Goodenough, J. B. *Angew. Chem. Int. Ed.* **2016**, *55* (41), 12768-12772.

[294] Zhang, F., Li, W., Xiang, X., Sun, M. *Chem. Eur.* **2017**, *23* (52), 12944-12948.

[295] Wang, H., Zhang, T., Chen, C., Ling, M., Lin, Z., Zhang, S., Pan, F., Liang, C. *Nano Res.* **2018**, *11* (1), 490-498.

[296] Qiu, S., Wu, X., Wang, M., Lucero, M., Wang, Y., Wang, J., Yang, Z., Xu, W., Wang, Q., Gu, M. *Nano Energy* **2019**, *64* 103941.

[297] Qin, H., Song, Z., Zhan, H., Zhou, Y. *J. Power Sources* **2014**, *249* 367-372.

[298] Liang, Y., Jing, Y., Gheytani, S., Lee, K.-Y., Liu, P., Facchetti, A., Yao, Y. *Nat. Mater.* **2017**, *16* (8), 841.

[299] Zhong, L., Lu, Y., Li, H., Tao, Z., Chen, J. *ACS Sustainable Chem. Eng.* **2018**, *6* (6), 7761-7768.

[300] Lim, H., Jung, J. H., Park, Y. M., Lee, H.-N., Kim, H.-J. *Appl. Surf. Sci.* **2018**, *446* 131-138.

[301] Deng, W., Shen, Y., Qian, J., Yang, H. *Chem. Commun.* **2015**, *51* (24), 5097-5099.

[302] Gu, T., Zhou, M., Liu, M., Wang, K., Cheng, S., Jiang, K. *RSC Adv.* **2016**, *6* (58), 53319-53323.

[303] Liu, Y., Zhang, B., Xiao, S., Liu, L., Wen, Z., Wu, Y. *Electrochim. Acta* **2014**, *116* 512-517.

[304] Deng, C., Zhang, S., Dong, Z., Shang, Y. *Nano Energy* **2014**, *4* 49-55.

[305] Kühnel, R.-S., Reber, D., Remhof, A., Figi, R., Bleiner, D., Battaglia, C. *Chem. Commun.* **2016**, *52* (68), 10435-10438.

[306] Suo, L., Borodin, O., Gao, T., Olguin, M., Ho, J., Fan, X., Luo, C., Wang, C., Xu, K. *Science* **2015**, *350* (6263), 938-943.

[307] Suo, L., Borodin, O., Sun, W., Fan, X., Yang, C., Wang, F., Gao, T., Ma, Z., Schroeder, M., von Cresce, A. *Angew. Chem. Int. Ed.* **2016**, *55* (25), 7136-7141.

[308] Suo, L., Borodin, O., Wang, Y., Rong, X., Sun, W., Fan, X., Xu, S., Schroeder, M. A., Cresce, A. V., Wang, F. *Adv. Energy Mater.* **2017**, *7* (21), 1701189.

[309] Nakamoto, K., Sakamoto, R., Ito, M., Kitajou, A., Okada, S. *Electrochemistry* **2017**, *85* (4), 179-185.

[310] Wu, W., Shabhag, S., Chang, J., Rutt, A., Whitacre, J. F. *J. Electrochem. Soc.* **2015**, *162* (6), A803-A808.

[311] Chen, R., Tanaka, H., Kawamoto, T., Asai, M., Fukushima, C., Na, H., Kurihara, M., Watanabe, M., Arisaka, M., Nankawa, T. *Electrochim. Acta* **2013**, *87* 119-125.

[312] Strmcnik, D., Kodama, K., Van der Vliet, D., Greeley, J., Stamenkovic, V. R., Marković, N. *Nat. Chem.* **2009**, *1* (6), 466.

[313] Escudero-Escribano, M., Zoloff Michoff, M. E., Leiva, E. P., Marković, N. M., Gutiérrez, C., Cuesta, Á. *ChemPhysChem* **2011**, *12* (12), 2230-2234.

[314] Nakamura, M., Sato, N., Hoshi, N., Sakata, O. *ChemPhysChem* **2011**, *12* (8), 1430-1434.

[315] Ragoisha, G., Auchynnikava, T., Streltsov, E., Rabchynski, S. *Electrochim. Acta* **2014**, *122* 218-223.

[316] Stoffelsma, C., Rodriguez, P., Garcia, G., Garcia-Araez, N., Strmcnik, D., Marković, N. M., Koper, M. T. *J. Am. Chem. Soc.* **2010**, *132* (45), 16127-16133.

[317] Tymoczko, J., Colic, V., Ganassin, A., Schuhmann, W., Bandarenka, A. S. *Catal. Today* **2015**, *244* 96-102.

[318] Katsounaros, I., Mayrhofer, K. J. *Chem. Commun.* **2012**, *48* (53), 6660-6662.

[319] Suntivich, J., Perry, E. E., Gasteiger, H. A., Shao-Horn, Y. *Electrocatalysis* **2013**, *4* (1), 49-55.

[320] Brauer (Hrsg.), G., *Handbuch der Präparativen Anorganischen Chemie*, 3. Aufl., Bd. III, Ferdinand Enke Verlag, Stuttgart, 1981, p. 1595.